

AD-A230 834

SERRATED CIRCULAR APERTURES:
OPTICAL FOURIER TRANSFORMS AND FRACTAL ANALYSIS

by

Madeleine Marie Beal

Submitted in Partial Fulfillment
of the
Requirements for the Degree

DOCTOR OF PHILOSOPHY

Supervised by
Nicholas George, Professor of Optics
The Institute of Optics
College of Engineering and Applied Science

University of Rochester
Rochester, New York

1990

91 1 14 102

REPORT DOCUMENTATION PAGE

| | | | |
|--|--------------------------------------|---|------------------------------|
| 1a. REPORT SECURITY CLASSIFICATION Unclassified | | 1b. RESTRICTIVE MARKINGS | |
| 2a. SECURITY CLASSIFICATION AUTHORITY | | 3. DISTRIBUTION/AVAILABILITY OF REPORT Approved for public release; distribution unlimited. | |
| 2b. DECLASSIFICATION/DOWNGRADING SCHEDULE | | 5. MONITORING ORGANIZATION REPORT NUMBER(S) ARO 24626.175-PH-VIR | |
| 4. PERFORMING ORGANIZATION REPORT NUMBER(S) | | 7a. NAME OF MONITORING ORGANIZATION U. S. Army Research Office | |
| 6a. NAME OF PERFORMING ORGANIZATION University of Rochester | 6b. OFFICE SYMBOL (If applicable) | 7b. ADDRESS (City, State, and ZIP Code) P. O. Box 12211 Research Triangle Park, NC 27709-2211 | |
| 6c. ADDRESS (City, State, and ZIP Code) The Institute of Optics Rochester, New York 14627 | | 9. PROCUREMENT INSTRUMENT IDENTIFICATION NUMBER DAAL03-86-K-0173 | |
| 8a. NAME OF FUNDING/SPONSORING ORGANIZATION U. S. Army Research Office | 8b. OFFICE SYMBOL (If applicable) | 10. SOURCE OF FUNDING NUMBERS | |
| 8c. ADDRESS (City, State, and ZIP Code) P. O. Box 12211 Research Triangle Park, NC 27709-2211 | | PROGRAM ELEMENT NO. | PROJECT NO. |
| | | TASK NO. | WORK UNIT ACCESSION NO. |
| 11. TITLE (Include Security Classification) Serrated Circular Apertures: Optical Fourier Transforms and Fractal Analysis | | | |
| 12. PERSONAL AUTHOR(S) Madeleine Marie Beal | | | |
| 13a. TYPE OF REPORT Technical | 13b. TIME COVERED FROM TO | 14. DATE OF REPORT (Year, Month, Day) September 1990 | 15. PAGE COUNT 241 |
| 16. SUPPLEMENTARY NOTATION The view, opinions and/or findings contained in this report are those of the author(s) and should not be construed as an official Department of the Army position, policy, or decision unless so designated by other documentation. | | | |
| 17. COSATI CODES | | 18. SUBJECT TERMS (Continue on reverse if necessary and identify by block number) | |
| FIELD | GROUP | Diffraction; optical transforms; serrated apertures; fractal | |
| | | | |
| 19. ABSTRACT (Continue on reverse if necessary and identify by block number) <p style="text-align: center;">Please see Abstract on pp. vi-vii.</p> | | | |
| 20. DISTRIBUTION/AVAILABILITY OF ABSTRACT <input type="checkbox"/> UNCLASSIFIED/UNLIMITED <input type="checkbox"/> SAME AS RPT. <input type="checkbox"/> DTIC USERS | | 21. ABSTRACT SECURITY CLASSIFICATION Unclassified | |
| 22a. NAME OF RESPONSIBLE INDIVIDUAL Nicholas George | | 22b. TELEPHONE (Include Area Code) 716-275-2417 | 22c. OFFICE SYMBOL |

DTIC
ELECTE
JAN 15 1991
S B D

Vita

Madeleine Marie Beal [REDACTED]

She spent her childhood and early adulthood in the Long Island town of Huntington and graduated as class salutatorian in 1977 from Huntington High School. She proceeded on to New York Institute of Technology, where her involvement in student activities led to her election as Vice-President of the Student Government Association. Academics, however, were most important to her, and her dedication to her studies was acknowledged with awards for high achievement in Physics and Mathematics as well as for general academic excellence. The Bachelor of Science degree in Physics was conferred upon her *summa cum laude* in 1981. She began her graduate studies in Optics at the University of Rochester that fall and joined the Opto-Electronics Research group of Professor Nicholas George in 1982. While at the Institute of Optics, the author was supported by fellowships from the New York State Science and Technology Foundation and the U.S. Army Research Office University Research Initiative program.

| | |
|---------------------------|-------------------------------------|
| Accession For | |
| NTIS GRA&I | <input checked="" type="checkbox"/> |
| DTIC TAB | <input type="checkbox"/> |
| Unannounced | <input type="checkbox"/> |
| Justification _____ | |
| By _____ | |
| Distribution/ | |
| Availability Codes | |
| Dist | Avail and/or Special |
| A-1 | |



Acknowledgements

Writing one's vita can be difficult, but acknowledging the people who have helped in creating the person described therein is a pleasure.

Professor Nicholas George suggested this research topic and helped with the growth and refinement which has led to the dissertation presented here. The education I received as his student goes far beyond these pages. Dr. Matthew Chang of NYIT was the first to nurture my interest in Optics. The members of my thesis committee were ready with questions and suggestions throughout the course of my research here in Rochester. I will never be able to open enough doors for Prof. Emil Wolf to repay him for opening so many doors of knowledge for me. Dr. Patrick Fleming and Dr. Robert Rolleston read the manuscript and made several helpful suggestions and humorous comments. Financial support for my research was provided by the New York State Science and Technology Foundation and by the U.S. Army Research Office under the University Research Initiative program.

P.K. and Bert, my FPAOMs, have lived up to their titles in every way possible. Keith and Scott have shared my joys and frustrations and administered chocolate as appropriate. The others who have been part of this research group over the years were always willing to help with a myriad of problems and made the problem-solving enjoyable: Bryan, Dennis, Don, Ed, Justin, Karen, Lyle, Momi, Mustafa, Shen-ge, Tom, and Eugene.

Others at the Institute and at the University have helped me keep a healthy perspective: Michele, Margie, Margie, Maria, and Evie; Laura, Teresa, Paul (wtb), Jim and Net; Sue, Karen, and Bill. Spontaneous, middle-of-the-day, long-distance phone calls

from Jack brought many smiles to my face. Liz has been the "bestest friend in the whole, wide world". Tom, Ed, Mary, Patrick, Jennifer, Flit, Sue, Marla, Mike, Cathy, Paul, Kathleen, Kurt, Carol, Laura, and Basil have shared the Light. Henry has shared as much of the present as he could and has offered me a precious glimpse of the future.

Mom and Dad, Grandma and Grandpa, and the "Beal Bros." have given me the support and encouragement that only a loving family can give -- and they have given it in abundance!

Many thanks to and for all these people, and many others, for being the supports upon which this story of my life has been built.

Second Edition Acknowledgement

During my extended stay in Rochester, one individual provided support for me and for my work in a multitude of ways. He helped me in the lab, read the new text, and suggested the "equal-area-equal-correlation-angle" concept. He encouraged me to keep swimming when I couldn't see the benefits he predicted. He cooked dinner when I was too tired to decide what and whether I wanted to eat. He helped me escape when I needed to, but always brought me back and kept me going. He was more a cheerleader than a coach, more a companion than a critic. Where he touched my life, I could see growth even when so much seemed stagnant and backwards.

Thank you, Patrick. I look ahead with love and trepidation to the time when I will have the opportunity to repay you.



Abstract

The optical transform of the transmission function of a serrated circular aperture is discussed, with particular emphasis on the relationship between the features in the transform and the parameters that describe the aperture serration. The transform is produced in a canonical optical processing system, where the scalar field distribution in the back focal plane of the lens is proportional to the two-dimensional spatial Fourier transform of the aperture transmission function. In the statistical diffraction theory, the quantity of interest is the two-point moment of the intensity, which is a fourth-order moment of this scalar field component.

A careful calculation of the diffracted field is performed. The two-point intensity moment is expanded in terms of second-order moments of the field. Due to the polar symmetry of the field, circularity does not hold and the two significant terms in the expansion are identical but for a π rotation. From the detailed expression for the remaining second-order moment, interesting features of the optical transform are extracted. These features are ring fragmentation, the number of transform spikes, and spike appearance, which correspond to serration roughness, correlation angle, and correlation function, respectively. The results of computer simulations and optical experiments support the predicted relationships between the aperture parameters and transform features. Detailed study and modeling of the errors introduced during fabrication of apertures for use in the experiments show that very small errors ($\sim 2 \mu\text{m}$) are easily seen in the optical Fourier transform.

The effects of the variations in the parameters of the serration on the fractal dimension of the aperture is also discussed. Geometric techniques are used to measure the fractal dimension of computer-designed apertures. The fractal dimension depends

on the roughness σ and correlation length L of a serrated aperture or edge by way of the ratio σ/L for a given correlation function shape. Changing the correlation function alters this dependence: the fractal dimension increases when the function is sharpened.

Table of Contents

| | Page |
|--|-------------|
| Vita | <i>ii</i> |
| Acknowledgements | <i>iii</i> |
| Dedication | <i>v</i> |
| Abstract | <i>vi</i> |
| Table of Contents | <i>viii</i> |
| List of Tables | <i>xii</i> |
| List of Figures | <i>xiii</i> |
| Chapter | |
| 1 Introduction | |
| 1.1. Statement of the Problem and Objectives | 1 |
| 1.2. Literature review | 3 |
| 1.3. Overview of this Dissertation | 6 |
| 2. Computer Simulation of the Serrated Aperture and Fourier Transform | |
| 2.1. Introduction | 13 |
| 2.2. Calculation of the Field Amplitude in the Fourier Transform Plane | 14 |
| 2.3. Generation of Serrated Circular Apertures | 18 |
| 2.3.1. Mean Radius | 21 |
| 2.3.2. Root-mean-square Roughness | 21 |
| 2.3.3. Serration Correlation Angle | 24 |
| 2.3.4. Serration Correlation Function | 26 |
| 2.3.5. Aperture Smoothness | 28 |
| 2.4. Computer Simulation of the Fourier Transform | 29 |
| 2.4.1. Aperture Roughness | 31 |

| | | |
|--------|--|----|
| 2.4.2. | Serration Correlation Angle | 33 |
| 2.4.3. | Serration Correlation Function | 33 |
| 3. | Comparison of the Statistical and Fractal Descriptions | |
| 3.1. | Introduction | 37 |
| 3.1.1. | Fractal Functions | 38 |
| 3.1.2. | Fractal Attributes of Random Processes | 41 |
| 3.1.3. | Determining the Fractal Dimension | 44 |
| 3.2. | Fractal Dimension Calculations for Serrated Apertures | 48 |
| 3.2.1. | Aperture Roughness | 50 |
| 3.2.2. | Correlation Angle of the Aperture Serration | 53 |
| 3.2.3. | Correlation Function of the Aperture Serration | 56 |
| 3.3. | Fractal Dimension of the Weierstrass Function | 56 |
| 3.3.1. | Original Function | 59 |
| 3.3.2. | Scaled Function | 61 |
| 3.3.3. | Bandlimited Function | 64 |
| 3.4. | Quantitative Analysis of the Statistical - Fractal Relationship | 65 |
| 3.4.1. | Similarities of Serrated Apertures and Edges | 66 |
| 3.4.2. | Dependence of the Fractal Dimension on the Roughness-to- Correlation-Length Ratio: Triangular Correlation | 68 |
| 3.4.3. | Definition of the Correlation Length | 70 |
| 3.4.4. | Dependence of D on α/d and on the Correlation Function .. | 75 |
| 3.5. | Summary | 82 |

| | |
|---|-----|
| 4. Statistical Diffraction Theory for Serrated Circular Apertures | |
| 4.1. Introduction | 87 |
| 4.2. The Two-Point Moment of Intensity | 88 |
| 4.2.1. Moment Expansion for Gaussian Fields | 90 |
| 4.2.2. Symmetry Considerations | 93 |
| 4.3. Second - Order Moment for Gaussian Roughness | 95 |
| 4.3.1. Second - Order Moment u_{12} | 96 |
| 4.3.2. Gaussian Characteristic Function Notation | 97 |
| 4.3.3. Second - Order Moment u_{12}^{\dagger} | 99 |
| 4.3.4. Symmetry of the Fourier Transform | 102 |
| 4.3.5. Illustrative Example | 104 |
| 4.4. Features in the Fourier Transform | 105 |
| 4.4.1. Aperture Roughness | 123 |
| 4.4.2. Fresnel Zones of the Aperture | 127 |
| 4.4.3. Correlation Angle of the Aperture Serration | 131 |
| 4.4.4. Correlation Function of the Aperture Serration | 138 |
| 5. Fabrication and Evaluation of Serrated Circular Apertures | |
| 5.1. Introduction | 145 |
| 5.2. Computer Simulation of the Fourier Transforms of Apertures from an Ensemble | 146 |
| 5.3. Experimental Optical Fourier Transforms | 157 |
| 5.3.1. The Optical Fourier Transform System | 157 |
| 5.3.2. Aperture Production by Photolithography | 160 |
| 5.3.3. Aperture Production by Electron-Beam Lithography | 167 |

| | |
|---|-----|
| 5.3.4. Comparison of Computer Simulations and Optical Experiments | 168 |
| 5.4. Electron-Beam Generated Masks with Controlled Deviations | 171 |
| 5.4.1. Model of Noise in the Fabrication Process | 171 |
| 5.4.2. Fourier Transforms of Noisy Apertures | 172 |
| 5.5. Conclusions | 180 |
| 6. Comparison of Features in the Experimental and Calculated Transforms | |
| 6.1. Introduction | 182 |
| 6.2. Aperture Roughness and Ring Fragmentation | 183 |
| 6.3. Correlation Angle of the Aperture Serration and the Number of Transform Spikes | 189 |
| 6.4. Correlation Function of the Aperture Serration and Spike Appearance | 194 |
| 6.5. Conclusions | 199 |
| Summary | 202 |
| Bibliography | 208 |
| Appendices | |
| A. Aperture Generation Process | 214 |
| A.1. Theoretical Analysis | 214 |
| A.2. Computer Program | 223 |
| B. Generation of the Curves Shown in Fig. 3.1. | 230 |
| C. Programs for Computing the Fractal Dimension | 233 |

List of Tables

| | Page |
|---|------|
| Table 3.1. Roughnesses and fractal dimensions determined by each method for aperture set 1. | 52 |
| Table 3.2. Correlation angles and fractal dimensions determined by each method for aperture set 2. | 55 |
| Table 3.3. Roughness σ and correlation length d for the edges represented in Fig. 3.11. | 80 |
| Table 5.1. Selected angular statistical quantities for individual apertures from the ensemble represented in Fig. 5.1. | 152 |
| Table 5.2. Error budget for photolithographic aperture production. | 165 |
| Table 5.3. Added rms noise and resulting rms roughness for an original aperture with 75 μm angular rms roughness. | 173 |
| Table 6.1. Statistical and fractal parameters for experimental set 1. | 183 |

List of Figures

| | Page |
|--|------|
| Fig. 2.1. Serrated aperture in Plane I ($r, \alpha, 0$) and optical Fourier transform in Plane II (ρ, ϕ, z_0). | 14 |
| Fig. 2.2. Apertures of varied average radius. | 22 |
| Fig. 2.3. Serrated apertures of varied roughness. | 23 |
| Fig. 2.4. Serrated apertures of varied correlation angle. | 25 |
| Fig. 2.5. Apertures and correlation functions. | 27 |
| Fig. 2.6. Calculated diffraction patterns for apertures of varied design rms roughness. | 30 |
| Fig. 2.7. Calculated diffraction patterns for apertures with different serration correlation angles. | 32 |
| Fig. 2.8. Calculated diffraction patterns corresponding to apertures of varied serration correlation function design. | 34 |
| Fig. 3.1. Four functions, each represented by a (Euclidean) one-dimensional line, but with different fractal dimensions. | 42 |
| Fig. 3.2. Generating a triadic Koch curve. | 49 |

| | | |
|------------|--|----|
| Fig. 3.3. | Richardson and interrogation curves for aperture set 1, with the curves for a smooth circle of radius 5 mm. | 51 |
| Fig. 3.4. | Richardson and interrogation curves for aperture set 2. | 54 |
| Fig. 3.5. | Richardson and interrogation curves for aperture set 3. | 57 |
| Fig. 3.6. | Calculated fractal dimension D for the original Weierstrass cosine function, Eq. (3.11), versus fundamental spatial frequency b | 60 |
| Fig. 3.7. | Calculated fractal dimension D for the amplitude-scaled Weierstrass cosine function, Eq. (3.14), | 62 |
| Fig. 3.8. | Calculated fractal dimension D for the frequency-scaled Weierstrass cosine function, Eq. (3.14), versus spatial rms deviation | 63 |
| Fig. 3.9. | Calculated fractal dimension D for the bandlimited Weierstrass cosine function, Eq. (3.14), versus summation index N_2 | 65 |
| Fig. 3.10. | Richardson curves for serrated aperture and serrated edge. | 67 |
| Fig. 3.11. | Fractal dimension D versus ratio σ_b / d for serrated edges. | 69 |
| Fig. 3.12. | Correlation functions $r_b(\Delta x)$ for serrated edges. | 77 |
| Fig. 3.13. | Typical edges produced with the correlation functions shown in Fig. 3.12. | 78 |
| Fig. 3.14. | Fractal dimension D versus ratio σ_b / d for serrated edges of varying correlation function. | 81 |

| | | |
|------------|--|-----|
| Fig. 4.1. | Sample plot of u_{12} and u_{12}^{\dagger} versus output angle ϕ_2 . | 106 |
| Fig. 4.2. | Sample plot of $ u_{12} ^2$ and $ u_{12}^{\dagger} ^2$ versus output angle ϕ_2 . | 106 |
| Fig. 4.3. | Terms in the expansion of $\langle I_1 I_2 \rangle$, calculated for varied radius values. | 111 |
| Fig. 4.4. | Two-point intensity moment $\langle I_1 I_2 \rangle$, calculated for varied radius values. | 116 |
| Fig. 4.5. | Angular intensity distribution $I(\rho, \phi)$, calculated for a single aperture at different radius values. | 120 |
| Fig. 4.6. | Angular intensity distribution $I(\rho, \phi)$, calculated for a single, Gaussian-correlated aperture at different radius values. | 124 |
| Fig. 4.7. | Coordinate system for Fresnel zone analysis. | 128 |
| Fig. 4.8. | Two-point intensity moment versus output angle ϕ_2 for aperture ensembles of varied rms roughness. | 132 |
| Fig. 4.9. | Calculated intensity for individual apertures from ensembles of varied rms roughness. | 132 |
| Fig. 4.10. | Calculated two-point intensity moment $\langle I_1 I_2 \rangle$ for aperture ensembles of varied correlation angle A . | 136 |
| Fig. 4.11. | Calculated intensity for individual apertures from ensembles with different correlation angles A . | 136 |

| | | |
|------------|---|-----|
| Fig. 4.12. | Calculated two-point intensity moment $\langle I_1 I_2 \rangle$ for aperture ensembles of varied correlation function. | 140 |
| Fig. 4.13. | Calculated intensity for individual apertures from ensembles of varied correlation function. | 140 |
| Fig. 5.1. | Twelve apertures from a single ensemble and the calculated Fourier transform of each. | 148 |
| Fig. 5.2. | Calculated ensemble average $\langle I(\rho_1, \phi_1) I(\rho_2, \phi_2) \rangle$, actual and estimated, for the ensemble represented in Fig. 5.1. | 155 |
| Fig. 5.3. | The angular autocorrelation of the intensity in the Fourier transform of selected individual apertures. | 155 |
| Fig. 5.4. | Schematic representation of the experimental apparatus for the study of the optical transform. | 158 |
| Fig. 5.5. | Microscope photographs of the tooling used to make the photolithographic chrome aperture, and the electron-beam lithographic aperture. | 163 |
| Fig. 5.6. | Three realizations of the transform of a single aperture design: the optical Fourier transforms of the photolithographic and electron-beam lithographic apertures, and the calculated Fourier transform. | 170 |
| Fig. 5.7. | Model used to simulated the noise introduced in fabricating serrated circular apertures for optical experiments. | 172 |

| | | |
|-----------|--|-----|
| Fig. 5.8. | Optical Fourier transforms of serrated circular apertures with added noise | 174 |
| Fig. 6.1. | Apertures from experimental set 1, with optical and calculated transforms. | 185 |
| Fig. 6.2. | Apertures from experimental set 2, with optical and calculated transforms. | 190 |
| Fig. 6.3. | Apertures from experimental set 3, with optical and calculated transforms. | 196 |
| Fig. B.1. | Correlation functions used in designing the curves shown in Fig. 3.1. . | 231 |

Chapter 1

Introduction

1.1. Statement of the Problem and Objectives

Since the very beginnings of geometry, people have been using regular shapes to approximate real objects. As children, we draw circular suns and five-pointed stars shining on triangular and spherical trees, under which stand square-bodied people smiling semi-circular smiles. When we grow older, these representations are too simple for us. Some of us leave it to the professional artist to create more realistic, more pleasing depictions of the world around us. Others turn to scientific pursuits, hoping to find the reason behind the irregular shapes in some underlying regularity in the universe¹. In the meantime, we move from our crude first approximations to more sophisticated models, always searching for the truest, the most pleasing explanation.

The realm of optical diffraction is far from untouched by the desire to understand the irregularities we encounter day by day. Kravstov, Rytov, and Tatarskii² have classified four types of statistical problems in diffraction theory, each of which deals with irregularity somewhere in the optical system: random sources, partial coherence, randomly shaped or positioned objects, and inhomogeneous media. The study of serrated circular apertures³, the subject of this dissertation, stands firmly in the third of these categories. Scattering by rough reflective surfaces and transmission through a rough diffuser, two fairly standard speckle problems that are still of interest today^{4,5}, are also in the category of randomly shaped objects.

We mention these other types of statistical diffraction and speckle problems in order to place our study in context for the reader. The basic differences can be seen in

the following integral expression for the diffracted field:

$$v(\xi, \eta, z) = \iint_A v_0(x, y, 0) K(x, y; \xi, \eta; z) dx dy, \quad (1.1)$$

where $v_0(x, y, 0)$ is the original field in plane $(x, y, 0)$ and $v(\xi, \eta, z)$ is the diffracted field in plane (ξ, η, z) , parallel to (x, y) and a distance z away. The ξ and η axes are parallel to the x and y axes, respectively. $K(x, y; \xi, \eta; z)$ is the propagation kernel between these two planes, and A is the aperture in plane $(x, y, 0)$ over which we integrate. In the case of a rough surface or diffuser, the statistical nature of the diffracted field enters the problem by way of the field $v_0(x, y, 0)$, which is taken to be the field immediately after interacting with the object. The object has imparted a random phase to this field. If we consider an inhomogeneous medium, we include the statistical nature of the problem in propagation kernel $K(x, y; \xi, \eta; z)$. The effects of random sources would be incorporated in the field $v_0(x, y, 0)$. For our case, that of the serrated aperture, the shape of the limiting aperture A introduces randomness to the problem. Mathematically, we can see that this is a much different problem, since the statistics are incorporated in the integration limits rather than in the integrand.

Despite this basic mathematical difference, our approach to determining the statistics of the diffracted field is basically the same as in other speckle problems. We are interested in the moments of the field. In particular, since the intensity is the measurable quantity, we calculate $\langle I_1 I_2 \rangle$, the two-point moment of the intensity. I_1 and I_2 are the intensities at two points in the transform, and the angle brackets $\langle \rangle$ denote an ensemble average. This two-point correlation is a fourth-order moment of the field. The essential second-order statistics of the field intensity can be determined from this correlation function.

We have two basic objectives in this research. The first is to determine the relationship between the statistical parameters of the aperture and the features of the field diffracted by the aperture, in particular, of the optical transform. This is accomplished through careful analysis of the dependence of the two-point moment of the intensity on the roughness, correlation angle, and correlation function of the aperture serration. In this way, we have a solid theoretical connection between aperture parameters and transform features.

Our second objective is to study the relationship between these same aperture parameters and the fractal dimension of the serration. Since fractal geometry was introduced by Benoit Mandelbrot⁶, it has been applied in numerous fields of study. Too often, though, those eager to apply this new technique have substituted fractal geometry for statistical analysis without first analyzing the relationship between the two methods. The results, then, can be difficult to compare with earlier results in a meaningful way. In demonstrating the interdependence of the fractal dimension and statistical parameters of the aperture serration, we show that both fractal geometry and statistical analysis contribute to our understanding of the apertures, each in a different, but nonindependent, manner.

1.2. Literature Review

Diffraction by a serrated circular aperture is a speckle-like problem. As is discussed in several early speckle papers^{7,8,9} and in overview literature^{10,11}, speckle arises in an imaging or diffracting configuration with coherent illumination. A simple description of the physical mechanism at work is as follows. From an object which is rough on the scale of a wavelength, light scattered by individual sections of the object surface (called scattering cells) interferes at an observation point. If this interference is

more constructive than destructive, we have a bright spot; destructive interference produces a dark spot. Speckle is thus due to the combined effects of the coherence of the light over relatively long distances, which allows interference, and the optical roughness of the object, which yields a haphazard arrangement of the regions of constructive and destructive interference. Although these studies, as discussed earlier, are quite different from the case of the serrated aperture, the methods and concepts presented are certainly applicable to our study.

Several articles¹², books^{13,14,15}, conferences^{16,17}, and journal special issues^{18,19} have been dedicated to reviews of the field of speckle. Such a review is beyond the scope of this dissertation, and so the reader is directed to these compilations for a more complete sketch of the speckle literature. A few papers which are particularly relevant to our research are discussed in this review; others will be cited where appropriate.

The precursory work to the study presented here is that of George and Morris on diffraction by serrated edges and gaps^{20,21}. Parts of the work presented in this dissertation echo that of this earlier study. We follow much the same mathematical approach, to expressing the moments of the scalar field component in terms of the characteristic functions of the probability density of the serration. Because of the circular nature of the aperture and our subsequent use of the cylindrical coordinate system, our moment expressions are unlike those in earlier work and we therefore take a different approach to the analysis of the diffraction pattern.

The complement of the serrated circular aperture is the roughened disk, which can be used to model a particle²² or a biological cell. The diffraction problems for apertures and disks are essentially the same. Thus, studies of diffraction from individual

particles or cells are relevant here. We note a recent study of the optical Fourier transforms of high-contrast images of planktonic animals which emphasizes the effects of edge variations on the Fourier spectra²³. We present the results of our study of the serrated circular aperture in general terms so that they can be applied to particulate and biological studies.

In the field of optics, an important area of investigation is the study of diffraction of light by fractal surfaces and objects²⁴. Although there has been some interest in the study of diffraction by regular fractal structures²⁵, the usefulness of fractal geometry in describing naturally occurring objects has led to its application in numerous statistical optics problems. Reflection from fractal surfaces has been studied by Berry and Blackwell²⁶. The contrast of the intensity pattern behind a fractal diffuser has been investigated by Jakeman and Jefferson²⁷, who report numerical results, and by Jordan, Hollins, and Jakeman²⁸, who present experimental data for the scattered field from roughened germanium. A technique for making fractal surfaces of specified surface height power spectrum is proposed by Berry²⁹. Her method involves exposing photoresist to multiple speckle patterns of controlled second-order statistics. A specific fractal function, the Weierstrass function, is used to describe the surfaces of the fractal phase screens studied by Jaggard and Kim^{30,31}. They have reported results for the field behind a single fractal phase screen and have used cascaded phase screens to model a volume fractal medium. These authors have also used the Weierstrass function to model atmospheric refractive index fluctuations³². Since the self-similarity property of fractals is useful in describing arbitrarily small structure, it has been applied in the study of X-ray and neutron scattering from rocks^{33,34}.

Of particular interest in our study are fractal models of particle contours, the geometric complement of serrated circular apertures. Kaye discusses methods for determining the fractal dimension of a particle³⁵. Results for the fractal characterization of small aluminum particles as they are eroded in an acid bath are reported by Kaye, Leblanc, and Abbot³⁶. The optical properties of a gas-evaporated coating have been derived by Niklasson from the fractal description of the metal fineparticle clusters that comprise the coatings³⁷. For pattern recognition applications, Caimi and Schmalz have compared fractal and spatial harmonic analyses of particle contours³⁸. A fractal particle surface model has been used by Bourrely, Torresani, and Chiappetta in their investigation of scattering of electromagnetic radiation by a rough object³⁹.

Our study of the relationship between fractal geometry and random processes connects the two in a new way and is an important contribution to the literature in both areas. We anticipate the application and extension of this work to problems in the field of statistical optics and beyond.

1.3 Overview of this Dissertation

The preliminary mathematical groundwork for the study of the serrated circular aperture is laid out in Chapter 2, where we begin by placing the aperture in our optical system and calculating the scalar field amplitude in the Fourier transform plane. We then discuss the important aperture parameters and demonstrate, with several sets of computer-designed apertures, the effects each parameter has on the aperture appearance. Computer simulations based on the result of our scalar field calculations show the effects of variations in the roughness, correlation angle, and correlation function of the aperture serration on the Fourier transform.

Chapter 3, which contains the study of the fractal nature of serrated apertures, begins with a comparison of fractals and random processes. We then present two methods for determining an unknown fractal dimension and test these methods on a standard fractal object. When applied to our serrated circular aperture, these methods demonstrate the interdependence of the fractal and statistical descriptions. We also determine the fractal dimension of the fractal Weierstrass function⁴⁰, which has been used in other studies to model surfaces³⁰, index fluctuations³², and apertures⁴¹. We end this chapter with a discussion of the quantitative dependence of the fractal dimension on the roughness and correlation angle of the aperture serration for a variety of correlation functions.

We return to our discussion of the optical transform in Chapter 4 with the presentation of the statistical diffraction theory. Using a Gaussian moment theorem, we expand the two-point moment of the intensity as a sum of second-order moments of the scalar field and note the significant terms in this expansion. We show that two of the four terms contribute significantly to the two-point properties of the moment and that the usual assumption of circularity is not valid for the optical Fourier transforms of real-valued objects such as our apertures. We then calculate the two significant second-order moments and demonstrate that they are identical but for a π rotation. From the resulting expression, we extract optical transform features which depend on the parameters of the aperture serration. An analysis of the transform based on the Fresnel zones of the aperture supports our choice for the roughness-related feature. Computer calculations of the two-point intensity moment for several aperture ensembles and of the transform intensity for representative members of these ensembles demonstrate the relationships

proposed between the parameters of the aperture serration and the features in the transform pattern.

Our objective in the fifth chapter is to demonstrate the accuracy needed in reproducing our aperture designs in chrome for use in optical experiments. To this end, we present a set of twelve designs from a single ensemble and investigate the properties of the individual apertures and transforms. These properties, such as the angular mean radius of the aperture and the number of spikes in the transform, are seen to vary among the apertures in the ensemble. Any fabrication error in our chrome apertures that produces variations smaller than those expected in an ensemble is deemed acceptable for our study of the transform features. We investigate two methods of fabricating apertures with this accuracy limit in mind. Comparison of the results of optical experiments using apertures made by each method with the results of our computer simulation confirm the usefulness of each technique. In addition to this study of the error tolerance, we investigate our ability to detect errors in the apertures using a set of precisely fabricated apertures designed to model the noise introduced in the making of chrome apertures.

To complete our work, we present three sets of apertures and the corresponding Fourier transforms from both optical experiments and computer calculations in Chapter 6. For each of these three sets, one parameter of the serration is varied. Thus, in the transforms, we can see the effects of the roughness, correlation angle, and correlation function. Comparison of the transforms of the different apertures in each set supports the results of our statistical diffraction theory, and comparison of the optical and computed Fourier transforms demonstrates the accuracy of our theory and our computer model in the regime of interest for a large range of serration parameters.

Chapter 1 References

1. J. Gleick, *Chaos: Making a New Science* (Viking Penguin, 1987). The bestseller status of this book has been an indication that the desire to see order in disorder is a popular one.
2. Y.A. Kravstov, C.M. Rytov, and V.I. Tatarskii, "Statistical problems in diffraction theory," *Usp. Fiz. Nauk* **115**, 239-262 (1975) [*Sov. Phys.-Usp.* **18**, 118-130 (1975)].
3. M.M. Beal and N. George, "Features in the optical transforms of serrated apertures and disks," *J. Opt. Soc. Am. A* **6**, 1815-1826 (1989).
4. K.J. Allardyce and N. George, "Diffraction analysis of rough reflective surfaces," *Appl. Opt.* **26**, 2364-2375 (1987).
5. L.G. Shirley and N. George, "Wide-angle diffuser transmission functions and far-zone speckle," *J. Opt. Soc. Am. A* **4**, 734-745 (1987).
6. B.B. Mandelbrot, *The Fractal Geometry of Nature* (W.H. Freeman, New York, 1983).
7. L.I. Goldfisher, "Autocorrelation function and power spectral density of laser-produced speckle patterns," *J. Opt. Soc. Am.* **55**, 247-253 (1965).
8. L.H. Enloe, "Noise-like structure in the image of diffusely reflecting objects in coherent illumination," *Bell System Tech. J.* **46**, 1479-1489 (1967).
9. S. Lowenthal and H. Arsenault, "Image formation for coherent diffuse objects: statistical properties," *J. Opt. Soc. Am.* **60**, 1478-1483 (1970).
10. N. George, "Speckle," *Applications of Speckle Phenomena*, W.H. Carter, ed., *Proc. SPIE* **243**, 124-140 (1980).
11. J.W. Goodman, "Statistical properties of laser speckle patterns," *Laser Speckle and Related Phenomena*, J.C. Dainty, ed. (Springer-Verlag, New York, 1975).

12. N. George, "Speckle at various planes in an optical system," *Opt. Eng.* **25**, 754-764 (1986).
13. J.C. Dainty, ed., *Laser Speckle and Related Phenomena* (Springer-Verlag, New York, 1975).
14. R.K. Erf, ed., *Speckle Metrology* (Academic Press, New York, 1978).
15. M. Françon, *Laser Speckle and Applications in Optics* (Academic Press, New York, 1979).
16. W.H. Carter, ed., *Applications of Speckle Phenomena*, Proc. SPIE **243** (1980).
17. H.H. Arsenault, ed., *International Conference on Speckle*, Proc. SPIE **556** (1985).
18. Special Issue on Speckle, *J. Opt. Soc. Am.* **66**, No. 11 (1976).
19. Special Issues on Speckle, *Opt. Eng.* **25**, Nos. 5-6 (1986).
20. N. George and G.M. Morris, "Diffraction by serrated apertures," *J. Opt. Soc. Am.* **70**, 6-17 (1980).
21. G.M. Morris, *Serrated Apertures: Statistical Diffraction Theory and Experiments* (Ph.D. Thesis, California Institute of Technology, 1979).
22. J.R. Hodgkinson, "Particle sizing by means of the forward scattering lobe," *Appl. Opt.* **5**, 839-844 (1966).
23. A.D. Poularikas and C. Katsinis, "Similarities of fourier spectra from random edge variations," *Opt. Eng.* **26**, 1120-1123 (1987).
24. M.V. Berry, "Diffractals," *J. Phys. A: Math. Gen.* **12**, 781-797 (1979).
25. A. Lakhtakia, N.S. Holter, V.K. Varadan, and V.V. Varadan, "Self-similarity in diffraction by a self-similar fractal screen," *IEEE Trans. on Antennas and Propag.* **AP-35**, 236-239 (1987).
26. M.V. Berry and T.M. Blackwell, "Diffractal echoes," *J. Phys. A: Math. Gen.* **14**, 3101-3110 (1981).

27. E. Jakeman and J.H. Jefferson, "Scintillation in the Fresnel region behind a sub-fractal diffuser," *Optica Acta* **31**, 853-865 (1984).
28. D.L. Jordan, R.C. Hollins, and E. Jakeman, "Experimental measurements of non-Gaussian scattering by a fractal diffuser," *Appl. Phys. B* **31**, 179-186 (1983).
29. E. Berry, "Making a multiscale random rough surface," *Optica Acta* **32**, 147-153 (1985).
30. D.L. Jaggard and Y. Kim, "Diffraction by band-limited fractal screens," *J. Opt. Soc. Am. A* **4**, 1055-1062 (1987).
31. Y. Kim and D.L. Jaggard, "Optical beam propagation in a band-limited fractal medium," *J. Opt. Soc. Am. A* **5**, 1419-1426 (1988).
32. Y. Kim and D.L. Jaggard, "Band-limited fractal model of atmospheric refractivity fluctuation," *J. Opt. Soc. Am. A* **5**, 475-480 (1988).
33. D.F.R. Mildner et. al., "Small-angle scattering of shaly rocks with fractal pore interfaces," *Appl. Phys. Lett.* **48**, 1314-1316 (1986).
34. P.-Z. Wong, J. Howard, and J.-S. Lin, "Surface roughening and the fractal nature of rocks," *Phys. Rev. Lett.* **57**, 637-640 (1986).
35. B.H. Kaye, "Specification of the ruggedness and/or texture of a fine particle profile by its fractal dimension," *Powder Technology* **21**, 1-16 (1978).
36. B.H. Kaye, J.E. Leblanc, and P. Abbot, "Fractal description of the structure of fresh and eroded aluminum shot fineparticles," *Particle Charact.* **2**, 56-61 (1985).
37. G.A. Niklasson, "Optical properties of gas-evaporated metal particles: effects of a fractal structure," *J. Appl. Phys.* **62**, 258-265 (1987).
38. F.M. Caimi and M.S. Schmalz, "Geometric properties of non-differentiable contours: concurrent spatial harmonic and fractal analyses," *SPIE Particle Sizing and Spray Analysis* **573**, 21-30 (1985).

39. C. Bourrely, B. Torresani, and P. Chiappetta, "Scattering of an electro-magnetic wave by an irregularly shaped object," *Opt. Commun.* **58**, 365-368 (1986).
40. M.V. Berry and Z.V. Lewis, "On the Weierstrass-Mandelbrot fractal function," *Proc. Roy. Soc. Lond. A* **370**, 459-484 (1980).
41. Y. Kim, H. Grebel, and D.L. Jaggard, "Diffraction from fractally serrated circular apertures," *Technical Digest of the Annual Meeting of the Optical Society of America*, 121 (1988).

Chapter 2

Computer Simulation of the Serrated Aperture and Fourier Transform

2.1. Introduction

The two-dimensional Fourier transform of the transmission function of a serrated circular aperture is the quantity of interest in this study. In this chapter, we derive the basic mathematical expression for the Fourier transform of the aperture in cylindrical coordinates and present computer-designed apertures and calculated transforms. This computer-aided investigation is the first step toward understanding the relationships between the aperture serration and the features of the Fourier transform.

We derive the expression for the Fourier transform of the transmission function of the aperture in Section 2.2, using the Fresnel impulse response for the optical Fourier transform system discussed therein. We define the mean radius, the root-mean-square (rms) roughness, and the correlation function of the serration for the aperture in Section 2.3. This section also contains the presentation of several apertures used to demonstrate the effects of changing each of these parameters. Computer simulations of the field intensity in the optical Fourier transform plane are presented for representative apertures. For these examples, discussed in Section 2.4, apertures with well-defined parameters are used to demonstrate qualitatively the corresponding transform features. For a thorough analysis of the Fourier transform based on statistical optics, the reader is referred to Chapter 4.

2.2. Calculation of the Field Amplitude in the Fourier Transform Plane

The optical configuration used to investigate a scalar component of the diffracted electric field amplitude from a serrated circular aperture is shown in Fig. 2.1. In Plane I, described by Cartesian coordinates $(x, y, z=0)$ or cylindrical coordinates $(r, \alpha, z=0)$, we have an aperture described by the curve defining the edge: $r = r_c = a + s(\alpha)$, where (r_c, α) is a point on the edge of the aperture, a is the average radius of the aperture, and $s(\alpha)$ is a zero-mean random variable which describes the aperture serration. We define the transmission function of the aperture by:

$$t(r, \alpha) = \begin{cases} 1, & \text{for } r \leq a + s(\alpha), \\ 0, & \text{for } r > a + s(\alpha). \end{cases} \quad (2.1)$$

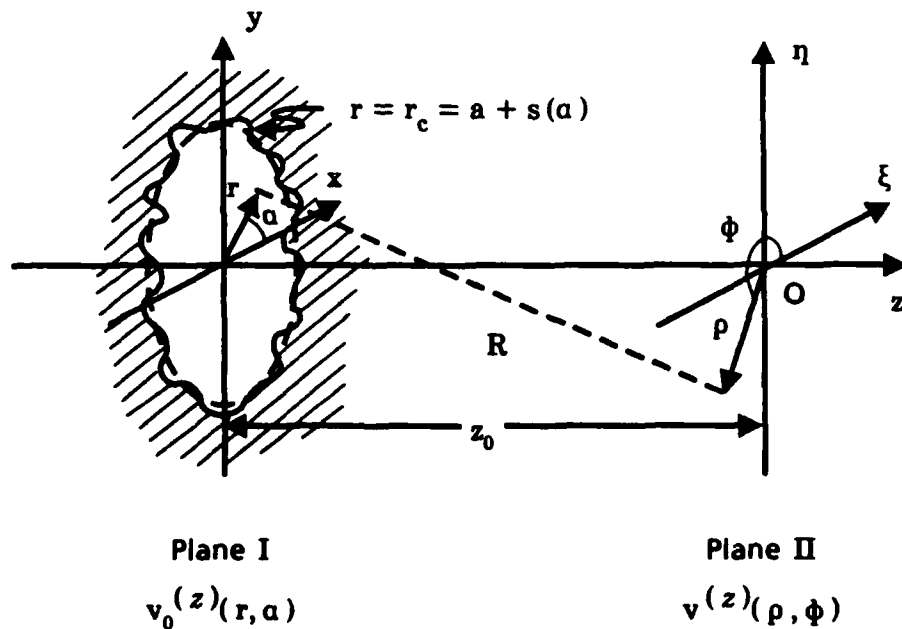


Fig. 2.1. Serrated aperture in Plane I $(r, \alpha, 0)$ and optical Fourier transform in Plane II (ρ, ϕ, z_0) .

Plane II, located a distance z_0 from Plane I, has Cartesian coordinates $(\xi, \eta, z=z_0)$ or cylindrical coordinates $(\rho, \phi, z=z_0)$, aligned as shown.

In the following derivations we make use of the results of Fourier optics using diffraction integrals that are directly traceable to Maxwell's equations.¹ However, in the actual solutions, we will use Kirchhoff's assertion as to the input electric field component, i.e., the transmission function notion, as well as the paraxial form of the kernel $K(r, \alpha; \rho, \phi; \nu)$ in the equations below.

When the aperture in Plane I is illuminated by a plane-polarized, monochromatic wave described by the scalar component $v_0^{(z)}(r, \alpha; \nu)$, the scalar distribution in Plane II is given by:

$$v^{(z)}(\rho, \phi; \nu) = \int_{-\pi}^{+\pi} \int_0^{\infty} v_0^{(z)}(r, \alpha; \nu) t(r, \alpha) K(r, \alpha; \rho, \phi; \nu) r dr d\alpha \quad (2.2)$$

For the paraxial case, the following well-known Fresnel impulse response for $K(r, \alpha; \rho, \phi; \nu)$ in Eq. (2.2) is appropriate²:

$$K(r, \alpha; \rho, \phi; \nu) = \frac{i \exp(-ikz_0)}{\lambda z_0} \left[\exp\left(\frac{-ik}{2z_0} [r^2 + \rho^2 - 2r\rho \cos(\alpha - \phi)]\right) \right], \quad (2.3)$$

in which ν is the temporal frequency of the illumination and k is equal to $2\pi\nu/c = 2\pi/\lambda$, where λ is the wavelength. This Fresnel approximation is valid when the system satisfies the condition $z_0^3 \gg \{\pi[r_1^2 + \rho_1^2 - 2r_1\rho_1 \cos(\alpha_1 - \phi_1)]^2/4\lambda\}_{\max}$, where (r_1, α_1) is any point within the aperture and (ρ_1, ϕ_1) is any observation point in Plane II. For our calculations, we have chosen to use the analytic signal representation of the field. In the Fourier transform domain, we denote this by the superscript ^(z). Hence, in illustration, an $\exp(+i2\pi\nu_1 t)$ time dependence in the space-time domain transforms into a $\delta(\nu - \nu_1)$ dependence in the space-temporal frequency domain. This dependence is suppressed in our analytic signal representation.

If we choose $v_0^{(z)}(r, \alpha; \nu)$ to be a convergent spherical wave with curvature $1/z_0$ in Plane I (i.e., in the aperture), we establish the well-known Fourier transform pattern in Plane II at $(\rho, \phi; \nu)$. The Fresnel approximation to the convergent wavefront $v_0^{(z)}(r, \alpha; \nu)$ given by

$$v_0^{(z)}(r, \alpha; \nu) = \exp\left(\frac{ik}{2z_0} r^2\right) \quad (2.4)$$

is substituted into Eq. (2.2) and using Eq. (2.3), we find the following form for the scalar diffracted field $v^{(z)}(\rho, \phi; \nu)$ in Plane II:

$$v^{(z)}(\rho, \phi; \nu) = \frac{i \exp\left[-ik\left(z_0 + \frac{\rho^2}{2z_0}\right)\right]}{\lambda z_0} \times \int_{-\pi}^{+\pi} \int_0^{\infty} t(r, \alpha) \exp\left(\frac{ik}{z_0} r \rho \cos(\alpha - \phi)\right) r dr d\alpha \quad (2.5)$$

The result in Eq. (2.5) is recognized as the two-dimensional Fourier transform of an arbitrary transmission function $t(r, \alpha)$ expressed in cylindrical coordinates. This can readily be converted to the more familiar Cartesian form.

For the serrated circular aperture, the limits in Eq. (2.1) are incorporated into Eq. (2.5), giving us the following result for the diffraction pattern of the aperture:

$$v^{(z)}(\rho, \phi; \nu) = \frac{i \exp\left[-ik\left(z_0 + \frac{\rho^2}{2z_0}\right)\right]}{\lambda z_0} \times \int_{-\pi}^{+\pi} \int_0^{a+s(\alpha)} \exp\left(\frac{ik}{z_0} r \rho \cos(\alpha - \phi)\right) r dr d\alpha \quad (2.6)$$

in which a is the average radius and $s(\alpha)$ is the fluctuation term. In Eq. (2.6), integration

over the radial coordinate r yields a single-integral form for $v^{(z)}(\rho, \phi; \nu)$:

$$v^{(z)}(\rho, \phi; \nu) = B \int_{-\pi}^{+\pi} \left\{ \exp[i\kappa(a + s(\alpha))] \left[\frac{1 - i\kappa a}{\kappa^2} + \frac{s(\alpha)}{i\kappa} \right] - \frac{1}{\kappa^2} \right\} d\alpha, \quad (2.7)$$

where the α -dependent, spatial-frequency-like variable κ is defined

$$\kappa = \frac{k\rho}{z_0} \cos(\alpha - \phi), \quad (2.8)$$

and coefficient B is defined

$$B = \frac{i}{\lambda z_0} \exp \left[-ik \left(z_0 + \frac{\rho^2}{2z_0} \right) \right]. \quad (2.9)$$

The expression given by Eq. (2.7) with Eqs. (2.8) and (2.9) for the Fourier transform of a serrated aperture in terms of the aperture function $s(\alpha)$ is the basic building block for the statistical diffraction theory presented in Chapter 4. We also use this expression in the computer calculations presented in Section 2.4.

In statistical calculations, we will find it convenient to contain the dependence of $v^{(z)}(\rho, \phi; \nu)$ on the random variable $s(\alpha)$ in the exponential. Thus, using the relation

$$s(\alpha) \exp[i\kappa s(\alpha)] = -i(\partial/\partial\kappa) \exp[i\kappa s(\alpha)], \quad (2.10)$$

we rewrite Eq. (2.7) as follows:

$$v^{(z)}(\rho, \phi; \nu) =$$

$$B \int_{-\pi}^{+\pi} \left[\exp(i\kappa a) \left(\frac{1 - i\kappa a}{\kappa^2} - \frac{1}{\kappa} \frac{\partial}{\partial\kappa} \right) \exp[i\kappa s(\alpha)] - \frac{1}{\kappa^2} \right] d\alpha. \quad (2.11)$$

The forms in Eqs. (2.7) and (2.11) are general and can be used to determine the scalar field in the Fourier transform plane of any aperture described by a single-valued function $s(\alpha)$.

For the case of a speckle pattern from a monochromatic source at $\nu = \nu_1$, we can find the time-varying analytic signal $V^{(z)}(\rho, \phi; t)$ corresponding to $v^{(z)}(\rho, \phi; \nu)$ by simply inverting the transform with $\delta(\nu - \nu_1)$ explicit, as follows:

$$V^{(z)}(\rho, \phi; t) = \int_{-\infty}^{+\infty} v^{(z)}(\rho, \phi; \nu) \delta(\nu - \nu_1) \exp(i2\pi\nu t) d\nu . \quad (2.12)$$

We integrate Eq. (2.12) to find the time-dependent analytic signal:

$$V^{(z)}(\rho, \phi; t) = v^{(z)}(\rho, \phi; \nu_1) \exp(i2\pi\nu_1 t) . \quad (2.13)$$

With the intensity I at point (ρ, ϕ) given by the equation

$$I(\rho, \phi) = V^{(z)}(\rho, \phi; t) \left[V^{(z)}(\rho, \phi; t) \right]^* \quad (2.14)$$

where the asterisk (*) denotes the complex conjugate, and with Eqs. (2.7) and (2.13), we have the desired expression for the intensity distribution in Plane II.

2.3. Generation of Serrated Circular Apertures

In this study we describe roughened circular apertures in terms of the mean radius, rms roughness, correlation angle, and correlation function. Although in Chapter 3 we will use fractal geometry to describe the apertures, these parameters provide an adequate description and are used to design apertures for digital and experimental studies.

The mean radius describes the circular shape of an aperture. We define an aperture by the curve describing the edge in plane (r, α) :

$$r = r_c = a + s(\alpha) , \quad (2.15)$$

where $s(\alpha)$ is a zero-mean random variable with variance denoted by

$$\text{var}[s(\alpha)] = \frac{1}{2\pi} \int_{-\pi}^{+\pi} s^2(\alpha) d\alpha . \quad (2.16)$$

For a particular aperture, the width and shape of the autocorrelation of $s(\alpha)$ are the correlation properties of interest.

Early work in the speckle field involved modeling rough surfaces by digital methods. Fujii, Uozumi, and Asakura³ used a convolution technique to generate correlated data for use as a model for rough surfaces. Their method involved convolving uncorrelated, random data with a window function to produce correlated data with the desired roughness and correlation properties. George and Morris⁴ used serrated edges and gaps in their diffraction study, and the thesis by Morris⁵ includes a detailed derivation of the relationship of the original, uncorrelated data and the window function to the correlated data. We reproduce this derivation in Appendix A for the reader's convenience and summarize the results below. Since the derivation involves the use of ensemble statistics, this summary describes the relationship between the original and correlated data in terms of ensemble parameters. We refer the interested reader to Appendix A, where the distinction between these ensemble parameters and the spatial parameters of the serration used heretofore is made.

Given a set of uncorrelated, Gaussian-distributed data $q(\alpha)$ with ensemble variance σ_q^2 and a window function $w(\alpha)$, we produce correlated data $s(\alpha)$ by convolving

$q(a)$ with $w(a)$:

$$s(a) = \int_{-\infty}^{+\infty} q(\xi) w(a-\xi) d\xi . \quad (2.17)$$

Then, under appropriate conditions, the ensemble variance σ^2 of $s(a)$ is approximately equal to the variance of $q(a)$:

$$\sigma^2 \approx \sigma_q^2 \quad (2.18)$$

and the normalized correlation function $r_s(\Delta a)$ of the ensemble of functions $s(a)$ is approximated by the auto-convolution of the window function:

$$r_s(\Delta a) \approx w(a) \star w(a) , \quad (2.19)$$

where \star denotes a convolution. Thus, by choosing the uncorrelated data and the window function carefully, we can generate correlated data with specified roughness and correlation properties for use as the serration function of an aperture.

In this section, we present several apertures generated by computer implementation of this convolution method. A copy of the program "stat.fft.c", used to design the apertures, is included in Appendix A. These apertures demonstrate the effects of varying in turn the mean radius, roughness, serration correlation angle, and serration correlation function of an aperture. Each aperture shown is a representative member of an ensemble of apertures, and the parameter values quoted are those of the ensemble. We do not intend with these limited examples to fully represent any ensemble of apertures; our purpose is to show typical serrated apertures and to demonstrate the effects of varying the aperture parameters.

2.3.1. Mean Radius

The first parameter we investigate is the average radius. Three sets of apertures were generated, each with design values of 250- μm rms roughness, $\pi/8$ -rad correlation angle, and triangular correlation function. This function is given by the equation:

$$\Lambda\left(\frac{\Delta\alpha}{A}\right) = \begin{cases} 1 - \frac{|\Delta\alpha|}{A}, & \text{for } \Delta\alpha \leq A ; \\ 0, & \text{otherwise,} \end{cases} \quad (2.20)$$

where $\Delta\alpha$ is the angular separation of two points on the aperture edge and A is the correlation angle. These nine apertures are shown in Fig. 2.2. Each of the apertures in a given column were generated from the same starter set of 512 Gaussian-distributed, uncorrelated random numbers⁶; different starter sets are used for each column of apertures. Each row of apertures has a different mean radius. The apertures in row (a) have a 2.5-mm mean radius; those in row (b), 5.0 mm; and those in row (c), 10.0 mm. As this mean radius increases, the apertures appear to be smoother, since the ratio of the roughness to the mean radius decreases. In addition, the correlation length along the edge increases as the mean radius increases, although the correlation angle remains constant. We see from these apertures the importance of specifying the mean radius when describing an aperture statistically. In our aperture designs, we will use a 5.0 mm mean radius. The apertures in Fig. 2.2 are the only exceptions to this.

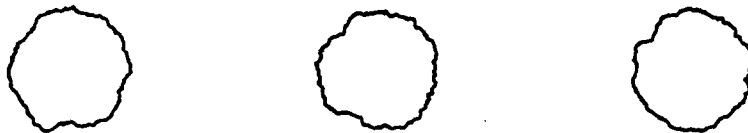
2.3.2. Root-mean-square Roughness

Three sets of apertures are used to investigate the effect of roughness variations and are shown in Fig. 2.3. The apertures in row (a) have a 125 μm rms roughness. Those in rows (b) and (c) have 250 and 500 μm rms roughnesses, respectively.

(a) 2.5 mm radius



(b) 5.0 mm radius



(c) 10.0 mm radius

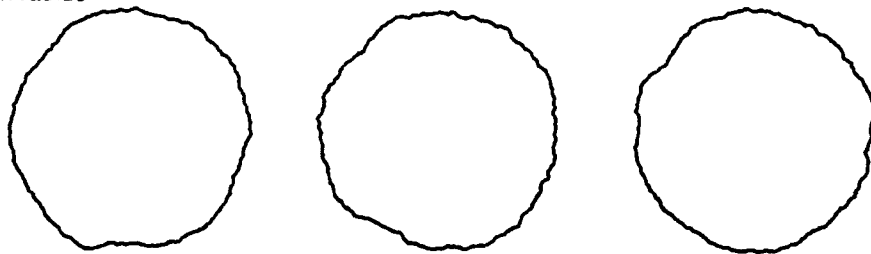
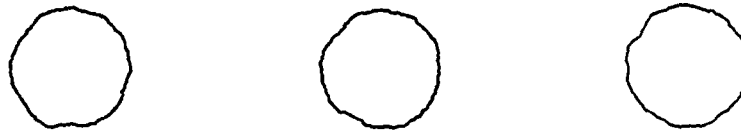
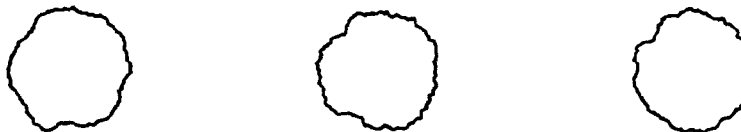


Fig. 2.2. Apertures of varied average radius. Each aperture has a design rms roughness of 250 μm . The correlation function is the triangle function, given by Eq. (2.20), with correlation angle $A = \pi/8$ rad. The mean radii for the aperture designs are (a) 2.5, (b) 5.0, and (c) 10.0 mm.

(a) 125 μm rms roughness



(b) 250 μm rms roughness



(c) 500 μm rms roughness

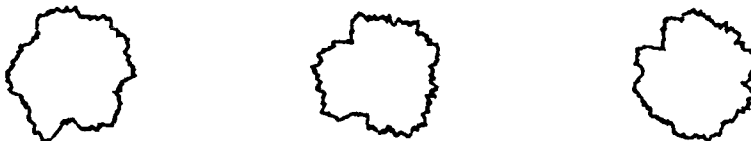


Fig. 2.3. Serrated apertures of varied roughness. All nine aperture designs have an average radius of 5.0 mm and the triangular correlation function of Eq. (2.20), with $A = \pi / 8$ rad. The ensembles represented in rows (a), (b), and (c) have 125, 250, and 500 μm roughnesses, respectively.

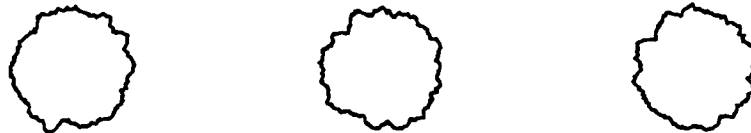
All nine apertures are designed with a 5.0 mm mean radius, a $\pi/8$ correlation angle, and a triangular correlation function, given by Eq. (2.20). The same starter set of 512 uncorrelated random numbers was used to generate each aperture in a column; a different starter set was used for each column. Specific aperture details, such as the bump located at 7 o'clock on the apertures in the left-hand column, are seen to scale with the roughness.

2.3.3. Serration Correlation Angle

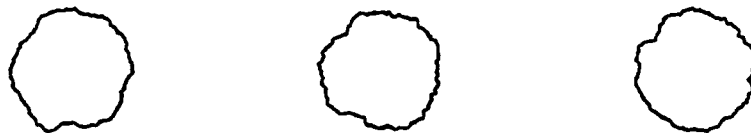
When we fix the mean radius, roughness, and correlation function in an aperture design and vary the width of the correlation function, we produce apertures such as those shown in Fig. 2.4. Again, each column of apertures forms a set which has been generated from a separate starter set of random numbers; each row consists of apertures with a particular correlation angle. Each aperture design has a 5.0 - mm mean radius, a 250 - μm rms roughness, and a triangular correlation function, given by Eq. (2.20). The apertures in row (a) are designed with a correlation angle of $\pi/16$ rad; in row (b), $\pi/8$ rad; and in row (c), $\pi/4$ rad.

We can see from these apertures that increasing the correlation angle results in a smoothing of the details of the aperture. This 'smoothness' differs from that of the apertures shown in Fig. 2.3; with changes in roughness, the aperture details remain but are scaled accordingly. Qualitatively, the apertures shown in Fig. 2.4 seem to become smoother as the correlation angle increases because specific features are broadened; quantitatively, we know that the rms roughness is constant.

(a) $\pi/16$ rad correlation angle



(b) $\pi/8$ rad correlation angle



(c) $\pi/4$ rad correlation angle

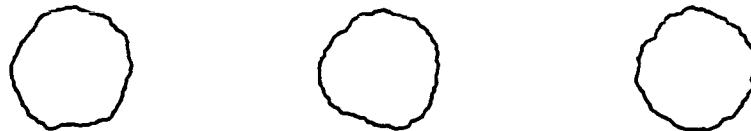


Fig. 2.4. Serrated apertures of varied correlation angle: A equal to (a) $\pi/16$, (b) $\pi/8$, and (c) $\pi/4$ rad. The average radius of all aperture designs is 5.0 mm; the rms roughness, 250 μm ; the correlation function, triangular, as given by Eq. (2.20).

2.3.4. Serration Correlation Function

Our fourth aperture parameter, the shape of the correlation function, controls the edge detail of the aperture. The apertures used to demonstrate this effect are shown in Fig. 2.5. Each of these apertures is designed with a mean radius of 5.0 mm, an rms roughness of 250 μm , and a correlation angle of $\pi/8$ rad. For each column of apertures, we use a separate starter set of uncorrelated random numbers. A different correlation function is associated with each row of apertures; these functions are shown in the right column of Fig. 2.5. For immediate purposes, the correlation angle for each function is defined as A in the following equations. We designed the apertures in row (a) with a triangular correlation function, given by Eq. (2.20):

$$\Lambda\left(\frac{\Delta a}{A}\right) = \begin{cases} 1 - \frac{|\Delta a|}{A}, & \text{for } \Delta a \leq A ; \\ 0, & \text{otherwise .} \end{cases} \quad [(2.20)]$$

The correlation function used in designing the apertures in row (b) is the negative exponential function, described by

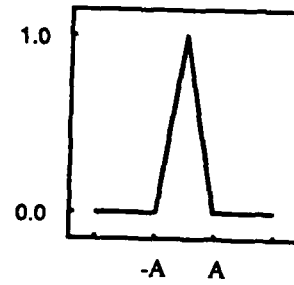
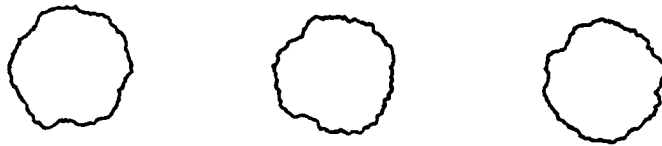
$$\text{nexp}\left(\frac{\Delta a}{A}\right) = \exp\left(-\frac{|\Delta a|}{A}\right). \quad (2.21)$$

A Gaussian function, given by

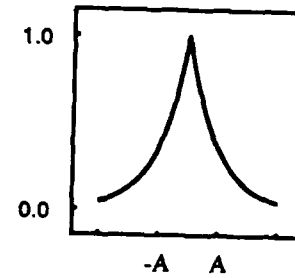
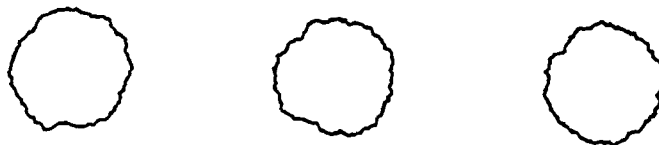
$$G\left(\frac{\Delta a}{A}\right) = \exp\left[-\left(\frac{\Delta a}{A}\right)^2\right], \quad (2.22)$$

is used in the design of the apertures in row (c). We choose this form of the Gaussian so that, for both the negative exponential and Gaussian functions, A is the half-width of the function at the e^{-1} point.

(a) Triangular correlation function



(b) Negative exponential correlation function



(c) Gaussian correlation function

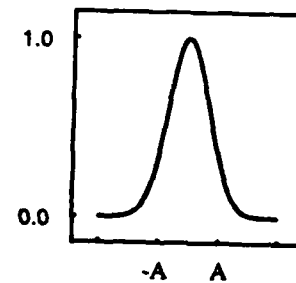
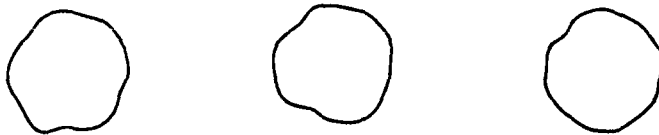


Fig. 2.5. (Left) apertures and (right) correlation functions: (a) triangular correlation, Eq. (2.20); (b) negative exponential correlation, Eq. (2.21); (c) Gaussian correlation, Eq. (2.22). Each of the aperture designs has a 5.0 mm mean radius, an rms roughness of 250 μm , and a correlation angle A of $\pi/8$ rad.

A striking feature of the apertures in a given column is the similarity of the general non-circular shape. This shape is fixed by the starter set and by the roughness and correlation angle of the serration. The shape of the correlation function affects the behavior of the edge of each aperture. Those shown in Fig. 2.5 (a) and (b) have jagged edges on top of their non-circular shapes. A common feature of these apertures is the sharp peak on the correlation function. If we use a smooth-peaked correlation function, the edge of each aperture we produce is significantly smoother. This is demonstrated by the Gaussian-correlated apertures in Fig. 2.5 (c). The shape of the correlation function of an aperture, and in particular the shape of the peak, is thus shown to affect the edge detail of the apertures.

2.3.5. Aperture Smoothness

In the preceding paragraphs, we discussed changes in the appearance of an aperture as we varied the mean radius, roughness, and correlation properties of that aperture. Smoothness, as a qualitative descriptor, has been mentioned multiple times. We noted that increasing the mean radius produced a smoother aperture, as did increasing the correlation angle. A smooth-peaked correlation function was shown to produce smooth-edged apertures. Certainly, we would be likely to describe apertures with small rms roughness as smooth. Hence, one can see that smoothness depends on all of these parameters. We must be careful to use these quantitative measures in order to describe our apertures accurately.

In Chapter 3, we will see that the fractal dimension can be used to describe the aperture smoothness, and that this fractal dimension depends in definite ways on these aperture parameters.

2.4. Computer Simulation of the Fourier Transform

At this early stage in our study, computer simulations of the Fourier transforms serve to develop our qualitative sense of the behavior of the transform as the aperture parameters are varied. This tool also provides quantitative information that will be useful in designing apertures for optical experiments. We use Eqs. (2.7) and (2.14) as the basis for our computer calculations. In this section, we take representative apertures from Figs. 2.3, 2.4, and 2.5 and show the calculated transforms as two-dimensional images. First, since film typically records intensity values logarithmically over two to three orders of magnitude, we choose to display this same range of values by selecting upper and lower cutoffs that are three orders of magnitude apart. Intensity values above or below this range are mapped to the upper or lower limit, respectively. The cutoff values are chosen so that the features of interest are clearly visible; here, with an input field of unity, the cutoff values chosen are 0.02 and 20.

To reproduce the computer screen images for this document, we used a camera system manufactured by Matrix instruments⁷ and connected with an I²S image processing system⁸. Using Polaroid 57 film⁹, we photographed the computer-generated images; these photographs were then enlarged to show the features clearly. In Chapters 5 and 6, we will compare calculated transforms with those obtained optically. We find that scaling our computed data logarithmically before using the complicated display-photograph-enlarge process described above produces images that compare well with the photographs taken in the optical system.

To summarize, then, the procedure used to produce the images shown in Figs. 2.6, 2.7, and 2.8 is as follows. Empirically-chosen cutoff values of 0.02 and 20 were applied to the calculated data. The data were then scaled logarithmically, and the new

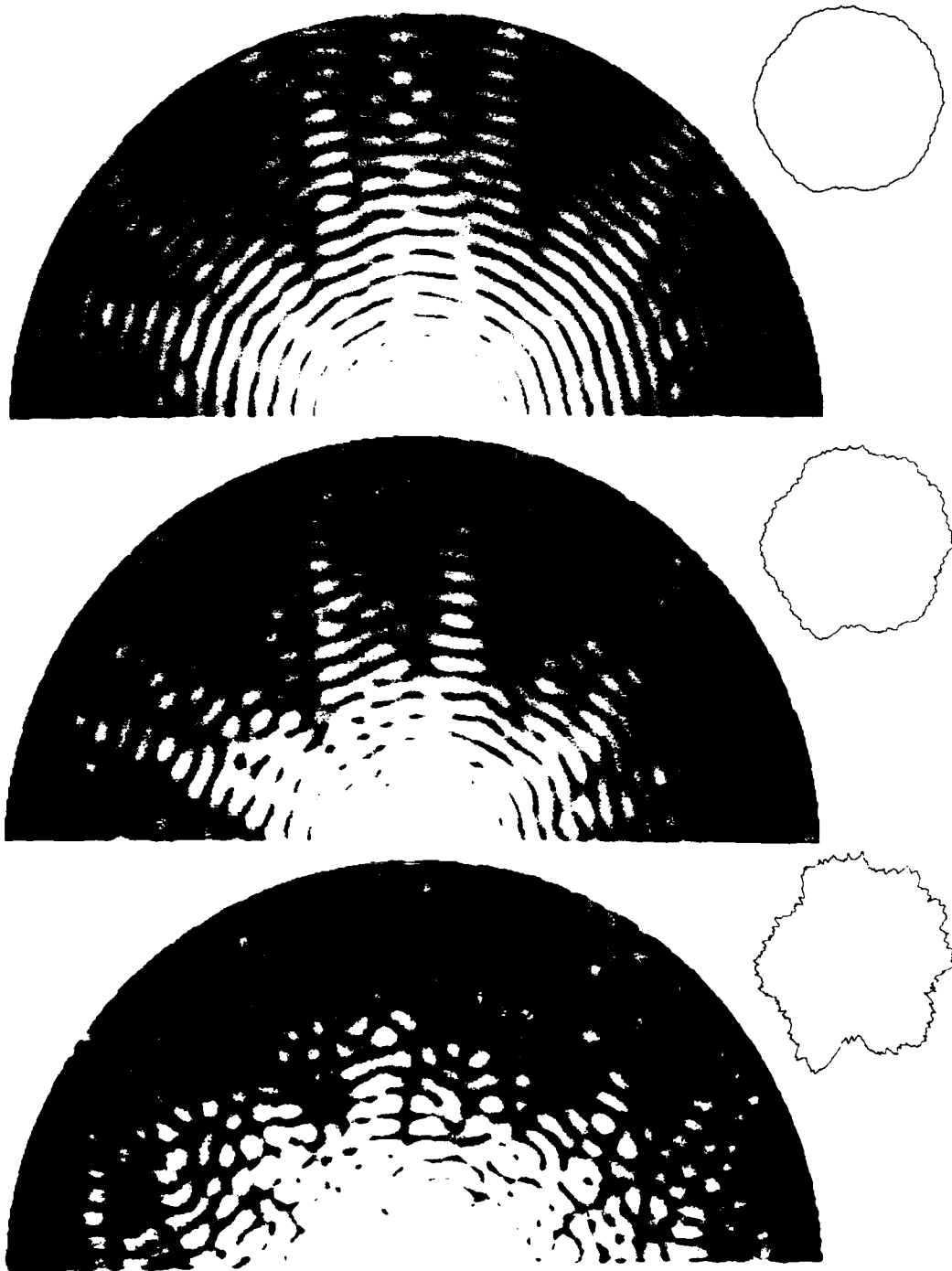


Fig. 2.6. Calculated diffraction patterns for apertures of varied rms design roughness: (upper) 125 μm , (middle) 250 μm , and (lower) 500 μm . Inset are the corresponding apertures, from the left-hand column of Fig. 2.3.

values were assigned linearly to values between 0, mapping intensity values of 0.02 and lower to black, and 255, mapping values of 20 and higher to white. (There are 256 grey levels available in the 8-bit-per-pixel display of the Matrix camera.) The resulting image data files were transferred to the I²S-Matrix system and the images were photographed with Polaroid 57 film. These photographs were enlarged and printed for use in this dissertation.

2.4.1. Aperture Roughness

The diffraction patterns shown in Fig. 2.6 correspond to the apertures in the left-hand column of Fig. 2.3; these apertures differ in roughness and are shown inset in Fig. 2.6 for convenience. Since the Fourier transforms are polar-symmetric, we calculate and display only half of the diffraction pattern, the region $0 \leq \phi \leq \pi$. The largest value of ρ used in the calculation, 0.50 mm, is chosen so that several diffraction rings can be observed. The wavelength λ is set at 0.5 μm ; focal length z_0 , at 500 mm.

The upper diffraction pattern in Fig. 2.6 is that of the aperture with 125- μm roughness. Even with just this small serration, we see that the rings at larger radial coordinates become uneven. The middle diffraction pattern corresponds to a 0.25-mm aperture roughness. In this case, some of the outer rings are broken and more of the inner rings are uneven. In the lower Fourier transform, corresponding to 500 μm rms roughness, we see that only the first few rings are intact. At large radii, the ring structure has degraded to a speckle pattern.

We see from these three diffraction patterns that aperture roughness first degrades the outermost rings. These rings become uneven in width and eventually, with

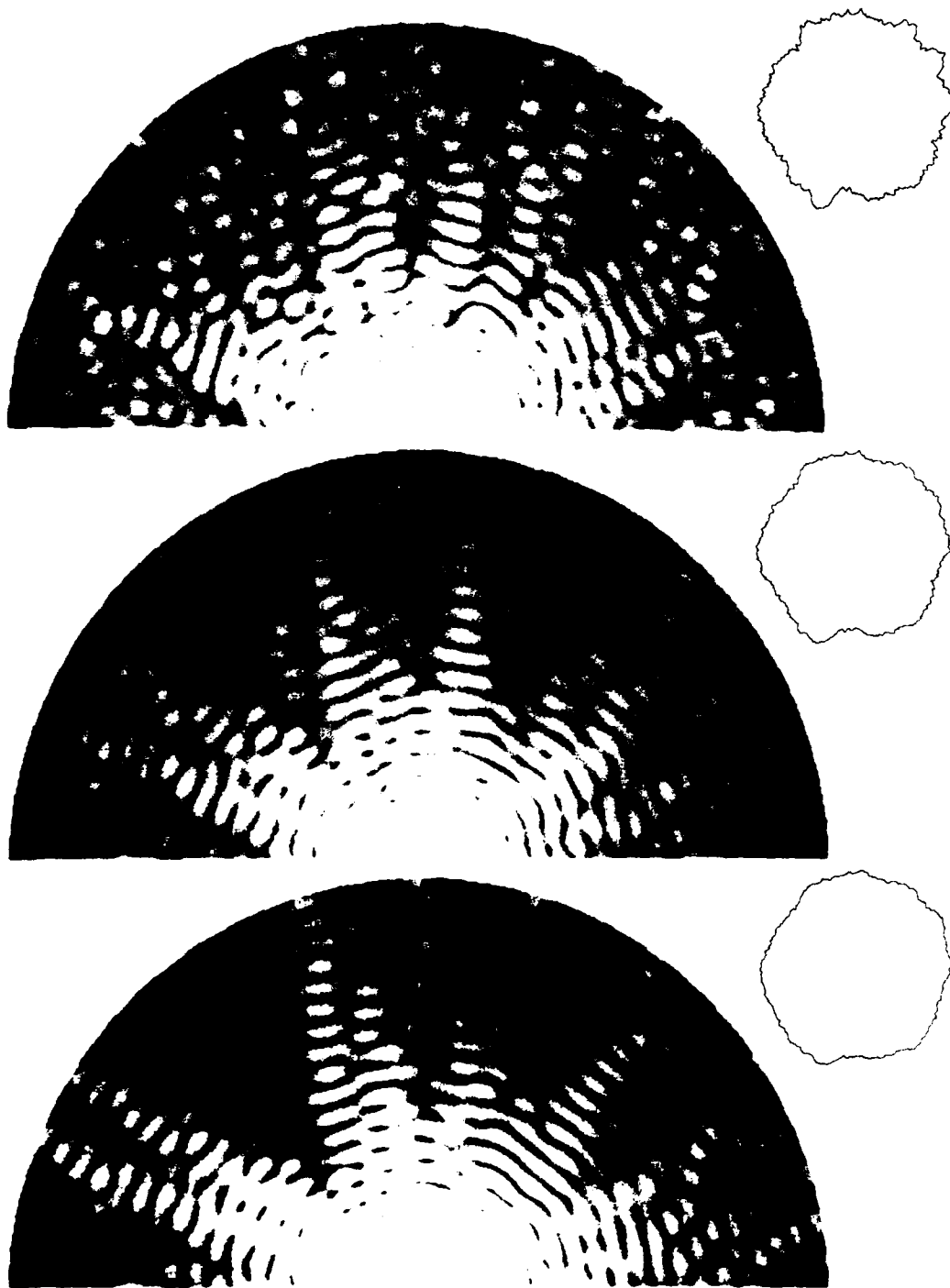


Fig. 2.7. Calculated diffraction patterns for apertures with different serration correlation angles: A equal to (upper) $\pi/16$, (middle) $\pi/8$, and (lower) $\pi/4$ rad. Inset are the corresponding apertures, from the left-hand column of Fig. 2.4.

increased roughness, break into ring fragments. As the roughness increases these degradation effects are seen at smaller radii in the transform.

2.4.2. Serration Correlation Angle

The Fourier transforms shown in Fig. 2.7 demonstrate the effect produced by changing the correlation angle. The apertures used in calculating these transforms are those shown in the left-hand column of Fig. 2.4 and inset in Fig. 2.7. We recall that as the serration correlation angle increases the bumps on the apertures broaden, producing smoother apertures even though the rms roughness remains constant. The upper, middle, and lower transforms in Fig. 2.7 correspond to correlation angles of $\pi/16$, $\pi/8$, and $\pi/4$ rad, respectively. They show how the change in the transform progresses as the correlation angle of the serration increases: the spikes broaden and their number decreases. (The counting of spikes in this type of display is somewhat subjective; the author counts 10 spikes in the upper transform, 8 in the middle transform, and 7 in the lower transform.) The decrease in the number of spikes indicates that the correlation angle of the intensity distribution has also increased. This result is intuitively pleasing, and the theory and computer simulations to be presented in Chapter 4 will support these observations.

2.4.3. Serration Correlation Function

The last set of calculated Fourier transforms, shown in Fig. 2.8, are those of the apertures with different correlation functions. The apertures chosen for these calculations are those shown in the left-hand column of Fig 2.5 and are inset in this figure. From top to bottom, we show the transforms of the apertures with triangular, negative exponential, and Gaussian correlations, respectively. The appearance of each diffraction

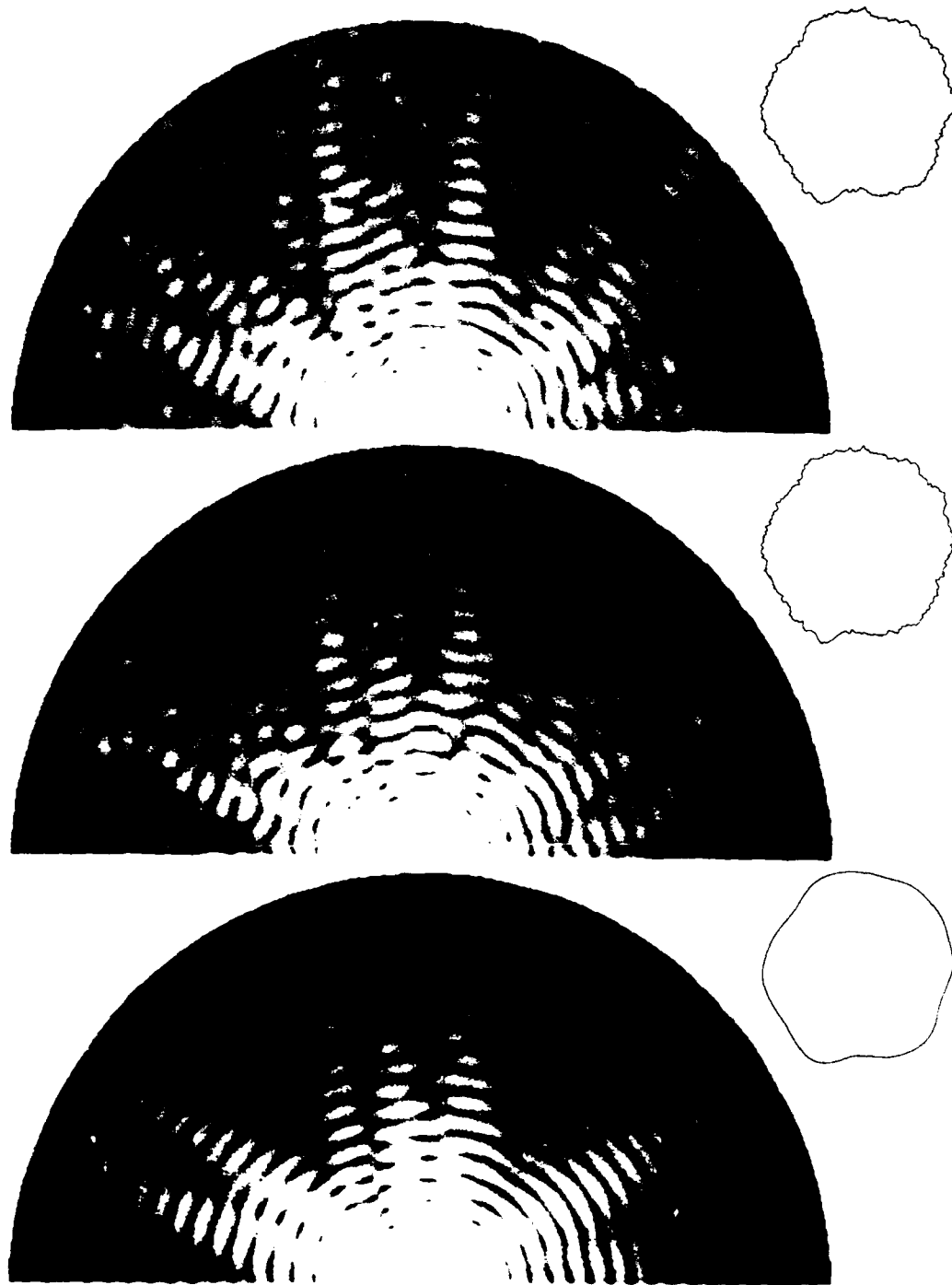


Fig. 2.8. Calculated diffraction patterns corresponding to apertures of varied correlation design: (upper) triangular, Eq. (2.20); (middle) negative exponential, Eq. (2.21); (lower) Gaussian, Eq. (2.22). Inset are the corresponding apertures, from the left-hand column of Fig. 2.5.

pattern depends on the shape of the peak of the corresponding correlation function. This striking variation has not been described in the literature, heretofore. We see that when the peak is sharp (here, the triangular and negative exponential cases), the bright radial spikes contain substructure which can make identification more difficult; when the peak is smooth (the Gaussian correlation function), the spikes are easier to see because the intensity varies smoothly in the angular direction, across the spikes.

The spike appearance coordinates with that of the apertures for the different correlation functions. As we saw in Fig. 2.5, the character of the edge of the non-circular apertures depends on the shape of the correlation function of the serration. When the peak is smooth, the edges are smooth; when the peak is sharp, the edges are rough. Similarly, in the calculated diffraction patterns we see that the smooth-peaked correlation function yields smooth spikes in the transform; the sharp-peaked function, uneven spikes. From these observations, we expect the following relationships to hold: the shape of the correlation function of the serration on the aperture influences the shape of the angular correlation of the transform; the smoother the aperture correlation is, the smoother the transform correlation will be; and a smooth angular correlation for the transform corresponds to uniform spikes in that transform. The theory presented in Chapter 4 and the experiments described in Chapter 6 will prove these points. First, we continue with our analysis of the apertures by considering the fractal nature of the serrated aperture.

Chapter 2 Notes and References

1. R. E. English and N. George, "Diffraction from a circular aperture: on-axis field strength," *Appl. Opt.* **26**, 2360-2363 (1987).
2. M. M. Beal and N. George, "Features in the optical transforms of serrated apertures and disks," *J. Opt. Soc. Amer. A*, **6**, 1815-1826 (1989).
3. H. Fujii, J. Uozumi, and T. Asakura, "Computer simulation study of image speckle patterns with relation to object surface profile," *J. Opt. Soc. Am.* **66**, 1222-1236 (1976).
4. N. George and G.M. Morris, "Diffraction by serrated apertures," *J. Opt. Soc. Am.* **70**, 6-17 (1980).
5. G.M. Morris, *Serrated Apertures: Statistical Diffraction Theory and Experiments* (Ph.D. Thesis, California Institute of Technology, 1979).
6. The uncorrelated random numbers were generated on a Masscomp 6700 computer. The routines "srandom (seed)" and "random ()", were used with an integer between 3 and 6 as the seed. The period of this random number generator is very large, approximately equal to $16 \times (2^{31} - 1)$. A transformation routine was used to convert the uniform distribution thus produced to a Gaussian distribution; see the program source code "stat.fft.c" in Appendix A.
7. Matrix Instruments, 1 Ramland Road, Orangeburg, NY 10962.
8. International Imaging Systems, 1500 Buckeye Drive, Milpitas, CA 95035.
9. Polaroid 57 film, which has an ISO number of 3000, is a product of Polaroid Corporation, Cambridge, MA 02139.

Chapter 3

Comparison of the Statistical and Fractal Descriptions

3.1. Introduction

The study of an irregular object has in the past implied the virtually exclusive application of statistical techniques. In the case of serrated apertures, George and Morris¹ gave a thorough description in terms of the rms roughness, the correlation angle, and the shape of the correlation function. We used these statistical parameters and the mean radius to describe serrated circular apertures in Chapter 2, and we will continue to use them throughout this study. However, the introduction of fractal mathematics² and the application of fractal geometry to physical systems offers a new approach for use in studies such as ours. In current literature, one can find both statistical and fractal descriptions of irregular objects. Although the studies in which a statistical approach is taken are far more numerous, interest in and applications of fractal geometry have increased enough to merit a study of the complementarity of these two methods³. Our objective in this portion of our study is to understand, in the case of the serrated aperture, the relationship between the fractal dimension of an object and the roughness, correlation angle, and correlation function.

In much of the work done with fractals, the approach has been to examine a fractal function or model in which the fractal dimension is explicitly expressed, to note the similarity to a physical object, and to manipulate the function to exploit those similarities. Our approach, however, will be to generate representative members of ensembles (in particular, of apertures with specific roughnesses, correlation angles, and correlation functions) and to determine the fractal dimensions. In this introduction, we first discuss

briefly an example of a fractal function, the Weierstrass function, and then look at the fractal properties of several functions generated by the convolution method described in Appendix A. Then, in Section 3.2, we describe two methods for determining an unknown fractal dimension and test these methods on a curve with a well-defined fractal dimension. We use these methods to determine the fractal dimensions of serrated apertures and report our results in Section 3.3. In Section 3.4, with a qualitative understanding of the relationships between aperture parameters and the fractal dimension, we look again at the Weierstrass function and investigate a disagreement between our results and the definition of the dimension of this fractal function. Finally, we investigate the quantitative dependence of the fractal dimension on the roughness, correlation length, and correlation function of a serration.

3.1.1. Fractal Functions

As a mathematical entity, a fractal curve is self-similar under scaling and non-differentiable². This self-similarity is dilation symmetry; when scaled appropriately, the structure at every level of scrutiny is the same. Continuing this dilation to infinitesimal scales, we can see that this self-similarity prohibits us from drawing a tangent to the curve at any point; there is always sub-structure which disallows the definition of the tangent. Therefore, the curve is not differentiable at any point.

An example of a fractal function is the Weierstrass function, named for the nineteenth-century mathematician who developed it out of his interest in continuous, yet non-differentiable, functions. The fractal properties of the Weierstrass function were first studied by Mandelbrot² and were further investigated by Berry and Lewis⁴, whose

publication includes several plots of the function for different values of the principal parameters.

The complex-valued Weierstrass function can be written as:

$$W_0(x) = \left(1 - b^{2(D_W - 2)}\right)^{-1/2} \sum_{n=-\infty}^{\infty} \left\{ b^{(D_W - 2)n} \times [1 - \exp(ib^n x)] \exp(i\phi_n) \right\} \quad (3.1)$$

where $b > 1$ is the real-valued fundamental spatial frequency and the phases ϕ_n are arbitrary; they can be either deterministic or random. If the value of D_W lies between one and two, then $W_0(x)$ is non-differentiable despite continuity. The frequency spectrum is discrete, with frequencies f_n forming a geometric progression:

$$f_n = b^n. \quad (3.2)$$

Since for each frequency f_n the next higher frequency is $f_n b$ and the next lower f_n / b , $W_0(x)$ is a self-similar function under scaling, as required of a true fractal function. The parameter D_W in Eq. (3.1) is assumed^{2,4} to be the fractal dimension of $W_0(x)$.

The real-valued Weierstrass cosine function,

$$W(x) = \left(1 - b^{2(D_W - 2)}\right)^{-1/2} \sum_{n=-\infty}^{+\infty} b^{(D_W - 2)n} \cos(2\pi b^n x + \phi_n), \quad (3.3)$$

has been used by Kim⁵ to model diffusers. The autocorrelation $R_W(\Delta x)$ of $W(x)$,

$$R_W(x + \Delta x, x) = \frac{1}{2} \left(1 - b^{2(D_W - 2)}\right)^{-1} \sum_{n=-\infty}^{\infty} b^{2(D_W - 2)n} \cos(b^n \Delta x), \quad (3.4)$$

is used to determine the variance σ_W^2 and normalized correlation function $r_W(\Delta x)$ of the Weierstrass cosine function, as follows:

$$\sigma_W^2 = R_W(0) = \frac{1}{2} \left(1 - b^{2(D_W - 2)} \right)^{-1} \sum_{n=-\infty}^{\infty} b^{2(D_W - 2)n}, \quad (3.5)$$

$$r_W(\Delta x) = \frac{R_W(\Delta x)}{\sigma_W^2} = \frac{\sum_{n=-\infty}^{\infty} b^{2(D_W - 2)n} \cos(b^n \Delta x)}{\sum_{n=-\infty}^{\infty} b^{2(D_W - 2)n}}. \quad (3.6)$$

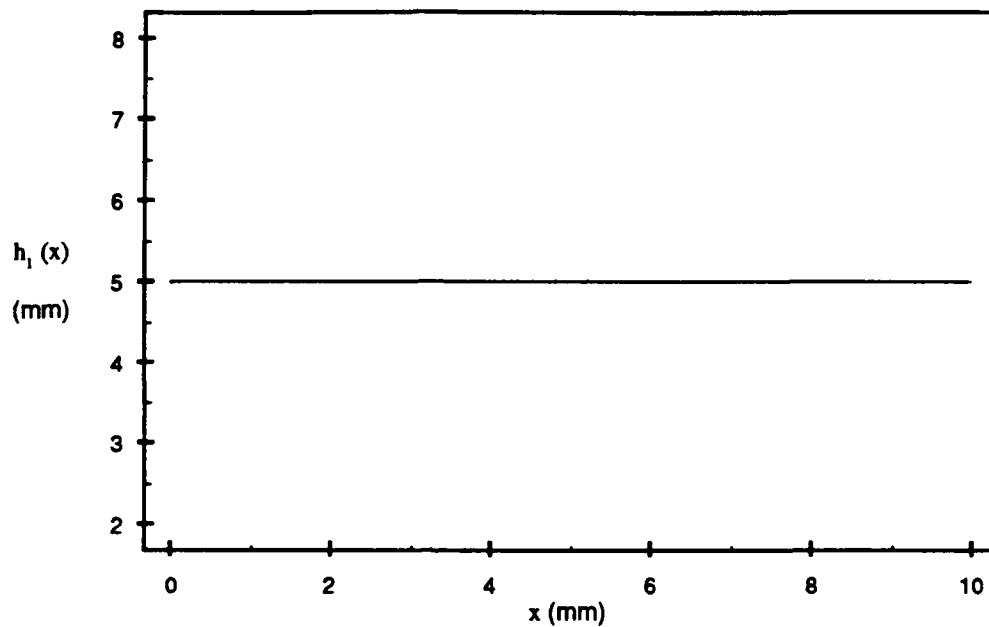
For the derivation of Eq. (3.4), we have assumed that the phases $\{\phi_n\}$ are uniformly distributed on the interval $(0, 2\pi]$. We see from Eqs. (3.5) and (3.6) that, given the parameters D_W and b for a particular set of functions $W(x)$, one can determine the quantities σ_W and $r_W(\Delta x)$.

Our approach to the application of fractal geometry differs from that described above. We wish to define the fractal dimension of a function, rather than define a function with a specific fractal dimension. To this end, we further clarify the concept of fractal dimension, look at the fractal attributes of our serrated apertures, and describe methods by which we can determine the fractal dimensions. When we have discussed techniques used to determine an unknown fractal dimension, we will return to our consideration of the Weierstrass function and the validity of equating D_W with the fractal dimension.

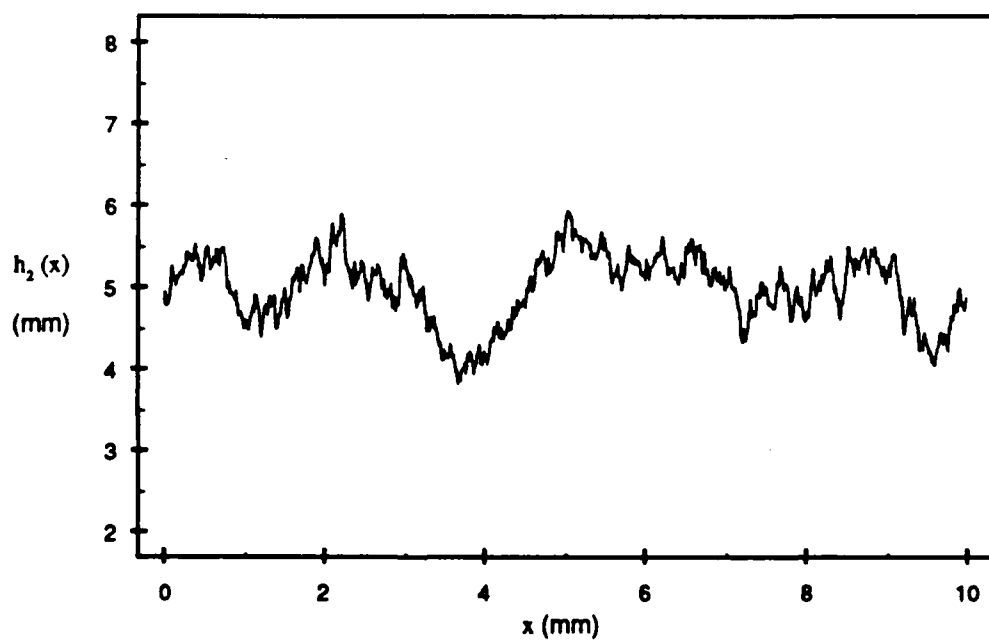
3.1.2. Fractal Attributes of Random Processes

Consider a function $h_i(x)$ described by the mean η , variance $\text{var}(h_i(x))$, correlation length L , and correlation function $r_h(\Delta x)$. This function could describe the edge of a serrated circular aperture, in which case x would be the angular coordinate, $h_i(x)$ would be the radius of the aperture at angle x , η would be the mean radius, and correlation angle would be used rather than correlation length. Four such functions, each a realization of a different random process, are shown in Fig. 3.1. We used the convolution method described in Appendix A to generate these functions; the different roughnesses and correlation functions used are given in Appendix B.

To understand our motivation for describing an aperture radius function in terms of the fractal dimension, consider the following description of these four functions. Function $h_1(x)$ is a straight line, $h_1(x) = 5$. This function is certainly one-dimensional. In Euclidean geometry, functions $h_2(x)$, $h_3(x)$, and $h_4(x)$ are also one-dimensional; each describes a line in the $(x, h_i(x))$ plane. However, successive functions in our series seem to take on a second dimension; function $h_4(x)$ approaches the limit of filling an area in the plane, thus prompting us to call it nearly two-dimensional. Fractal geometry helps us to overcome the troublesome interpretation of a one-dimensional function filling two-dimensional space. We assign a fractal dimension with a value between one and two based on the space-filling ability of these curves. Following Mandelbrot's convention, we use D to denote the fractal dimension and E for the Euclidean dimension. Smooth lines and curves such as $h_1(x)$ are assigned a fractal dimension of 1.00, while curve $h_4(x)$, which nearly fills an area, has a fractal dimension $D = 1.95$, close to two. Curves such as $h_2(x)$, with $D = 1.24$, and $h_3(x)$, $D = 1.67$, have fractal dimensions between these two extremes. Each of the functions in Fig. 3.1 has a Euclidean dimension E equal to one, while

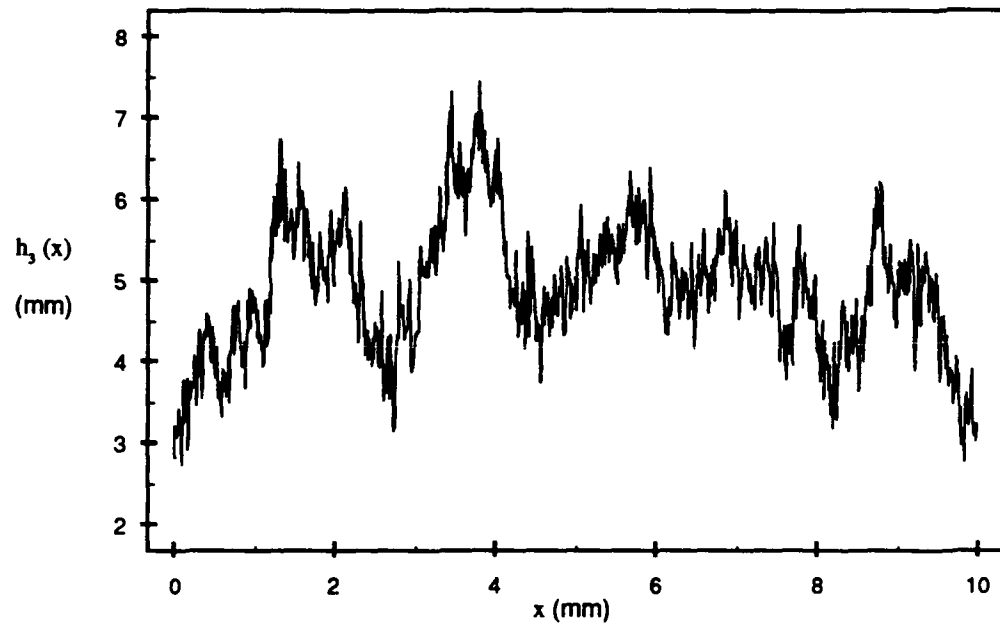


(a)

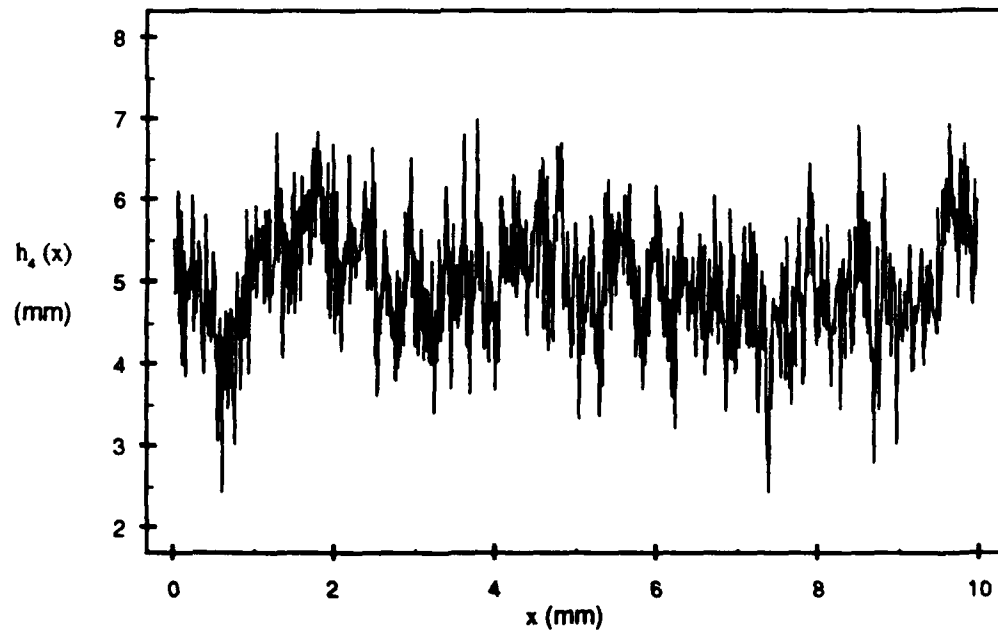


(b)

Fig. 3.1. Four functions, each represented by a (Euclidean) one-dimensional line, but with different fractal dimensions: (a) $D = 1.00$, (b) $D = 1.24$. Details of the generation of these functions are included in Appendix B.



(c)



(d)

Fig. 3.1. (Continued) (c) $D = 1.67$, (d) $D = 1.95$.

each has a different fractal dimension, $1 \leq D \leq 2$. We can extend this concept to objects with other Euclidean dimensions. A fractal dimension between zero and one can be assigned to a collection of points which tends to form a line; a surface which tends to fill a volume can be described by a fractal dimension between two and three.

In Appendix B, we describe the differences between these functions by the differences in the rms deviation and the correlation function. Changes in the fractal dimension also describe the differences between the curves. Herein, we will explore the relationship between the fractal dimension and the variance, correlation angle, and correlation function of a curve.

3.1.3. Determining the Fractal Dimension

The existence of sub-structure at progressively smaller scales suggests many physical realities. We can view an irregular object with a wide range of magnifications and discover at large magnifications details unseen at lesser ones. Often the details at all levels possess similar structure. This self-similarity can be described fractally. An example is pointed out by Mandelbrot⁶ who, prompted by the work of Richardson⁷, applies fractal geometry to the coast of Britain. In particular, he considers the task of measuring the coastline of Britain. With successively smaller measuring sticks, we must include the perimeters of successively smaller bays and peninsulas, eventually (in theory) measuring boulders, rocks, pebbles, etc. Each decrease in the length of our measuring stick allows and requires us to measure finer details of the coastline, and to add these measurements to our perimeter. Thus, more accurate measurements yield longer coastline approximations.

In a given physical system, there are constraints that limit our accuracy and therefore place an upper bound on our length measurement. Physical objects have smallest and/or largest scales. Fractals, however, have no such limits. This distinction is made by Jaggard and Kim⁸, who use the terminology *band-limited fractal* to describe a function with a bounded range of component frequencies. Such a function would describe a physical object with limited fractal properties. In this section, we show how Richardson's method is used to determine the fractal dimension of a serrated circular aperture, which is an example of a bandlimited fractal.

Following Mandelbrot, we use the following method to define the fractal dimension of a serrated circular aperture. Let w be the length of our hypothetical measuring stick and $P(w)$ the aperture perimeter approximation made with it. The functional relationship between w and $P(w)$ is defined:

$$P(w) = P(1)w^{1-D}, \quad (3.7)$$

where D is the fractal dimension of the measured curve. A plot of $\log[P(w)]$ against $\log(w)$ is a curve with negative slope, since $P(w)$ increases as w decreases. For the sake of this discussion, we call such plots Richardson curves⁹. Since from Eq. (3.7) we have

$$\log [P (w)] = \log [P (1)] + (1 - D) \log (w) , \quad (3.8)$$

the slope m of a Richardson curve is given by:

$$m = 1 - D ; \quad (3.9)$$

D takes values between one and two. Thus, as D increases, the slope of the plot becomes steeper.

We implement this method on a computer, estimating the perimeter of an aperture with successively smaller steps, plotting the associated Richardson curve, and

using the slope of this curve to determine D . In this way we are able to determine quickly the fractal dimension of several apertures through a series of user-interactive programs. This approach is particularly well suited to our computer-designed apertures. The program "frac.c" used to perform the perimeter estimation is included in Appendix C. With this program we find the intersections of the continuous aperture with steps of a given length, using linear interpolation between the discrete data points to define the aperture. If there are multiple intersections, the intersection point chosen is the one farthest away along the aperture edge from the other endpoint of the step. In this way, we get the coarsest approximation of the perimeter at each step size.

A second method, also used by Kaye¹⁰, is the grid interrogation method. The basis of this method is the relationship between the fractal dimension of an aperture and the frequency with which it intersects a regular square grid of a given spacing. If a grid with spacing w intersects a curve $N(w)$ times, then a doubly logarithmic plot of $w \cdot N(w)$ versus w can be used to determine the fractal dimension of that curve in a manner similar to the Richardson method. Here we present a detailed description of the grid interrogation method as implemented for this study.

The actual coordinates of any point of intersection between the grid and the aperture are unimportant, since the quantity of interest is the number of intersections. Therefore, in our implementation, we determine whether each grid point lies inside the aperture, outside the aperture, or on the perimeter. Then for the number of intersections we use the number of adjacent point pairs of either type (in, out) or type (out, in). To this number we add one half the number of grid points which lie on the perimeter. The resulting number is an estimate of the number of intersections. One possible source of error is the use of half the number of boundary points; we are assuming that half of these

points are intersection points, and the other half are points where the grid grazes the aperture. This estimate is suggested by Kaye. We note that the error introduced is negligible, since so few grid points fall on the edge of the aperture. A more serious error occurs when, for example, two points adjacent on the grid lie within the aperture, but an even number of intersections lie between them. In this case, the intersections would not be counted, and a low estimate would result. This error is a consistent one because of the self-similarity of fractals. Since the fractal dimension is calculated from the slope of the plotted data, this counting error should not significantly affect the resulting value for the fractal dimension.

Program "grid.c", used to calculate the number of aperture-grid intersections for a range of grid sizes, is included in Appendix C. As in the program "frac.c" used to calculate the Richardson curve data, we use linear interpolation between the aperture points. The data calculated with "grid.c" are used to plot the grid interrogation curve for each aperture. We then determine the slope of the curve in order to find the fractal dimension.

Although in implementation the grid interrogation and Richardson methods are quite different, the quantity being measured at the different step or grid sizes is a perimeter estimate in each case. The quantity $N_w \cdot w$ is the length of a path along the grid that lies close to the aperture edge. As w decreases, this path comes closer to coincidence with the aperture edge and our perimeter approximation increases. This estimate will be consistently higher than the corresponding Richardson length estimate because the steps are constrained to the grid directions. However, a plot of $\log(N_w \cdot w)$ against $\log(w)$ has a negative slope m from which we determine the fractal dimension by the relationship

$$D = 1 - m \quad (3.10)$$

We see that this part of the analysis is identical to that of the Richardson method and note that the interrogation curve will have zero slope when the aperture is Euclidean. In our study, we use both techniques in order to corroborate the results of each.

In order to test the accuracy of these two methods as realized in our computer calculations, we used a regular fractal structure of known fractal dimension as input to our series of programs. The generation of the triadic Koch curve is outlined in Fig. 3.2. Starting with equilateral triangle (a), we replace each side with the scaled generator (b) to yield the Star of David shape (c). Next, each of the twelve sides of this new shape is replaced by the generator; this procedure is repeated (in theory, *ad infinitum*) to generate the triadic Koch curve, shown in (d) after five iterations. This curve has fractal dimension $\log 4 / \log 3 = 1.2619$ ¹¹.

The Koch curve is an appropriate input object for our program series, since it resembles an aperture. From the Richardson method, we calculate a fractal dimension of 1.264; from the grid method, 1.262. Standard practice¹² is to use four digits beyond the decimal place for a theoretically defined fractal dimension and two digits beyond the decimal place for experimentally determined dimensions. By this standard, our results from both methods are excellent for the Koch curve.

3.2. Fractal Dimension Calculations for Serrated Apertures

We now apply our two techniques to representative serrated apertures in order to determine the fractal dimensions. The apertures are chosen from those presented in Section 2.3 and are used to investigate the effects of the roughness,

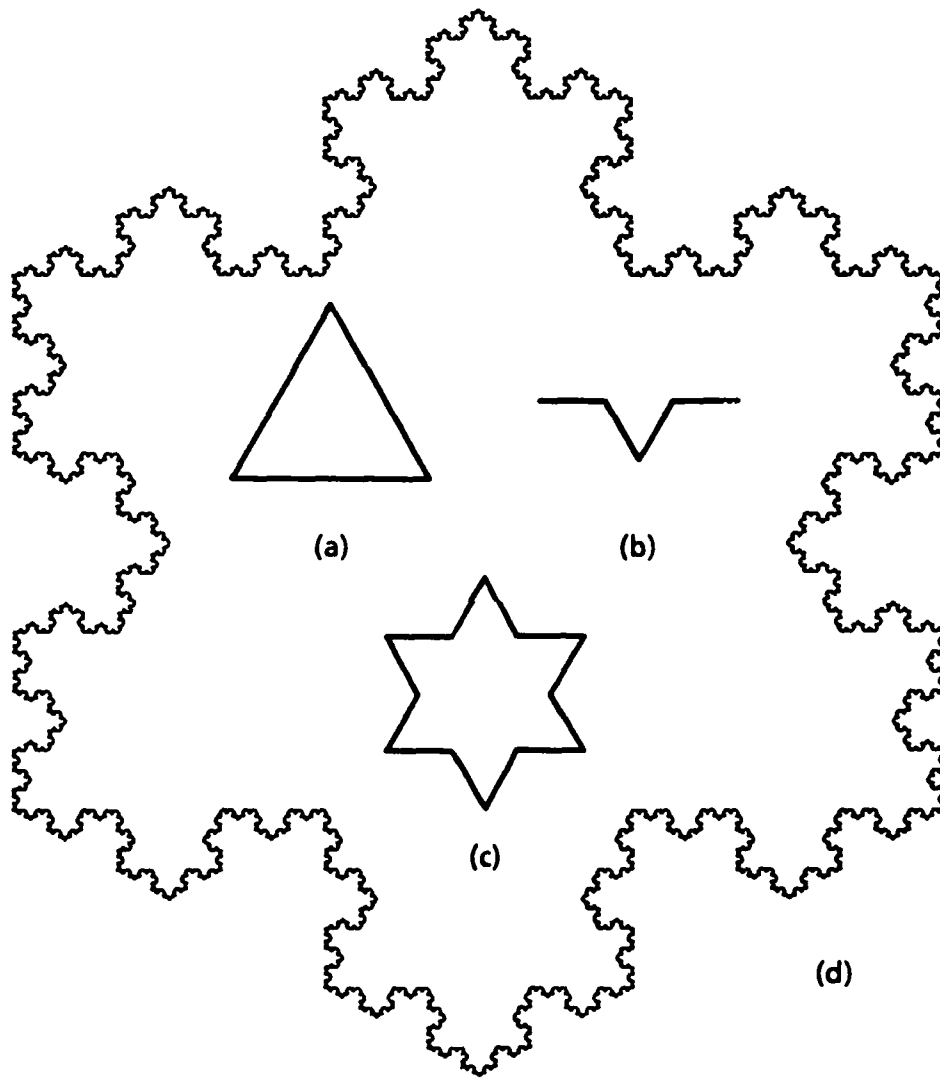


Fig. 3.2. Generating a triadic Koch curve. (a) initial triangle, (b) generator, (c) first generation, (d) fifth generation.

correlation angle, and correlation function of the aperture serration on the shapes of the Richardson and grid interrogation curves and thus on the fractal dimension.

3.2.1. Aperture Roughness

The Richardson and grid interrogation curves shown in Fig. 3.3 are those of the apertures in the left column of Fig. 2.3. These apertures, which vary only in roughness, comprise aperture set 1. Each has a triangular correlation function and a $\pi/8$ rad correlation angle; the roughnesses are listed in the figure key and in Table 3.1. Also included in Fig. 3.3 are the Richardson and interrogation curves for a circle. With the Richardson method, measuring the circle with the same step sizes as the apertures, we rapidly approach an upper limit to $P(w)$ as w decreases. The circle is a Euclidean object, with no sub-structure to add to our perimeter measurement as we use successively smaller measuring steps. The slope of the corresponding Richardson curve is equal to zero. The same is true of the interrogation curve. If we were to continue measuring any physical object beyond the scale of the smallest detail, we would find this result. At scales smaller than this, a physical object is Euclidean. Thus for the circle we see that the Richardson and interrogation curves are straight lines with zero slope, indicating a fractal dimension of unity. As the roughness increases, the curves of both types grow steeper; the absolute value of the slope increases, indicating an increase in the fractal dimension.

The Richardson curve for a particular aperture is noticeably smoother than the interrogation curve, particularly at larger step sizes. By studying an individual Richardson curve, we can learn more about the fractal qualities of the apertures. The slope of each curve takes on different values for different ranges of w . For small step sizes, the slope approaches zero. This corresponds to a fractal dimension of unity or a Euclidean object, reflecting the lower limit placed on our resolution in the design process;

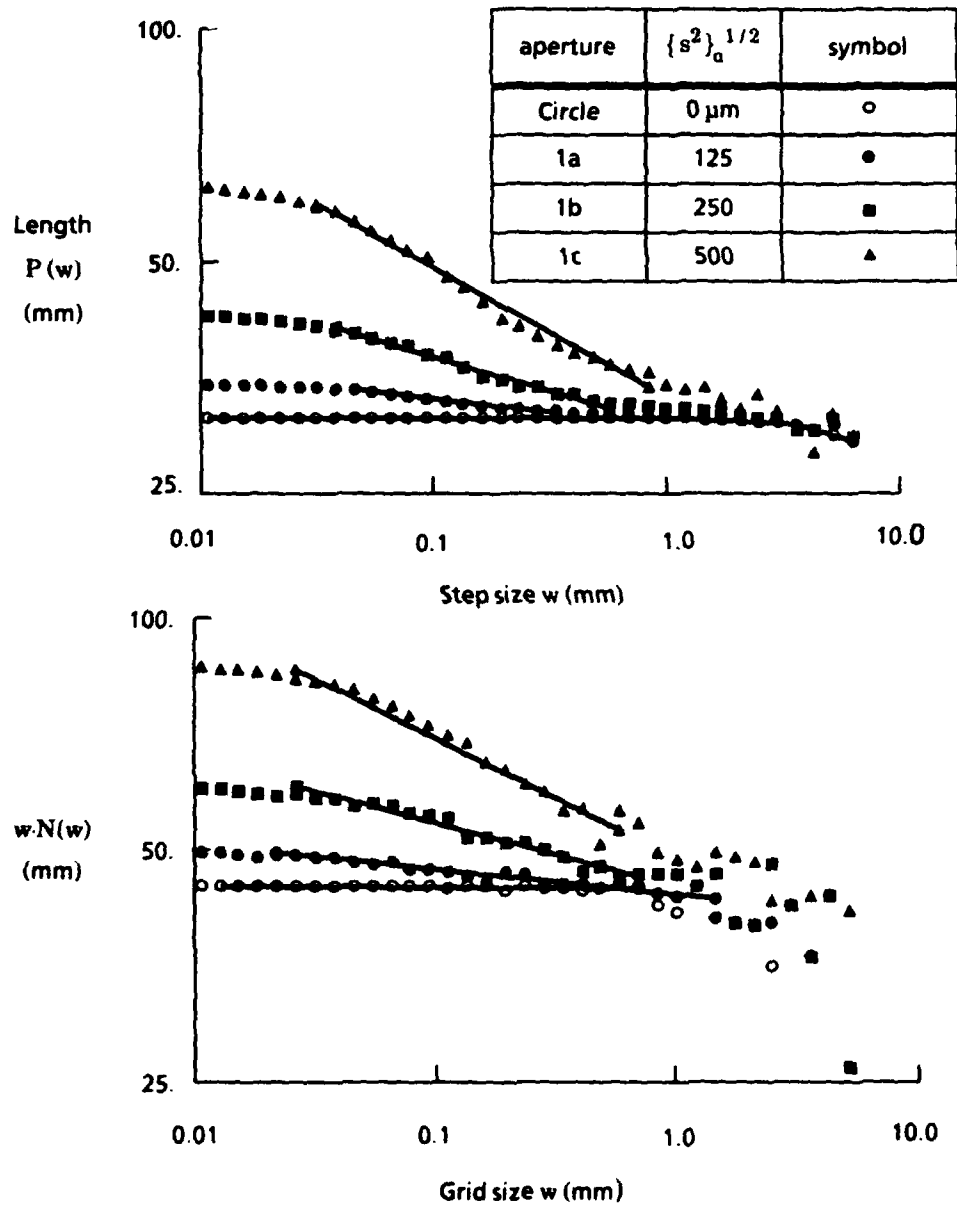


Fig. 3.3. (Upper) Richardson and (lower) interrogation curves for aperture set 1, with the curves for a smooth circle of radius 5 mm. The key at the upper right applies to both plots. The fractal dimension of each aperture is determined from the slope of the corresponding Richardson or interrogation curve and is listed in Table 3.1.

| Aperture # | Roughness (μm) | Fractal dimension D, Richardson method | Fractal dimension D, grid method |
|------------|--------------------------------|---|-------------------------------------|
| 1a | 125 | 1.03 | 1.03 |
| 1b | 250 | 1.09 | 1.08 |
| 1c | 500 | 1.17 | 1.16 |

Table 3.1. Roughnesses and fractal dimensions determined by each method for aperture set 1.

a finite number of points was used to define the aperture. For step sizes greater than our resolution but significantly less than the correlation length of the aperture (approximately 2 mm in this case), the curve has a relatively steep slope, especially for larger roughnesses. This section of the plot corresponds to the high-frequency detail on the edge of each aperture. When the step size is on the order of the correlation length, we have a gentler slope which reflects the overall non-circular shape of the aperture. Thus, we see three distinct fractal dimensions for our apertures: one which describes the general shape of the aperture, one which corresponds to the fine-scale roughness, and a value of unity which indicates the Euclidean nature of the aperture below our design resolution. The three distinct sections of the Richardson curves show that these aperture functions are not completely self-similar under scaling, as true fractal functions would be. This effect is also noted by Mandelbrot, Passoja, and Paullay in their study of fracture surfaces of metals¹³. At different scales an aperture has different features which will be seen to depend significantly on the correlation function of the aperture.

In Fig. 3.3, we have indicated with a line segment superimposed on each curve the range of w used to calculate the fractal dimension of each aperture by each

method. The steep-sloped section of the Richardson curves ($0.05 < w < 1.0$, approximately) was used since it corresponds to the smooth range of the interrogation curve, thus allowing a comparison of the results from the two methods. The values of D for the apertures, as determined by each of the two methods, are listed in Table 3.1. As is obvious from the curves, D increases as the roughness increases. We also note excellent agreement between the results from the Richardson and grid interrogation methods.

3.2.2. Correlation Angle of the Aperture Serration

Richardson and interrogation curves for aperture set 2 are shown in the plot in Fig. 3.4. This set consists of the apertures shown in the first column of Fig. 2.4. Each of the apertures in this set has the same rms roughness, $250 \mu\text{m}$, and a triangular correlation function; the variable is the correlation angle. The aperture with the broadest correlation angle, with A equal to $\pi/4$ rad in Eq. (2.20), has the shallowest slope and thus the smallest fractal dimension. (These fractal dimensions are measured over the fine-scale roughness range of w , as shown by the line segment superimposed on each curve.) As the correlation angle decreases the slope of the Richardson curve grows steeper, indicating an increase in the fractal dimension. The correlation angles and fractal dimensions for this set are listed in Table 3.2. Here, as in Table 3.1 for aperture set 1, the two methods show close agreement. We also note that the increase in D with decreasing A agrees qualitatively with our expectations. Apertures with short correlation angles have more jagged edges which better fill two-dimensional space; they should have larger fractal dimensions. As the correlation angle increases, the aperture becomes less jagged and more like the smooth aperture; the fractal dimension D should be closer to the Euclidean dimension, $E = 1$. The curves in Fig. 3.4 and the data in Table 3.2 support this inverse relationship between correlation angle and fractal dimension.

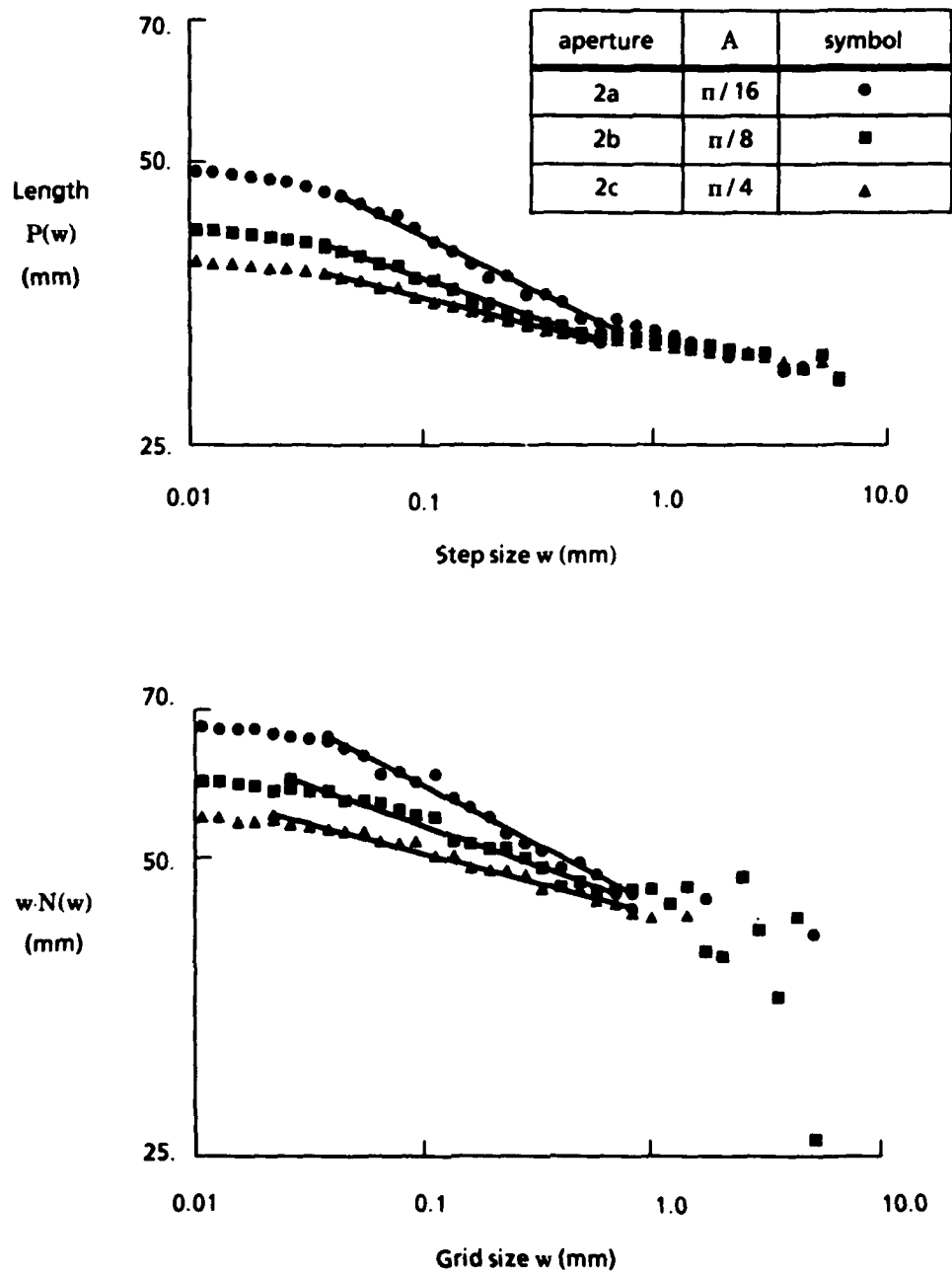


Fig. 3.4. (Upper) Richardson and (lower) interrogation curves for aperture set 2. The key at the upper right applies to both plots; fractal dimensions are listed in Table 3.2.

| Aperture # | Correlation angle A (rad) | Fractal dimension D, Richardson method | Fractal dimension D, grid method |
|------------|------------------------------|---|-------------------------------------|
| 2a | $\pi / 16$ | 1.12 | 1.12 |
| 2b | $\pi / 8$ | 1.09 | 1.08 |
| 2c | $\pi / 4$ | 1.06 | 1.06 |

Table 3.2. Correlation angles and fractal dimensions determined by each method for aperture set 2.

For the Richardson curves for this set, we again note the three different sections, corresponding to three different fractal dimensions. We note, however, that the value of w which separates the steep-sloped section of the curve from the more gently-sloped section decreases somewhat with the correlation angle. This supports the idea that the gentler slope is a measure of the overall shape of the curve, for which the range of w changes with the correlation angle. As the correlation angle increases, the larger-scale bumps on the aperture broaden. When the step size is on the order of or greater than the correlation angle, the three curves have nearly the same slope; the significant difference between the three curves is in the edge detail portion of the curve. This is the range on which we calculate the fractal dimension. As the correlation angle increases, the peak of the correlation function broadens. The shape of the peak controls the edge detail of the aperture, with sharper peaks giving more high-frequency roughness. We expect, then, that apertures with shorter correlation angles will have higher fractal dimensions in this region of the curve; the plots in Fig. 3.4 and our calculations show that this is true.

3.2.3. Correlation Function of the Aperture Serration

The relationship between the shape of the correlation function of the serration and the shapes of the associated Richardson and interrogation curves is demonstrated most dramatically by Fig. 3.5, which shows these curves for apertures varying in correlation function. The apertures represented are those shown in the first column of Fig. 2.5 and constitute aperture set 3. As in our statistical analysis, we note a distinct difference between sharp- and smooth-peaked correlation functions. For step sizes on the order of or greater than the correlation length of the aperture, the curves for the three apertures are quite similar for each method, showing the similarity in the general shape of the three apertures. However, as we take smaller step sizes, the curves corresponding to the triangular and negative exponential correlation functions continue to have a non-zero slope, while the curve levels off in the Gaussian-correlated case. Here, we see the difference in edge detail produced by the smooth- and sharp-peaked correlation functions. Recalling the appearance of these apertures (see Fig. 2.5), we note that the Gaussian correlation produces an aperture with no small-scale roughness, although it has the same basic non-circular shape as the apertures with triangular and negative exponential functions for the correlation of the serration. Thus, we expect the Gaussian-correlated case to approach the Euclidean limit more quickly as the step size decreases, as is demonstrated by the curves in Fig. 3.5.

3.3. Fractal Dimension of the Weierstrass Function

With this new understanding of the relationship between the fractal dimension and statistical parameters of serrated apertures, we now turn to variations of the fractal function described in Section 3.1.1, the Weierstrass cosine function:

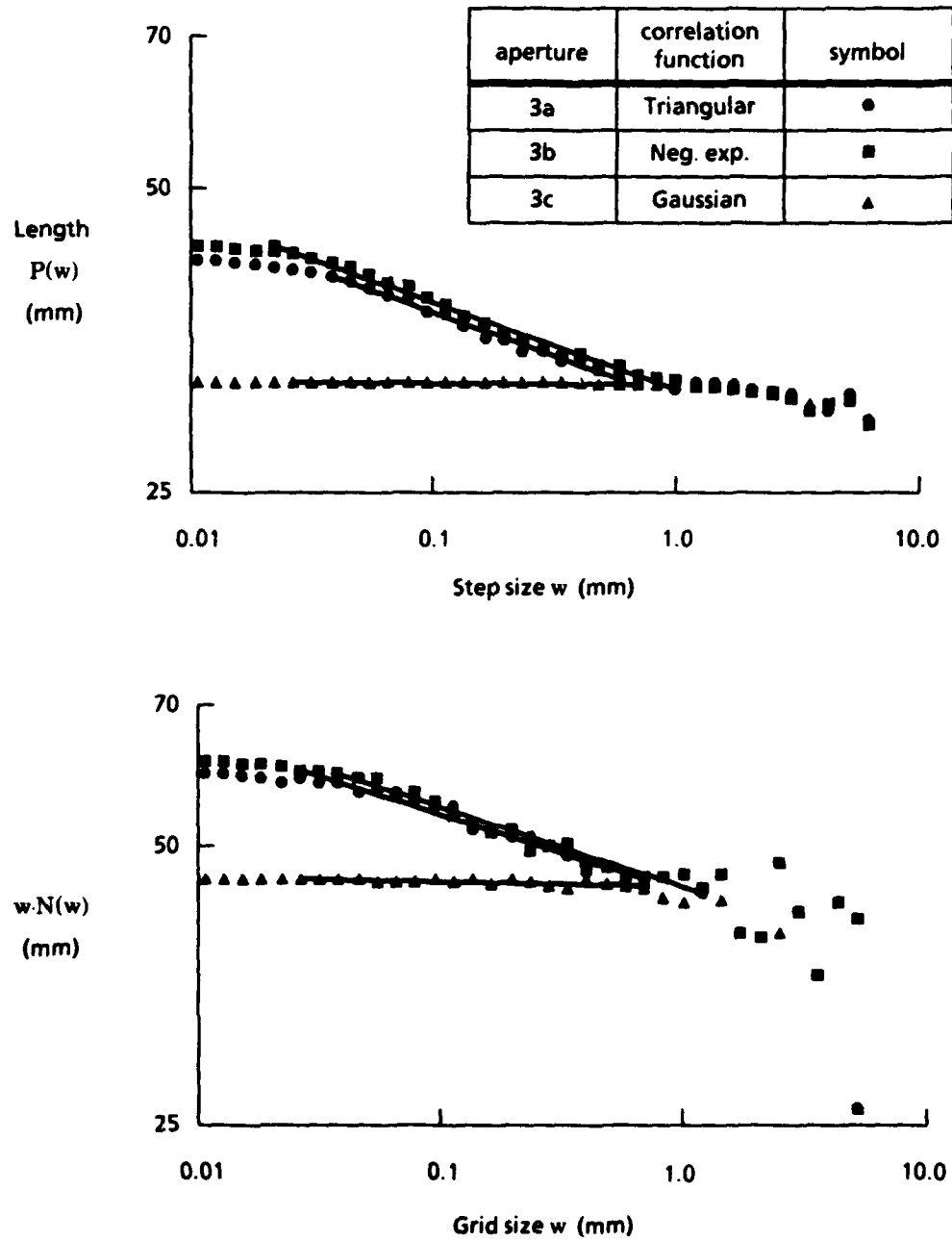


Fig. 3.5. (Upper) Richardson and (lower) interrogation curves for aperture set 3. The key at the upper right applies to both plots.

$$W(x) = \left(1 - b^{2(D_W - 2)}\right)^{-1/2} \sum_{n=-\infty}^{\infty} b^{(D_W - 2)n} \times \left[\cos(\phi_n) - \cos(b^n x + \phi_n) \right], \quad (3.11)$$

with variance

$$\sigma_W^2 = R_W(0) = \frac{1}{2} \left(1 - b^{2(D_W - 2)}\right)^{-1} \sum_{n=-\infty}^{\infty} b^{2(D_W - 2)n} \quad (3.12)$$

and normalized correlation function

$$r_W(\Delta x) = \frac{R_W(\Delta x)}{\sigma_W^2} = \frac{\sum_{n=-\infty}^{\infty} b^{2(D_W - 2)n} \cos(b^n \Delta x)}{\sum_{n=-\infty}^{\infty} b^{2(D_W - 2)n}} \quad (3.13)$$

As stated earlier, $b > 1$ is the fundamental spatial frequency of $W(x)$ and $\{\phi_n\}$ is a set of arbitrary phases; here we have assumed that these phases are uniformly distributed on the interval $(0, 2\pi]$. In proposing the real-valued, bandlimited fractal function⁸

$$W_b(x) = q \left(1 - b^{2(D_W - 2)}\right)^{-1/2} \sum_{n=N_1}^{N_2} b^{(D_W - 2)n} \cos(2\pi p b^n x + \phi_n), \quad (3.14)$$

Jaggard and Kim postulated that the variable D_W in Eq. (3.14) is the fractal dimension of the function. In Eq. (3.14), q and p are magnitude and frequency scaling factors, respectively. The variance of $W_b(x)$ is given by

$$\sigma_b^2 = \frac{q^2}{2} \left(1 - b^{2(D_W - 2)}\right)^{-1} \sum_{n=N_1}^{N_2} b^{2(D_W - 2)n}; \quad (3.15)$$

the normalized correlation function, by

$$r_b(\Delta x) = \frac{\sum_{n=N_1}^{N_2} b^{2(D_W-2)n} \cos(2\pi p b^n \Delta x)}{\sum_{n=N_1}^{N_2} b^{2(D_W-2)n}} \quad (3.16)$$

Our study of serrated apertures has revealed an increase in the fractal dimension with an increase in the rms deviation, and we trust that this applies to other random processes, as well. We note in Eq. (3.15) that the value of α_b can be changed easily by varying the scaling parameter q while holding the other parameters, including D_W , constant. In addition, a change in the frequency scale factor p affects the width of the correlation function $r_b(\Delta x)$ of Eq. (3.16), thus changing the correlation length of the data. We expect the fractal dimension to change under such conditions. These observations are in opposition to the results achieved for serrated apertures if D_W is truly the fractal dimension. To investigate this disagreement, we apply the Richardson and grid interrogation methods to edges defined by the Weierstrass cosine function $W(x)$ of Eq. (3.11) as well as edges defined by the scaled, bandlimited Weierstrass cosine function $W_b(x)$ of Eq. (3.14).

3.3.1. Original Function

In their paper on the Weierstrass function as a fractal function, Berry and Lewis² present an argument for the use of D_W as the fractal dimension. We investigated this claim by using the Richardson method to determine D for several realizations of $W(x)$. For these calculations, we used Eq. (3.11) and followed the example of Berry and Lewis in using enough terms in the summation to ensure that additional terms would not

produce a visually noticeable change in the function. For each realization, we calculated $W(x)$ for 512 values of x , evenly spaced between 0.0 and 4.0; D_W and b were varied. For the phases ϕ_n , we chose random numbers uniformly distributed on the interval $(0, 2\pi]$. The values of D calculated for these functions are shown versus the fundamental spatial frequency b in the plot of Fig. 3.6. We note that, for a given value of D_W , the measured fractal dimension D varies little as the fundamental frequency b changes, and that it is close in value to D_W . (We note a discrepancy between D and D_W for larger values; our measurement technique is less accurate for large fractal dimensions.)

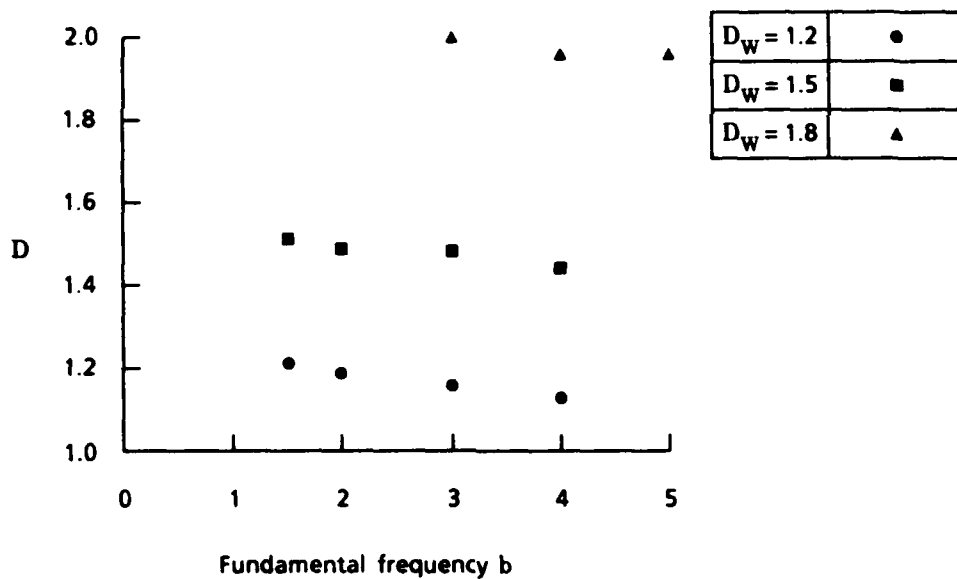


Fig. 3.6. Calculated fractal dimension D for the original Weierstrass cosine function, Eq. (3.11), versus fundamental spatial frequency b . Three values of parameter D_W are represented, as shown in the key.

One might conclude from a quick inspection of Eq. (3.12) that since an increase in b would decrease the period of each $\cos(bn \Delta x)$ term, $n > 1$, the correlation length of $W(x)$ would decrease and the fractal dimension would increase. However, we note that each cosine term is multiplied by $b^{2(D_W - 2)n} < 1$, which decreases as b increases. Apparently, this decrease in the magnitude of these coefficients reduces the contribution of the higher-frequency cosine terms in the summation so that the correlation length and the fractal dimension remain fairly constant. The evidence presented in Fig. 3.6 thus supports the claim that, as used by Berry and Lewis and by Mandelbrot, D_W is a good estimate of the true fractal dimension of the function.

3.3.2. Scaled Function

We now consider the amplitude- and frequency-scaled Weierstrass cosine function, which is given by Eq. (3.14) with N_1 and N_2 equal to 0 and ∞ , respectively. (We begin our summation at n equal to zero to avoid large coefficients $b^{(D_W - 2)n}$.) This function is a non-bandlimited version of the function used by Jaggard and Kim; we will discuss the effect of bandlimiting shortly. The arbitrary scaling factor q incorporates the case of normalization to a selected variance as well as the elimination of the coefficient $(1 - b^{2(D_W - 2)})^{-1/2}$ of the sum. This scaled Weierstrass function and the claim that D_W is the fractal dimension contradict our findings on the relationship between roughness and fractal dimension.

We again choose 512 equispaced values of x ranging from 0.0 to 4.0. For the first three sets of functions generated, fundamental frequency b is fixed at 1.1 and frequency scale factor p is assigned a value of 0.15. This value of p is chosen so that the quantity $2\pi p$ is approximately equal to unity; in this case, the cosine argument is equivalent to that from Eq. (3.11). D_W values of 1.2, 1.5, and 1.8 are used as indicated.

Then q for each function is chosen to produce a specified spatial rms deviation $\{w(x)^2\}_x^{1/2}$, where $w(x)$ is equal to $W(x) - \{W\}_x$ and thus has zero mean. The calculated fractal dimensions of these functions are shown plotted against $\{w(x)^2\}_x^{1/2}$ in Fig. 3.7. We note that, for large enough values of $\{w(x)^2\}_x^{1/2}$, D_W is a good approximation of D . However, as $\{w(x)^2\}_x^{1/2}$ decreases, D becomes significantly less than D_W . We note also that this result is valid for differing values of the fundamental spatial frequency b , as shown by the functions which have D_W values of 1.5 and b -values of 1.1, 1.2 and 1.5. This

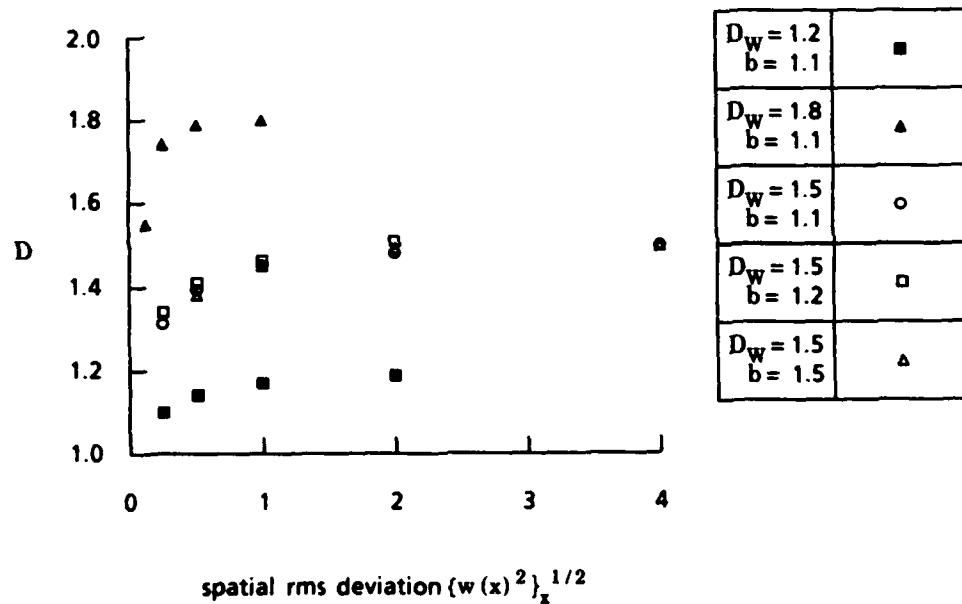


Fig. 3.7. Calculated fractal dimension D for the amplitude-scaled Weierstrass cosine function, Eq. (3.14), $0 \leq n < \infty$. The function was scaled to produce specific values of the spatial rms deviation $\{w(x)^2\}_x^{1/2}$ as denoted by the abscissa. Frequency scale factor p is fixed at 0.15 for each realization of the function. Fundamental spatial frequency b and parameter D_W vary as indicated in the key.

corroborates our results for serrated apertures and cautions against the use of D_W as the fractal dimension of an amplitude-scaled Weierstrass function.

The choice of frequency scale factor p in the previous example results in the convenient upper limit of D_W on D . This, however, is not true for other values of p , as can be seen in Fig. 3.8. Here, we have plotted fractal dimension D versus spatial rms roughness $\{w(x)^2\}_x^{1/2}$ for three different values of p . For p equal to 0.05, the upper limit on D is noticeably smaller than D_W ; for p equal to 1.00, the upper limit on D increases.

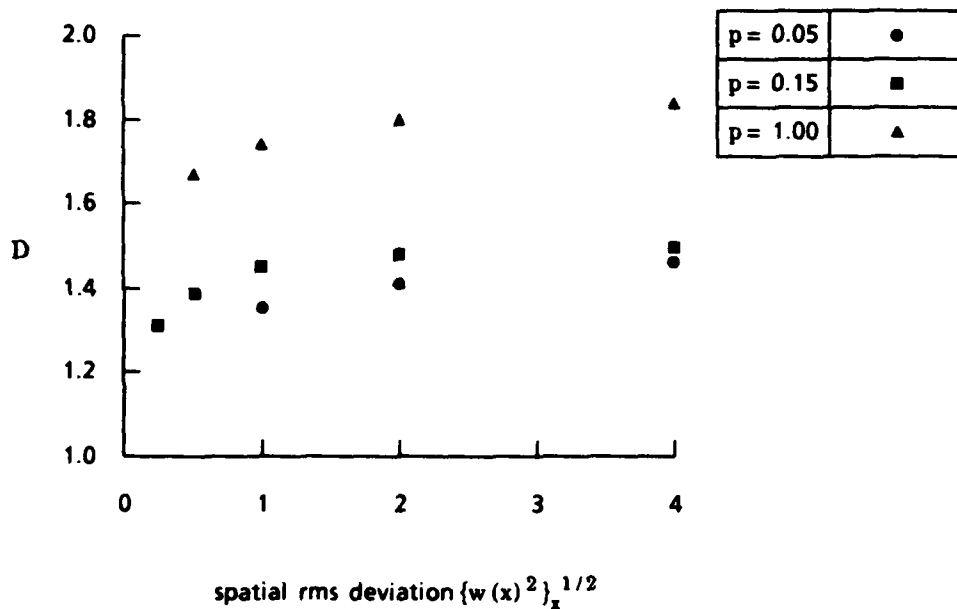


Fig. 3.8. Calculated fractal dimension D for the frequency-scaled Weierstrass cosine function Eq. (3.14), versus spatial rms deviation $\{w(x)^2\}_x^{1/2}$. D is plotted here for three values of the frequency scaling parameter p as indicated in the key. For each realization of the function, parameter D_W and fundamental spatial frequency b are equal to 1.5.

Thus, we must also avoid frequency scaling in order to use D_W as the fractal dimension of the generated Weierstrass function.

The increase in D with an increase in frequency scale p can be more thoroughly understood from the following perspective. From Eq. (3.16), we see that the normalized correlation function $r_b(\Delta x)$ of the scaled and bandlimited Weierstrass function $W_b(x)$ is expressed as a sum of weighted cosines with frequencies $2\pi p b^n$. If we increase p , we increase each of these frequencies proportionately and thus narrow the correlation function. This effectively decreases the correlation length of $W_b(x)$, since the weighting factor $b^{2(D_W-2)n}$ does not change. We have seen earlier that a decrease in the correlation length (or correlation angle, as appropriate) results in an increase in the fractal dimension. Thus, we expect that increasing frequency scale p will have the same effect.

3.3.3. Bandlimited Function

Finally, we investigate the effect of bandlimiting on the validity of D_W as the fractal dimension. For this example, we choose D_W equal to 1.5 and b equal to 1.1; the same range of values is used here for x as in the previous examples. Amplitude scale factor q is chosen to yield $\{w(x)^2\}_x^{1/2}$ equal to 1.0, and p is set at 0.15. To perform the bandlimiting, we fix N_1 at zero and set N_2 at successively lower values. The fractal dimension is calculated for each function, and the results are plotted versus N_2 and shown in Fig. 3.9. We can see that by placing an upper limit on N_2 , and thus on the highest component frequency, we can significantly affect the fractal dimension. As N_2 decreases D decreases, gradually at first and then more rapidly as N_2 approaches zero. This is expected when we consider the Euclidean nature of a function consisting of just the first few terms in Eq. (3.14). In addition, we are again affecting the width of the correlation

function, increasing it as we cut out higher frequencies and thus decrease the fractal dimension. We conclude that, although the bandlimited Weierstrass model is useful when considering physical fractals, we must be careful in assigning the fractal dimension, just as we must use caution when scaling the function in frequency and/or amplitude.

3.4. Quantitative Analysis of the Statistical - Fractal Relationship

We turn now to an empirical analysis of the quantitative relationship between the aperture parameters and the fractal dimension. We have already noted for the apertures discussed that D increases with an increase in the rms roughness and also with a decrease in the correlation angle. These two relationships suggest that D may be a function of the ratio between the roughness and the correlation angle, increasing with

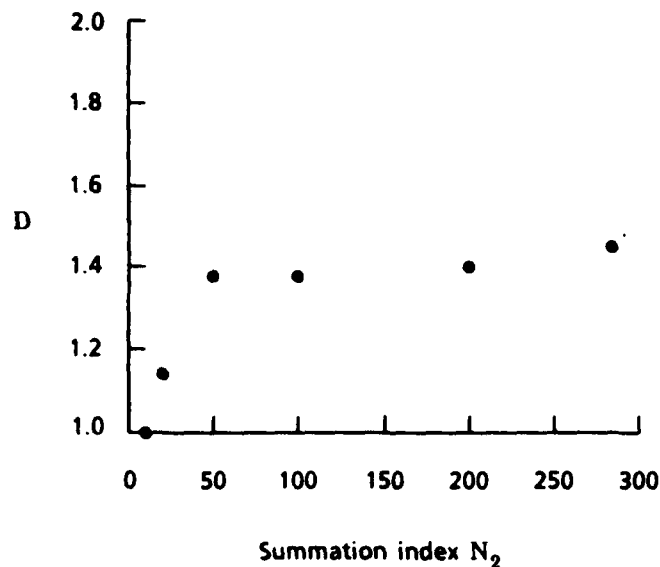


Fig. 3.9. Calculated fractal dimension D for the bandlimited Weierstrass cosine function, Eq. (3.14), versus summation index N_2 . For each realization of the function, $D_w = 1.5$, $b = 1.1$, $\{w^2\}_a^{1/2} = 1.0$, and $p = 0.15$.

this quantity. In our investigation of this dependence, we use serrated edges rather than serrated apertures in order to simplify the analysis and to allow a larger range for the rms roughness; in our aperture design method, a large roughness value can result in the self-intersection of the aperture edge. We first show, however, that the Richardson curves for these two cases are similar enough to permit this change in the basic object of study.

3.4.1. Similarities of Serrated Apertures and Edges

Richardson curves for a serrated aperture and for a serrated edge are shown in Fig. 3.10. We generated both the aperture and the edge from the same set of uncorrelated random numbers; they also have identical rms roughnesses, correlation lengths, and correlation functions. The difference between the two is the rule by which the correlated data are assigned to generate the aperture or edge. If the function $S(\cdot)$ describes the correlated data, then the rule used to generate the serrated aperture is

$$r_c(a_i) = S(a_i), \quad (3.17)$$

in which $r_c(a_i)$ is the radius of the aperture at angle a_i . For the serrated edge, we use the rule

$$h(x_i) = S(x_i), \quad (3.18)$$

where $h(x_i)$ is the height of the edge at abscissa value x_i . The sample spacings are chosen so that the correlation lengths of both the aperture and the edge will be the same. The requirement for this condition is:

$$x_{i+1} - x_i = \{S\}_a(a_{i+1} - a_i), \quad (3.19)$$

where $\{S\}_a$ is the spatial average of $S(a_i)$. In discussing apertures, we have referred to correlation angle A ; in our discussion of edges, we will use correlation length L . Since L

is equal to $\{S\}_q \cdot A$, the fractal dimension will have the same functional dependence on both L and A , but for the scale factor $\{S\}_q$.

The two Richardson curves shown in Fig. 3.10 are nearly coincident in the range of interest, indicating that there is no significant difference between the fractal dimension of the aperture and that of the edge. There is a notable deviation between the curves for large step sizes, but this is expected. When we use a large step size to

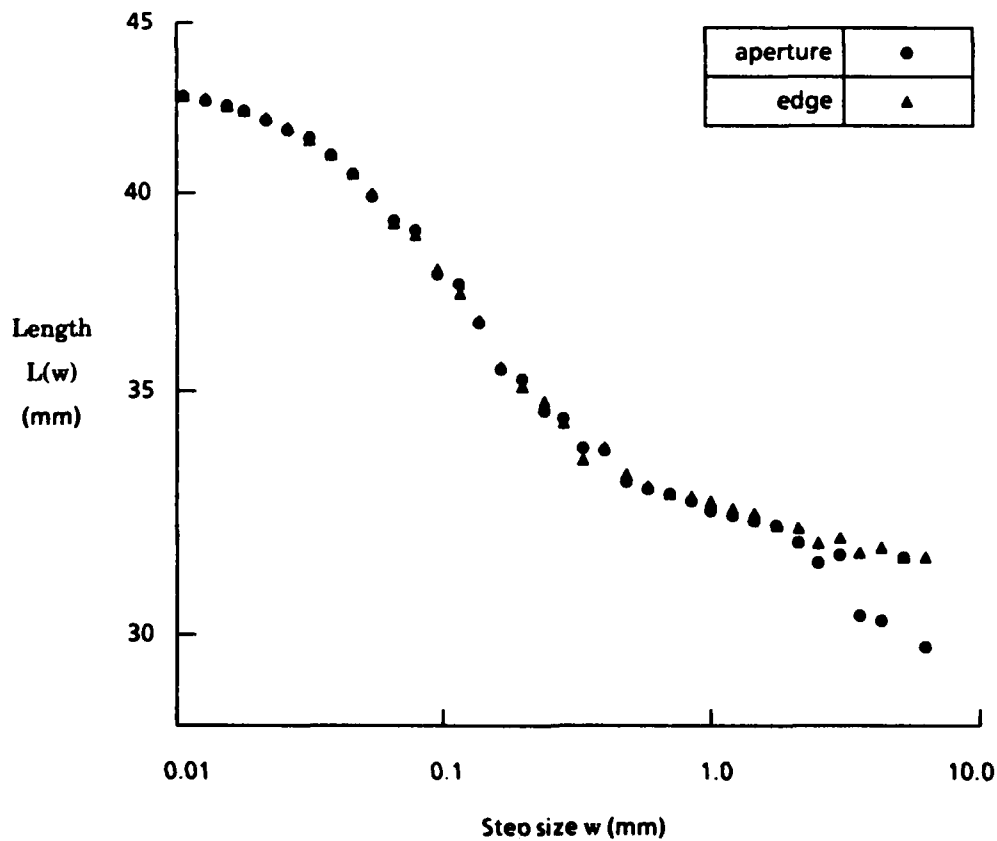


Fig. 3.10. Richardson curves for serrated aperture and serrated edge. The edge and the aperture have the same rms roughness and correlation function.

estimate the perimeter of the aperture, the polygon we generate is scribed mostly within the aperture and has a perimeter much less than that of the aperture and that of the circle with equivalent mean radius. The value of the estimated perimeter is bounded below by twice the diameter of the aperture. When we estimate the length of the serrated edge, however, we use a series of line segments stretched out almost parallel to the x-axis. For large step sizes the sum of the lengths of these segments is approximately equal to the length of the edge projected onto the x-axis and is bounded below by this value. Thus, for large step sizes, we expect the estimated edge length to be greater than the estimated aperture perimeter.

For a serrated edge, equal scaling in both the x and h(x) directions will not affect the fractal dimension. For example, the function $h_2(x)$ shown in Fig. 3.1(b) would have the same fractal dimension if both axes were labeled in microns, inches, or kilometers rather than millimeters. Scaling an edge equally in the x and h directions would scale the correlation length and rms roughness, respectively, by the same factor. Thus the ratio of roughness to correlation length would remain unchanged. We are therefore assured that the fractal dimension will depend on the rms roughness and the correlation length as this ratio. With this view, we investigate the dependence empirically.

3.4.2. Dependence of the Fractal Dimension on the Roughness-to-Correlation-Length Ratio: Triangular Correlation

For this study, we generated digital models of several serrated edges, each with the ratio of roughness to correlation length approximately equal to one of the following values: 0.255, 0.509, 0.764, 1.02, 1.16, 2.04, 3.26, or 4.08. (These values are approximate because the spatial rms roughness of a given edge deviates from the design

value; see Appendix A.) For notational simplicity, we use the symbol σ_h to represent the rms deviation of the edge, $\{[h(x) - \{h(x)\}_x]^2\}_x^{1/2}$. Throughout this study, the sampling step size along the x direction is equal to $10\pi/1024$ mm:

$$x_{i+1} - x_i = 10\pi/1024 \text{ mm} \approx 0.03 \text{ mm} \quad (3.20)$$

In this first stage, all edges have a triangular correlation function; the correlation angle is defined as A in Eq. (2.20). Using the procedure that was described in Section 3.2.1 for our serrated apertures, we calculated the fractal dimension of each edge by the Richardson method. The results of this process are shown in Fig. 3.11, where the fractal dimension D

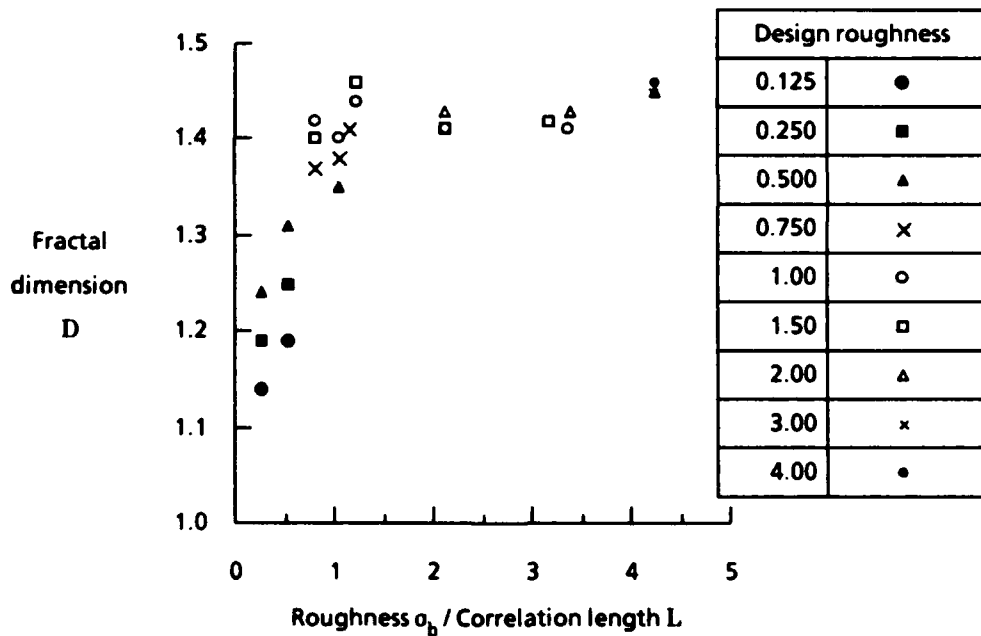


Fig. 3.11 Fractal dimension D versus ratio σ_h/L for serrated edges. Each edge has a triangular correlation function, given by Eq. (3.27); each point represents the average dimension for four edges with the same design roughness. D is determined by the Richardson method.

is plotted against the ratio σ_h/L for each edge. As specified in the figure key, each symbol used corresponds to a different value of the design roughness, *i.e.*, the value used as input to the design program. For small values of the ratio σ_h/L , there is some dependence of the fractal dimension on the roughness value, but as the ratio increases this dependence becomes less significant. Overall, the plot shows that the fractal dimension increases with the ratio of the roughness to the correlation length, as we expect.

3.4.3. Definition of the Correlation Length

The second stage of this investigation involves variations in the correlation function. Essential to this is the use of correlation functions with different peak shapes. In Section 2.3.4, we saw the effects of the use of Gaussian and triangular correlation functions on the appearance of our apertures. We expect similar results for serrated edges. However, because of the wide range of peak shapes to be used here, we redefine the correlation length uniformly so that correlation functions of equal area will have equal correlation lengths. The basis for this definition is as follows.

Consider a large set of normally-distributed, correlated, random numbers from which we select m consecutive numbers to represent edge $h_1(x)$. (The edge functions $h_j(x)$ used here are generally not those from Section 3.2.1.) The mean edge height of $h_1(x)$ is given by the spatial average

$$\{h_1\}_x = \frac{1}{m} \sum_{i=1}^m h_1(x_i); \quad x_i = i \Delta x . \quad (3.21)$$

We can then choose another m points in the same way to represent edge $h_2(x)$, and continue in this same manner to generate a set of N edges. (This procedure is a simple

way to represent the effect of holding all input parameters, except the seed in the random number generator, constant in designing several apertures.) Once we have this set of edges, we can calculate the mean edge height $\{h_j\}_x$ of each edge. We can also calculate the variance of the mean edge height for the set; *i.e.*,

$$\text{var}\left(\{h_j\}_x\right) = \frac{1}{N} \sum_{j=1}^N \left(\{h_j\}_x - \frac{1}{N} \sum_{j=1}^N \{h_j\}_x \right)^2 . \quad (3.22)$$

Since the data from which the h_j were selected are normally distributed, we can apply the following theorem from the theory of statistics¹⁴:

Let $\{h_j\}_x$ denote the sample mean of a random sample of size M from a normal distribution with mean a and variance $\text{var}(h_j(x))$. Then $\{h_j\}_x$ has a normal distribution with mean a and variance

$$\text{var}\left(\{h_j\}_x\right) = \frac{\text{var}\left(h_j(x)\right)}{M} . \quad (3.23)$$

When we apply this theorem, the key phrase in the above statement is *random sample*, which implies that the sample points are independent. When we sample the large set of normally-distributed, correlated, random numbers to define a serrated edge by taking a subset that consists of consecutive points, the m points we choose are not independent. However, we can apply the theorem as stated if we let M be the number of independent samples in the subset of points chosen. The number M , then, is less than m , and we use M to define the correlation length of the edge:

$$L = \frac{P}{M} , \quad (3.24)$$

where P is the projected length of the edge onto the x -axis,

$$P = m \Delta x , \quad (3.25)$$

and L is the correlation length of the edge. The correlation length and the variance of the mean edge heights, then, are mutually dependent terms.

From the theory presented in Appendix A, we can write an edge function $h_j(x)$ as a convolution:

$$h_j(x) = \int_0^P q_j(\xi) w(x - \xi) d\xi , \quad (3.26)$$

where $q_j(\xi)$ represents a set of uncorrelated random numbers and $w(x)$ is the convolving window function. The edge height is assumed to be zero outside the range $[0, P]$. The mean edge height is then given by

$$\{h_j(x)\}_x = \frac{1}{P} \int_0^P h_j(x) dx = \frac{1}{P} \int_0^P \left[\int_0^P q_j(\xi) w(x - \xi) d\xi \right] dx , \quad (3.27)$$

which, interchanging the x and ξ integrations, we rewrite as

$$\{h_j(x)\}_x = \frac{1}{P} \int_0^P q_j(\xi) \left[\int_0^P w(x - \xi) dx \right] d\xi . \quad (3.28)$$

Since the x integration is now simply over the shifted window function, we can eliminate the shift and express the mean edge height as the product

$$\{h_j(x)\}_x = \{q_j(x)\}_x \int_0^P w(x) dx = \{q_j(x)\}_x A_w , \quad (3.29)$$

where A_w is the area under the window function. We use Eq. (3.29) in Eq. (3.22) to write the following expression for the variance of the mean edge height:

$$\begin{aligned}
\text{var}\left(\{h_j\}_x\right) &= \frac{1}{N} \sum_{j=1}^N \left(\{q_j(x)\}_x A_w - \frac{1}{N} \sum_{j=1}^N \{q_j(x)\}_x A_w \right)^2 \\
&= A_w^2 \frac{1}{N} \sum_{j=1}^N \left(\{q_j(x)\}_x - \frac{1}{N} \sum_{j=1}^N \{q_j(x)\}_x \right)^2 \\
\text{var}\left(\{h_j\}_x\right) &= A_w^2 \text{var}\left(\{q_j(x)\}_x\right) \tag{3.30}
\end{aligned}$$

Thus, the variance of the mean edge heights is equal to the product of the square of the area of the window function with the variance of the mean value of the original uncorrelated data set.

For convenience, we prefer to express the area of the window function in terms of the correlation function. From Appendix A, we have

$$r_h(x) = w(x) \star w(x), \tag{A.25}$$

where \star denotes a convolution. Using $R_h(f_x)$ and $W(f_x)$ to denote the Fourier transforms of $r_h(x)$ and $w(x)$, respectively, we write the transform of Eq. [(A.25)] as

$$R_h(f_x) = W^2(f_x). \tag{3.31}$$

With a square root and an inverse transform, we express the window function in terms of $R_h(f_x)$:

$$w(x) = F^{-1} \left\{ \left[R_h(f_x) \right]^{1/2} \right\}, \tag{3.32}$$

where we use F^{-1} to denote the inverse Fourier transform. The area under the window function can now also be written in terms of $R_h(f_x)$:

$$A_w = \int_0^P w(x) dx = \int_0^P F^{-1} \left\{ \left[R_h(f_x) \right]^{1/2} \right\}$$

$$A_w = \int_0^P \left[\int_{-\infty}^{+\infty} \left[R_h(f_x) \right]^{1/2} \exp(-i2\pi f_x x) df_x \right] dx \quad (3.33)$$

Since the window function is identically equal to zero outside the range $[0, P]$, we have:

$$A_w = \int_{-\infty}^{+\infty} \left[\int_{-\infty}^{+\infty} \left[R_h(f_x) \right]^{1/2} \exp(-i2\pi f_x x) df_x \right] dx \quad (3.34)$$

and, interchanging the order of the f_x and x integrations,

$$A_w = \int_{-\infty}^{+\infty} \left[R_h(f_x) \right]^{1/2} \left[\int_{-\infty}^{+\infty} \exp(-i2\pi f_x x) dx \right] df_x \quad (3.35)$$

$$A_w = \int_{-\infty}^{+\infty} \left[R_h(f_x) \right]^{1/2} \delta(f_x) df_x = \left[R_h(0) \right]^{1/2}, \quad (3.36)$$

where $\delta(f_x)$ is the Dirac delta function. We note that

$$R_h(0) = \int_{-\infty}^{+\infty} r_h(x) \exp(i2\pi f_x x) dx \Big|_{f_x=0} = \int_{-\infty}^{+\infty} r_h(x) dx \quad (3.37)$$

and thus

$$A_w^2 = \int_{-\infty}^{+\infty} r_h(x) dx. \quad (3.38)$$

The squared area of the window function is equal to the area under the correlation function. Using Eq. (3.38) in Eq. (3.30), we write the variance of the mean edge height in terms of the correlation function:

$$\text{var}\left(\{h_j\}_x\right) = \text{var}\left(\{q_j(x)\}_x\right) \int_{-\infty}^{+\infty} r_h(x) dx . \quad (3.39)$$

Finally, using Eqs. (3.23) and (3.39) in Eq. (3.24) and recalling that with the normalization chosen in Appendix A $\text{var}(h_j)$ is equal to $\text{var}(q_j)$, we have an expression for the correlation angle in terms of the original, uncorrelated data function q and the

correlation function of the edge data:

$$L = P \frac{\text{var}\left(\{h_j(x)\}_x\right)}{\text{var}(h_j(x))} = P \frac{\text{var}\left(\{q_j(x)\}_x\right)}{\text{var}(q_j(x))} \int_{-\infty}^{+\infty} r_h(x) dx . \quad (3.40)$$

We conclude from this expression for the correlation length that if two edges are generated from the same set of uncorrelated data, the correlation length of each will be the same if the areas under the correlation functions are equal. We now apply this condition in defining correlation functions for serrated edges.

3.4.4. Dependence of D on the Ratio σ_b/L and on the Correlation Function

Recall the definition of the Gaussian correlation function,

$$G\left(\frac{\Delta x}{X}\right) = \exp\left[-\left(\frac{\Delta x}{X}\right)^2\right], \quad (3.41)$$

where X is the half-width-at- e^{-1} of the function, and the triangular function,

$$\Lambda\left(\frac{\Delta x}{X}\right) = \begin{cases} 1 - \frac{|\Delta x|}{X} & , \quad \text{for } |\Delta x| \leq X ; \\ 0 & , \quad \text{otherwise} \end{cases} . \quad (3.42)$$

where X is the full-width-at-half-maximum of this function. We will use these two correlation functions, shown in Fig. 3.12 (a) and (b), in generating serrated edges. In

addition, we expand our collection of correlation functions with two functions that have sharper peaks than the triangular function. We expect these correlation functions to produce even more jagged edges than those already seen. The new functions are of the form:

$$\text{Eif} \left(\frac{\Delta x}{X}, \beta \right) = \left\{ \begin{array}{ll} 1 - \left(\frac{|\Delta x|}{X} \right)^\beta, & \text{for } |\Delta x| \leq X, \\ 0, & \text{otherwise} \end{array} \right\}, \quad (3.43)$$

where the exponent β is a number in the range $(0, 1]$. As β decreases, the peak becomes sharper. We choose β equal to 0.5 and 0.25 for our correlation functions; they are shown in Fig. 3.12 (c) and (d). Because of the shape of this function, we call it the Eiffel function¹⁵. We note that when β is equal to 1 this function is the triangular function. For each function shown in Fig. 3.12, X was chosen to satisfy the equal areas condition discussed in the previous section. A typical edge for each of these four correlation functions is shown in Fig. 3.13.

We generated several serrated edges with each correlation function for a range of values of the ratio σ_b / L ; the data for these sets are listed in Table 3.3. For each edge, we determined the fractal dimension by the Richardson method. Then, for each combination of correlation function and ratio value, we calculated the average fractal dimension. The results of these calculations are shown in the plot in Fig. 3.14 as large points with shapes corresponding to the correlation function. Each point in this plot represents edges with three different values for the design roughness, as listed in Table 3.3. The value of L used to calculate the ratio in plotting each point is the effective correlation length, determined from the area of the correlation function. The resulting variations in the ratio are indicated by small points to the left and right of the large plotted point, indicating the rms deviation in the ratio value. Also shown, above and

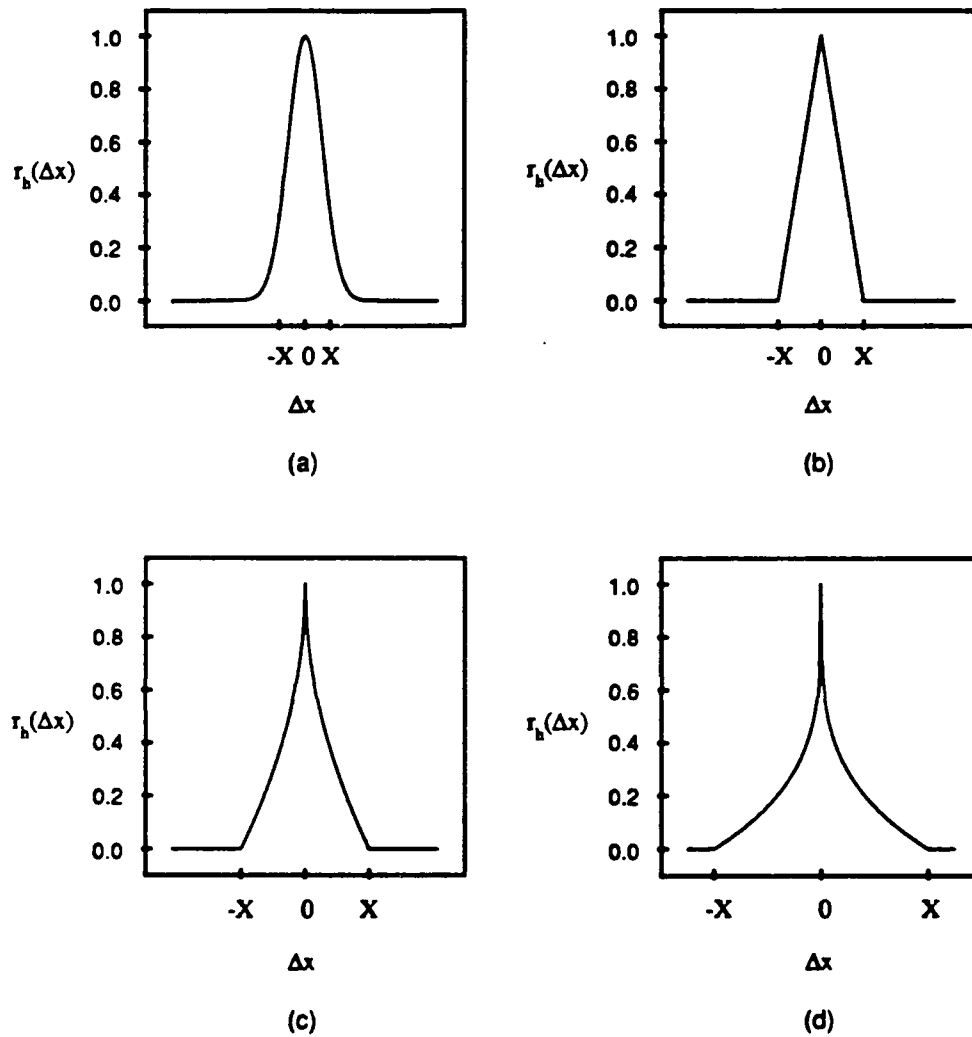
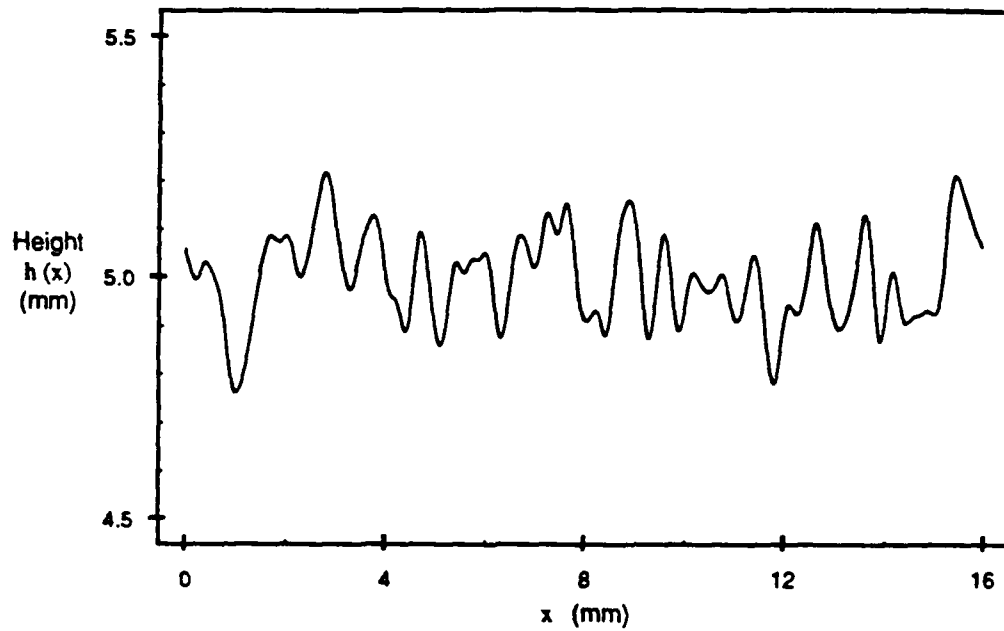
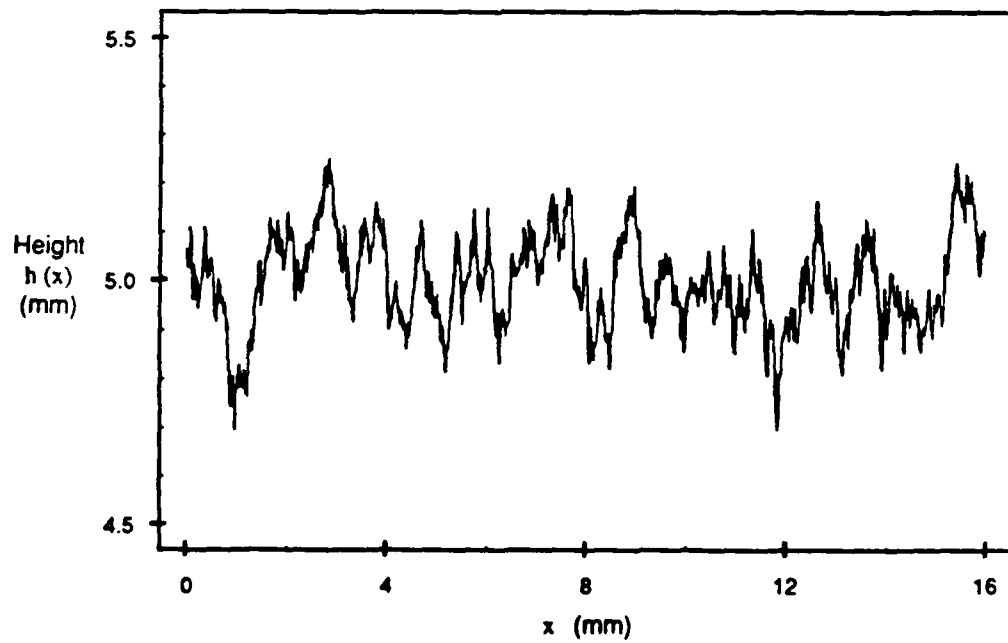


Fig. 3.12. Correlation functions $r_b(\Delta x)$ for serrated edges, versus separation Δx : (a) Gaussian, Eq. (3.41); (b) triangular, Eq. (3.42); (c) Eiffel, Eq. (3.43), $\beta=0.5$; and (d) Eiffel, $\beta=0.25$. For each function, width X is chosen so that all four functions have the same area.

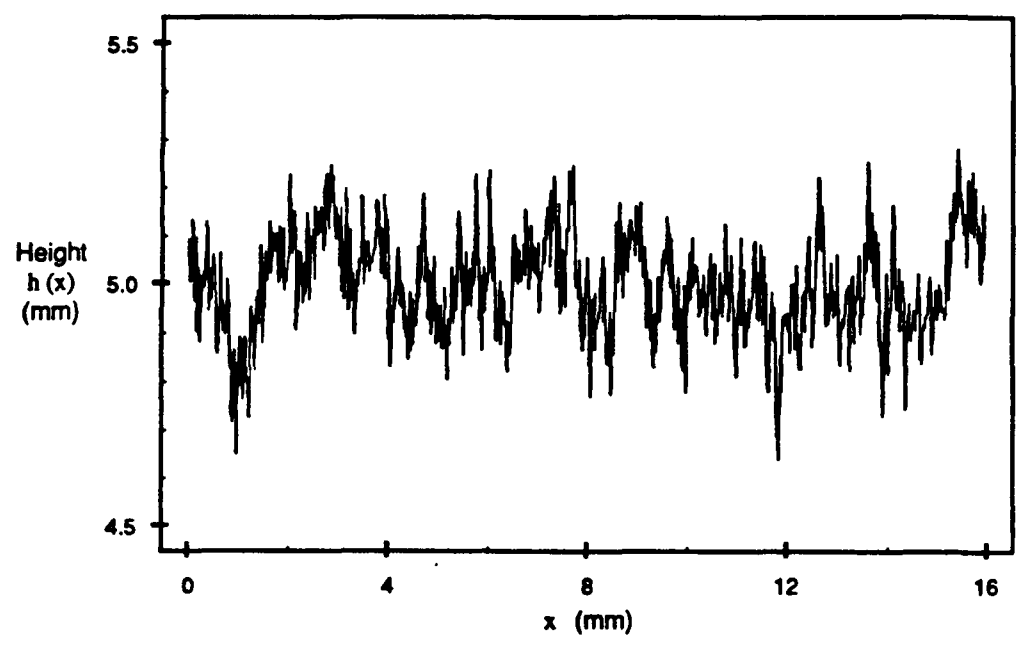


(a)

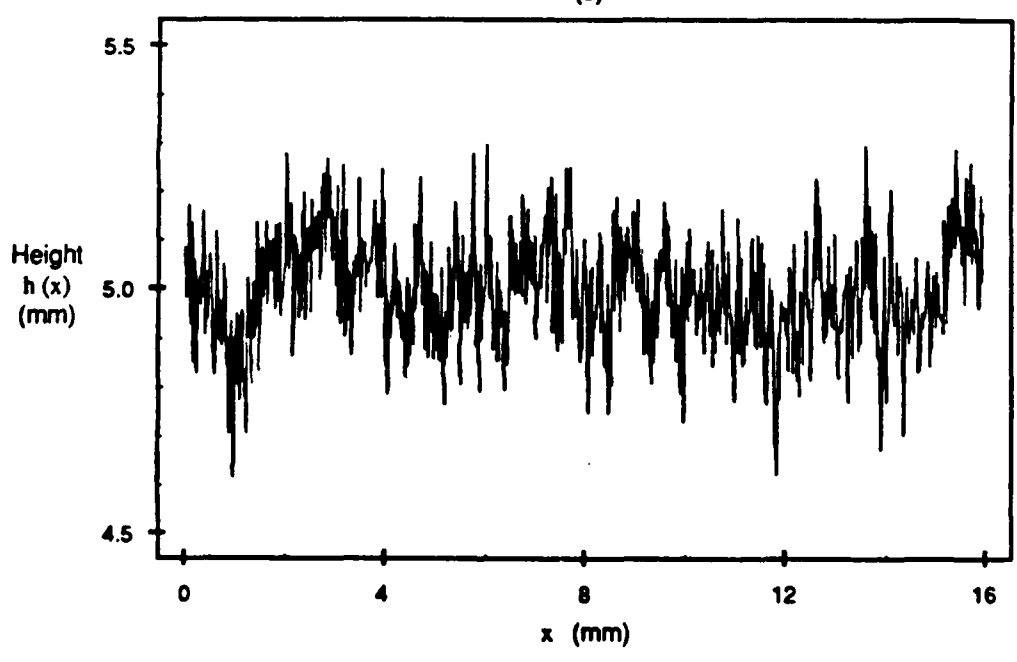


(b)

Fig. 3.13. Typical edges produced with the correlation functions shown in Fig. 3.12: (a) Gaussian, Eq. (3.41); (b) triangular, Eq. (3.42).



(c)



(d)

Fig. 3.13. (Continued) Eiffel, Eq. (3.43), (c) $\beta=0.5$ and (d) $\beta=0.25$

below each large point, are small points marking the rms deviation in the fractal dimension.

In Fig. 3.14, as in Fig. 3.11, we see that the fractal dimension increases when the ratio of roughness to correlation length, σ_h/L , increases. Figure 3.14 also shows the dependence of the fractal dimension on the shape of the correlation function. For a given value of the ratio σ_h/L , the fractal dimension is largest for the edges with the sharpest correlation function (namely, the Eiffel function, Eq. (3.43), with β equal to 0.25). As the peak of the correlation function broadens, the fractal dimension decreases; the smooth-peaked Gaussian function corresponds to the smallest fractal dimension for a given ratio value. We also note that for each correlation function the fractal dimension approaches an upper limit. These limits range from slightly more than 1.0 for the

| | | | | | | | | |
|--------------|-------|-------|-------|-------|-------|-------|-------|-------|
| σ_h/L | 0.255 | 0.509 | 0.764 | 1.02 | 1.16 | 2.04 | 3.26 | 4.08 |
| σ_h | 0.125 | 0.125 | 0.750 | 0.500 | 0.750 | 1.00 | 1.00 | 2.00 |
| L | 0.491 | 0.245 | 0.982 | 0.491 | 0.675 | 0.491 | 0.307 | 0.491 |
| σ_h | 0.250 | 0.250 | 1.00 | 0.750 | 1.00 | 1.50 | 1.50 | 3.00 |
| L | 0.982 | 0.491 | 1.32 | 0.736 | 0.859 | 0.736 | 0.491 | 0.736 |
| σ_h | 0.500 | 0.500 | 1.50 | 1.00 | 1.50 | 2.00 | 2.00 | 4.00 |
| L | 1.96 | 0.982 | 1.97 | 0.982 | 1.29 | 0.982 | 0.614 | 0.982 |

Table 3.3. Roughness σ and correlation length L for the design of the sets of edges represented in Fig. 3.14. Four edges were used from each set and the fractal dimension was averaged for each ratio value and correlation function.

Gaussian correlation to nearly 2.0 for the Eiffel function, $\beta = 0.25$. These results thus indicate that a given correlation function shape can be used to produce an edge with a fractal dimension up to some limit. The sharper the correlation function peak, the higher this limit will be.

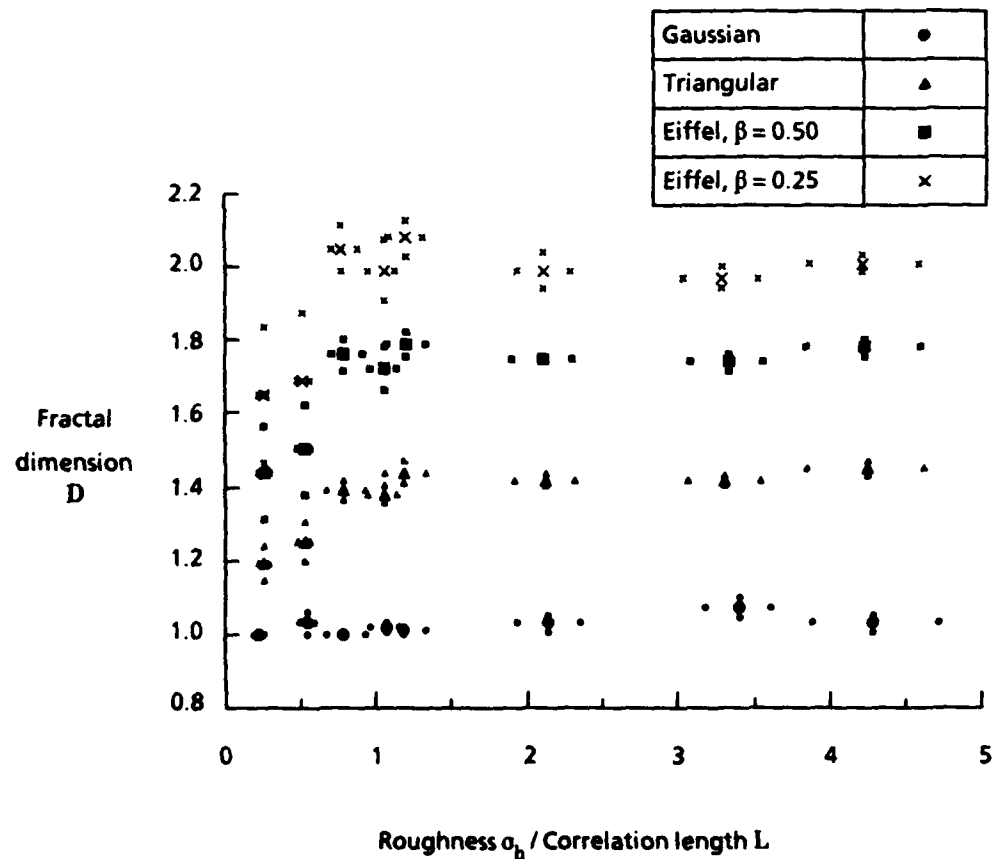


Fig. 3.14. Fractal dimension D versus ratio σ_b / L for serrated edges of varying correlation function. Each point represents the average of the fractal dimensions of edges with a particular correlation function shape and ratio value. Roughness and correlation length data for the edges are listed in Table 3.3.

The results presented here suggest the concept of a fractal set of edges which would incorporate several statistical sets. A fractal set would include all edges that have a particular fractal dimension and would include several statistical sets with varied roughness and correlation length values, just as a horizontal line drawn on Fig. 3.14 would intersect several curves. Smoothness of an aperture, as discussed in Section 2.3.5, could then be associated with a fractal set rather than with a particular statistical parameter.

3.5 Summary

In this chapter, we investigate the fractal nature of the serrated circular aperture. Our objective is to study the relationship between the fractal dimension and the parameters of the aperture. An important step in this study is to determine the fractal dimensions of random processes. To this end two techniques, namely the Richardson and grid interrogation methods, are used. To test these methods and the programs we use to carry them out, we applied them to the triadic Koch curve, shown in Fig. 3.2, which has a well-defined fractal dimension. We next applied these methods to serrated circular apertures. In examining the Richardson and interrogation curves shown in Figs. 3.3, 3.4, and 3.5, we noted that, as expected, fractal dimension increases with increasing rms roughness and with decreasing correlation angle. The Richardson curves in particular show that a serrated aperture can have different fractal dimensions at different levels of scrutiny. Below the resolution of the aperture design process, a fractal dimension of unity indicates a Euclidean aperture. At scales greater than the correlation length, the apertures have a fractal dimension between one and two that corresponds to the general, non-circular shape of the aperture. Between these two scales, the fractal

dimension of the edge roughness is measured; the fractal dimension measured in this range has a strong dependence on the shape of the correlation function of the serration.

With these results in mind, we returned to the fractal function described in Section 3.1.1, the Weierstrass cosine function. We applied the Richardson method to several realizations of the Weierstrass cosine function, Eq. (3.11), and found that for this function D_w is close in value to the fractal dimension. These results are shown in Fig. 3.6. However, scaling and/or bandlimiting the function changes the fractal dimension. For the amplitude-scaled Weierstrass cosine function we found that the fractal dimension decreases as the roughness decreases, as expected from our results for serrated apertures. This is valid for different values of the fundamental spatial frequency b , as shown in Fig. 3.7. The data presented in Fig. 3.8 show that the fractal dimension also depends on the frequency scaling parameter p . Since increasing this parameter decreases the correlation length, the fractal dimension increases as p increases. The effect of bandlimiting the Weierstrass function is demonstrated in Fig. 3.9. The fractal dimension decreases as fewer terms are used in the summation. When only a few terms are used, the function produced is essentially Euclidean, as it has only a handful of component frequencies. The results of this investigation caution us to use fractal functions with care and to develop a sense of the relationships between the fractal dimension and the parameters that describe a random process.

The final step in this fractal study is to develop a more quantitative relationship between the parameters of the serration and the fractal dimension. In Fig. 3.11 we see the relationship between D and the ratio of the spatial rms roughness to the correlation length, σ_b/L , for a serration with a triangular correlation function. The fractal dimension increases with σ_b/L , i.e., as the roughness increases and/or the

correlation length decreases. This increase is for the most part independent of σ_h and L except in the ratio. When we repeat this analysis for other correlation functions, we find similar behavior; this is demonstrated by the data presented in Fig. 3.14. We note a major difference, though, between the results for different correlation functions: the sharper the correlation peak, the larger the fractal dimension at a given value of the ratio.

Our investigation of the relationship between the edge parameters and the fractal dimension has led to the concept of a fractal set of edges. Statistical sets with a specific fractal dimension D would form subsets of the fractal set with that dimension. As our understanding of the mathematics of fractals grows, we will find further use for fractal sets. For now, we use statistical concepts to study the serrated aperture and leave the continuation of the fractal analysis for future pursuit.

Chapter 3 Notes and References

1. N. George and G.M. Morris, "Diffraction by serrated apertures," *J. Opt. Soc. Am.* **70**, 6-17 (1980).
2. B.B. Mandelbrot, *The Fractal Geometry of Nature* (W.H. Freeman, New York, 1983). p. 388.
3. A literature search of the Inspec database of scientific publications (covering engineering, physics, and computer science) of the term *statistic\$*, where *\$* denotes a wild card, finds 30,170 citations published in the years 1980 through 1984 and 33,254 from 1985 to 1989. In contrast, 458 publications on fractals are found from the first time period and 2602 from the second.
4. M.V. Berry and Z.V. Lewis, "On the Weierstrass-Mandelbrot fractal function," *Proc. Roy. Soc. Lond. A* **370**, 459-484 (1980).
5. Y. Kim, *Wave Propagation in Bandlimited Fractal Media* (Ph.D. Thesis, University of Pennsylvania, 1987).
6. B.B. Mandelbrot, "How long is the coast of Britain? Statistical self-similarity and fractional dimension," *Science* **156**, 636-638 (1967).
7. L.F. Richardson, "The problem of contiguity: an appendix to *Statistics of Deadly Quarrels*," *General Systems Yearbook* **6**, 139-187 (1961).
8. D.L. Jaggard and Y. Kim, "Diffraction by band-limited fractal screens," *J. Opt. Soc. Am. A* **4**, 1055-1062 (1987).
9. B.H. Kaye, J.E. Leblanc, and P. Abbot, "Fractal description of the structure of fresh and eroded aluminum shot fineparticles," *Part. Charact.* **2**, 56-61 (1985).
10. B.H. Kaye, "Specification of the ruggedness and/or texture of a fine particle profile by its fractal dimension," *Powder Technology* **21**, 1-16 (1978).
11. Ref. 1, p. 36.

12. *ibid.*, p. 24.
13. B.B. Mandelbrot , D.E. Passoja, and A.J. Paullay, "Fractal character of fracture surfaces of metals," , Nature 308, 712-722 (1984).
14. A.M. Mood, F.A. Graybill, and D.C. Boes, *Introduction to the Theory of Statistics*, 3rd ed., McGraw-Hill, New York (1963), p. 241.
15. The centennial of the Parisian tower is here noted and honored. The value of β for the tower is approximately 0.34.

Chapter 4

Statistical Diffraction Theory for Serrated Circular Apertures

4.1. Introduction

The diffraction of light by a serrated circular aperture can be understood through the application of statistical techniques. If apertures in a set are realizations of the same random process, the Fourier transforms of the transmission functions of those apertures will be similar to each other in a statistical sense. In this chapter, we combine the diffraction theory of Chapter 2 with methods of statistical optics in order to derive quantitative results for the angular correlation of intensity.

The basic quantity of interest in this chapter is the two-point intensity moment, defined in Section 4.2. Since the intensity is equal to the squared modulus of the scalar component of the field, this second-order intensity moment is a fourth-order moment of this scalar field. By using a general moment expansion for Gaussian fields and applying symmetry conditions, we determine that two terms in the expansion of the fourth-order moment are significant. As shown in Section 4.2.2, these terms are second-order moments of the field. We proceed with the details of the calculation of these second-order moments in Section 4.3, expressing them in terms of the characteristic functions of the aperture serration. An illustrative example is used to verify the symmetry conditions derived for the second-order moments of the Fourier transform of a real-valued object.

To extract from this theory the relationship between features in the Fourier transform and statistical parameters of the aperture serration, we examine our expression for the significant second-order moment in Section 4.4. We identify important terms in

the integrand for the second-order moment and discuss the effects of variations in the serration parameters on these terms. In Section 4.4.2, Fresnel zone analysis is used to gain some physical intuition about the relationship between the aperture roughness and the transform ring fragmentation. In Sects. 4.4.3 and 4.4.4, the correlation angle and correlation function of the aperture serration are shown to alter the number and appearance, respectively, of the spikes in the transform. We support these predictions with calculated examples of $\langle I(\rho_1, \phi_1) I(\rho_2, \phi_2) \rangle$ for selected aperture ensembles and with calculated intensity distributions for individual members of these ensembles. These theoretical findings presage the experimental work to be presented in Chapter 6.

4.2. The Two-Point Moment of Intensity

Since in experimental studies we are able to measure the intensity, given by Eq. (2.14), of the Fourier transform, the function of interest is the two-point intensity moment. This fourth-order moment of the field is written:

$$\begin{aligned} \langle I(\rho_1, \phi_1) I(\rho_2, \phi_2) \rangle &= \langle V^{(z)}(\rho_1, \phi_1; t) V^{*(z)}(\rho_1, \phi_1; t) \\ &\quad \times V^{(z)}(\rho_2, \phi_2; t) V^{*(z)}(\rho_2, \phi_2; t) \rangle, \end{aligned} \quad (4.1)$$

where subscripts 1 and 2 denote two points in the transform plane, each with a corresponding optical frequency, and the angle brackets $\langle \rangle$ denote the expected value over an ensemble of apertures. This ensemble averaging is mathematically and physically distinct from the spatial averaging used in previous chapters. Details of the differences are included in Appendix A.

The ensemble average $\langle I(\rho_1, \phi_1) I(\rho_2, \phi_2) \rangle$ would be measured experimentally as follows for a single optical frequency, $\nu_1 = \nu_2$. Two single detectors are

placed in the transform plane of an optical system, one at point 1: (ρ_1, ϕ_1) , the other at point 2: (ρ_2, ϕ_2) . With one serrated aperture from the ensemble of interest in the aperture plane of the system, the intensities at points 1 and 2 are measured with the detectors. The product $I(\rho_1, \phi_1)I(\rho_2, \phi_2)$ is calculated and stored. The serrated aperture is replaced by another from the ensemble, and the same measurement, calculation, and storage procedure is followed. After all the apertures have been used in this way, the average value of $I(\rho_1, \phi_1)I(\rho_2, \phi_2)$ is determined for the ensemble; this quantity is the ensemble average $\langle I(\rho_1, \phi_1)I(\rho_2, \phi_2) \rangle$. In theory, the number of apertures in an ensemble is infinite; thus, in practice, some large but finite number of apertures would be used to approximate $\langle I(\rho_1, \phi_1)I(\rho_2, \phi_2) \rangle$ by this method. We note that, unlike this ensemble average, a spatial average would depend on the particular ensemble member chosen.

The reader is cautioned against confusing the two-point intensity moment $\langle I(\rho_1, \phi_1)I(\rho_2, \phi_2) \rangle$ with the usual two-dimensional correlation function in Cartesian coordinates. One can readily show that the two-point moment in a cylindrical coordinate system is an entirely different function. We will see later that this two-point moment of intensity is particularly interesting in a reduced form for the study of features in the transform. We will fix the ρ coordinate (i.e., set ρ_1 equal to ρ_2) and study the two-point intensity moment as a one-dimensional angular correlation function. For present considerations, we keep the full two-dimensional representation.

With this understanding, we continue with our investigation of the fourth-order moment of the field. Equations (2.13) and (4.1) are combined to yield the basic result:

$$\begin{aligned} \langle I(\rho_1, \phi_1) I(\rho_2, \phi_2) \rangle &= \langle v^{(z)}(\rho_1, \phi_1; \nu_1) v^{*(z)}(\rho_1, \phi_1; \nu_1) \\ &\quad \times v^{(z)}(\rho_2, \phi_2; \nu_2) v^{*(z)}(\rho_2, \phi_2; \nu_2) \rangle . \end{aligned} \quad (4.2)$$

This expression for the two-point intensity moment is applicable to the study of the wavelength dependence of the moment as well as the spatial dependence. It should be clear from the derivation of Eq. (4.2) that we are not treating optical mixing of the two frequencies.

4.2.1. Moment Expansion for Gaussian Fields

In this section, we use a moment expansion in order to simplify the fourth-order moment in Eq. (4.2) to a sum of second-order moments. When calculating correlations of scalar fields, one often encounters high-order moments of complex Gaussian processes. Reed¹ has presented a moment theorem which has been used extensively²⁻⁷ in statistical optics to simplify the higher-order moments. We will show that, for the Fourier transform calculation at hand, the usual assumption that the scalar field obeys circular complex Gaussian statistics is not valid. Hence, we proceed with a general moment expansion, following Shirley and George^{8,9} in applying Reed's theorem to the two-point moment of intensity of a scalar field.

The scalar field $v^{(z)}$ is defined as an integral in Eq. (2.7). This integral can be interpreted as a sum of functions of random variables $s(\alpha)$; by the central limit theorem, $v^{(z)}$ is thus Gaussian-distributed. Assuming neither circular statistics nor zero mean we can write the fourth-order moment as^{8,9}:

$$\langle I(\rho_1, \phi_1) I(\rho_2, \phi_2) \rangle =$$

$$\begin{aligned} & \langle v^{(z)}(\rho_1, \phi_1; \nu_1) v^{*(z)}(\rho_1, \phi_1; \nu_1) \rangle \langle v^{(z)}(\rho_2, \phi_2; \nu_2) v^{*(z)}(\rho_2, \phi_2; \nu_2) \rangle \\ & + \langle v^{(z)}(\rho_1, \phi_1; \nu_1) v^{*(z)}(\rho_2, \phi_2; \nu_2) \rangle \langle v^{*(z)}(\rho_1, \phi_1; \nu_1) v^{(z)}(\rho_2, \phi_2; \nu_2) \rangle \\ & + \langle v^{(z)}(\rho_1, \phi_1; \nu_1) v^{(z)}(\rho_2, \phi_2; \nu_2) \rangle \langle v^{*(z)}(\rho_1, \phi_1; \nu_1) v^{*(z)}(\rho_2, \phi_2; \nu_2) \rangle \\ & - 2 \langle v^{(z)}(\rho_1, \phi_1; \nu_1) \rangle \langle v^{(z)}(\rho_2, \phi_2; \nu_2) \rangle \\ & \times \langle v^{*(z)}(\rho_1, \phi_1; \nu_1) \rangle \langle v^{*(z)}(\rho_2, \phi_2; \nu_2) \rangle . \end{aligned} \quad (4.3)$$

We note that $\langle v^{(z)}(\rho_1, \phi_1; \nu_1) v^{*(z)}(\rho_1, \phi_1; \nu_1) \rangle \langle v^{(z)}(\rho_2, \phi_2; \nu_2) v^{*(z)}(\rho_2, \phi_2; \nu_2) \rangle$ is the product of the ensemble averages of the intensities at points 1 and 2 and that the fourth term is a four-fold product of field ensemble averages. Thus, the two-point properties are contained in the second and third terms, for which we use the notation

$$\begin{aligned} |u_{12}|^2 &= |\langle v^{(z)}(\rho_1, \phi_1; \nu_1) v^{*(z)}(\rho_2, \phi_2; \nu_2) \rangle|^2 \\ &= \langle v^{(z)}(\rho_1, \phi_1; \nu_1) v^{*(z)}(\rho_2, \phi_2; \nu_2) \rangle \langle v^{*(z)}(\rho_1, \phi_1; \nu_1) v^{(z)}(\rho_2, \phi_2; \nu_2) \rangle \end{aligned} \quad (4.4)$$

and

$$\begin{aligned} |u_{12}^\dagger|^2 &= |\langle v^{(z)}(\rho_1, \phi_1; \nu_1) v^{(z)}(\rho_2, \phi_2; \nu_2) \rangle|^2 \\ &= \langle v^{(z)}(\rho_1, \phi_1; \nu_1) v^{(z)}(\rho_2, \phi_2; \nu_2) \rangle \langle v^{*(z)}(\rho_1, \phi_1; \nu_1) v^{*(z)}(\rho_2, \phi_2; \nu_2) \rangle . \end{aligned} \quad (4.5)$$

These two terms are spatial cross-terms. Since we have chosen to discuss monochromatic fields, the ensemble averages u_{12} and u_{12}^\dagger are not spectral intensities. A fairly standard technique¹⁰ used in speckle problems to simplify the moment expansion of Eq. (4.3) is to assume that $v^{(z)}$ possesses circular complex Gaussian statistics; i.e., that

$$\begin{aligned} & \langle v^{(z)}(\rho_1, \phi_1; \nu_1) v^{(z)}(\rho_2, \phi_2; \nu_2) \rangle \\ & = \langle v^{(z)}(\rho_1, \phi_1; \nu_1) \rangle \langle v^{(z)}(\rho_2, \phi_2; \nu_2) \rangle . \end{aligned} \quad (4.6)$$

We can see that with this assumption Eq. (4.3) reduces to

$$\begin{aligned} & \langle I(\rho_1, \phi_1) I(\rho_2, \phi_2) \rangle = \\ & \langle v^{(z)}(\rho_1, \phi_1; \nu_1) v^{*(z)}(\rho_1, \phi_1; \nu_1) \rangle \langle v^{(z)}(\rho_2, \phi_2; \nu_2) v^{*(z)}(\rho_2, \phi_2; \nu_2) \rangle \\ & + \langle v^{(z)}(\rho_1, \phi_1; \nu_1) v^{*(z)}(\rho_2, \phi_2; \nu_2) \rangle \langle v^{*(z)}(\rho_1, \phi_1; \nu_1) v^{(z)}(\rho_2, \phi_2; \nu_2) \rangle \\ & - \langle v^{(z)}(\rho_1, \phi_1; \nu_1) \rangle \langle v^{(z)}(\rho_2, \phi_2; \nu_2) \rangle \\ & \times \langle v^{*(z)}(\rho_1, \phi_1; \nu_1) \rangle \langle v^{*(z)}(\rho_2, \phi_2; \nu_2) \rangle . \end{aligned} \quad (4.7)$$

and thus that the two-point properties of $\langle I(\rho_1, \phi_1) I(\rho_2, \phi_2) \rangle$ are essentially contained in the second term in Eq. (4.3), $|u_{12}|^2$. Many authors also assume a zero mean for the field, in which case the last term in this expansion is equal to zero. However, neither the assumption of circularity nor that of zero mean is valid everywhere in the Fourier transform of a real-valued object, as is discussed below. Certainly on-axis we expect a non-zero mean, since the optical Fourier transform has a large on-axis value due

to the light that remains undiffracted as it passes through the real-valued object, although far enough off-axis the mean field is usually small enough to be negligible.

As we will see from the calculation presented below, the circularity assumption, Eq. (4.6), does not hold, and furthermore u_{12}^{\ddagger} has significant properties which contribute to $\langle I(\rho_1, \phi_1) I(\rho_2, \phi_2) \rangle$ and cannot be neglected. The reason for this lies in the symmetry properties of a Fourier transform at polar-symmetric points. Here, we demonstrate the symmetry relationship between $|u_{12}|^2$ and $|u_{12}^{\ddagger}|^2$ for arbitrary real-valued objects; later in this chapter, we examine the specific case of the serrated circular aperture in greater detail.

4.2.2. Symmetry Considerations

To study the symmetry properties of the Fourier transform, we rewrite Eq. (2.11) as

$$v(\rho, \phi; v) = B T(\rho, \phi), \quad (4.8)$$

where B is defined as in Eq. (2.9):

$$B = \frac{i}{\lambda z_0} \exp \left[-ik \left(z_0 + \frac{\rho^2}{2z_0} \right) \right]. \quad (4.9)$$

We have chosen B such that $T(\rho, \phi)$ is exactly the two-dimensional Fourier transform of aperture function $t(r, \alpha)$, expressed in cylindrical coordinates:

$$T(\rho, \phi) = \int_{-\pi}^{+\pi} \int_0^{a+s(\alpha)} \exp \left(\frac{ik}{z_0} r \rho \cos(\alpha - \phi) \right) r dr d\alpha. \quad (4.10)$$

Since in our calculation $t(r, \alpha)$ is real-valued, the Fourier transform $T(\rho, \phi)$ has the well-known symmetry property¹¹:

$$T(\rho, \phi) = T^*(\rho, \phi + \pi) . \quad (4.11)$$

For convenience of notation, let a subscript 3 denote the point that is polar symmetric to point 2, (ρ_2, ϕ_2) ; i.e., point 3 has cylindrical coordinates given by:

$$\rho_3 = \rho_2 \quad (4.12)$$

and

$$\phi_3 = \phi_2 + \pi . \quad (4.13)$$

We also let the scalar field at points 2 and 3 have the same optical frequency. From Eq. (4.9), it is evident that B_3 satisfies the equation

$$B_3 = B_2 \quad (4.14)$$

and, with Eq. (4.11), that the scalar field values at points 2 and 3 are related by the equation:

$$B_3 T(\rho_3, \phi_3) = B_2 T^*(\rho_2, \phi_2) . \quad (4.15)$$

This symmetry property results in the following important relationships:

$$v^{(z)}(\rho_1, \phi_1; \nu_1) v^{*(z)}(\rho_2, \phi_2; \nu_2) = B_1 B_2^* T(\rho_1, \phi_1) T^*(\rho_2, \phi_2) , \quad (4.16)$$

and

$$v^{(z)}(\rho_1, \phi_1; \nu_1) v^{(z)}(\rho_3, \phi_3; \nu_3) = B_1 B_2 T(\rho_1, \phi_1) T^*(\rho_2, \phi_2) . \quad (4.17)$$

We take the ensemble average of these quantities to determine u_{12} and u_{13}^\dagger :

$$u_{12} = B_1 B_2^* \langle T(\rho_1, \phi_1) T^*(\rho_2, \phi_2) \rangle \quad (4.18)$$

and

$$u_{13}^\dagger = B_1 B_2 \langle T(\rho_1, \phi_1) T^*(\rho_2, \phi_2) \rangle . \quad (4.19)$$

To calculate the fourth-order moment as expressed in Eq. (4.3), we need the squared moduli of these quantities. These are given by

$$\begin{aligned} |u_{12}|^2 &= |B_1 B_2^* \langle T(\rho_1, \phi_1) T^*(\rho_2, \phi_2) \rangle|^2 \\ &= |B_1 B_2^*|^2 |\langle T(\rho_1, \phi_1) T^*(\rho_2, \phi_2) \rangle|^2. \end{aligned} \quad (4.20)$$

and

$$\begin{aligned} |u_{13}^\dagger|^2 &= |B_1 B_2 \langle T(\rho_1, \phi_1) T^*(\rho_2, \phi_2) \rangle|^2 \\ &= |B_1 B_2|^2 |\langle T(\rho_1, \phi_1) T^*(\rho_2, \phi_2) \rangle|^2. \end{aligned} \quad (4.21)$$

Noting that $|B_1 B_2|^2$ is equal to $|B_1 B_2^*|^2$, we have :

$$|u_{13}^\dagger|^2 = |u_{12}|^2. \quad (4.22)$$

Since points 2 and 3 are polar symmetric, we infer from Eq. (4.22) that the function $|u_{12}^\dagger|^2$ is simply $|u_{12}|^2$, rotated by π . The contribution of $|u_{12}^\dagger|^2$ to the transform intensity moment $\langle I(\rho_1, \phi_1) I(\rho_2, \phi_2) \rangle$ is as important as that of $|u_{12}|^2$. This result is valid for objects with arbitrary real-valued transmission functions.

4.3. Second - Order Moment for Gaussian Roughness

We now proceed to show in some detail the calculation of u_{12} for serrated circular apertures. We will then determine the functional form of u_{12}^\dagger in a similar manner and compare it to u_{12} . The results of this calculation will verify the aforementioned symmetry property for the case at hand, and a computed example will demonstrate it graphically.

4.3.1. Second - Order Moment u_{12}

In the calculation of the second-order moments, we greatly simplify the algebra necessary by using the zero-mean field, denoted by the italicized function $v^{(z)}(\rho, \phi; \nu)$ and defined by

$$v^{(z)}(\rho, \phi; \nu) = v^{(z)}(\rho, \phi; \nu) - \langle v^{(z)}(\rho, \phi; \nu) \rangle . \quad (4.23)$$

This zero-mean field is then used to calculate the second-order central moment, μ_{12} :

$$\mu_{12} = \langle v^{(z)}(\rho_1, \phi_1; \nu_1) v^{*(z)}(\rho_2, \phi_2; \nu_2) \rangle . \quad (4.24)$$

We can easily rewrite u_{12} in terms of μ_{12} and expected values of the field:

$$u_{12} = \mu_{12} + \langle v^{(z)}(\rho_1, \phi_1; \nu_1) \rangle \langle v^{*(z)}(\rho_2, \phi_2; \nu_2) \rangle . \quad (4.25)$$

Thus, the two-point dependency of u_{12} is contained in μ_{12} .

Using Eq. (2.11) and (4.23) in Eq. (4.24), we can write out the second-order central moment:

$$\begin{aligned} \mu_{12} &= B_1 B_2^* \int_{-\pi}^{+\pi} \int_{-\pi}^{+\pi} da' da'' \exp[i(\kappa_1' - \kappa_2'') a] \\ &\times \left(\frac{1 - i\kappa_1' a}{\kappa_1'^2} - \frac{1}{\kappa_1'} \frac{\partial}{\partial \kappa_1'} \right) \left(\frac{1 + i\kappa_2'' a}{\kappa_2''^2} - \frac{1}{\kappa_2''} \frac{\partial}{\partial \kappa_2''} \right) \\ &\times \langle [\exp(i\kappa_1' s') - \Psi_s(\kappa_1')] [\exp(-i\kappa_2'' s'') - \Psi_s(-\kappa_2'')] \rangle . \quad (4.26) \end{aligned}$$

In this expression, the subscripted 1 and 2 denote two points in the observation plane, while the single and double primes correspond to the integration variables a' and a'' . Thus, s' and s'' are equivalent to $s(a')$ and $s(a'')$, respectively, and κ_1' and κ_2'' are

defined as in Eq. (2.8), with the appropriate subscripts and primes added. $\Psi_s(\kappa) = \langle \exp[i\kappa s(a)] \rangle$ is the first-order characteristic function of $s(a)$. Expanding the terms within the angle brackets in Eq. (4.26), we find:

$$\begin{aligned} & \langle [\exp(i\kappa_1' s') - \Psi_s(\kappa_1')] [\exp(-i\kappa_2'' s'') - \Psi_s(-\kappa_2'')] \rangle \\ & = \Phi_s(\kappa_1', -\kappa_2'', r_s) - \Psi_s(\kappa_1') \Psi_s(-\kappa_2''), \end{aligned} \quad (4.27)$$

where $\Phi_s(\kappa_1', \kappa_2'', r_s) = \langle \exp[i(\kappa_1' s(a') - \kappa_2'' s(a''))] \rangle$ is the second-order characteristic function of $s(a)$ and

$$\begin{aligned} r_s(a', a'') & = \frac{\langle (s(a') - \langle s(a) \rangle)(s(a'') - \langle s(a) \rangle) \rangle}{\langle (s(a) - \langle s(a) \rangle)^2 \rangle} \\ & = \frac{\langle s(a') s(a'') \rangle}{\langle (s(a))^2 \rangle} \end{aligned} \quad (4.28)$$

is the normalized correlation function of the aperture serration, which takes on values in the interval $[0, 1]$. The dependence of Φ_s on the correlation function $r_s(a', a'')$ arises when we take the ensemble average of the product $\exp(i\kappa_1' s') \exp(-i\kappa_2'' s'')$, which is essentially the product of $\exp(i\kappa s)$ evaluated at two points. We continue to limit our discussion to statistically stationary correlation functions, *i.e.*, to those functions which depend on a' and a'' only as the difference between them: $r_s(a', a'') = r_s(a'' - a')$.

4.3.2. Gaussian Characteristic Function Notation

We now assume that the random variable $s(a)$ is Gaussian-distributed. The first- and second-order characteristic functions are

$$\Psi_s(\mathbf{k}) = \exp\left(-\frac{\sigma^2}{2} \mathbf{k}^2\right) \quad (4.29)$$

and

$$\Phi_s(\kappa_1', -\kappa_2''; r_s) = \exp\left(-\frac{\sigma^2}{2} (\kappa_1'^2 - 2r_s \kappa_1' \kappa_2'' + \kappa_2''^2)\right), \quad (4.30)$$

where $\sigma^2 = \langle (s(\alpha))^2 \rangle$ is the variance of $s(\alpha)$. Equation (4.30) is rewritten to emphasize temporal frequency dependence⁷, as follows:

$$\Phi_s(\kappa_1', -\kappa_2''; r_s) = \exp\left(-\frac{\sigma^2}{2} (\kappa_1' - \kappa_2'')^2\right) \exp[-\sigma^2 \kappa_1' \kappa_2'' (1 - r_s)]. \quad (4.31)$$

The first exponential in Eq. (4.31) contains the essential temporal frequency dependence in $(\kappa_1' - \kappa_2'') = 2\pi[\nu_1 \rho_1 \cos(\alpha' - \phi_1) - \nu_2 \rho_2 \cos(\alpha'' - \phi_2)]/z_0 c$, while the dependence on the correlation function r_s is contained in the second exponential term. Evaluating Eq. (4.26) for the Gaussian case, we find:

$$\begin{aligned} \mu_{12} &= B_1 B_2^* \int_{-\pi}^{+\pi} \int_{-\pi}^{+\pi} da' da'' \exp[i(\kappa_1' - \kappa_2'')a] \exp\left(-\frac{\sigma^2}{2} (\kappa_1' - \kappa_2'')^2\right) \\ &\quad \times \left\{ \left(\exp[-\sigma^2 \kappa_1' \kappa_2'' (1 - r_s)] - \exp[-\sigma^2 \kappa_1' \kappa_2''] \right) \right. \\ &\quad \times \left(\frac{1 - i\kappa_1' a}{\kappa_1'^2} + \sigma^2 \right) \left(\frac{1 - i\kappa_2'' a}{\kappa_2''^2} + \sigma^2 \right) \\ &\quad \left. - \exp[-\sigma^2 \kappa_1' \kappa_2'' (1 - r_s)] \right. \\ &\quad \left. \times \frac{\sigma^2 r_s}{\kappa_1' \kappa_2''} [2 - i(\kappa_1' - \kappa_2'')a + \sigma^2(\kappa_1'^2 + \kappa_2''^2 - \kappa_1' \kappa_2'') r_s] \right\}. \quad (4.32) \end{aligned}$$

Equation (4.32) is the basic result of this section and our working expression for μ_{12} . Although we now continue our analysis by considering the remaining term in the expression for u_{12} given in Eq. (4.25), we will return to Eq. (4.32) because it contains the essential two-point dependency of u_{12} , and therefore that of $\langle I(\rho_1, \phi_1) I(\rho_2, \phi_2) \rangle$, in a relatively concise form.

Using the same Gaussian distribution assumption, we express the second term in Eq. (4.25) as:

$$\begin{aligned} \langle v^{(z)}(\rho_1, \phi_1; \nu_1) \rangle &= \langle v^{*(z)}(\rho_2, \phi_2; \nu_2) \rangle \\ &= B_1 \int_{-\pi}^{+\pi} d\alpha' \left[\exp(i \kappa_1' a) \exp\left(-\frac{\sigma^2}{2} \kappa_1'^2\right) \left(\frac{1 - i \kappa_1' a}{\kappa_1'^2 + \sigma^2} - \frac{1}{\kappa_1'^2} \right) \right] \\ &\quad \times B_2^* \int_{-\pi}^{+\pi} d\alpha'' \left[\exp(-i \kappa_2'' a) \exp\left(-\frac{\sigma^2}{2} \kappa_2''^2\right) \left(\frac{1 + i \kappa_2'' a}{\kappa_2''^2 + \sigma^2} - \frac{1}{\kappa_2''^2} \right) \right] \end{aligned} \quad (4.33)$$

Equations (4.32) and (4.33), along with Eq. (4.25), yield the desired expression for u_{12} .

4.3.3. Second - Order Moment u_{12}^{\ddagger}

We now use the same steps to determine u_{12}^{\ddagger} . First, we define the central moment, μ_{12}^{\ddagger} :

$$\begin{aligned} \mu_{12}^{\ddagger} &= \langle [v^{(z)}(\rho_1, \phi_1; \nu_1) - \langle v^{(z)}(\rho_1, \phi_1; \nu_1) \rangle] \\ &\quad \times [v^{(z)}(\rho_2, \phi_2; \nu_2) - \langle v^{(z)}(\rho_2, \phi_2; \nu_2) \rangle] \rangle ; \end{aligned} \quad (4.34)$$

we can now express u_{12}^{\ddagger} in terms of μ_{12}^{\ddagger} :

$$u_{12}^{\dagger} = \mu_{12}^{\dagger} + \langle v^{(2)}(\rho_1, \phi_1; \nu_1) \rangle \langle v^{(2)}(\rho_2, \phi_2; \nu_2) \rangle . \quad (4.35)$$

As before, we evaluate the central moment first. We use Eq. (2.11) in Eq. (4.34):

$$\begin{aligned} \mu_{12}^{\dagger} &= B_1 B_2 \int_{-\pi}^{+\pi} \int_{-\pi}^{+\pi} da' da'' \exp[i(\kappa_1' + \kappa_2'') a] \\ &\times \left(\frac{1 - i\kappa_1' a}{\kappa_1'^2} - \frac{1}{\kappa_1'} \frac{\partial}{\partial \kappa_1'} \right) \left(\frac{1 - i\kappa_2'' a}{\kappa_2''^2} - \frac{1}{\kappa_2''} \frac{\partial}{\partial \kappa_2''} \right) \\ &\times \langle [\exp(i\kappa_1' s') - \Psi_s(\kappa_1')] [\exp(i\kappa_2'' s'') - \Psi_s(\kappa_2'')] \rangle . \end{aligned} \quad (4.36)$$

Equation (4.36) for μ_{12}^{\dagger} is analogous to Eq. (4.26) for μ_{12} . Next, we assume that $s(a)$ is Gaussian-distributed. Again expressing the second-order characteristic function to emphasize temporal frequency dependence [Eq. (4.31)], we find:

$$\begin{aligned}
\mu_{12}^{\dagger} &= B_1 B_2 \int_{-\pi}^{+\pi} \int_{-\pi}^{+\pi} da' da'' \exp[i(\kappa_1' + \kappa_2'')a] \exp\left(-\frac{\sigma^2}{2}(\kappa_1' - \kappa_2'')^2\right) \\
&\times \left\{ \left(\exp[-\sigma^2 \kappa_1' \kappa_2''(1 + r_s)] - \exp[-\sigma^2 \kappa_1' \kappa_2''] \right) \right. \\
&\quad \times \left(\frac{1 - i\kappa_1' a}{\kappa_1'^2} + \sigma^2 \right) \left(\frac{1 - i\kappa_2'' a}{\kappa_2''^2} + \sigma^2 \right) \\
&\quad \left. - \exp[-\sigma^2 \kappa_1' \kappa_2''(1 + r_s)] \right. \\
&\quad \left. \times \frac{\sigma^2 r_s}{\kappa_1' \kappa_2''} [2 - i(\kappa_1' + \kappa_2'')a + \sigma^2(\kappa_1'^2 + \kappa_2''^2 + \kappa_1' \kappa_2'' r_s)] \right\}. \quad (4.37)
\end{aligned}$$

We can also express the second term in Eq. (4.35) under the same Gaussian distribution assumption:

$$\begin{aligned}
\langle v^{(2)}(\rho_1, \phi_1; \nu_1) \rangle &\langle v^{(2)}(\rho_2, \phi_2; \nu_2) \rangle \\
&= B_1 \int_{-\pi}^{+\pi} da' \left\{ \exp[i\kappa_1' a] \exp\left(-\frac{\sigma^2}{2} \kappa_1'^2\right) \left(\frac{1 - i\kappa_1' a}{\kappa_1'^2} + \sigma^2 \right) - \frac{1}{\kappa_1'^2} \right\} \\
&\times B_2 \int_{-\pi}^{+\pi} da'' \left\{ \exp[i\kappa_2'' a] \exp\left(-\frac{\sigma^2}{2} \kappa_2''^2\right) \left(\frac{1 - i\kappa_2'' a}{\kappa_2''^2} + \sigma^2 \right) - \frac{1}{\kappa_2''^2} \right\} \quad (4.38)
\end{aligned}$$

From Eqs. (4.35), (4.37), and (4.38), we have an expression for u_{12}^{\dagger} analogous to our expression for u_{12} .

4.3.4. Symmetry of the Fourier Transform

We now will verify the symmetry condition of Eq. (4.22), i.e., that $|u_{13}^\dagger|^2$ is equal to $|u_{12}|^2$, where points 2 (ρ_2, ϕ_2) and 3 (ρ_3, ϕ_3) are polar symmetric. Using Eqs. (4.12) and (4.13) and holding the frequency constant so that $k_3 = k_2$, we have from Eq. (2.8):

$$\kappa_3^r = \frac{k_2 \rho_2}{z_0} \cos(\alpha^r - \phi_2 - \pi) = -\frac{k_2 \rho_2}{z_0} \cos(\alpha^r - \phi_2) = -\kappa_2^r. \quad (4.39)$$

Using Eqs. (4.14) and (4.39) in Eq. (4.37), we express μ_{13}^\dagger as:

$$\begin{aligned} \mu_{13}^\dagger &= B_1 B_2 \int_{-\pi}^{+\pi} \int_{-\pi}^{+\pi} da' da'' \exp[i(\kappa_1' - \kappa_2'')a] \exp\left(-\frac{\sigma^2}{2}(\kappa_1' + \kappa_2'')^2\right) \\ &\times \left\{ \left(\exp[\sigma^2 \kappa_1' \kappa_2''(1 + r_s)] - \exp[\sigma^2 \kappa_1' \kappa_2''] \right) \right. \\ &\times \left(\frac{1 - i\kappa_1' a}{\kappa_1'^2} + \sigma^2 \right) \left(\frac{1 + i\kappa_2'' a}{\kappa_2''^2} + \sigma^2 \right) \\ &\left. - \exp[\sigma^2 \kappa_1' \kappa_2''(1 + r_s)] \right\} \\ &\times \frac{\sigma^2 r_s}{\kappa_1' \kappa_2''} [2 - i(\kappa_1' - \kappa_2'')a + \sigma^2(\kappa_1'^2 + \kappa_2''^2 - \kappa_1' \kappa_2'' r_s)]. \quad (4.40) \end{aligned}$$

The equalities

$$\begin{aligned} &\exp\left(-\frac{\sigma^2}{2}(\kappa_1' + \kappa_2'')^2\right) \exp[\sigma^2 \kappa_1' \kappa_2''(1 + r_s)] \\ &= \exp\left(-\frac{\sigma^2}{2}(\kappa_1' - \kappa_2'')^2\right) \exp[\sigma^2 \kappa_1' \kappa_2''(1 - r_s)] \quad (4.41) \end{aligned}$$

and

$$\begin{aligned} & \exp\left(-\frac{\sigma^2}{2}(\kappa_1' + \kappa_2'')^2\right) \exp[\sigma^2 \kappa_1' \kappa_2''] \\ &= \exp\left(-\frac{\sigma^2}{2}(\kappa_1' - \kappa_2'')^2\right) \exp[\sigma^2 \kappa_1' \kappa_2''] \end{aligned} \quad (4.42)$$

are easily verified. The integral in our expression for u_{13}^\dagger is therefore identical to that for u_{12} given by Eq. (4.32); only the coefficients of the integrals differ. We also use Eqs. (4.14) and (4.39) in Eq. (4.38) to write $\langle v^{(z)}(\rho_1, \phi_1; \nu_1) \rangle \langle v^{(z)}(\rho_3, \phi_3; \nu_3) \rangle$ as:

$$\begin{aligned} & \langle v^{(z)}(\rho_1, \phi_1; \nu_1) \rangle \langle v^{(z)}(\rho_3, \phi_3; \nu_3) \rangle \\ &= B_1 \int_{-\pi}^{+\pi} d\alpha' \left\{ \exp[i \kappa_1' a] \exp\left(-\frac{\sigma^2}{2} \kappa_1'^2\right) \left(\frac{1 - i \kappa_1' a}{\kappa_1'^2 + \sigma^2} - \frac{1}{\kappa_1'^2} \right) \right\} \\ & \times B_2 \int_{-\pi}^{+\pi} d\alpha'' \left\{ \exp[-i \kappa_2'' a] \exp\left(-\frac{\sigma^2}{2} \kappa_2''^2\right) \left(\frac{1 + i \kappa_2'' a}{\kappa_2''^2 + \sigma^2} - \frac{1}{\kappa_2''^2} \right) \right\}. \end{aligned} \quad (4.43)$$

Comparing Eq. (4.43) to Eq. (4.33), we see that these expressions also differ only in the coefficients. Thus, the only difference between u_{12} and u_{13}^\dagger is a coefficient: the integrals in u_{13}^\dagger are multiplied by $B_1 B_2$; those in u_{12} by $B_1 B_2^*$. However, when we calculate $|u_{12}|^2$ and $|u_{13}^\dagger|^2$, these coefficients contribute the same value:

$$|B_1 B_2^*|^2 = |B_1 B_2|^2. \quad (4.44)$$

We have thus verified Eq. (4.22) for the specific case of a serrated circular aperture:

$$|u_{12}|^2 = |u_{13}^\dagger|^2. \quad (4.45)$$

4.3.5. Illustrative Example

An example of the relationship between these two functions is shown in the plot in Fig. 4.1. Here we have plotted μ_{12} and μ_{12}^{\ddagger} versus output angle ϕ_2 , using the mathematical forms in Eqs. (4.32) and (4.37). For these calculations, we have simplified B to $1/\lambda z_0$ to produce a real-valued function with the correct scaling. The fixed output coordinates are $\rho_1 = \rho_2 = 0.498$ mm and $\phi_1 = \pi/4$ rad. For $s(\alpha)$, we have chosen a triangular correlation function, a correlation angle of $\pi/8$ rad, and an rms roughness of $75 \mu\text{m}$. The mean radius a is 5.0 mm. In this calculation the wavelength is set at $\lambda_1 = \lambda_2 = 0.6328 \mu\text{m}$ and the focal length at $z_0 = 500$ mm. With this choice of system and aperture parameters, the value of ρ corresponds to the fifteenth ring in the transform. We have chosen points 1 and 2 at the same radius so that the angular properties are demonstrated. In this case, the two-point moment $\langle I(\rho, \phi_1) I(\rho, \phi_2) \rangle$ is a one-dimensional angular correlation function of the intensity. Thus, in Fig. 4.1, we expect to see the correlation peaks contributed by u_{12} and u_{12}^{\ddagger} to the angular correlation. We also note that the output radius chosen lies in the degraded region of the transform pattern; here, the Airy rings are fragmented. At this radius we expect to see narrow correlation peaks, since the transform has little angular uniformity.

From the plot in Fig. 4.1 we can see that each function has a significant peak and that these two peaks are separated by π rad. Examination of the detail of the plots confirms that $|\mu_{12}^{\ddagger}|^2$ is a rotated version of $|\mu_{12}|^2$. Because of the polar symmetry of the transform, we expect the maxima of the intensity moment $\langle I(\rho_1, \phi_1) I(\rho_2, \phi_2) \rangle$ to occur when points 1 and 2 coincide and also when they are polar symmetric. The term μ_{12} contributes one peak, while μ_{12}^{\ddagger} provides the other. Hence μ_{12}^{\ddagger} contributes significantly to the behavior of $\langle I(\rho_1, \phi_1) I(\rho_2, \phi_2) \rangle$. The circularity assumption

expressed by Eq. (4.6) clearly does not hold, and we must keep both these terms in the expansion of $\langle I(\rho_1, \phi_1) I(\rho_2, \phi_2) \rangle$ in Eq. (4.3).

For completeness, we also show a plot of $|u_{12}|^2$ and $|u_{12}^\dagger|^2$ under the same system conditions; see Fig. 4.2. The term $\langle v^{(z)}(\rho_1, \phi_1; v_1) \rangle \langle v^{*(z)}(\rho_2, \phi_2; v_2) \rangle$ in Eq. (4.25) and the term $\langle v^{(z)}(\rho_1, \phi_1; v_1) \rangle \langle v^{(z)}(\rho_2, \phi_2; v_2) \rangle$ in Eq. (4.35) contribute constant background levels to u_{12} and u_{12}^\dagger , respectively; this is evident when the plots in Figs. 4.1 and 4.2 are compared. The ratio of the peak heights to this background is significant in determining the angular correlation properties of the transform intensity. As we continue our examination of $\langle I(\rho_1, \phi_1) I(\rho_2, \phi_2) \rangle$, we will use further computer calculations to demonstrate this and similar effects.

4.4. Features in the Fourier Transform

In considering the two-point dependency of the intensity moment $\langle I(\rho_1, \phi_1) I(\rho_2, \phi_2) \rangle$, the two terms of interest are $|u_{12}|^2$ and $|u_{12}^\dagger|^2$. Since they are identical except for the aforementioned rotation, we need only examine our mathematical expression for u_{12} , and in particular for μ_{12} , to identify features in the Fourier transform which will yield information about the aperture statistics. To start, rather than integrating over α' and α'' in Eq. (4.32), we identify the significant terms in the integrand and evaluate the behavior of these terms. With this discussion, we present computer calculations of $\langle I(\rho_1, \phi_1) I(\rho_2, \phi_2) \rangle$ to demonstrate the features of the transforms of a few representative ensembles.

We repeat Eq. (4.32) here for convenience,

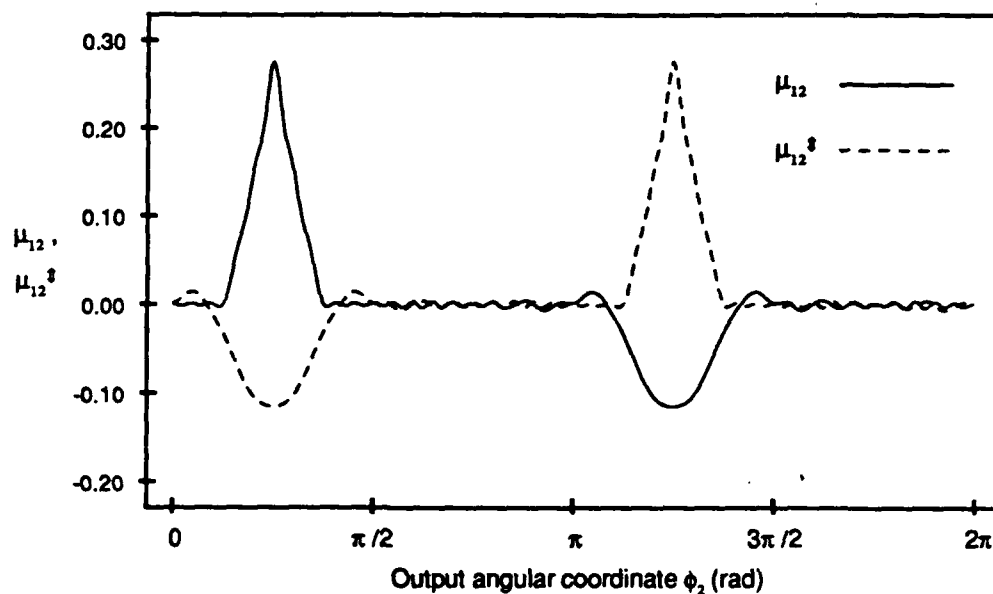


Fig. 4.1. Sample plot of μ_{12} and μ_{12}^3 versus output angle ϕ_2 . The fixed output coordinates are set as follows: $\rho_1 = \rho_2 = 0.498$ mm, $\phi_1 = \pi/4$ rad. The serration correlation is triangular, given by Eq. (2.20) with correlation angle Λ equal to $\pi/8$ rad; σ is equal to $75 \mu\text{m}$. For the optical system, we have chosen a 500-mm focal length and a wavelength of $0.6328 \mu\text{m}$.

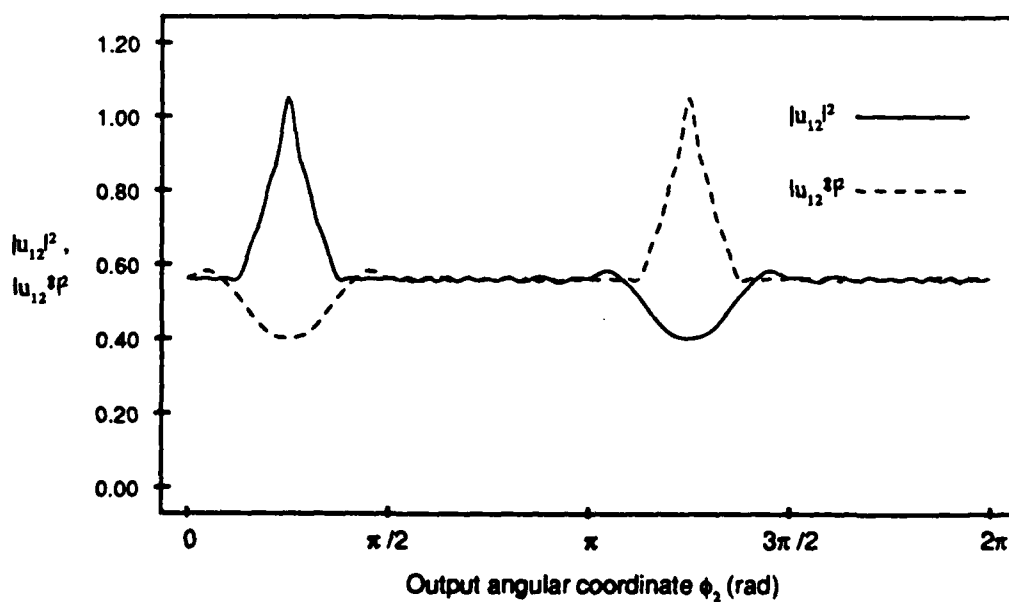


Fig. 4.2. Sample plot of $|u_{12}|^2$ and $|u_{12}|^3P$ versus output angle ϕ_2 . The system and aperture parameters are chosen as in Fig. 4.1.

$$\begin{aligned}
\mu_{12} = & B_1 B_2^* \int_{-\pi}^{+\pi} \int_{-\pi}^{+\pi} da' da'' \exp[i(\kappa_1' - \kappa_2'')a] \exp\left(-\frac{\sigma^2}{2}(\kappa_1' - \kappa_2'')^2\right) \\
& \times \left\{ \left(\exp[-\sigma^2 \kappa_1' \kappa_2''(1 - r_s)] - \exp[-\sigma^2 \kappa_1' \kappa_2''] \right) \right. \\
& \times \left(\frac{1 - i\kappa_1' a}{\kappa_1'^2 + \sigma^2} \right) \left(\frac{1 - i\kappa_2'' a}{\kappa_2''^2 + \sigma^2} \right) \\
& - \exp[-\sigma^2 \kappa_1' \kappa_2''(1 - r_s)] \\
& \left. \times \frac{\sigma^2 r_s}{\kappa_1' \kappa_2''} [2 - i(\kappa_1' - \kappa_2'')a + \sigma^2(\kappa_1'^2 + \kappa_2''^2 - \kappa_1' \kappa_2'' r_s)] \right\}, \quad [(4.32)]
\end{aligned}$$

and identify the terms of interest as the exponential terms that have real arguments:

$$T_1 = \exp\left(-\frac{\sigma^2}{2}(\kappa_1' - \kappa_2'')^2\right), \quad (4.46)$$

$$T_2 = \exp[-\sigma^2 \kappa_1' \kappa_2''(1 - r_s)] - \exp[-\sigma^2 \kappa_1' \kappa_2''], \quad (4.47)$$

$$T_3 = \exp[-\sigma^2 \kappa_1' \kappa_2''(1 - r_s)]. \quad (4.48)$$

Because of the peaked nature of these exponentials, T_1 , T_2 , and T_3 largely determine the functional form of μ_{12} . We note that term T_1 multiplies the rest of the integrand, while terms T_2 and T_3 are multiplied by secondary terms and added. The shape of the peak of each of these exponentials and thus the degree of influence it has on the magnitude and functional form of μ_{12} depend on the choice of system and aperture parameters. For

example, T_1 is maximized when κ_1' and κ_2'' are equal. The magnitude of T_1 drops to e^{-1} when $(\kappa_1' - \kappa_2'')^2$ is equal to $2/\sigma^2$. For example, if we choose the same radial coordinate and wavelength for points 1 and 2, then for typical system parameters¹² T_1 decreases to approximately e^{-1} when $|\cos(\alpha' - \phi_1) - \cos(\alpha'' - \phi_2)|$ is equal to $0.1\text{mm}/\sigma$. For σ equal to $500\ \mu\text{m}$ and for $\alpha' - \phi_1$ equal to $\pi/2$, $\alpha'' - \phi_2$ must change by about 11° to reduce T_1 to e^{-1} . As σ increases, this angular distance and the width of T_1 decrease. Term T_1 controls, in a delta-function-like way, the contributions to μ_{12} from the other terms in the integrand. Terms T_2 and T_3 , as a sum, work together to control the shape of the term in braces. Although the remaining terms in braces affect the relative contributions of T_2 and T_3 , we are more concerned with the mutual contribution of T_2 and T_3 to the form of μ_{12} . As we examine the effect of three aperture parameters, namely the aperture roughness, the correlation angle, and the correlation function of the serration, r_s in Eq. (4.28), we will see how these terms interplay. In the following sections, we will show how these parameters affect the radial and angular dependence of the Fourier transform.

Although many of the important properties of $\langle I(\rho_1, \phi_1) I(\rho_2, \phi_2) \rangle$ are incorporated in μ_{12} and we will base predictions of the behavior of the intensity pattern on μ_{12} , we must consider the full moment expansion, Eq. (4.3), of $\langle I(\rho_1, \phi_1) I(\rho_2, \phi_2) \rangle$ in order to fully understand the two-point intensity moment and the related properties of the intensity distribution. Herein, we use a computer to calculate the terms that contribute to $\langle I(\rho_1, \phi_1) I(\rho_2, \phi_2) \rangle$. In particular, we choose to fix the radial coordinate ρ and the optical frequency ν ; the quantity then calculated is

$$\langle I(\rho_1, \phi_1) I(\rho_2, \phi_2) \rangle = \langle I(\rho, \phi_1; \nu) I(\rho, \phi_2; \nu) \rangle \quad (4.49)$$

We note that in this specific case, the only variables that change as points 1 and 2 are moved are the angular coordinates ϕ_1 and ϕ_2 . Thus, we can consider the moment

$\langle I(\rho, \phi_1) I(\rho, \phi_2) \rangle$ to be a correlation function; it is the angular correlation function of the intensity at a fixed radius ρ in the Fourier transform plane of the optical system. In practice, we fix ϕ_1 and vary ϕ_2 to calculate $\langle I(\rho, \phi_1) I(\rho, \phi_2) \rangle$ as a function of angle.

This angular correlation, calculated at different radial positions, contains information about the changes in the ring structure as ρ changes. We can also study the relationship between the width and shape of the peak of the angular intensity correlation function and the spike structure in the transform. We proceed, then, to calculate $\langle I(\rho, \phi_1) I(\rho, \phi_2) \rangle$ for variations in the radial output coordinate ρ and the aperture ensemble rms roughness, correlation angle, and correlation function.

We begin with an aperture ensemble design with an rms roughness equal to $75 \mu\text{m}$ on a mean radius of 5.0 mm and a triangular correlation function with correlation angle $\pi/8 \text{ rad}$. Our first set of calculations will be for this ensemble; we will vary the output radial coordinate ρ and examine the behavior of $\langle I(\rho, \phi_1) I(\rho, \phi_2) \rangle$ and of $I(\rho, \phi)$ over the angular range $[0, 2\pi]$ as we move away from the center of the transform. The fixed angular output coordinate of the optical system is equal to $\pi/4 \text{ rad}$, the focal length is 500 mm , and the wavelength $\lambda = c/v$ is set at $0.6328 \mu\text{m}$. For convenience and clarity, we will use the following shorthand notation in writing the terms in the expansion of $\langle I(\rho, \phi_1) I(\rho, \phi_2) \rangle$: $\langle v^{(z)}(\rho, \phi_1) v^{*(z)}(\rho, \phi_1) \rangle \langle v^{(z)}(\rho, \phi_2) v^{*(z)}(\rho, \phi_2) \rangle = \langle v_1 v_1^* \rangle \langle v_2 v_2^* \rangle$, $|u_{12}|^2 = \langle v^{(z)}(\rho, \phi_1) v^{*(z)}(\rho, \phi_2) \rangle \langle v^{*(z)}(\rho, \phi_1) v^{(z)}(\rho, \phi_2) \rangle = \langle v_1 v_2^* \rangle \langle v_1^* v_2 \rangle$, $|u_{12}^\dagger|^2 = \langle v^{(z)}(\rho, \phi_1) v^{(z)}(\rho, \phi_2) \rangle \langle v^{*(z)}(\rho, \phi_1) v^{*(z)}(\rho, \phi_2) \rangle = \langle v_1 v_2 \rangle \langle v_1^* v_2^* \rangle$, and $2 \langle v^{(z)}(\rho, \phi_1) \rangle \langle v^{*(z)}(\rho, \phi_1) \rangle \langle v^{(z)}(\rho, \phi_2) \rangle \langle v^{*(z)}(\rho, \phi_2) \rangle = 2 \langle v_1 \rangle \langle v_1^* \rangle \langle v_2 \rangle \langle v_2^* \rangle$. We will also use $\langle I_1 I_2 \rangle$ for $\langle I(\rho, \phi_1) I(\rho, \phi_2) \rangle$ in the figures, where the correlation properties of the two-point intensity moment are particularly clear. This notation will only be used when we discuss $\langle I(\rho, \phi_1) I(\rho, \phi_2) \rangle$.

that is, the specific case in which the two-point moment reduces to the angular intensity correlation.

The four terms in the expansion of $\langle I(\rho, \phi_1) I(\rho, \phi_2) \rangle$ calculated at the following six values of ρ : 0.085 mm, 0.182 mm, 0.340 mm, 0.498 mm, 0.657 mm, and 0.815 mm, correspond to rings 2, 5, 10, 15, 20, and 25 in the optical Fourier transform. They are shown plotted against angular coordinate ϕ_2 in Fig. 4.3 for each of these values of ρ . In each of these six sets of curves, we note the following details. First, as expected from the transform symmetry and as seen in Fig. 4.2, term $|u_{12}^\ddagger|^2$ is a rotated version of $|u_{12}|^2$; the peaks in these two terms are separated by π rad. We also note that the first term, $\langle v_1 v_1^* \rangle \langle v_2 v_2^* \rangle$, is constant and equal to the peak value of $|u_{12}|^2$; this is easily seen to be the case when we set ϕ_2 equal to ϕ_1 and write $|u_{12}|^2$ as

$$|u_{11}|^2 = \langle v_1 v_1^* \rangle \langle v_1^* v_1 \rangle = |\langle v_1 v_1^* \rangle|^2 \quad (4.50)$$

Clearly, when points 1 and 2 coincide, the first and second terms are equal. The fourth term, $2\langle v_1 \rangle \langle v_1^* \rangle \langle v_2 \rangle \langle v_2^* \rangle$, is also constant. From our study of $|u_{12}|^2$ we know that the constant background in $|u_{12}|^2$ is equal to $|\langle v_1 \rangle \langle v_2^* \rangle|^2$ or $\langle v_1 \rangle \langle v_1^* \rangle \langle v_2 \rangle \langle v_2^* \rangle$; see Eq. (4.25). Thus, we expect that this fourth term will have twice the magnitude of the background of $|u_{12}|^2$. The plots shown in Fig. 4.3 support this fact. We note that when the fourth term is subtracted from the sum of the first three in Eq. (4.3), the result will be the exact cancellation of the contribution from the background of $|u_{12}|^2 + |u_{12}^\ddagger|^2$. We will consider the results of this cancellation more closely when we look at the plots of $\langle I(\rho, \phi_1) I(\rho, \phi_2) \rangle$. First, we consider the effects of changing the output radius on the four contributing terms.

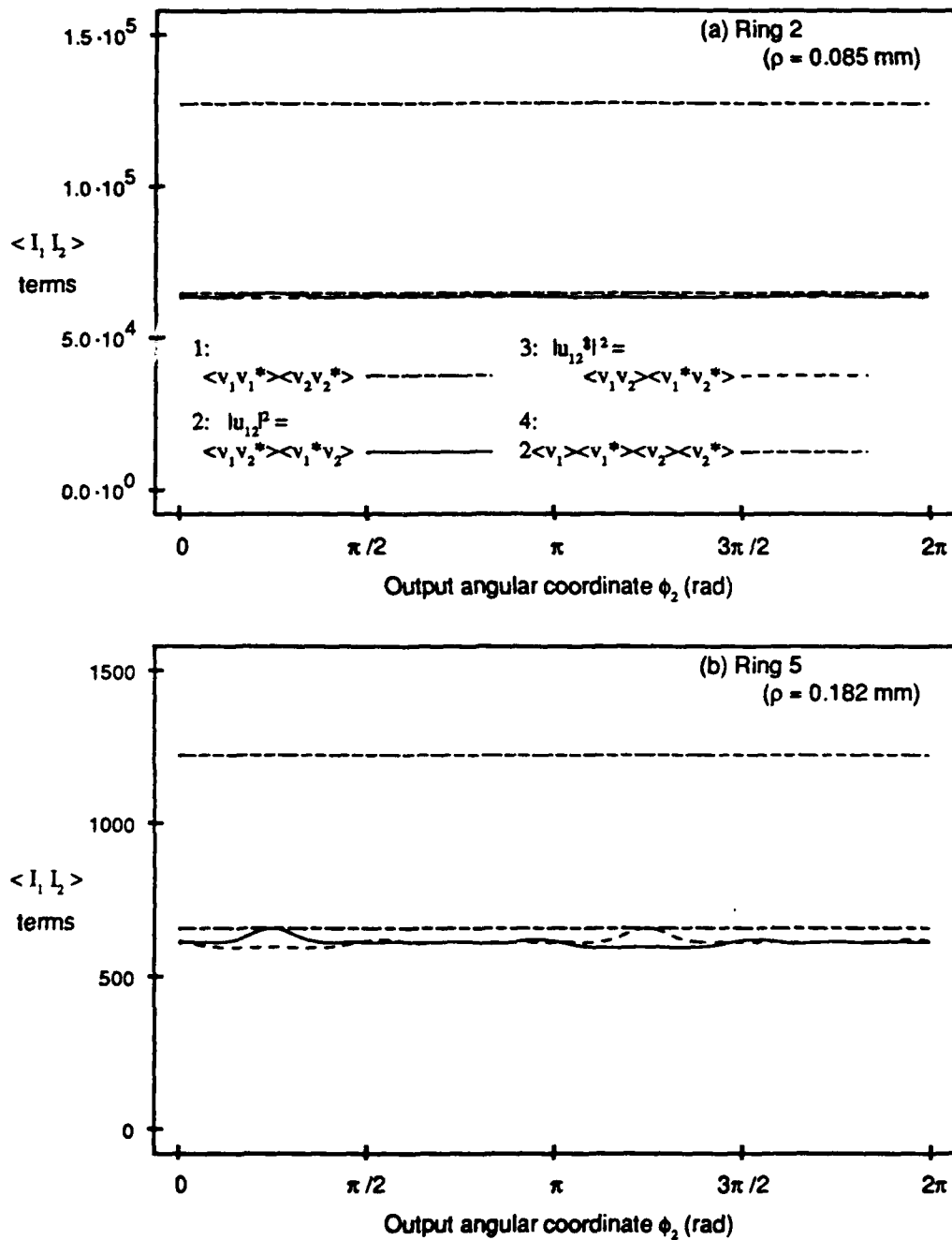


Fig. 4.3. Terms in the expansion of $\langle I_1 I_2 \rangle$, calculated for varied radius values as indicated. The output angular coordinate ϕ_1 is set to $\pi/4$ rad; the focal length is 500 mm, and the wavelength is $0.6328 \mu\text{m}$. For the aperture ensemble represented, the rms roughness is $75 \mu\text{m}$ on a 5.0 mm mean radius, the correlation angle is $\pi/8$ rad, and the correlation function is triangular. The curve legend included on Fig. 4.3(a) is for all the plots.

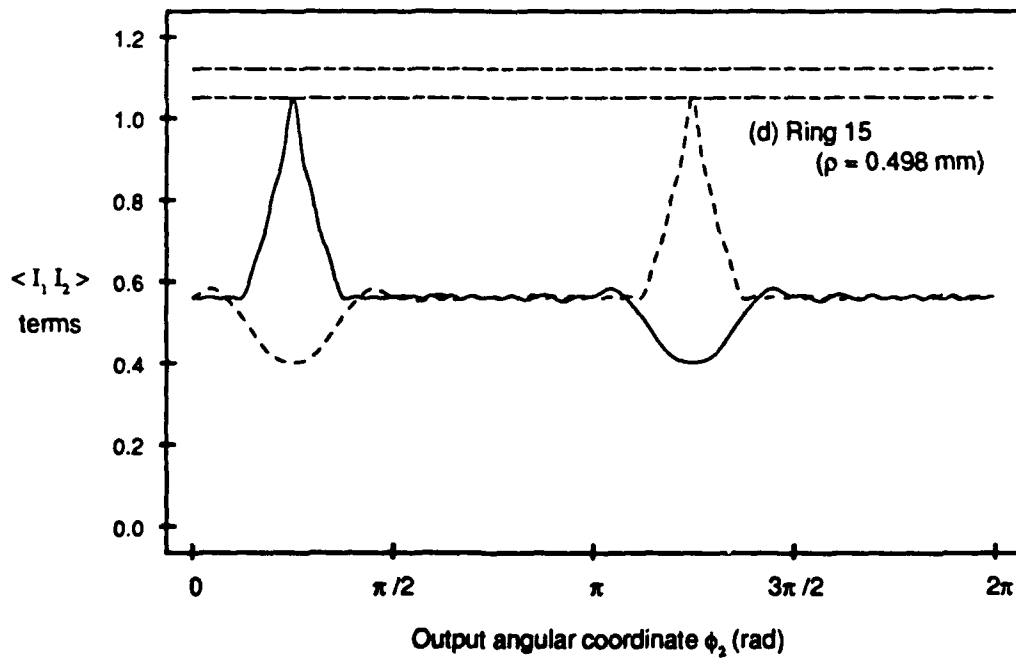
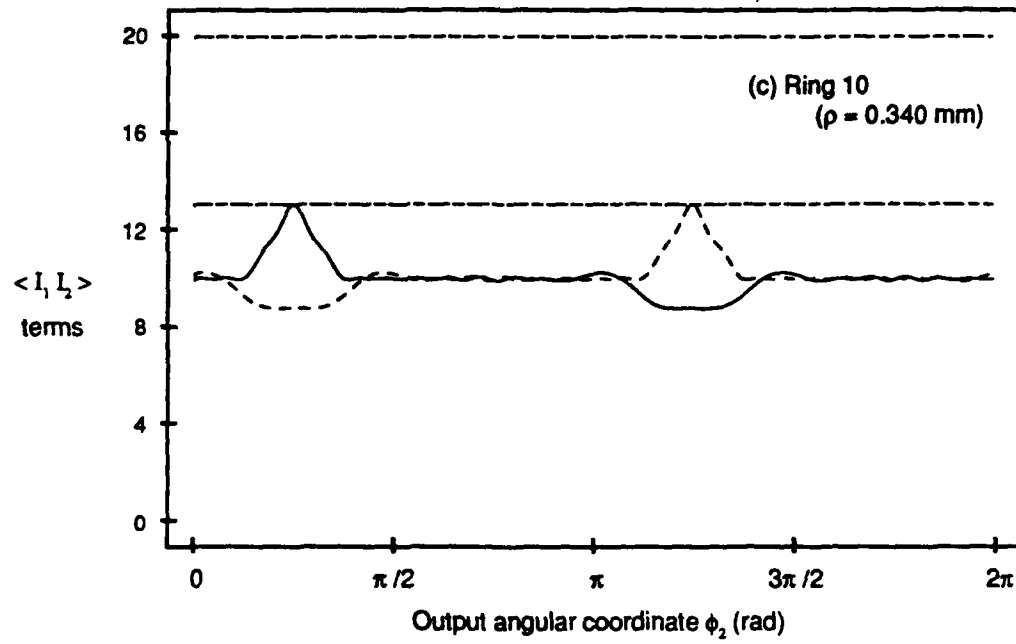


Fig. 4.3. (Continued) See legend on Fig. 4.3 (a).

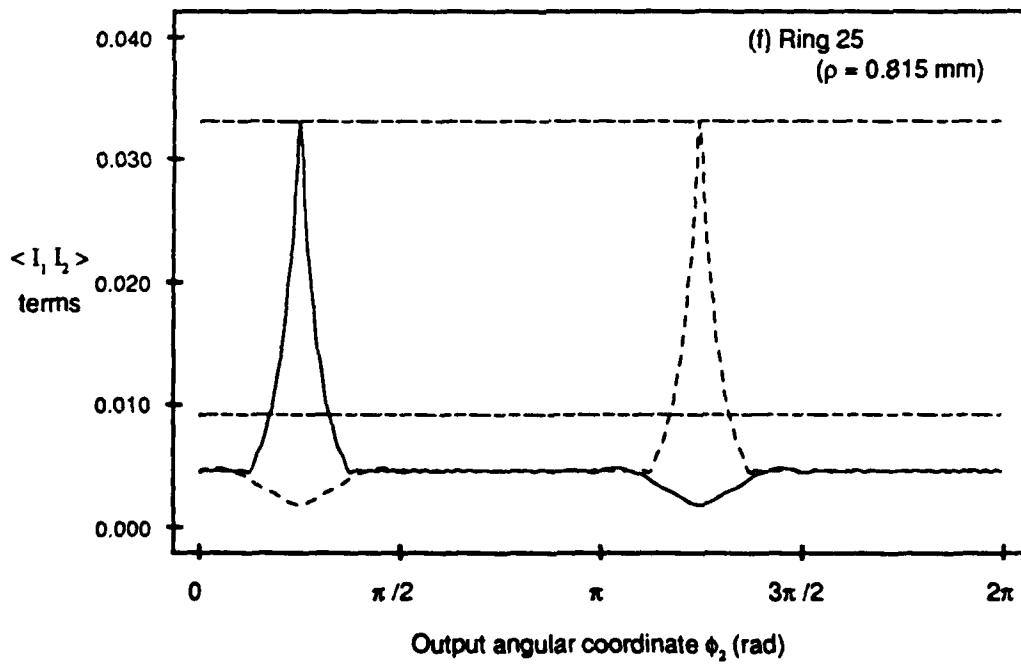
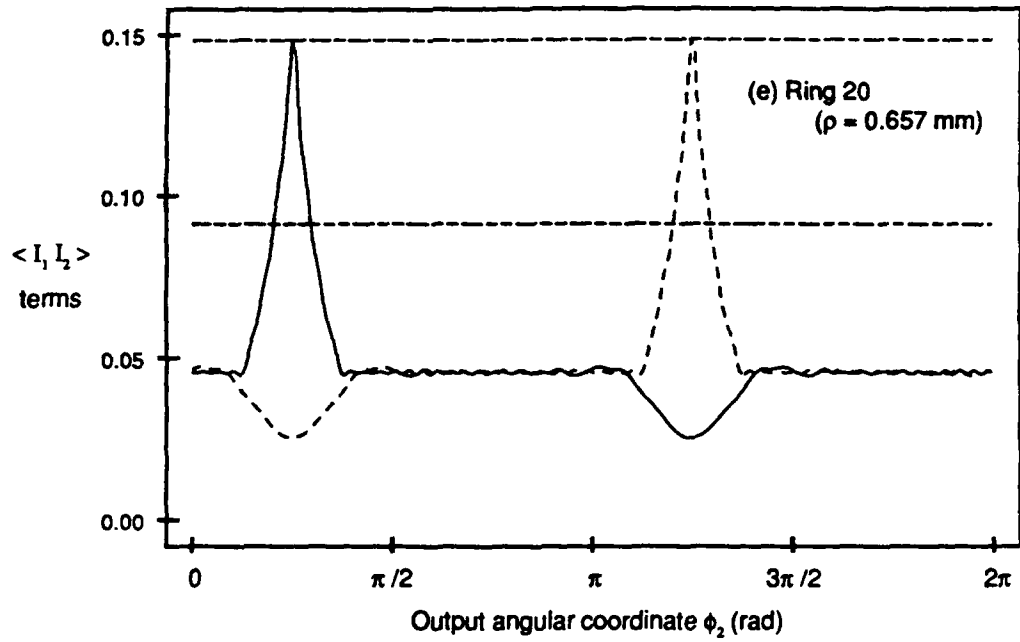


Fig. 4.3. (Continued) See legend on Fig. 4.3 (a).

We know that the peak intensity of the rings in the Airy diffraction pattern decreases rapidly as we move away from the center of the pattern, and we have seen the same behavior in the Fourier transform of the serrated circular aperture. Likewise, the magnitude of the two-point intensity moment will decrease as ρ increases; this is seen clearly in Fig. 4.3 (a) - (f), where we have not normalized these correlation functions. (We have carefully chosen our values of ρ to lie at ring maxima, avoiding the nulls in the pattern.)

As we look at these six plots, the most striking feature is the change in $|u_{12}|^2$ and $|u_{12}^\dagger|^2$. Close to the center of the transform, maxima are barely discernible at $\phi_2 = \phi_1$ in $|u_{12}|^2$ and at $\phi_2 = \phi_1 + \pi$ in $|u_{12}^\dagger|^2$. Figure 4.3 (a) alone shows no convincing evidence of the peaks seen in the subsequent plots. As we move away from the center of the transform, the ratio of the peak height to the background level increases. A second feature of interest is the dip in each term at the peak of the other. As ρ increases, the magnitude of this dip also increases (with respect to the background level), but not as quickly as the peak height. Thus this feature will only slightly reduce the peak height when the two terms are added.

As noted earlier, the term $\langle v_1 v_1^* \rangle \langle v_2 v_2^* \rangle$ follows the peaks of $|u_{12}|^2$ and $|u_{12}^\dagger|^2$, while $2\langle v_1 \rangle \langle v_1^* \rangle \langle v_2 \rangle \langle v_2^* \rangle$ drops off as the background level of $|u_{12}|^2$ and $|u_{12}^\dagger|^2$ decreases. This last term is approximately twice as large as the others at the second ring [Fig. 4.3 (a)], but decreases to be nearly equal to $\langle v_1 v_1^* \rangle \langle v_2 v_2^* \rangle$ at ring 15 [Fig. 4.3 (d)]. Out at ring 25, $2\langle v_1 \rangle \langle v_1^* \rangle \langle v_2 \rangle \langle v_2^* \rangle$ is still twice as great as the background on $|u_{12}|^2$ and $|u_{12}^\dagger|^2$, but lies well below the maxima of these terms, as seen in Fig. 4.3 (f).

When these four terms are combined as described by Eq. (4.3) to form $\langle I(\rho, \phi_1) I(\rho, \phi_2) \rangle$, the result will be a function with peaks at $\phi_2 = \phi_1$ and $\phi_2 = \phi_1 + \pi$. The background of $|u_{12}|^2$ and $|u_{12}^\dagger|^2$ will be removed by the subtraction of $2\langle v_1 \rangle \langle v_1^* \rangle \langle v_2 \rangle \langle v_2^* \rangle$; the peaks of $\langle I(\rho, \phi_1) I(\rho, \phi_2) \rangle$ will sit on a background level equal to $\langle v_1 v_1^* \rangle \langle v_2 v_2^* \rangle$. Although this background is equal to the peak value of $|u_{12}|^2$ and $|u_{12}^\dagger|^2$, we note that the peak-to-background ratio of $\langle I(\rho, \phi_1) I(\rho, \phi_2) \rangle$ is not unity for the following reasons. The background of $|u_{12}|^2 + |u_{12}^\dagger|^2$ has been subtracted, and the dips in $|u_{12}|^2$ and $|u_{12}^\dagger|^2$ decrease the peak of the sum.

The two-point moment $\langle I(\rho, \phi_1) I(\rho, \phi_2) \rangle$ is shown plotted in Fig. 4.4 for each of the cases included in Fig. 4.3. In these plots, we see the result of combining the four terms in Eq. (4.3): the peak-to-background ratio of $\langle I(\rho, \phi_1) I(\rho, \phi_2) \rangle$ increases as ρ increases. At the second diffraction ring, $\langle I(\rho, \phi_1) I(\rho, \phi_2) \rangle$ is nearly flat, as seen in Fig. 4.4 (a). We thus expect relatively small variations in the angular intensity distribution of this ring. As we look at subsequent plots, we are able to see the peak more clearly against the background; each plot is labeled with the peak-to-background ratio for reference. In these ratio calculations, we used our calculated value of $\langle v_1 v_1^* \rangle \langle v_2 v_2^* \rangle$ for the background. As this ratio increases, we expect to see more variations in the angular intensity distribution, leading first to fragmentation of the rings and eventually to a complete degradation of the ring structure. To examine these effects, we have taken a representative member of the ensemble and calculated the intensity against angle ϕ at each of these radius values. The results of these calculations are shown in Fig. 4.5.

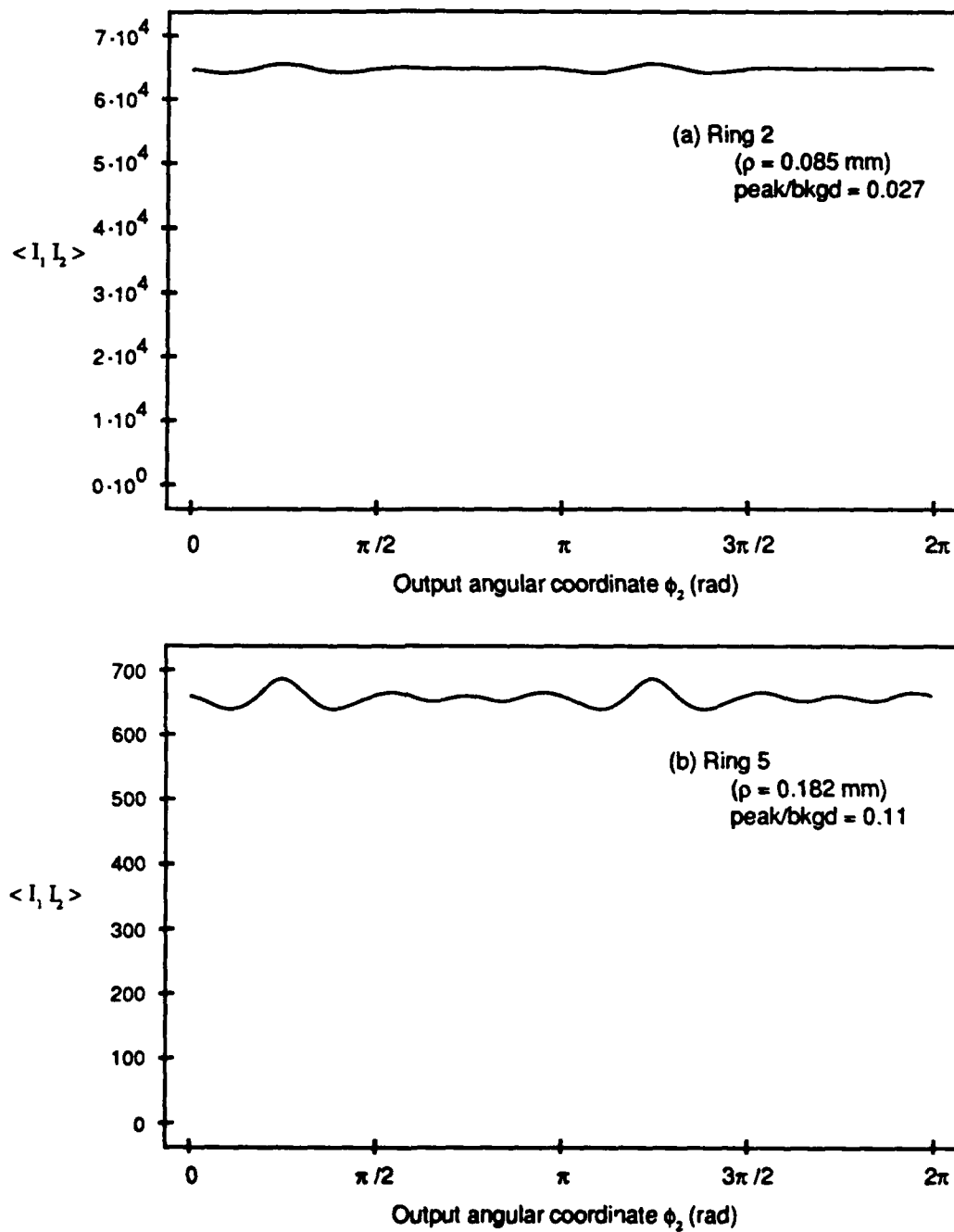


Fig. 4.4. Two-point intensity moment $\langle I_1, I_2 \rangle$, calculated for varied radius values as indicated. The output angular coordinate ϕ_1 is set to $\pi/4$ rad; the focal length is 500 mm, and the wavelength is $0.6328 \mu\text{m}$. For the aperture ensemble represented, the rms roughness is $75 \mu\text{m}$ on a 5.0 mm mean radius, the correlation angle is $\pi/8$ rad, and the correlation function is triangular. The peak-to-background ratio is included on each plot.

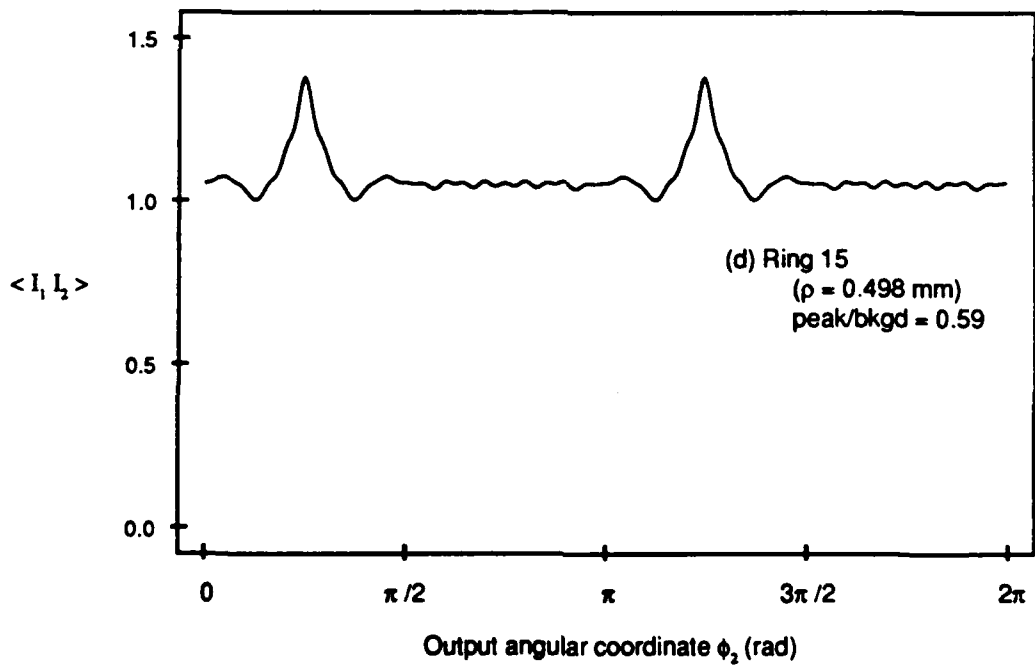
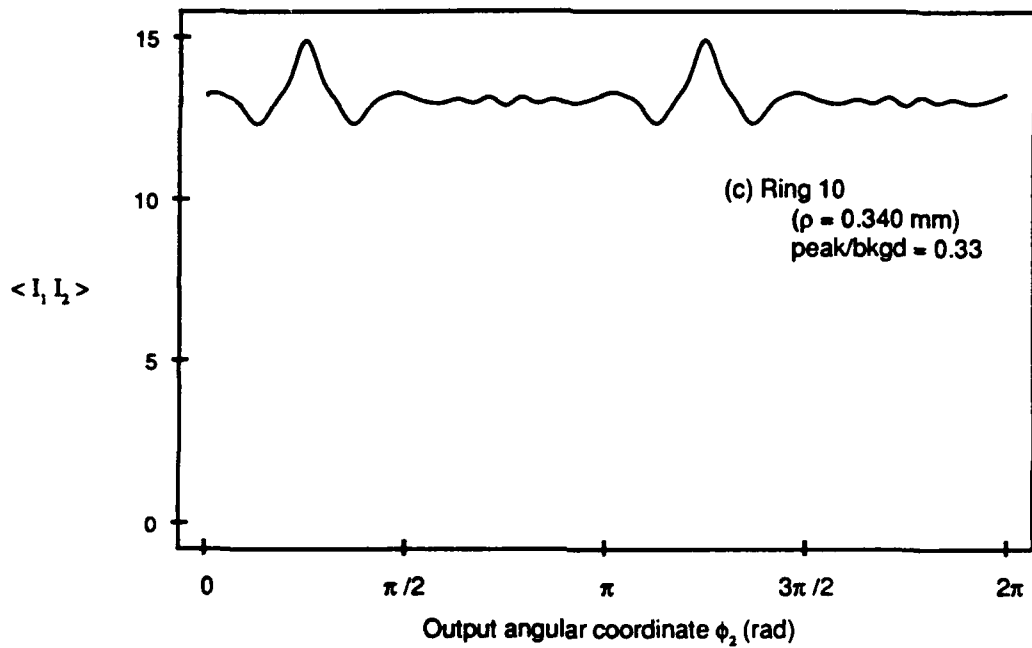


Fig. 4.4. (Continued)

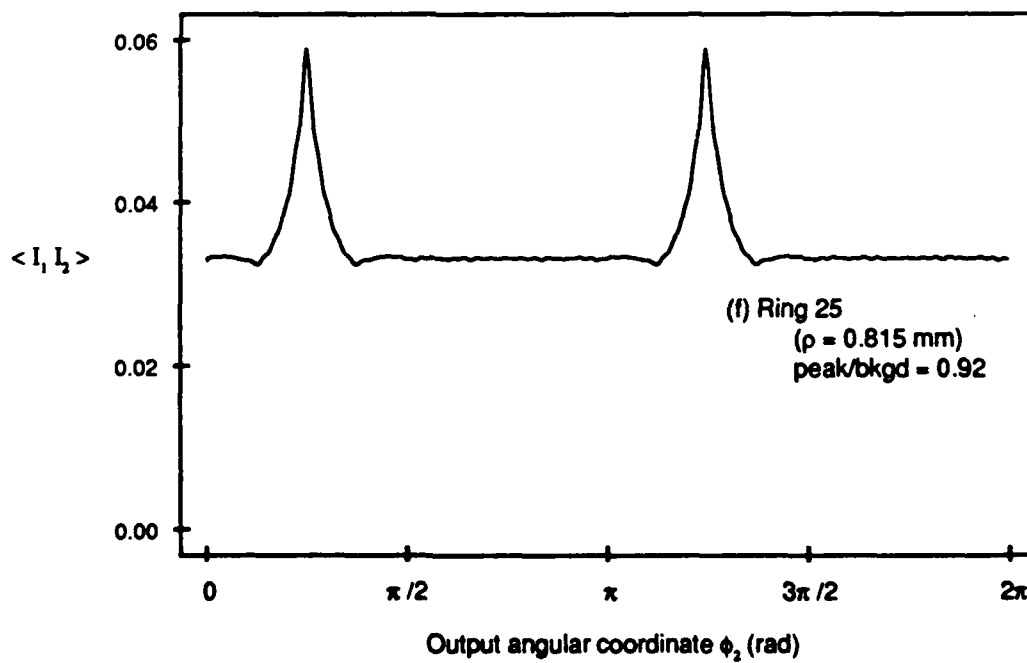
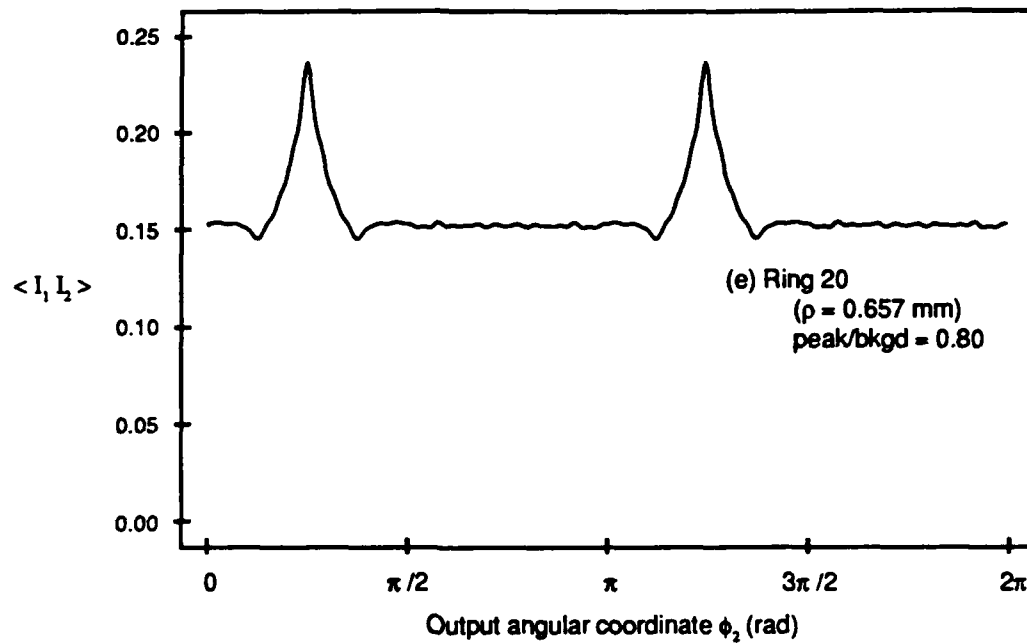


Fig. 4.4. (Continued)

In studying the plots of intensity versus angle shown in Fig. 4.5, we note two effects as the output radius increases. First, the number of local maxima that occur in 2π radians increases. In the diffraction pattern of this aperture, we therefore expect to see broad spikes that break into thinner spikes as the distance from the center of the pattern increases. This feature is associated with sharp-peaked correlation functions, as seen in Fig. 2.8. For comparison, we will present the results of similar intensity calculations for a Gaussian-correlated aperture in Fig. 4.6.

At this point, we also demonstrate a method for determining the number of spikes in an optical Fourier transform. First, we choose a value of the radius ρ at which to count the spikes; we choose ρ equal to 0.498 mm, which is ring 15 in our example. We then draw a horizontal line on the $I(\phi)$ versus ϕ plot at the mean value of the intensity and count the number of times the intensity curve crosses this line. Half of this number is the spike count. As can be seen in Fig. 4.5 (d), there are 16 spikes at the fifteenth ring of this transform. The results of this objective analysis agree with the number counted subjectively in the center diffraction pattern of Fig. 2.7, which is for an aperture with the same correlation angle, $A = \pi/8$ rad.

The second effect we note in the plots of Fig. 4.5 is an increase in the heights of the intensity variations. At ring 2, the intensity has a minimum value that is approximately $2/3$ of the maximum value. As ρ increases, this ratio decreases, and minima of nearly zero are seen beyond ring 20. This effect is what we call ring fragmentation: when the rings are no longer intact, the minimum intensity approaches zero (as for a null in the pattern) while the maximum intensity remains relatively large (as for a bright ring in the pattern).

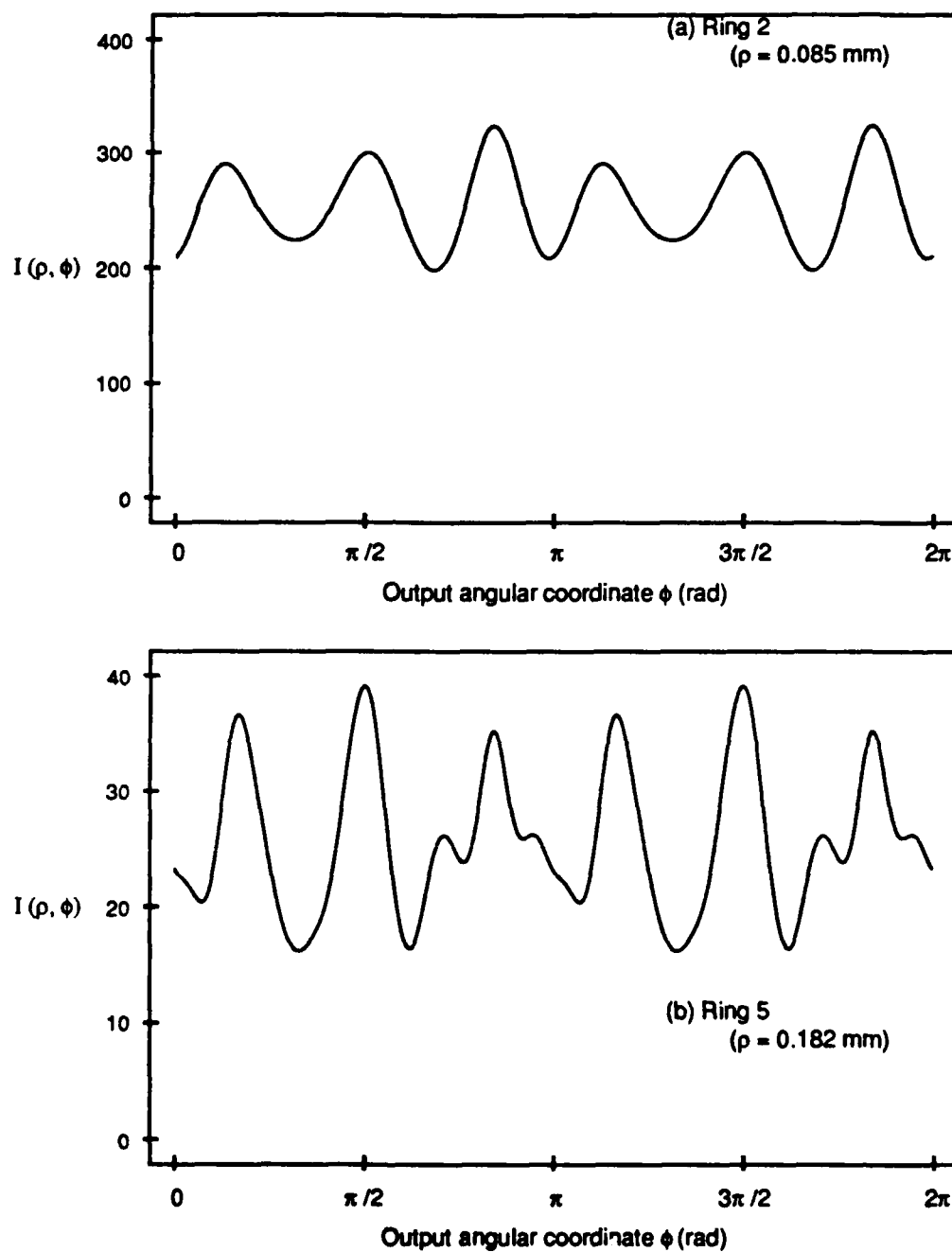


Fig. 4.5. Angular intensity distribution $I(\rho, \phi)$, calculated for a single aperture at different radius values as indicated. The focal length is 500 mm, and the wavelength is $0.6328 \mu\text{m}$. The aperture is taken from an ensemble with rms roughness $75 \mu\text{m}$, mean radius 5.0 mm, correlation angle $\pi/8$ rad, and a triangular correlation function. Each plot is labeled with the contrast value.

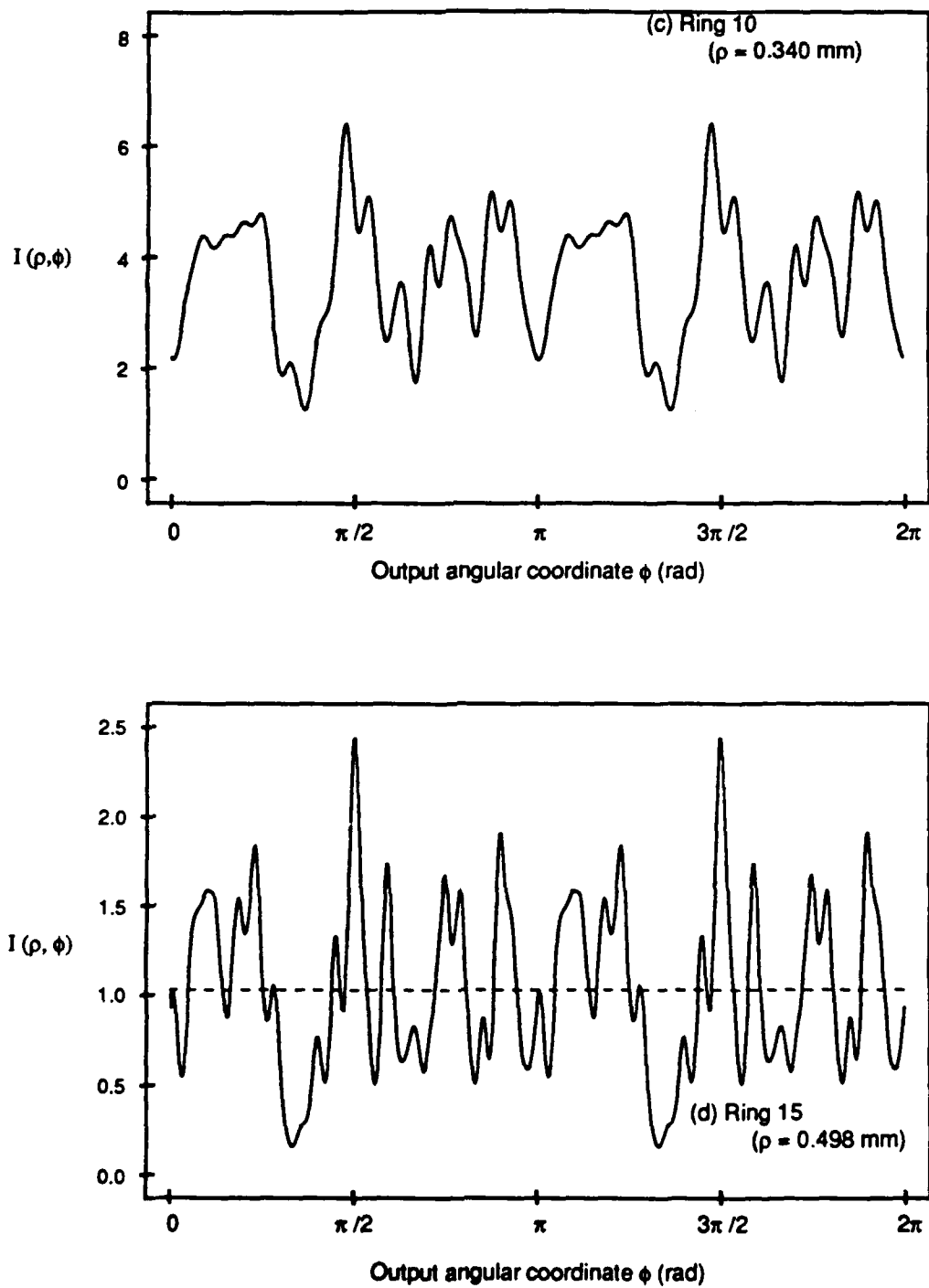


Fig. 4.5. (Continued) The dashed, horizontal line on (d) marks the mean intensity value and is used in counting the number of spikes.

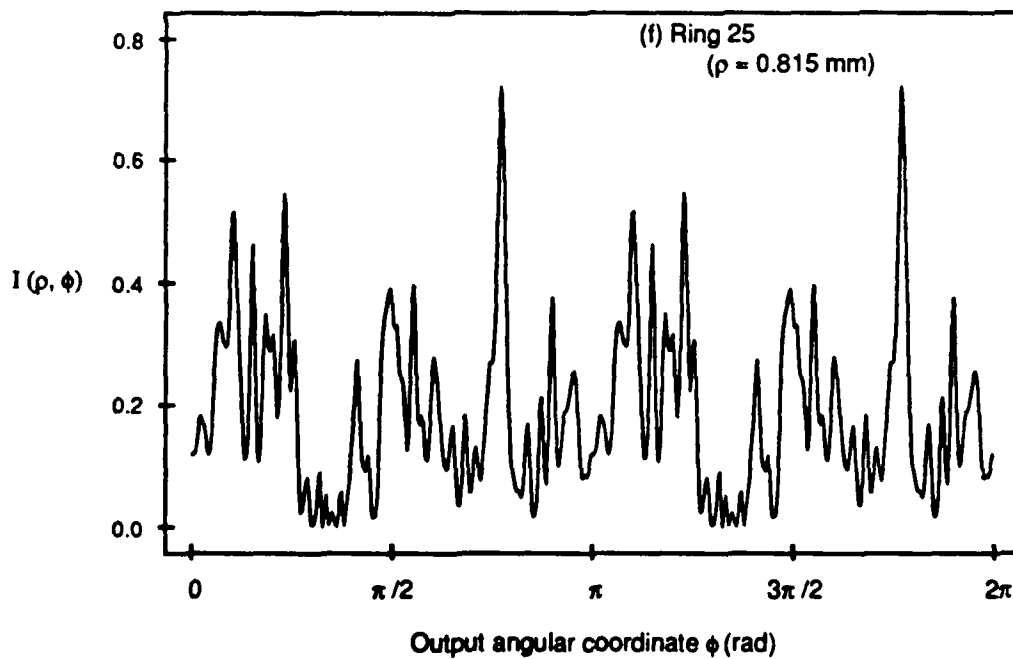
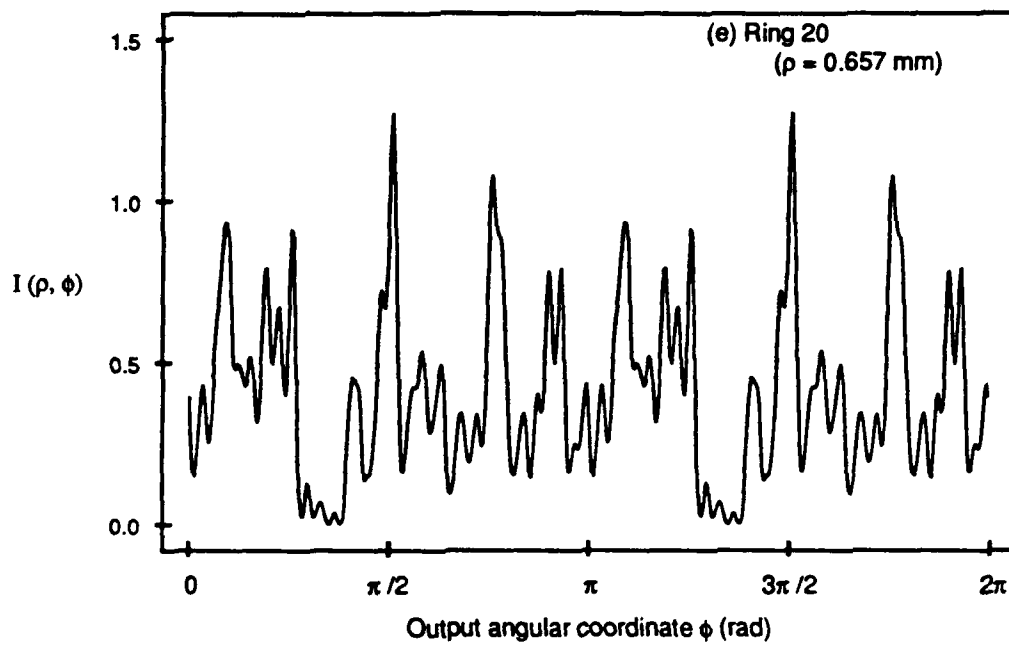


Fig. 4.5. (Continued)

The above discussion of spikes prompts us to look closely at the Fourier transform of a Gaussian-correlated aperture. We therefore calculate the angular intensity distribution $I(\rho, \phi)$ for an aperture with a Gaussian correlation function at the same six radius values and under the same system conditions. The mean radius, rms roughness, and correlation angle are also the same as for the calculations presented in Fig. 4.5. The plots of $I(\rho, \phi)$ versus ϕ are shown in Fig. 4.6. At the inner rings (2 and 5, here), there is only a slight difference between the transforms of the triangular- and Gaussian-correlated apertures. As the radius ρ increases, we note that the triangular aperture correlation has produced an intensity distribution with more local maxima. Although there is still a close correspondence between the spikes in the two transforms at the fifteenth ring, as shown in Fig. 4.5 (d) and Fig. 4.6 (d), the transform of the triangular-correlated aperture is beginning to show further division in the spikes. We note that the spike count for the Gaussian-correlated aperture is 12 at this ring, compared to 16 counted for the case of triangular correlation. Out at ring 25, the difference between the two transforms is quite pronounced; the transform of the Gaussian-correlated aperture, Fig. 4.6 (f), has broader (and many fewer) spikes than that of the triangular-correlated aperture, Fig. 4.5 (f). These observations show in greater detail the difference in the character of the transform spikes under different aperture correlation function conditions, as was demonstrated by the two-dimensional Fourier transforms shown in Fig. 2.8.

4.4.1. Aperture Roughness

We now consider the effects of variations in aperture roughness on the behavior of μ_{12} . We note that in terms T_1 , T_2 , and T_3 [Eqs. (4.46) - (4.48)] the standard deviation of the roughness, σ , only occurs in the products $\sigma\alpha_1'$ and $\sigma\alpha_2''$. Recalling the

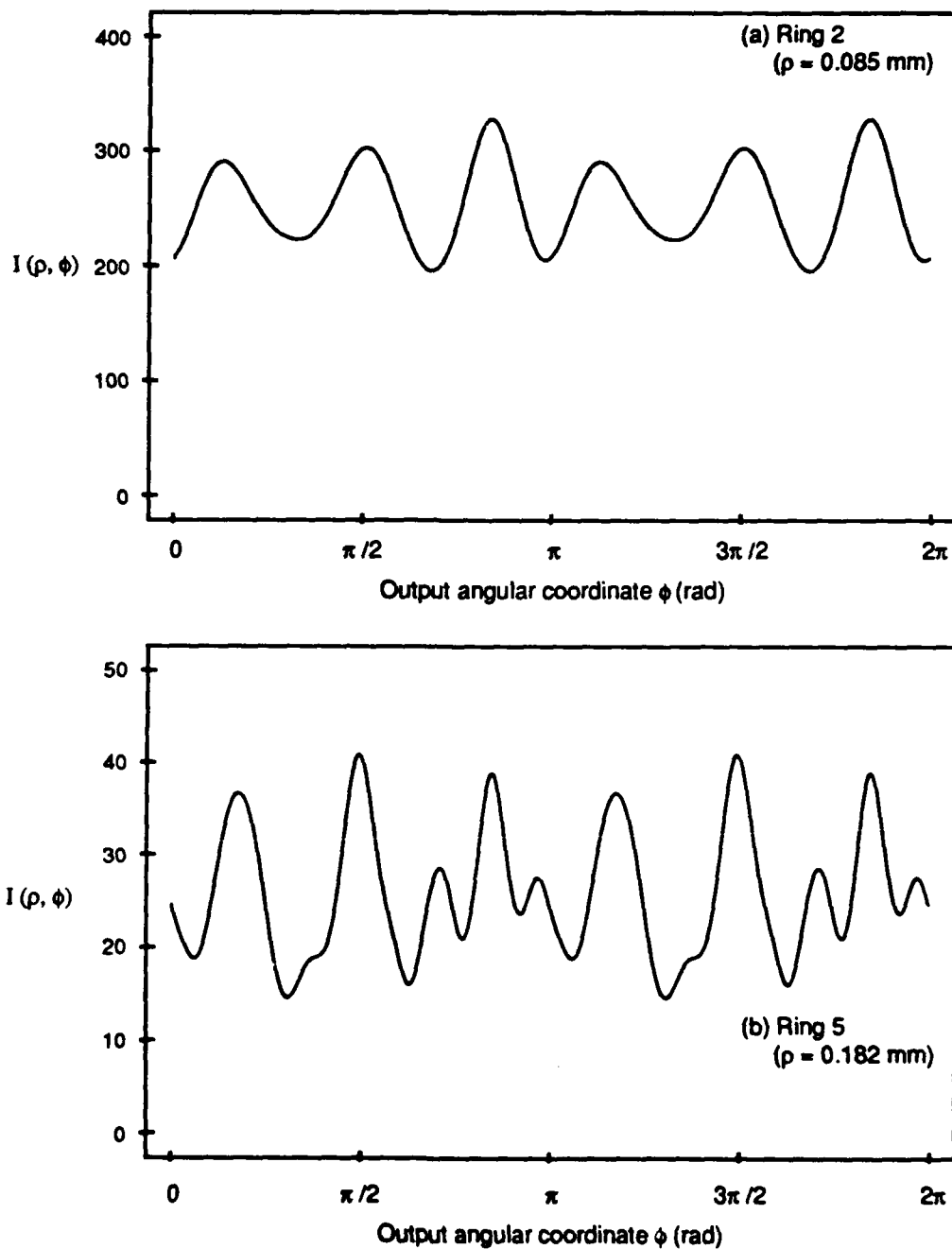


Fig. 4.6. Angular intensity distribution $I(\rho, \phi)$, calculated for a single, Gaussian-correlated aperture at different radius values as indicated. The system focal length is 500 mm, and the wavelength is $0.6328 \mu\text{m}$. The aperture is taken from an ensemble with rms roughness $75 \mu\text{m}$, mean radius 5.0 mm, and correlation angle $\pi/8$ rad.

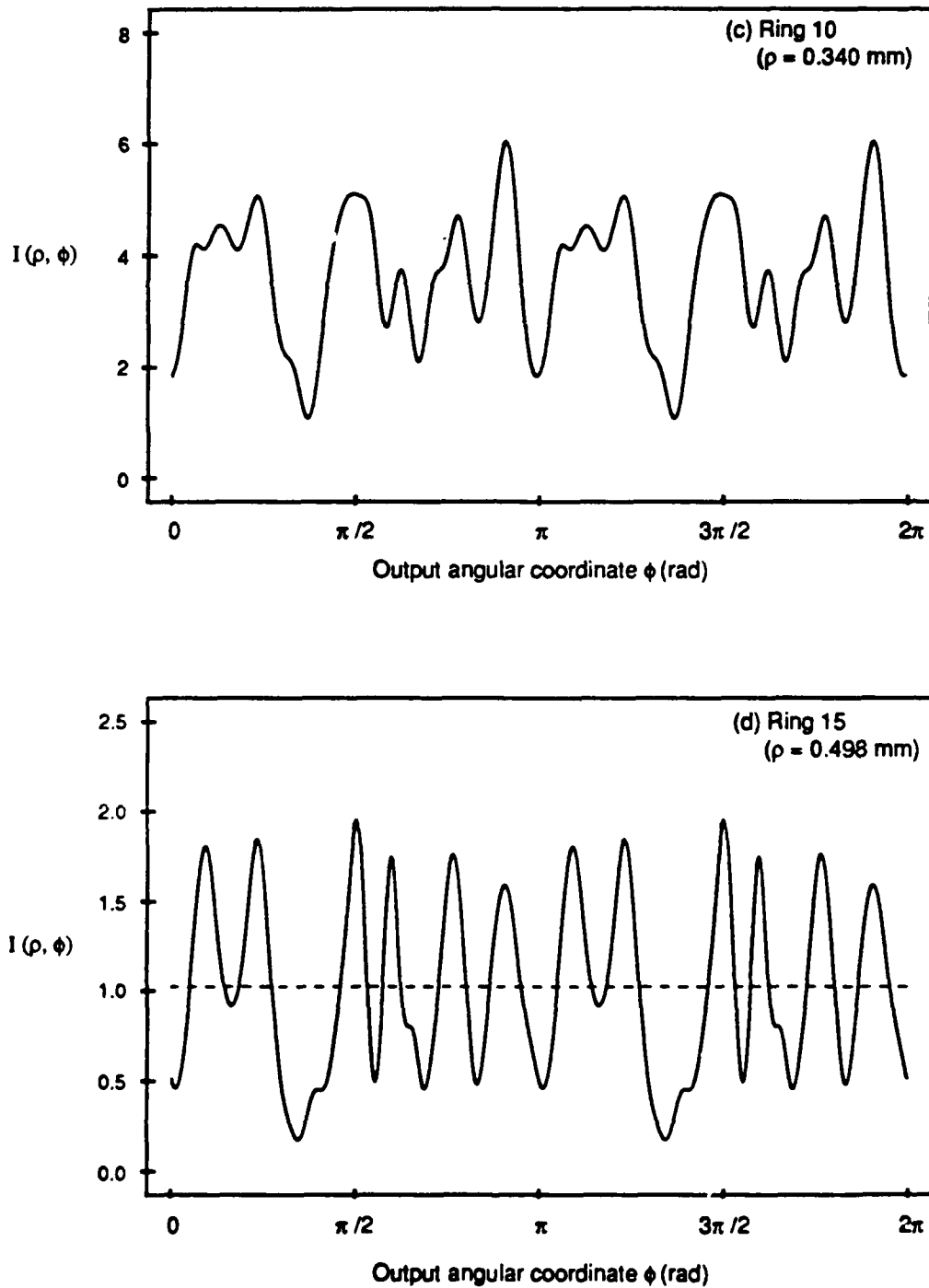


Fig. 4.6. (Continued) The mean value is marked with a dashed, horizontal line on (d) for use in determining the number of spikes.

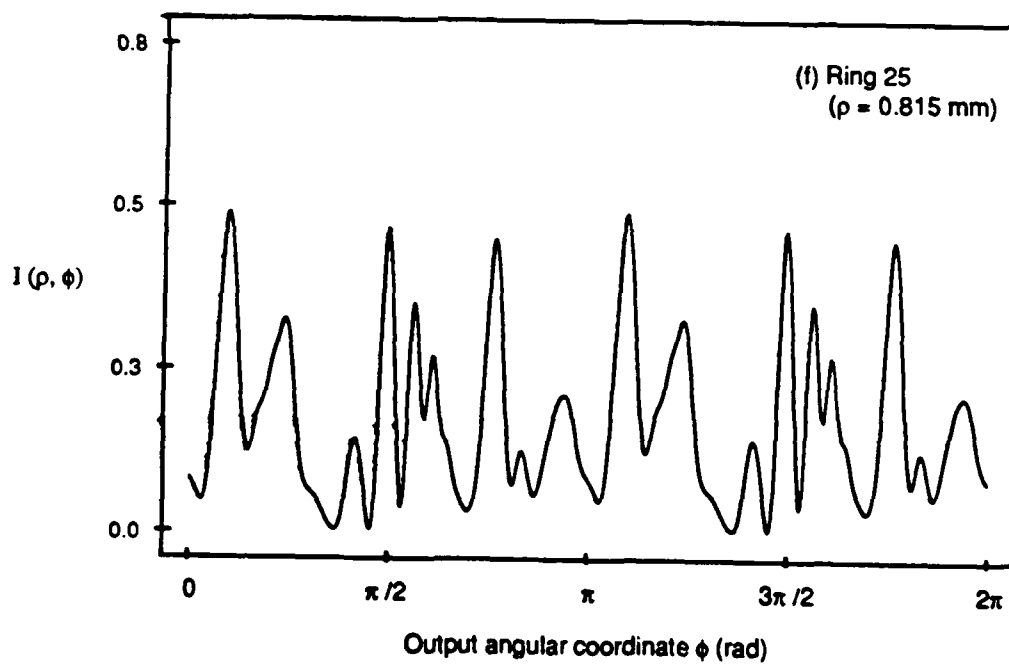
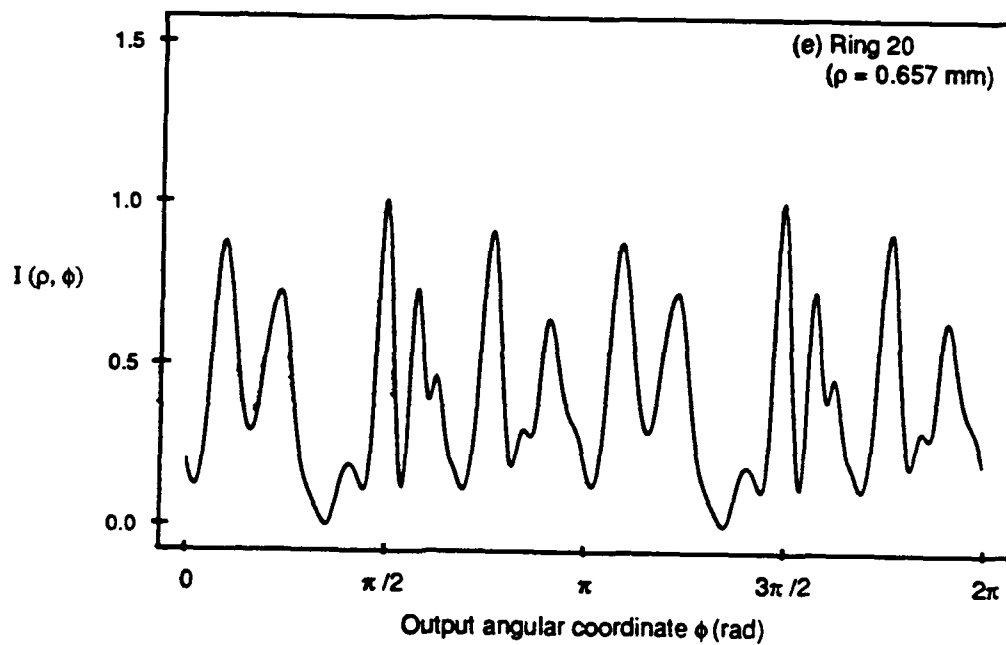


Fig. 4.6. (Continued)

definitions of κ_1' and κ_2'' ,

$$\kappa_1' = \frac{k_1 \rho_1}{z_0} \cos(\alpha' - \phi_1), \quad \kappa_2'' = \frac{k_2 \rho_2}{z_0} \cos(\alpha' - \phi_2), \quad (4.51)$$

we see that for fixed values of k_1 , k_2 , and z_0 (i.e., for fixed wavelengths and focal length), holding the quantities $\sigma\rho_1$ and $\sigma\rho_2$ constant will yield basically the same functional form for μ_{12} , since the significant terms would not change except over integration and observation angles.

When we take a pattern recognition approach to the analysis of the Fourier transform, we look for transform features that can be related to the degree of aperture serration. In this study, we have chosen ring fragmentation as the roughness-related feature, since the radius of the first broken transform ring decreases as the aperture roughness increases (see Fig. 2.6). From the discussion of terms T_1 , T_2 , and T_3 in the preceding paragraph, we would expect the radius ρ_f of the first fragmented ring to be such that $\sigma\rho_f$ is constant over the set of apertures. This is apparent from our expression for μ_{12} , but we would also like to understand this through a more physically intuitive method. Thus, we consider Fresnel zones¹³.

4.4.2. Fresnel Zones of the Aperture

In the next few paragraphs for the discussion of Fresnel zones of the aperture, it is simpler algebraically to use a Cartesian coordinate system. In Fig. 2.1, we have shown overlaid both the Cartesian and cylindrical coordinates for the optical system. Now, in Fig 4.7 consider two points in the aperture, $P_1(x_1, y_1, 0)$ and $P_2(x_2, y_2, 0)$, and an observation point on the ξ axis, $P_0(\rho_f, 0, z_0)$, all described in Cartesian coordinates. (Choosing P_0 on the ξ axis simplifies the algebra without loss of generality.) We define R_1

and R_2 as the distances from points P_1 and P_2 to the observation point P_o , respectively. In the aperture, we have a wavefront converging to the on-axis point in the observation plane. The phase of the light arriving from point P_1 at P_o is the phase in the aperture plus the phase change due to propagation and is given by:

$$\Phi_1 = \frac{-\pi}{\lambda z_0} (x_1^2 + y_1^2) + \frac{2\pi}{\lambda} R_1 ; \quad (4.52)$$

an analogous expression defines phase Φ_2 , corresponding to point P_2 . We are interested in the phase difference at P_o between light from points P_1 and P_2 . In the paraxial regime, *i.e.*, when the condition $(x_i - \rho_f)^2 + (y_i)^2 \ll z_0^2$, $i = 1, 2$, is met, we can approximate distances R_1 and R_2 :

$$R_i \approx z_0 + \frac{(x_i - \rho_f)^2 + y_i^2}{2z_0} , \quad (4.53)$$

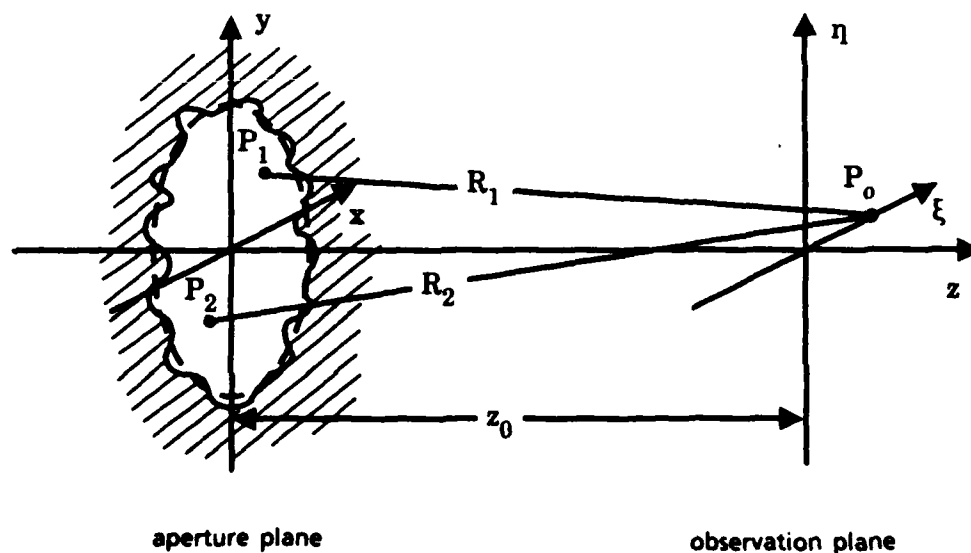


Fig. 4.7. Coordinate system for Fresnel zone analysis.

and similarly for R_2 . The phase difference $\Phi_2 - \Phi_1$ is then given approximately by:

$$\Phi_2 - \Phi_1 \approx \frac{\pi}{\lambda z_0} 2 \rho_f (x_1 - x_2) . \quad (4.54)$$

A Fresnel zone in the aperture is defined by the boundaries of the zone, which are equiphase lines with respect to point P_0 . The phases on the two boundaries differ by π . If our aperture points P_1 and P_2 are chosen to lie on opposite boundaries of a single zone, we can use Eq. (4.54) to determine the zone width, d_z :

$$d_z = |x_1 - x_2| = \frac{\lambda z_0}{2 \rho_f} . \quad (4.55)$$

The zone boundaries are perpendicular to the direction of displacement of point P_0 ; in the case described, the boundaries are parallel to the y-axis.

For this investigation, we ask the following question. How many standard deviations of the aperture roughness should fit into one Fresnel zone at the aperture edge in order to produce ring fragmentation? We assume this number of standard deviations, denoted by n , to be constant. As roughness increases, ρ_f , the value of radial output coordinate ρ which corresponds to the first fragmented ring, will decrease because the aperture deviates more from the smooth, circular aperture; this is consistent with our hypothesis that the quantity $\rho \rho_f$ will be constant for a series of apertures with varied roughness. Eq. (4.55) shows that a decrease in ρ_f corresponds to an increase in the associated Fresnel zone width. By speculating that n is constant, we are assuming that this increase in the zone width corresponding to ρ_f is proportional to the increase in the roughness. Thus, in Eq. (4.55) we set d_z equal to $n \sigma$ and find the following expression for n :

$$n = \frac{\lambda z_0}{2 \sigma \rho_f} \quad (4.56)$$

If we can verify that n is constant for apertures with varying roughness, we will have shown that $\sigma \rho_f$ is constant, as expected from examination of μ_{12} as expressed in Eq. (4.32). Thus, the prediction based in our integral expression would be substantiated. This is one of our basic objectives in the experiments to be described in Chapter 6.

To further study the effects of changing the aperture roughness, we now repeat our earlier calculations of $\langle I(\rho, \phi_1) I(\rho, \phi_2) \rangle$ for aperture ensembles of varied rms roughness. We choose one output radius value ($\rho = 0.498$ mm, the fifteenth ring) and calculate $\langle I(\rho, \phi_1) I(\rho, \phi_2) \rangle$ as ϕ_2 varies for ensembles with a large range of roughness values. We keep the remaining aperture parameters at the same values as in Figs. 4.3 through 4.5: each aperture ensemble has a mean radius a of 5.0 mm, a triangular correlation function, and a correlation angle A equal to $\pi/8$ rad. For the optical system, the focal length z_0 is equal to 500 mm, the wavelength λ is 0.6328 μm , and the fixed output angle ϕ_1 is $\pi/4$ rad. We calculated $\langle I(\rho, \phi_1) I(\rho, \phi_2) \rangle$ for ϕ_2 in the range $[0, 2\pi]$, using five aperture ensembles with rms roughnesses of 25, 50, 75, 100, and 125 μm . The results of these calculations are presented in the plot in Fig. 4.8. Two effects are seen here. First, as the roughness increases, the background decreases. We recall that the output radius is constant for this set of curves and that the background of $\langle I(\rho, \phi_1) I(\rho, \phi_2) \rangle$ is $\langle v_1 v_1^* \rangle \langle v_2 v_2^* \rangle$, or $\langle I(\rho, \phi_1) \rangle \langle I(\rho, \phi_2) \rangle$. We conclude that, at a fixed radius in the transform plane, the mean intensity decreases when the roughness increases. At the same time, the correlation peak grows taller, indicating a decrease in the uniformity of the ring intensity. From these two observations, we conclude that the ring we are observing is becoming fragmented, and plots of the calculated intensity $I(\rho, \phi)$ versus angle ϕ confirm this conclusion. These plots are shown

in Fig. 4.9. An interesting feature of these plots is the consistency in the shape of the angular intensity curve as the aperture roughness changes, similar to the effect seen on the apertures shown in Fig. 2.3. We also point out that each curve is drawn on the same scale. As the aperture roughness increases, the minimum value of the intensity decreases. As stated earlier in connection with the plot series in which ρ increases, this decrease in the intensity minimum while significant maxima are still observed is ring fragmentation.

4.4.3. Correlation Angle of the Aperture Serration

The second aperture parameter we investigate is the correlation angle in the function $r_g(\alpha'' - \alpha')$ of Eq. (4.28). Returning to Eq. (4.32), we note first that the integrand is identically zero when $r_g(\alpha'' - \alpha')$ is zero. Furthermore, two of the significant terms in the integrand, namely T_2 and T_3 , depend on the correlation function $r_g(\alpha'' - \alpha')$. These two terms are defined in Eqs. (4.47) and (4.48). The maximum values of these terms occur when $r_g(\alpha'' - \alpha')$ is equal to one and generally decrease as the correlation function decreases. We note that the cosine dependence of κ_1' and κ_2'' may prevent these terms from displaying simple decreasing behavior as $r_g(\alpha'' - \alpha')$ decreases; however, these terms will broaden with an increase in the correlation angle. Thus the correlation angle, which determines the width of $r_g(\alpha'' - \alpha')$, also determines the width of these significant exponential terms and the non-zero range of the integrand.

The remaining exponential term, T_1 of Eq. (4.46), peaks when κ_1' and κ_2'' are equal; the location of these peaks is a function of both the output coordinates and the integration variables. Since this exponential is independent of $r_g(\alpha'' - \alpha')$, changing the correlation angle will not affect it. However, increasing the correlation angle will result in greater overlap of the r_g -dependent and r_g -independent terms in the integrand, resulting in a larger range of output point pairs which show a significant correlation. Essentially,

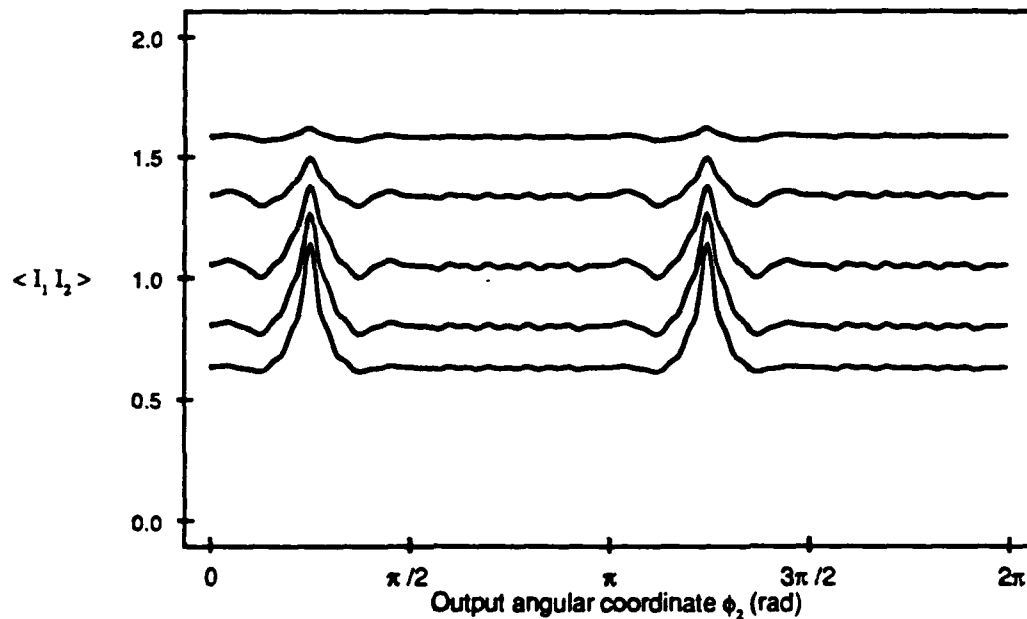


Fig. 4.8. Two-point intensity moment versus output angle ϕ_2 for aperture ensembles of varied rms roughness: (top to bottom) 25, 50, 75, 100, and 125 μm . For each ensemble, the mean radius is 5.0 mm, the correlation function is triangular, and the correlation angle is $\pi/8$ rad. The fixed output coordinates are $\rho_1 = \rho_2 = 0.498$ mm and $\phi_1 = \pi/4$ rad. The wavelength is 0.6328 μm ; the focal length, 500 mm.

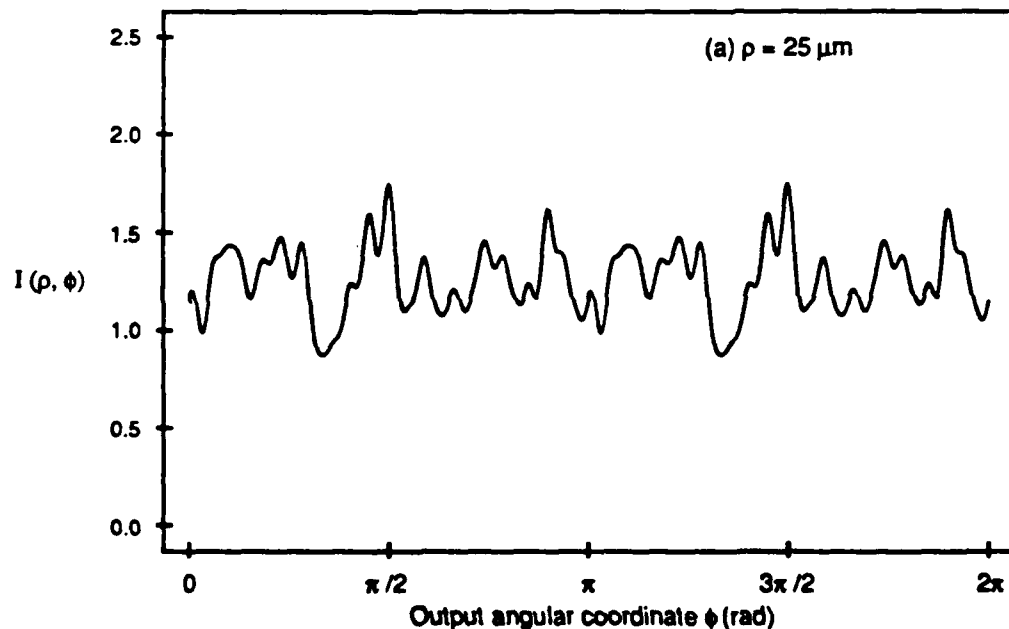


Fig. 4.9. Calculated intensity for individual apertures from ensembles of varied rms roughness, as indicated. The remaining aperture and system parameters are as described for Fig. 4.7. The contrast value is included on each plot for reference.

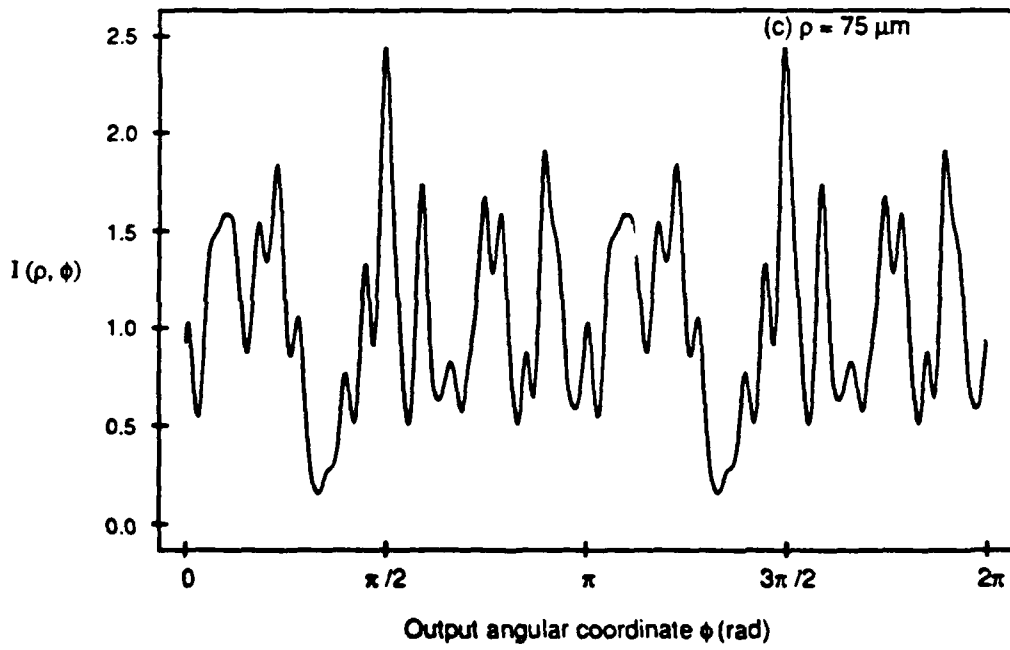
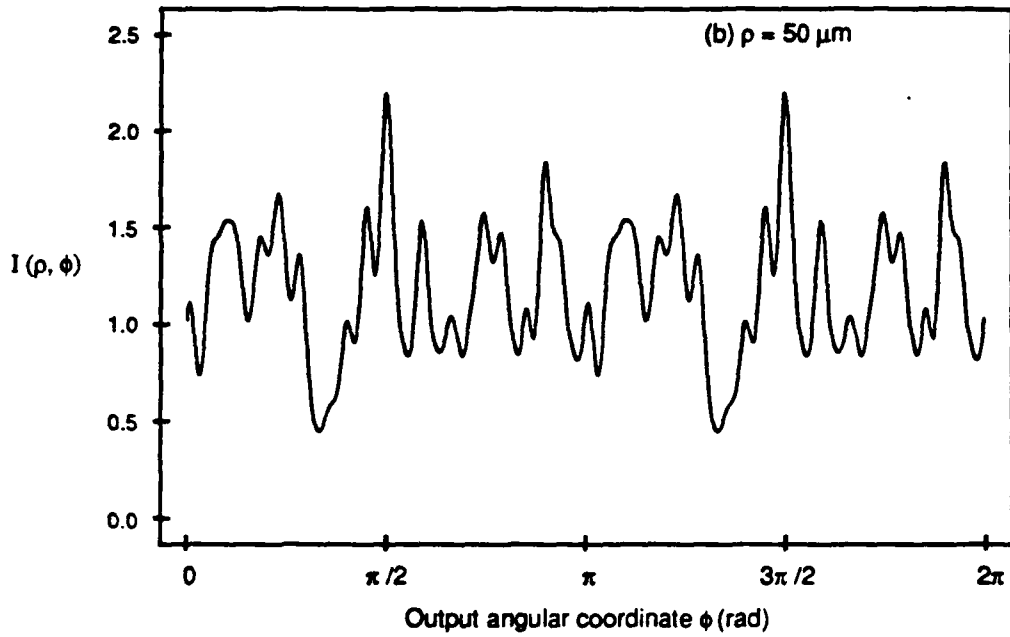


Fig. 4.9. (Continued)

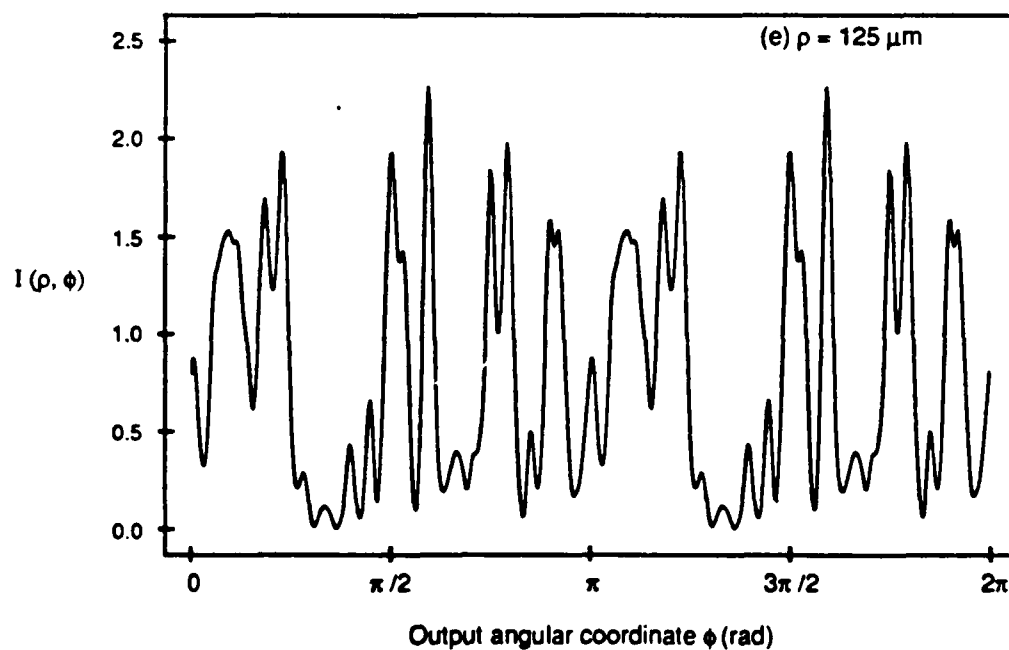
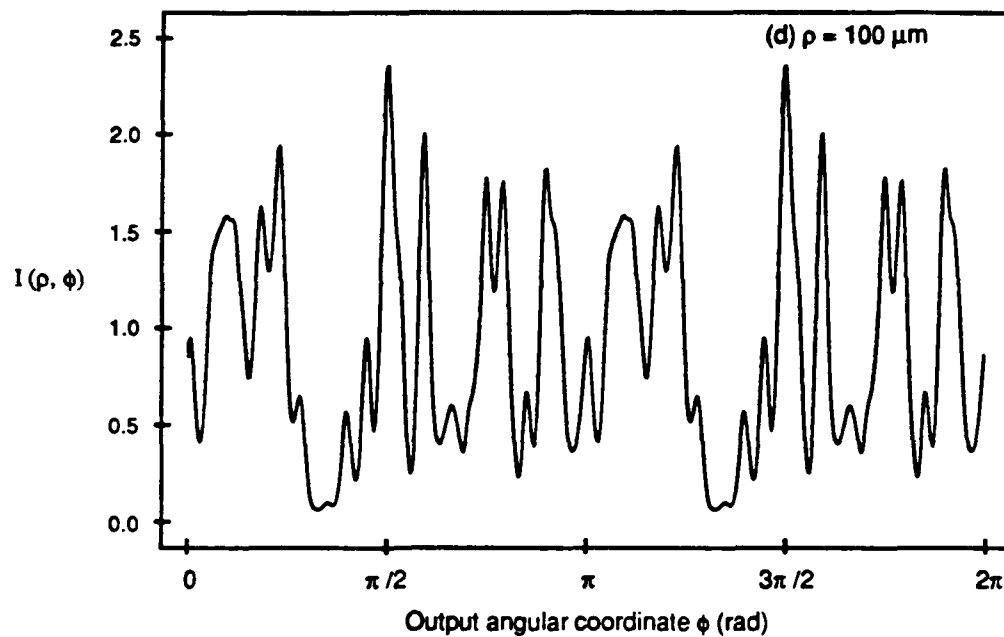


Fig. 4.9. (Continued)

increasing the correlation angle of the serration will increase the correlation angle of the diffracted field. With the following illustrative calculations, we will show that an increase in the transform correlation angle will decrease the number of spikes in the transform. This is also demonstrated by the computer simulation in two dimensions, as shown in Fig. 2.7.

For these calculations of the two-point intensity moment $\langle I(\rho, \phi_1) I(\rho, \phi_2) \rangle$, we have chosen aperture ensembles with three different values of the aperture correlation angle: $\pi/16$, $\pi/8$, and $\pi/4$ rad. The rms roughness of each aperture ensemble is $75 \mu\text{m}$, and the remaining aperture and system parameters are chosen as in the calculations for Figs. 4.8 and 4.9. In Fig. 4.10, we can clearly see that, as predicted, the width of the peak in $\langle I(\rho, \phi_1) I(\rho, \phi_2) \rangle$ increases as the correlation angle of the aperture serration increases. We expect this increase in the peak width to correspond to a decrease in the number of transform spikes; this is the effect seen in the calculated transform patterns shown in Fig. 2.7. To investigate this relationship in greater detail, we plot the transform intensity $I(\rho, \phi)$ against the output angular coordinate ϕ at a fixed output radius for one representative aperture from each ensemble; these plots are shown in Fig. 4.11. Each of these intensity curves is plotted on the same scale.

The number of spikes at this radius in each of these transforms is determined as described for Fig. 4.5(d). The count yields the following values: for A equal to $\pi/16$ rad, 18 spikes; for $\pi/8$ rad, 16 spikes; for $\pi/4$ rad, 16 spikes. One could argue that 18 spikes can be counted in Fig. 4.11 (b), since in addition to the 16 spikes noted the curve touches the dashed line twice. One could even push the point and claim that these "touches" should each count as half a spike, giving a count of 17 that lies neatly between the 18 and 16

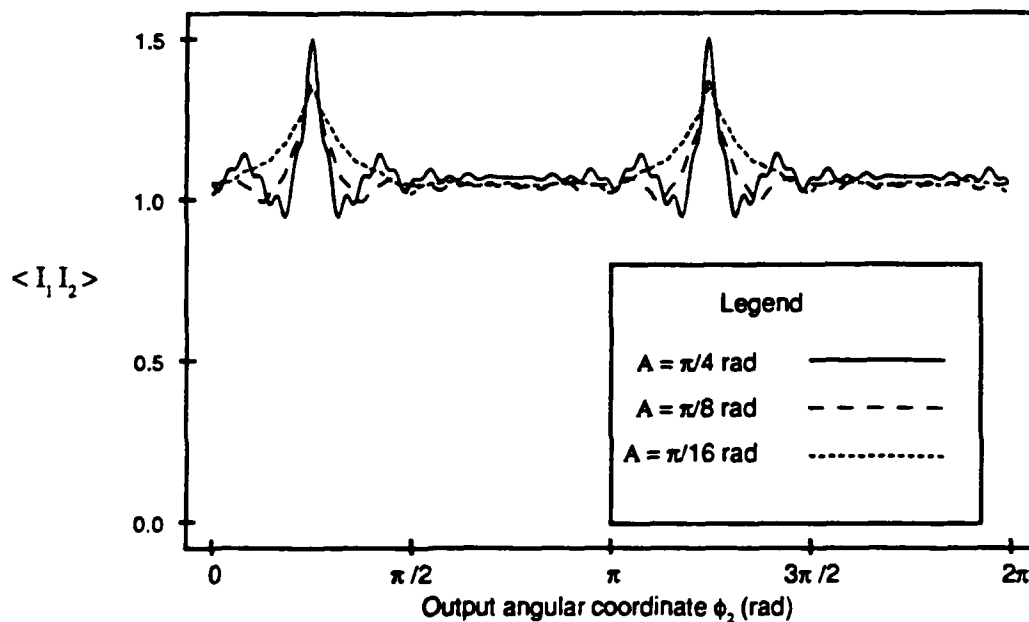


Fig. 4.10. Calculated two-point intensity moment $\langle I_1 I_2 \rangle$ for aperture ensembles of varied correlation angle A . Each aperture ensemble has $75 \mu\text{m}$ rms roughness, 5.0 mm mean radius, and the triangular correlation function. The system focal length is 500 mm , the wavelength, $0.6328 \mu\text{m}$. The fixed output angle is $\phi_1 = \pi/4$ rad and the fixed output radius is 0.498 mm , corresponding to ring 15 in the transform.

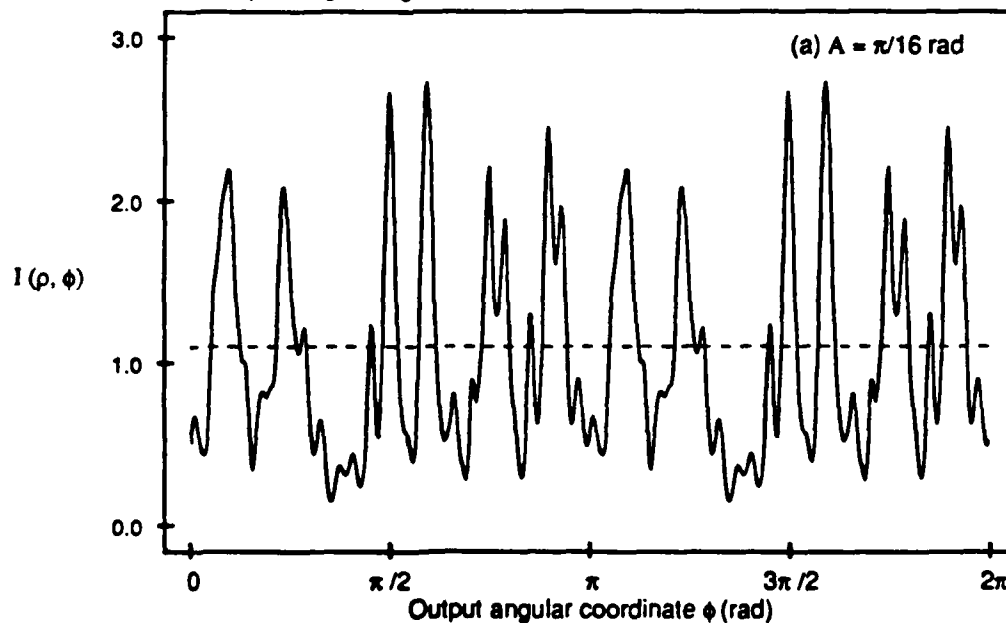


Fig. 4.11. Calculated intensity for individual apertures from ensembles with different correlation angles A , as indicated. The remaining aperture and system parameters are as described for Fig. 4.10. The dashed, horizontal lines on each plot mark the mean intensity values and are used in finding the number of transform spikes.

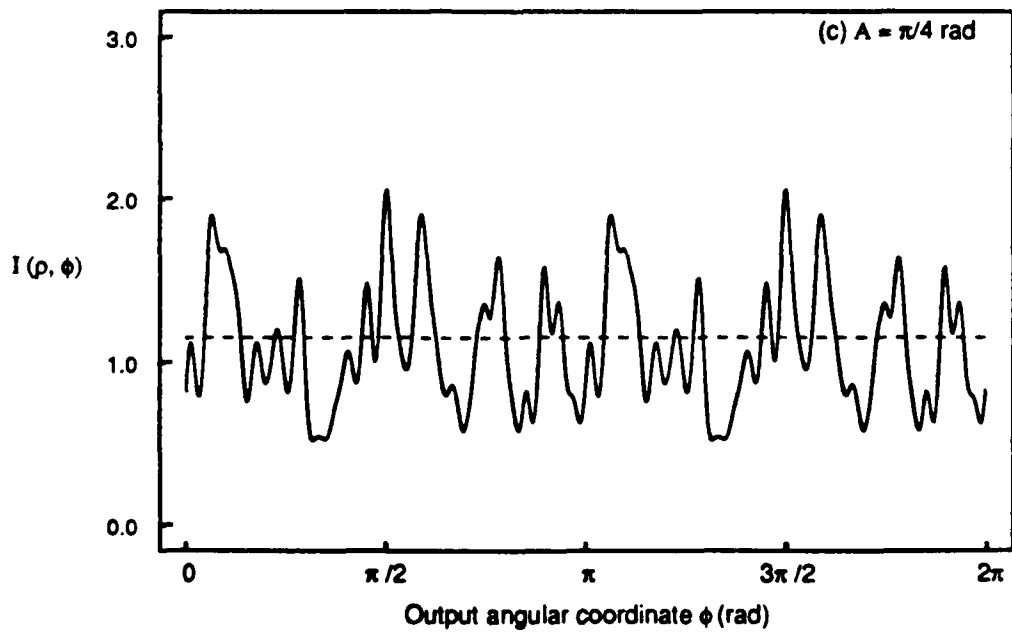
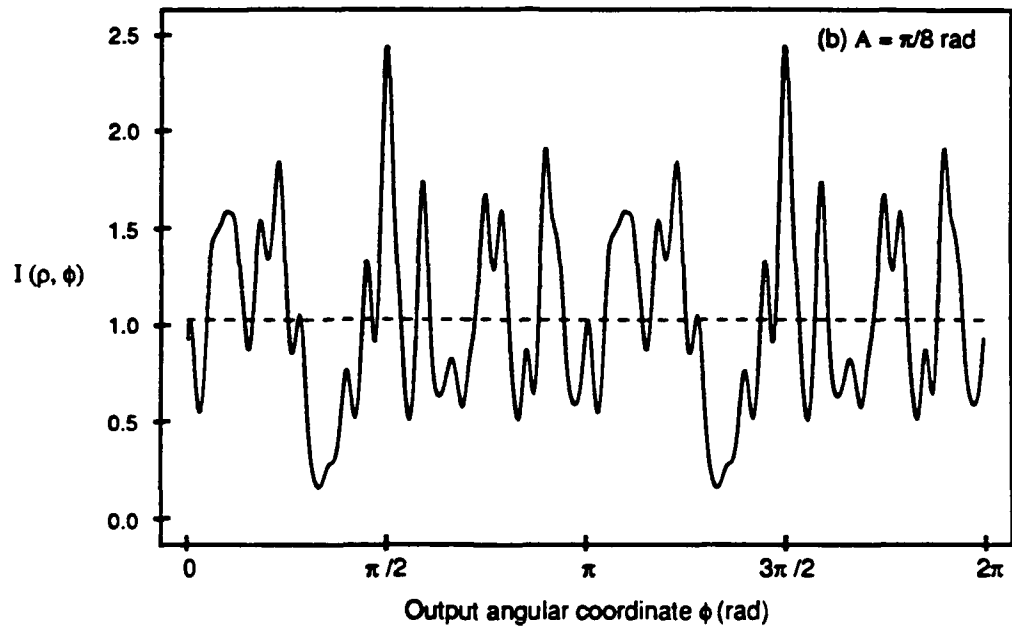


Fig. 4.11. (Continued)

spikes in (a) and (c). We prefer, however, to note that this is only one aperture and caution against expecting (and forcing) complete agreement between an individual set of apertures and the conclusions drawn from our ensemble expected value $\langle I(\rho, \phi_1) I(\rho, \phi_2) \rangle$. A more significant point to be made is that the number of spikes increases as the aperture correlation angle increases, but does not do so proportionately; doubling the aperture correlation angle does not double the number of spikes. In Chapter 6, we will discuss experiments designed to investigate and support these observations further.

4.4.4. Correlation Function of the Aperture Serration

The third aperture parameter of interest is the shape of the correlation function, $r_g(\alpha'' - \alpha')$ in Eq. (4.28). We recall that the significant correlation-function-dependent terms in Eq. (4.32) are T_2 and T_3 ; the functional form of $r_g(\alpha'' - \alpha')$ will largely determine the shapes of these terms. If $r_g(\alpha'' - \alpha')$ has a smooth peak, these exponentials will have smoother peaks than if $r_g(\alpha'' - \alpha')$ were a sharp-peaked function. The shape of terms T_2 and T_3 will significantly affect the shape of μ_{12} ; we expect a smooth-peaked serration correlation function to produce a smooth-peaked field correlation function. Visually, the shape of the correlation function will affect the appearance of the transform spikes, as was seen in the results of our computer simulation of the transform, shown in Fig. 2.8. Experimental results described in Chapter 6 will also support this relationship between the correlation functions of the serration and of the transform. We look now at the results of computer simulations of $\langle I(\rho_1, \phi_1) I(\rho_2, \phi_2) \rangle$ and of $I(\rho, \phi)$ that demonstrate this feature.

In this final set of computer calculations of $\langle I(\rho_1, \phi_1) I(\rho_2, \phi_2) \rangle$, we again use this two-point moment as an angular correlation. We have calculated

$\langle I(\rho, \phi_1) I(\rho, \phi_2) \rangle$ versus ϕ_2 for three correlation functions of the serration: Gaussian, Eq. (3.41); triangular, Eq. (3.42); and Eiffel, Eq. (3.43), with β equal to 0.5. The resulting plots are shown in Fig. 4.12. In this figure, we include a detail plot of the peak region, where we note that the three aperture correlation functions produce different intensity correlations with slightly different peak heights and widths. (The correlation angle of each aperture ensemble is defined in accord with the equal-area condition described in Section 3.4.3.) The peak shape of $\langle I(\rho, \phi_1) I(\rho, \phi_2) \rangle$ varies as the shape of the correlation function changes. Although none of the peaks are as sharp as the triangular and Eiffel functions, shown in Fig. 3.12, the shape of $\langle I(\rho, \phi_1) I(\rho, \phi_2) \rangle$ changes in accord with the aperture correlation, becoming sharper as the aperture correlation does so. For the Gaussian- and triangular-correlated apertures, the peaks of $\langle I(\rho, \phi_1) I(\rho, \phi_2) \rangle$ have approximately the same area, but the peak area is less in the case of the Eiffel correlation function. The equal-area-equal-correlation-angle condition used in defining the aperture ensemble does not translate into equal-area intensity correlation peaks.

Our earlier comparison of the Fourier transform of the triangular- and Gaussian-correlated apertures in Figs. 4.5 and 4.6 is repeated in Fig. 4.13 for the fifteenth ring ($\rho = 0.498$ mm). With these two curves we now include the Fourier transform intensity of an aperture from an ensemble with the Eiffel correlation function, β equal to 0.5. With all three intensity patterns drawn to the same scale, we note the increase in intensity variation for the sharper correlation functions. The nearly one-to-one correspondence between the spikes shown in Fig. 4.13 (a) and (b) is not seen in Fig. 4.13 (c). The number of spikes, as defined for Fig. 4.5 (d), has increased at this output radius. We conclude that the shape of the correlation function affects the number of spikes in the transform, but we recall that the spike number depends on the value of ρ

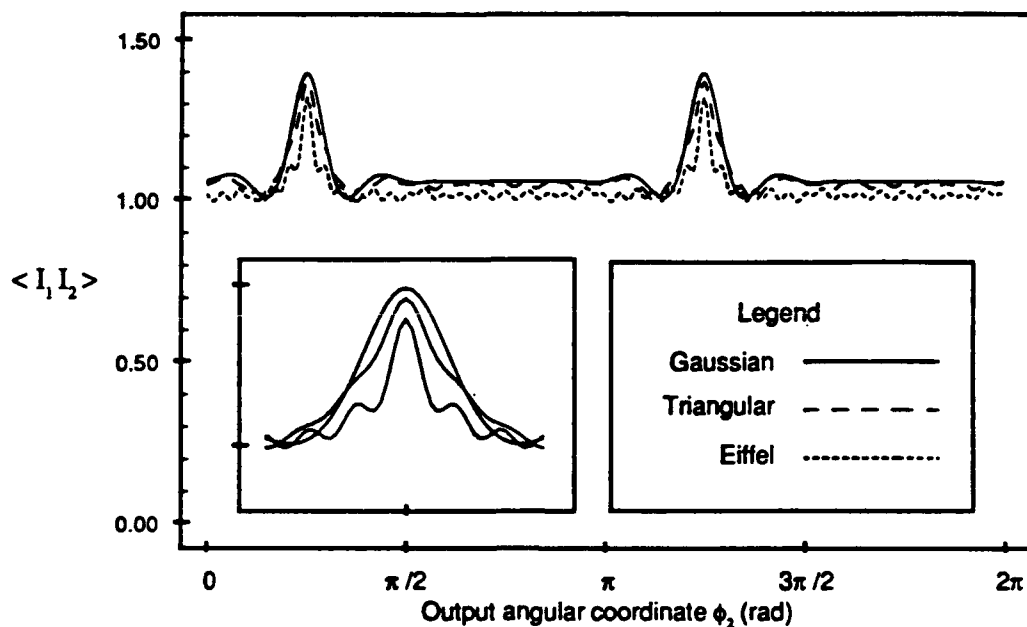


Fig. 4.12. Calculated two-point intensity moment $\langle I_1 I_2 \rangle$ for aperture ensembles of varied correlation function. Each aperture ensemble has $75 \mu\text{m}$ rms roughness, 5.0 mm mean radius, and $\pi/8$ area-normalized correlation angle. The system focal length is 500 mm , the wavelength, $0.6328 \mu\text{m}$. The fixed output angle is $\phi_1 = \pi/4$ rad, and the fixed output radius is 0.498 mm , corresponding to ring 15 in the transform.

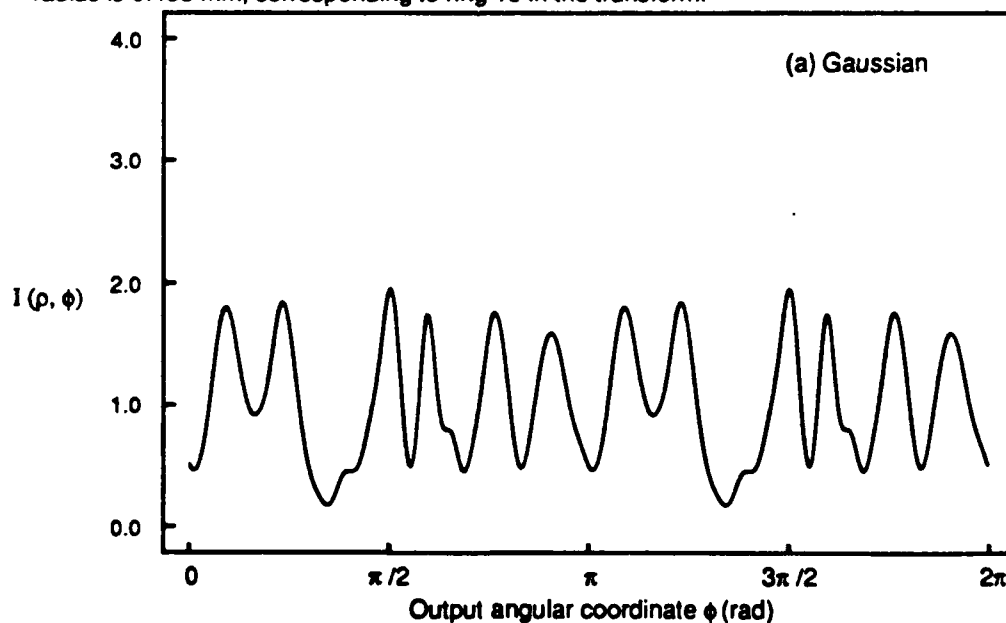


Fig. 4.13. Calculated intensity for individual apertures from ensembles of varied correlation function, as indicated. The remaining aperture and system parameters are as described for Fig. 4.12.

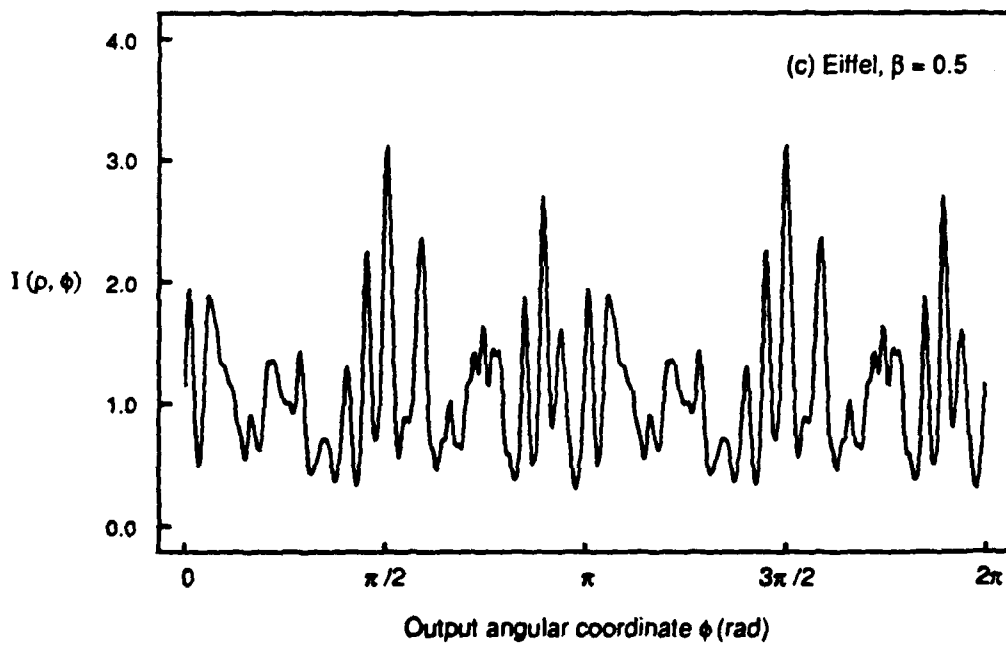
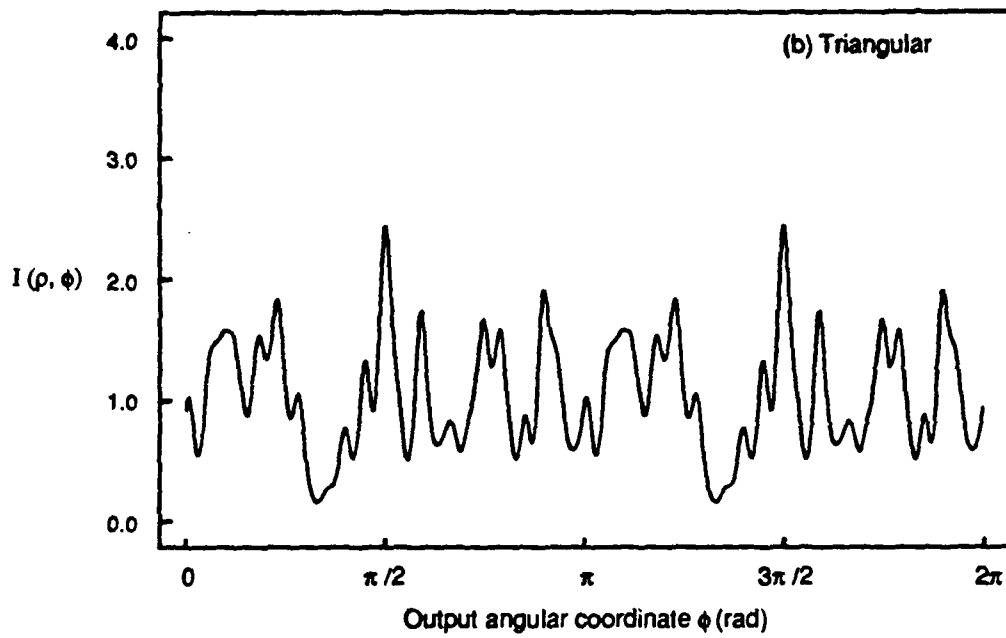


Fig. 4.13. (Continued)

and also that the correlation angle of $\langle I(\rho, \phi_1) I(\rho, \phi_2) \rangle$ is apparently less for the Eiffel aperture correlation, as shown in Fig. 4.12. In Fig. 4.13 (c), we see an extreme case of the spike appearance; when the aperture correlation function is very sharp, the spikes break quickly into smaller spikes as the output radius increases. By the time we reach ring 15, the spike count is dramatically greater for this correlation function.

Our closing comment for this chapter arises from the results of this computer-aided study of the two-point intensity moment as a one-dimensional angular correlation. We were able to predict successfully the behavior of $\langle I(\rho, \phi_1) I(\rho, \phi_2) \rangle$ as a function of the various aperture parameters from an examination of the integrand of μ_{12} . However, the dependence of the features of the optical Fourier transform on the changes in $\langle I(\rho, \phi_1) I(\rho, \phi_2) \rangle$ is less predictable. An individual transform feature is typically affected by more than one aperture or system parameter. The number of spikes, as an example, was seen to be influenced by the width and shape of the correlation function of the aperture, as well as by the output radius at which the spikes are identified. We must be careful, too, not to draw quick conclusions from the behavior of one aperture in an ensemble. Although we expect the properties of most, if not all, apertures to be indicative of the ensemble properties, assuming that a look at one aperture comprises a complete study of the ensemble would be unwise. Our experimental work, then, will begin with an investigation of the properties of the transforms of an ensemble of apertures. Then when we study single apertures in our experimental work, we will have some understanding of what behavior to expect from the ensemble.

Chapter 4 References

1. I.S. Reed, "On a moment theorem for complex Gaussian processes," IRE Trans. Inf. Theory IT-8, 194-195 (1962).
2. J.C. Marron, "Accuracy of Fourier-magnitude estimation from speckle intensity correlation," J. Opt. Soc. Am. A 5, 864-870 (1988).
3. U. Vry, "Calculation of complex correlation coefficients of two speckle fields of different wavelengths and their application to two-wavelength-measurement techniques," J. Opt. Soc. Am. A 5, 114-125 (1988).
4. B.M. Levine, "Non-Gaussian speckle caused by thin phase screens of large root-mean-square phase variations and long single-scale autocorrelations," J. Opt. Soc. Am. A 3, 1283-1292 (1986).
5. B. Ruffing, "Application of speckle-correlation methods to surface-roughness measurement: a theoretical study," J. Opt. Soc. Am. A 3, 1297-1304 (1986).
6. N. Takai and T. Asakura, "Statistical properties of laser speckles produced under illumination from a multimode optical fiber," J. Opt. Soc. Am. A 2, 1282-1290 (1985).
7. N. George and A. Jain, "Space and wavelength dependence of speckle intensity," Appl. Phys. 4, 201-212 (1974).
8. L.G. Shirley, *Laser Speckle from Thin and Cascaded Diffusers* (Ph.D. Thesis, University of Rochester, 1988), Appx. A.
9. L.G. Shirley and N. George, "Speckle from a cascade of thin diffusers," J. Opt. Soc. Am. A 6, 765-781 (1989).
10. See, for example, J.W. Goodman, *Statistical Optics* (Wiley-Interscience, New York, 1985), pp.108-109.

11. R.N. Bracewell, *The Fourier Transform and its Applications* (McGraw-Hill, New York, 1985), pp. 14-16.
12. We have chosen $\rho = 0.5$ mm, $\lambda = 0.5$ μm , and $z_0 = 500$ mm for this "back-of-an-envelope" calculation.
13. E. Hecht and A. Zajac, *Optics*, (Addison-Wesley, Reading, Mass., 1979), p. 365 et seq.

Chapter 5

Fabrication and Evaluation of Serrated Circular Apertures

5.1. Introduction

From the statistical diffraction theory presented in Chapter 4, we obtained an expression for the two-point moment of the intensity of the Fourier transform of a serrated circular aperture. From this expression, we predicted the changes in the Fourier transform features that would result when certain aperture parameters were varied. Our goal in this chapter is to examine the transforms of apertures from different ensembles to verify our predictions. We will also investigate the features in the transform of a particular aperture and those in the transforms of an ensemble of apertures; through this study, we will understand how well the transform of a particular aperture represents the ensemble to which it belongs.

Two methods are available for producing the transforms of interest: computer simulations such as those presented in Chapter 2 and optical experiments using apertures with controlled statistics. In this chapter we will examine these two methods, keeping in mind the level of detail that is of interest to us. Finding complete agreement between the experimental and simulated Fourier transforms of a particular aperture is an unreasonable objective because of inevitable experimental noise. However, we are interested in the ring and spike structure of the transform, which are larger features, and we anticipate agreement between the computer simulation and the experimental transforms at this feature level.

Ideally, the differences between the simulated and experimental transforms will be well within the range of variations seen in the transforms of an ensemble of

apertures. Thus, in preparation for the comparison of simulation and experiment, we start in Section 5.2 with an examination of several apertures from one ensemble and of the transforms of those apertures. For this portion of the study, computer-simulated transforms are used. In Section 5.3, we discuss experimental optical Fourier transforms, describing the optical system to be used and two methods, photolithography and electron-beam lithography, for making experimental apertures from our computer-calculated designs. We recognize the possible errors in producing an experimental aperture and therefore study the impact of these aperture errors on the Fourier transform of the aperture by designing and producing "noisy" apertures for use in our optical system. The results of this error investigation are presented in Section 5.4.

The results presented in this chapter show that very small deviations in the apertures are visible in the transforms, but that at the feature level the simulations and experiments show excellent agreement. From these observations, we conclude that photolithography is an adequate aperture production method for our purposes.

5.2. Computer Simulation of the Fourier Transforms of Apertures from an Ensemble

Our method for generating aperture designs, described in Appendix A, is well-suited to generating a set of apertures from one ensemble. Changing the seed given to the random number generator while keeping all other input parameters constant produces in effect a new realization of the same random process. In this case, each realization is a member of the ensemble of apertures.

Using an ensemble mean radius of 5.0 mm, an rms roughness of 75 μm , a correlation angle of $\pi/8$ rad, and a triangular correlation function, we varied the random number generator seed to produce twelve apertures from one ensemble. For each of

these apertures, we then calculate the Fourier transform for the output coordinates in the range $0 \leq \rho \leq 0.75$ mm and $0 \leq \phi \leq \pi$ rad. With the wavelength and focal length fixed at 0.6328 μm and 500 mm, respectively, this range shows more than 20 rings for half the diffraction pattern; since the Fourier transform of an aperture is polar-symmetric, the second half of each transform ($\pi \leq \phi \leq 2\pi$ rad) is identical to the part calculated. Each aperture is shown with the corresponding Fourier transform in Fig. 5.1.

We note again that representative apertures from the ensemble are different from each other. We see differences in the apertures but expect that these differences will fall within a reasonable range. For a detailed discussion of the ensemble statistics of quantities such as the spatial mean and spatial rms deviation, the reader is referred to the section on sampling from the normal distribution in the book by Mood, Graybill and Boes¹ and to Section 3.4.3 in this dissertation. Herein, we consider the properties of individual apertures from the ensemble at hand. For example, we calculated the angular spatial average radius $\{S(\alpha)\}_a = \{a + s(\alpha)\}_a$ and the angular rms roughness $[\{s^2(\alpha)\}_a]^{1/2}$ for each of these twelve apertures; the values are listed in Table 5.1. For this set, the angular average radius values lie between 4.98 and 5.04 mm; the angular rms roughness, between 59 and 100 μm . For reference, we note that the ensemble mean radius is 5.0 mm and the ensemble rms roughness is 75 μm . Likewise, the Fourier transforms of these apertures are distinct from each other. The intensity distributions shown in Fig. 5.1 display different spike patterns and, at the higher spatial frequencies, different speckle patterns. One of the features that identify these transforms as those of apertures from a single ensemble is the number of spikes. Using the method described in Section 4.4 in connection with Fig. 4.5(d), we determined the number of spikes in each transform in Fig. 5.1 at $\rho = 0.498$ mm (the fifteenth ring); these counts are included in Table 5.1. (We use only half the transform in this count because of the polar symmetry of the transform.) Clearly, the

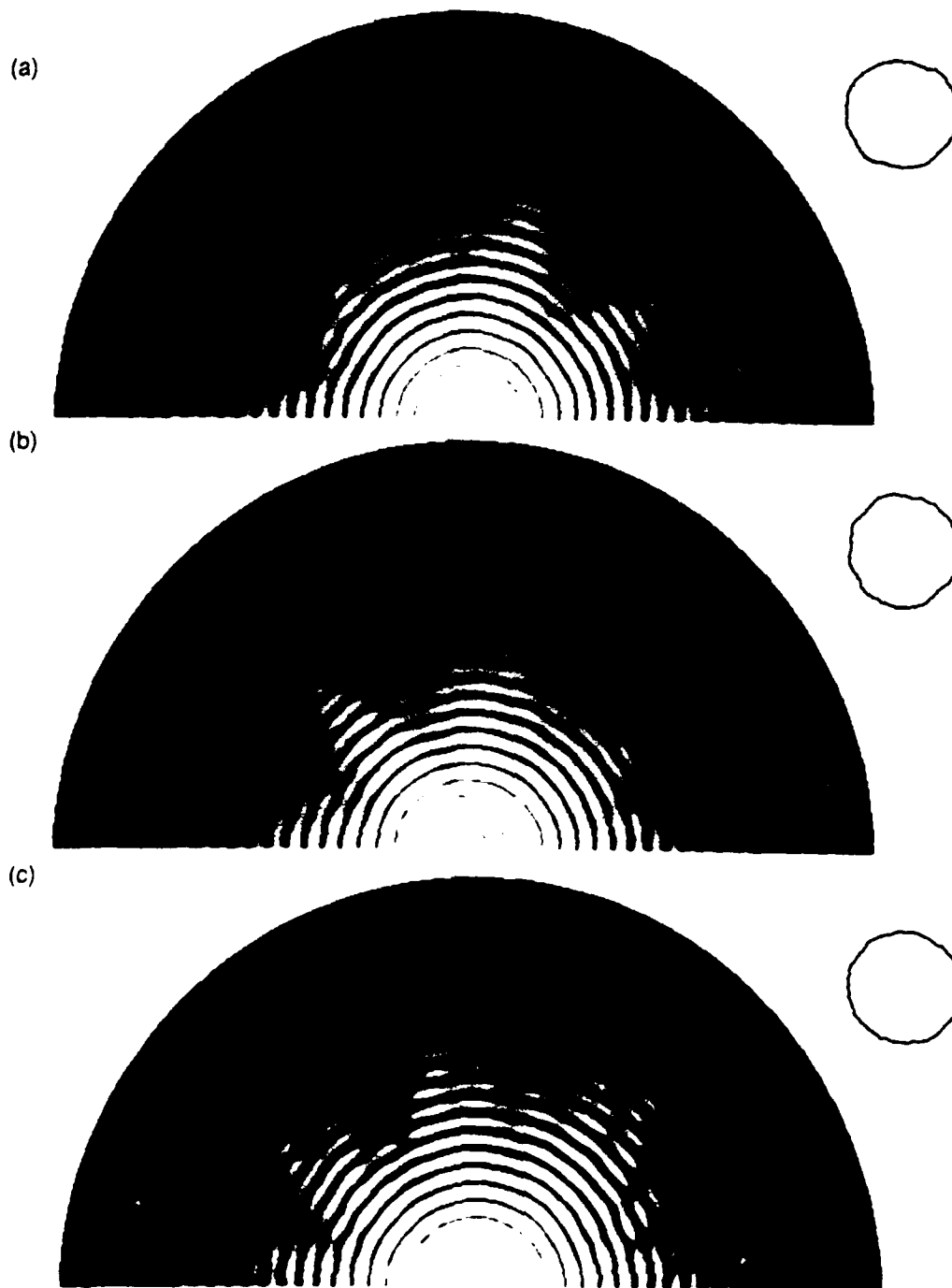


Fig. 5.1. Twelve apertures from a single ensemble and the calculated Fourier transform of each. For the ensemble, the mean radius is 5.0 mm; the rms roughness, 75 μm ; the correlation angle, $\pi/8$ rad; and the correlation function, triangular. The system focal length is 500 mm; the wavelength is 0.6328 μm . The transforms are calculated for $0 < \rho < 0.75$ mm and $0 < \phi < \rho$.

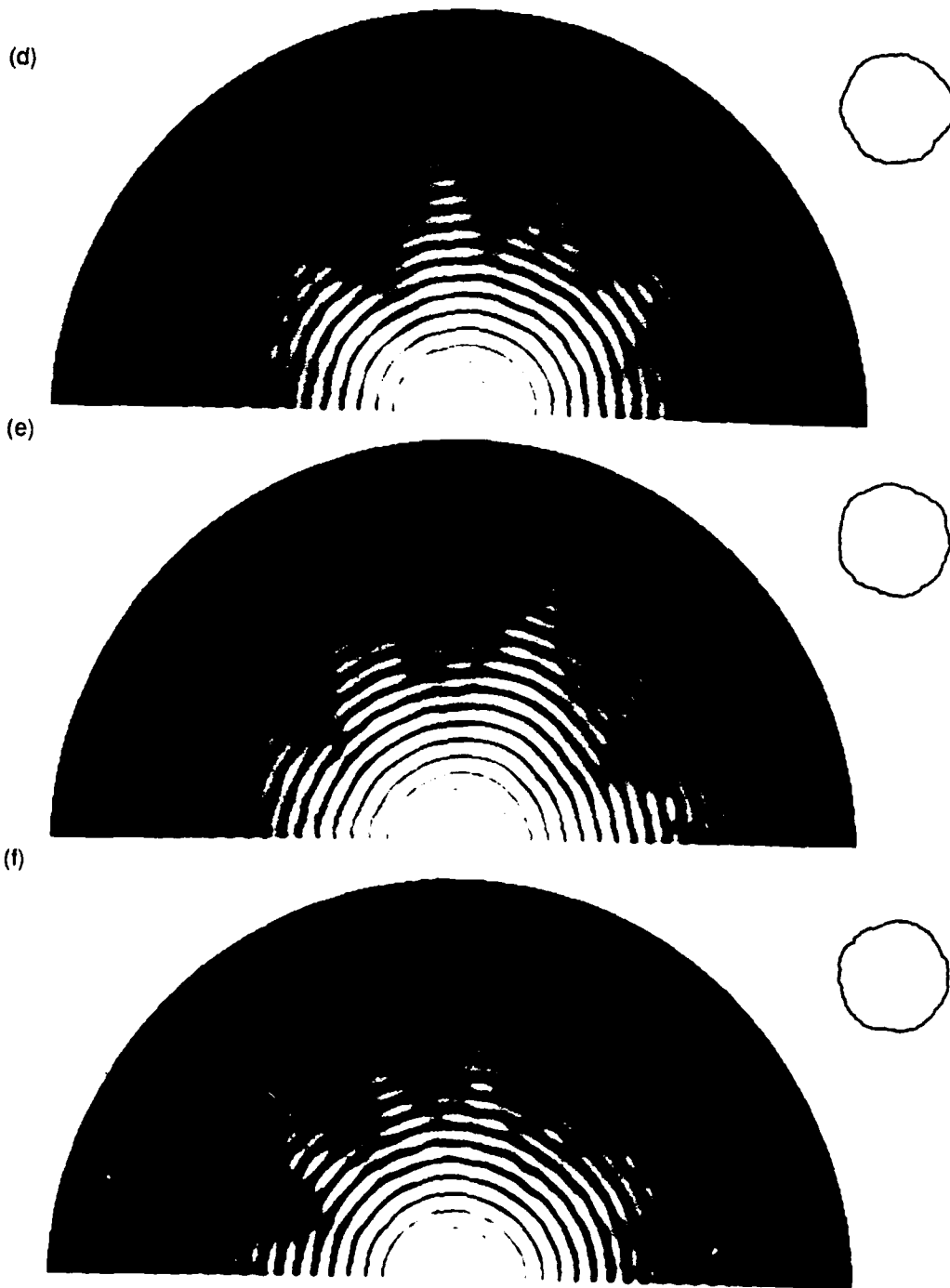


Fig. 5.1. (Continued)

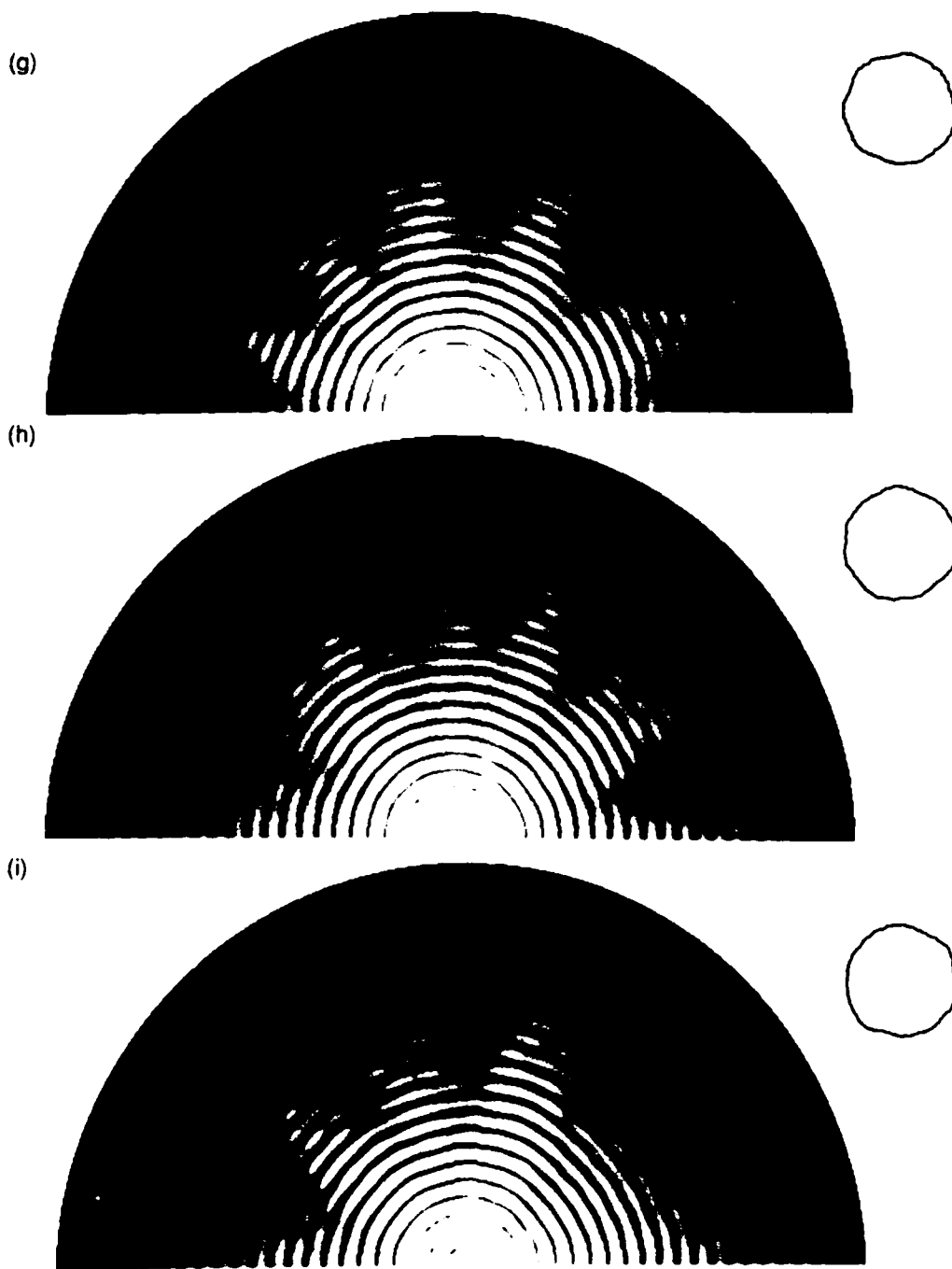


Fig. 5.1. (Continued)

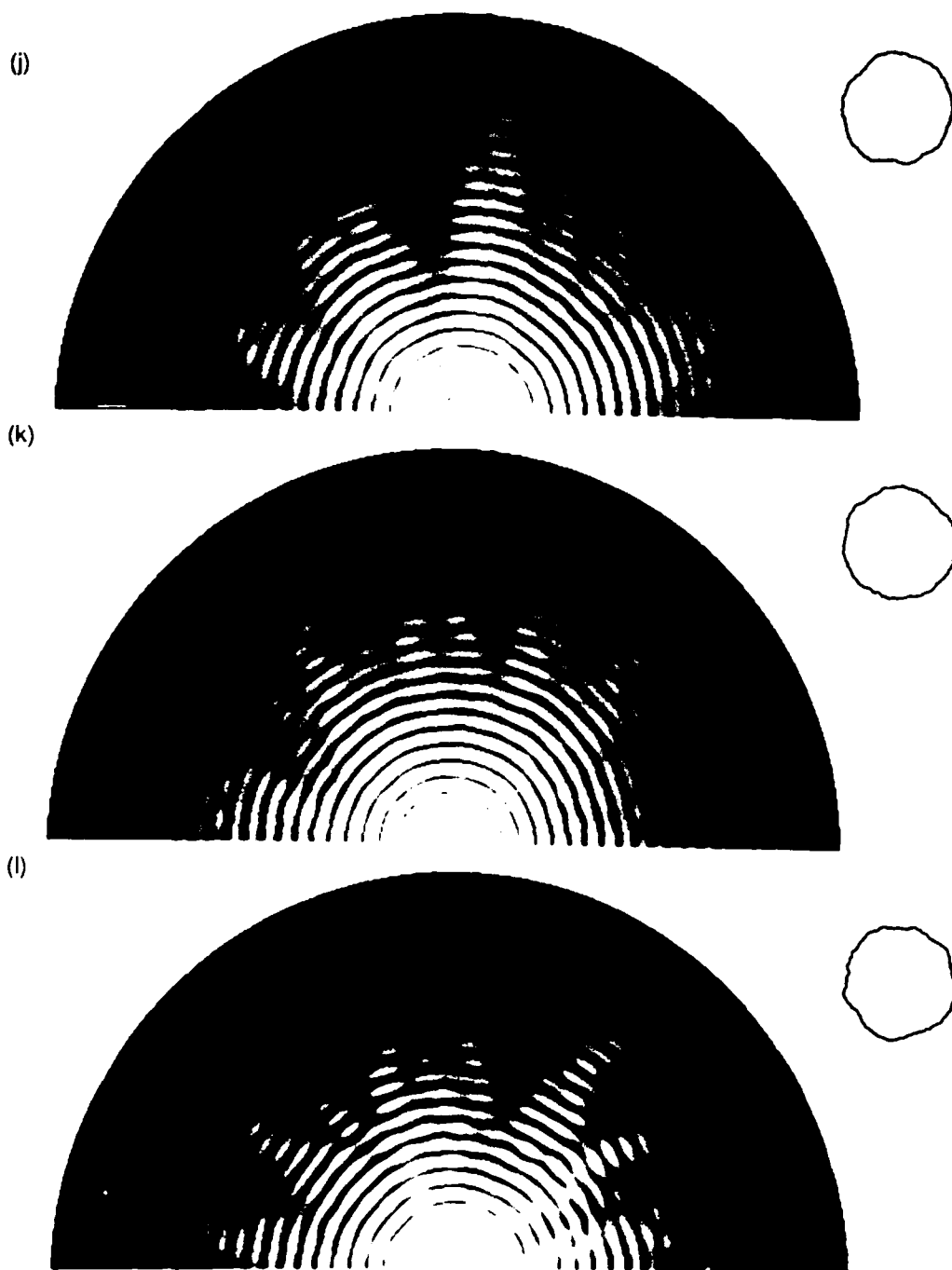


Fig. 5.1. (Continued)

number of spikes is fairly constant, varying only $\pm 2\frac{1}{2}$ spikes about the mean in the half transform.

| Aperture | Angular average radius $\{S(a)\}_a$ (mm) | Angular rms roughness $[\{s^2(a)\}_a]^{1/2}$ (μm) | Number of spikes in half transform |
|-------------------|---|---|--|
| a | 5.00 | 65 | 8 |
| b | 4.98 | 88 | 9 |
| c | 5.01 | 59 | 10 |
| d | 4.99 | 93 | 9 |
| e | 5.03 | 96 | 6 |
| f | 4.98 | 62 | 9 |
| g | 5.01 | 68 | 7 |
| h | 5.04 | 65 | 7 |
| i | 4.99 | 71 | 7 |
| j | 5.00 | 86 | 9 |
| k | 5.02 | 77 | 9 |
| l | 5.00 | 100 | 11 |
| mean ¹ | 5.00 | 78 | 8.4 |

Table 5.1. Selected angular statistical quantities for individual apertures from the ensemble represented in Fig. 5.1. The correlation angle for the ensemble is $\pi/8$ rad.

These variations in the ensemble and the resulting potential for overlap of two ensembles may present difficulties for one who wishes to sort apertures by ensemble. However, these same variations determine the accuracy needed in producing experimental apertures.

We complement our observations of these apertures and transforms with computer calculations of the two-point intensity moment and related angular correlations. Using the ensemble and system parameters given with Fig. 5.1 and setting ρ_1 and ρ_2 equal to 0.498 mm in the output plane, we calculate $\langle I(\rho_1, \phi_1) I(\rho_2, \phi_2) \rangle$ for ϕ_1 equal to $\pi/4$ rad and ϕ_2 varying from 0 to 2π rad, as in Chapter 4. (See, for example, Fig. 4.4 and the accompanying discussion.) This ensemble average can be approximated with the following sum:

$$\langle I(\rho_1, \phi_1) I(\rho_2, \phi_2) \rangle \approx \frac{1}{M} \sum_{i=1}^M I_i(\rho_1, \phi_1) I_i(\rho_2, \phi_2) , \quad (5.1)$$

in which index i corresponds to the i^{th} member of the ensemble; $I_i(\rho, \phi)$ is the intensity of the optical Fourier transform of aperture i at point (ρ, ϕ) . As M approaches infinity, this sum becomes $\langle I(\rho_1, \phi_1) I(\rho_2, \phi_2) \rangle$, but for small values of M there is little resemblance between the two quantities.

To approximate $\langle I(\rho_1, \phi_1) I(\rho_2, \phi_2) \rangle$ under the ensemble and system conditions described in the preceding paragraph, we generated 5000 apertures from the ensemble, calculated $I(\rho, \phi)$ at ρ equal to 0.498 mm for each aperture, and determined the sum in Eq. (5.1) with ϕ_1 fixed at $\pi/4$ rad and ϕ_2 in the range $[0, 2\pi]$. The resulting curve is shown plotted with $\langle I(\rho_1, \phi_1) I(\rho_2, \phi_2) \rangle$ in Fig. 5.2, where we note excellent

agreement between theory-based $\langle I(\rho_1, \phi_1) I(\rho_2, \phi_2) \rangle$ and the calculation-intensive sum.

In an experimental situation, 5000 members of an ensemble are rarely available; often one has only a single aperture. In this typical case, some other method of estimating $\langle I(\rho_1, \phi_1) I(\rho_2, \phi_2) \rangle$ is needed. The angular autocorrelation of the intensity,

$$\int_{-\infty}^{+\infty} I(\rho, \phi_1) I(\rho, \phi_1 + \Delta\phi) d\Delta\phi, \quad (5.2)$$

approximates the two-point moment when only a single aperture is used. We note that each member of the ensemble will have a different intensity autocorrelation, since this autocorrelation is a property not of the ensemble but of the individual aperture. If we keep in mind that each of these *spatial* autocorrelations only approximates the *ensemble* average $\langle I(\rho_1, \phi_1) I(\rho_2, \phi_2) \rangle$, we are in little danger of confusing the two quantities.

The intensity autocorrelations of three apertures from the ensemble under discussion, with the system conditions described for Fig. 5.2, are shown plotted in Fig. 5.3. In the region of interest, namely, near the correlation peaks at ϕ equal to $\pi/4$ and $5\pi/4$, the curves are quite similar to each other and to $\langle I(\rho_1, \phi_1) I(\rho_2, \phi_2) \rangle$, shown in Fig. 5.2. Farther from these peaks, in the region where $\langle I(\rho_1, \phi_1) I(\rho_2, \phi_2) \rangle$ is relatively flat, the spatial autocorrelation curves show very different structures. Therefore, estimating $\langle I(\rho_1, \phi_1) I(\rho_2, \phi_2) \rangle$ with the intensity autocorrelation of a single aperture is valid only near the two correlation peaks. Fortunately, we are often interested primarily in these short-range correlation properties, within a correlation length of a given point.

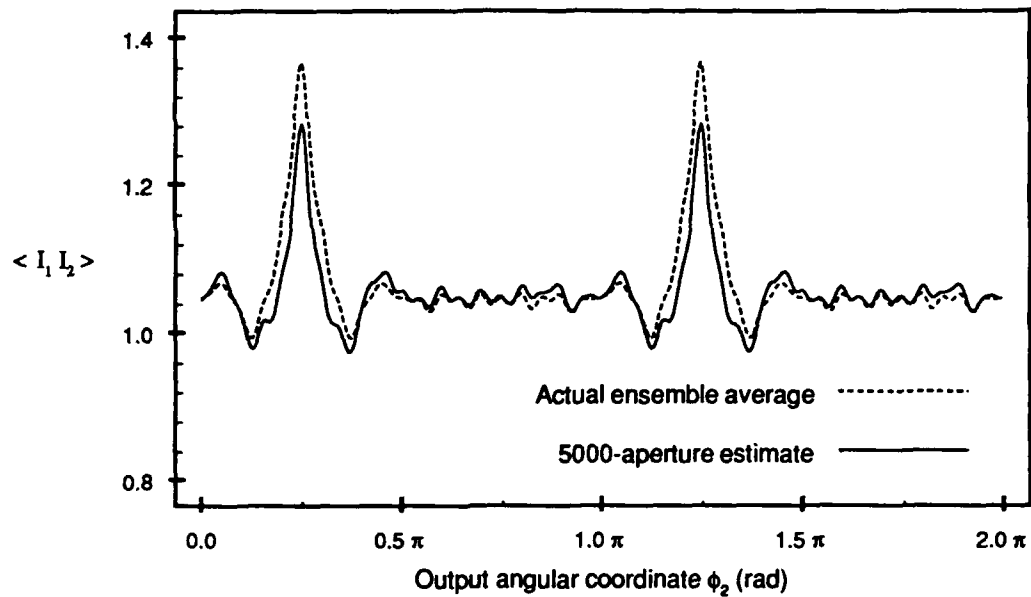


Fig. 5.2. Calculated ensemble average $\langle I(\rho_1, \phi_1) I(\rho_2, \phi_2) \rangle$, actual and estimated, for the ensemble represented in Fig. 5.1. The system focal length is 500 mm; the wavelength is $0.6328 \mu\text{m}$. The output radial coordinate ρ is set at 0.498 mm, and the fixed angular coordinate ϕ is $\pi/4$ rad. At the peaks, the rms deviation of the estimate is approximately 0.02; away from the peaks, this deviation is 0.01.

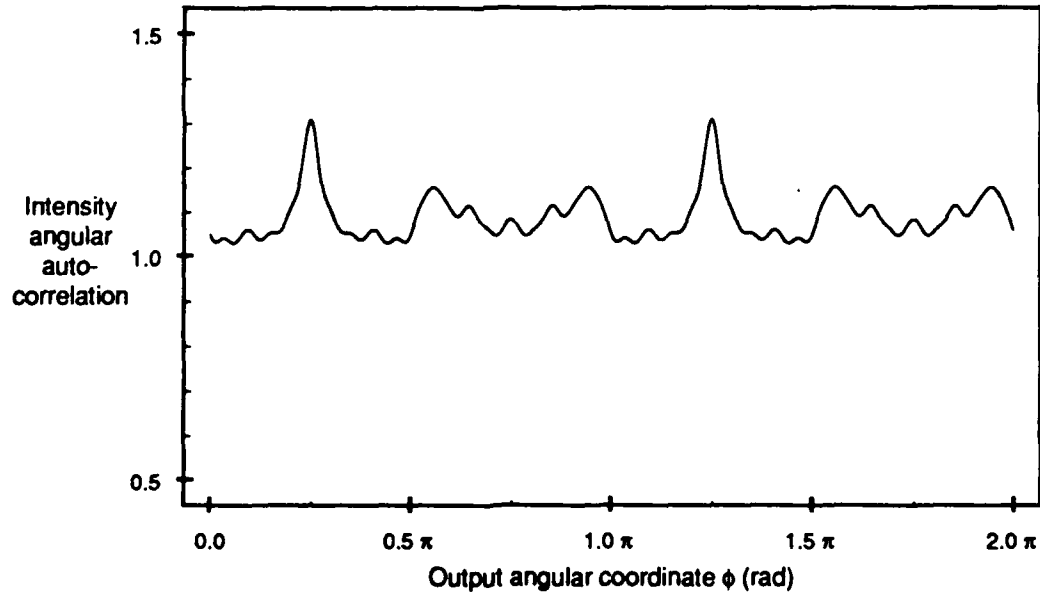


Fig. 5.3. The angular autocorrelation of the intensity in the Fourier transform of selected individual apertures. The apertures are from the ensemble represented in Fig. 5.1, and the system parameters are as described for Fig. 5.2.

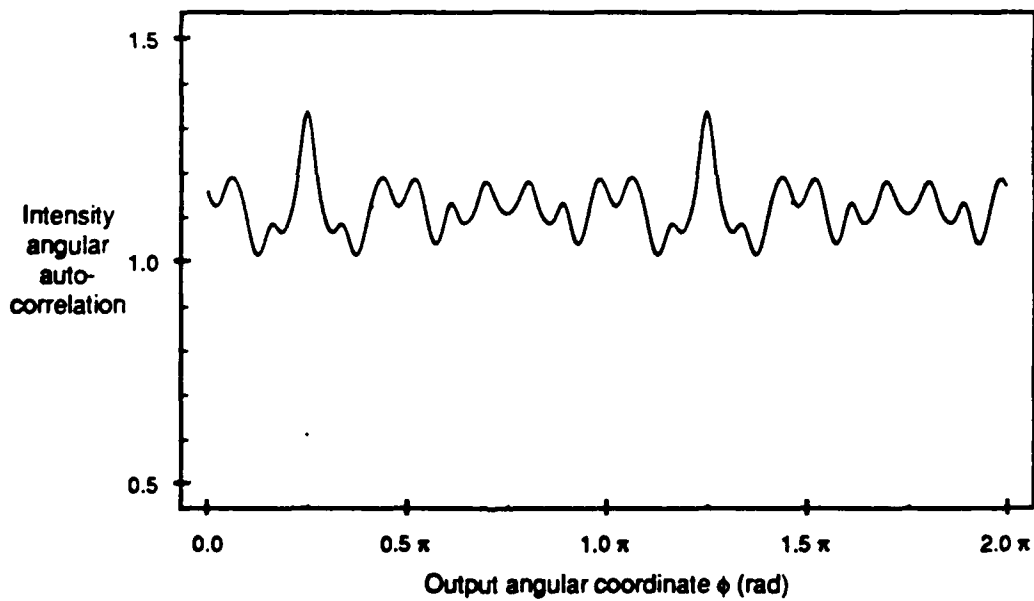
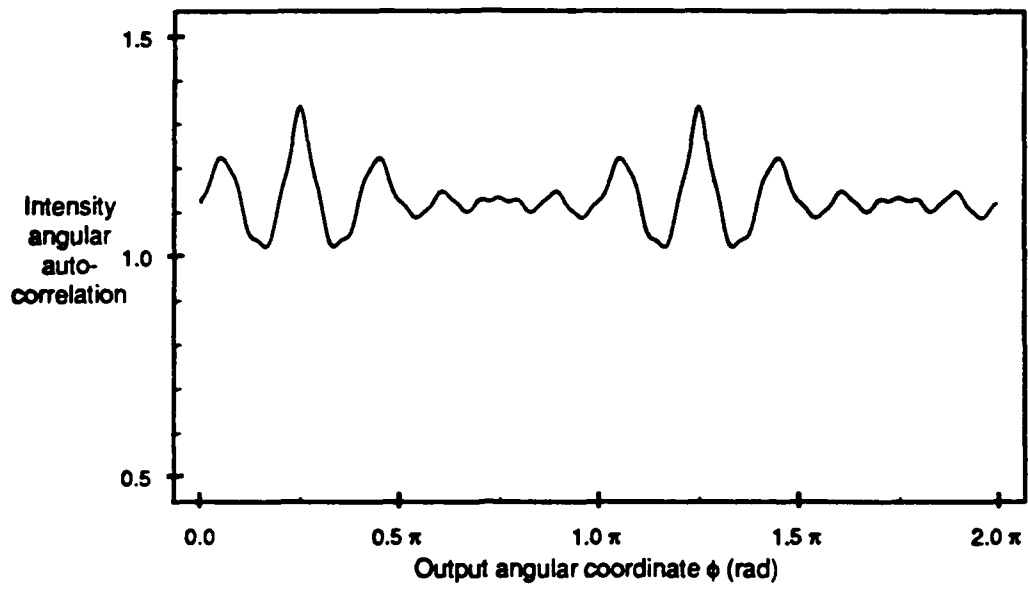


Fig. 5.3. (Continued)

We see from Figs. 5.1 and 5.3 that, despite the variations in the transforms of an ensemble of apertures, some useful information can be obtained from a single member of the ensemble. However, the variations are also important in our study. If errors introduced in the experimental process result in changes in the diffraction pattern details, we will not be surprised. If these errors do not produce variations in the fragmentation and spike structures of the transform greater than those expected within the ensemble, we will accept the errors as reasonable for our purposes.

5.3. Experimental Optical Fourier Transforms

5.3.1. The Optical Fourier Transform System

In order to produce experimentally the optical transform of a serrated aperture, we use the optical system shown schematically in Fig. 5.4. A Spectra-Physics Model 145-02 helium-neon laser, which has 4 mW maximum power output, is the source of coherent illumination. The beam is expanded with 20X microscope objective M. Pinhole P has a 15 μm diameter; placed at the focal point of the objective, it spatially filters the beam. Lens L, with focal length F equal to 500 mm and measuring 3 inches in diameter, is located slightly downstream from the collimating position, *i.e.*, at a distance $F + \Delta$ from the pinhole. The beam thus converges to a point in the transform plane, which is at a distance $(z_0)_{\text{max}}$ from the lens. Distance Δ determines the system focal length: $(z_0)_{\text{max}}$ and is varied to suit the particular application. Generally, Δ is between 30 and 50 mm, yielding a system focal length between 8.8 m and 5.5 m, as described later in this section. Two-inch diameter relay mirrors are used to confine the beam to an area which measures approximately 1 meter by 4 meters.

The maximum value of z_0 attainable is the distance from the lens to the camera located in the transform plane and is determined by F and Δ , where Δ is the displacement of the lens from the collimating position. Lens L effectively images the pinhole onto the camera; from the lens law, we thus have:

$$\frac{1}{F + \Delta} + \frac{1}{(z_0)_{\max}} = \frac{1}{F} \quad (5.3)$$

Solving for $(z_0)_{\max}$ we find:

$$(z_0)_{\max} = \frac{F(F + \Delta)}{\Delta} \quad (5.4)$$

As an example, consider a 500-mm focal length lens which is displaced by 50 mm. In this case, the maximum value of z_0 is 5.5 meters. Smaller values of z_0 can be achieved in a fixed

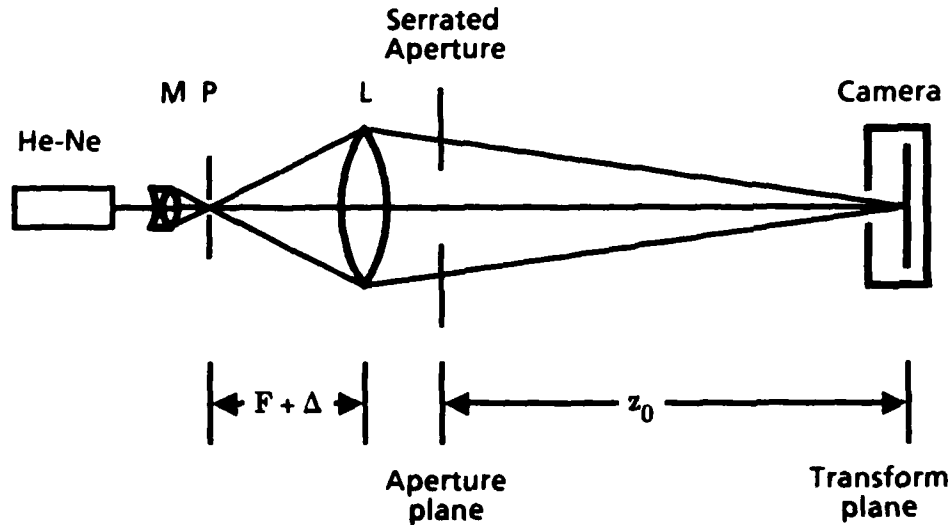


Fig. 5.4. Schematic representation of the experimental apparatus for the study of the optical transform: HeNe, helium-neon laser; M, microscope objective; P, pinhole; L, transform lens, focal length $F = 500$ mm; I, object (aperture) plane; II, optical transform plane.

system by moving the aperture away from the lens and toward the camera. Since the beam is converging, there is a smallest value of z_0 beyond which the aperture will not be fully and uniformly illuminated. In our experiments, this has not been a limiting factor, since we are interested in longer focal lengths which allow us to see the detail of the optical transforms of our relatively large (5 mm mean radius) apertures.

The serrated aperture is located between the lens and the transform plane in a position where it is, for practical purposes, uniformly illuminated by the beam. In this configuration, as described in the theory presented in Section 2.2, the field in the optical transform plane is proportional to the two-dimensional spatial Fourier transform of the serrated aperture.

The apertures used in these experiments are designed using the convolution method described in Appendix A. Briefly, the convolution of a set of Gaussian-distributed random numbers with a window function imposes a specific correlation function on the data. Careful choice of the height, width, and shape of this window function controls the rms deviation, correlation angle, and correlation function of the resulting data. We use these zero-mean data to form the function that describes the deviation of the serrated aperture from a circle, i.e., $s(\alpha)$ in Eq. (2.1), where α is the angular coordinate in the aperture plane. Thus, when the mean radius a is added to each data point in this correlated set, the new set describes the radius of the aperture as a function of angle at discrete points. Linear interpolation is used to define the continuous aperture edge.

Two lithographic methods were readily available for use in converting our computer-generated designs to chrome apertures. The application of photolithography

and of electron-beam lithography in fabrication of serrated apertures are described in the next two sections.

To record the optical Fourier transform for careful analysis, we place a lensless camera in the system so that the film plane of the camera coincides with the optical transform plane and is centered on the optical axis. With the camera, we photograph the two-dimensional intensity pattern on Kodak Panatomic-X film², which offers a slow speed and low contrast. The total and average intensities in the transform plane are not measured because of the typically high intensity on the optical axis: such a measurement would likely damage the detector used to make it.

5.3.2. Aperture Production by Photolithography

To fabricate chrome apertures by a photolithographic method, we first plot the aperture function, denoted by $r = a + s(a)$ in cylindrical coordinate plane (r, a) as shown in Fig. 2.1, in ink on vellum in 10X enlargement. This aperture outline is filled completely to produce the artwork from which the apertures are made. The artwork is then sent to Applied Image³, where a 10X reduction negative of the artwork is made in emulsion on film or on glass⁴. This tooling is then used to make our experimental chrome apertures by contact photolithography. When a negative photoresist is used, the resist-coated glass plate is placed in contact with the tooling and exposed to light. The resist in the exposed region (i.e., inside our aperture) becomes less soluble than that in the unexposed regions. The resist is then developed and, in the unexposed region, washed away. The plate and remaining resist are coated with chrome. Finally, the exposed resist and the chrome in that region are removed with a solvent, leaving chrome only in the

area where the original resist had not been exposed. The resulting mask is our experimental aperture in chrome on glass.

The chrome masks made by this photolithographic method are accurate reproductions of the original artwork to 2 μm on the scale of the aperture, a value reported in the literature^{5,6} and by manufacturing firms^{3,7}. As reported herein, the results of an examination of the masks used in these experiments supports accuracy of 5 μm or better in the chrome photolithographic process. Morris⁸ reported that the photolithographic process introduced the greatest error in the production of serrated edges and gaps in chrome on glass. Therefore, we choose our smallest non-zero roughness and our smallest correlation length to be several times this limit so that our design will be adequately reproduced in the chrome-on-glass masks. We prefer to study a series of apertures with a significant range of values for the ratio of the roughness to the mean radius. We also require that there be at least a few correlation lengths along the aperture perimeter. These constraints force us to use fairly large apertures; each experimental aperture has a mean radius of 5 mm. A long-focal-length ($\sim 6\text{m}$) optical transform system produces aperture transforms that are large enough for easy viewing and measuring. As described in Section 5.3.1, such a system is easy to achieve, and therefore the necessarily large aperture size does not present significant experimental difficulties.

To check the accuracy of the chrome lithography, we compared the chrome masks to the tooling from which they were made; an example of this comparison follows. The tooling in this case is a 10X reduction negative of the original artwork in emulsion on glass. The aperture is a one-to-one positive copy of the tooling and is made by contact exposure. When both are viewed under a microscope with a 10X objective, faithful

reproduction of all visible details is noted; see Fig. 5.5(a). The upper photo is of the emulsion-on-glass tooling, while the center photograph is of the chrome aperture. (The lower photograph in Fig. 5.5(a) is of the aperture produced by electron-beam lithography, to be described in the next section.) The scale shown below the photographs is marked in 10 μm and 100 μm increments. Measuring the details, we find them to be on the order of 5 to 10 μm . When a 50X objective is used to view the same aperture and tooling, we see that the grain of the film now influences our ability to resolve the edge of the tooling, as shown in Fig. 5.5(b). Again, the upper photograph is of the tooling, the center photograph is of the chrome aperture, and the lower photograph is of the electron-beam lithographic aperture. (Due to imaging difficulties associated with which side of the glass is coated with emulsion or chrome, the tooling and aperture images are oriented as mirror images.) The details we are able to see in these photographs are reproduced crisply in the chrome. The scale included in Fig. 5.5(b) gives 10 μm increments, and we can see details half this width reproduced in the chrome. Thus, we claim that the chrome lithographic process is, in our case, accurate to 5 μm or better.

The remaining question, then, is on the accuracy of the tooling. Is the tooling what we designed it to be? As outlined above, several steps are needed to convert the computer design to the tooling from which the chrome apertures are made. We also observe that the 512 points used to define an aperture with a 5-mm mean radius would be spaced approximately 60 μm apart on the edge; the details visible in the microscope images of Fig. 5.5 are below this design resolution. (The photographs in Fig. 5.5(a) show about 900 μm of the edge.) Therefore, at some stage prior to the tooling, errors are introduced. The problem is most likely at the artwork stage, where a 0.5 mm pen is used to draw the 10X enlargement of the aperture in ink on vellum. Although this pen size corresponds to 50 μm on the reduced scale, pen jitter and ink bleeding may add

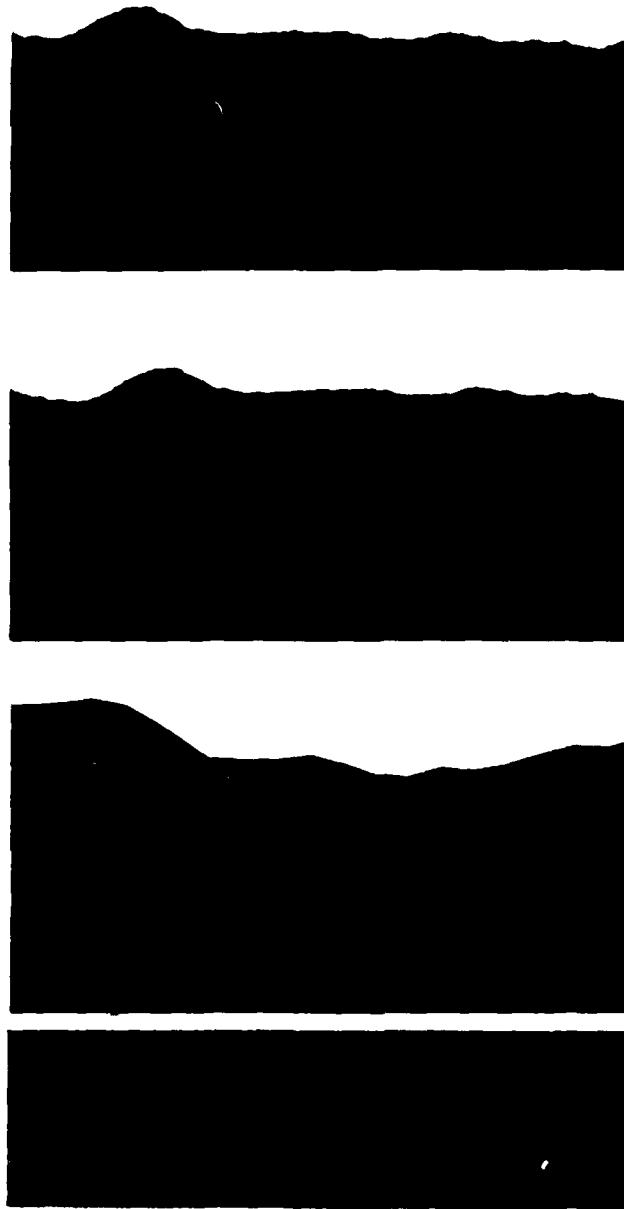


Fig. 5.5. Microscope photographs of (upper) the tooling used to make (center) the photolithographic chrome aperture, and (lower) the electron-beam lithographic aperture: (a) with 10X objective.

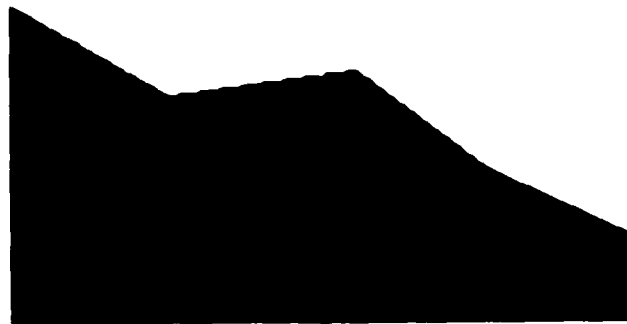
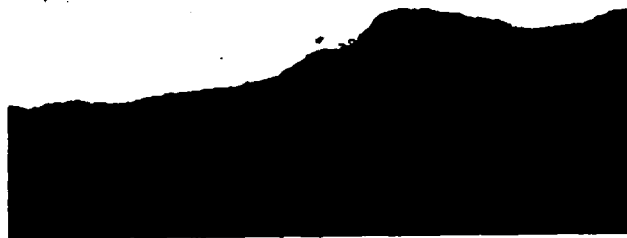
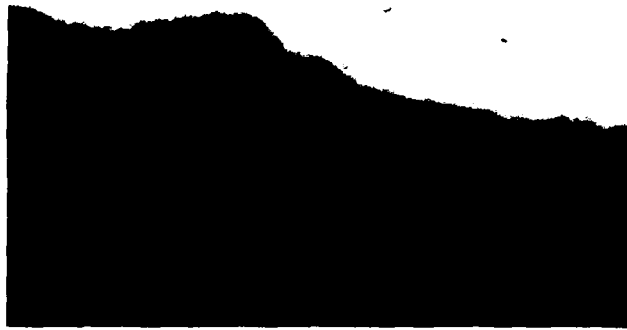


Fig 5.5 (Continued) (b) with 50X objective

to the imprecision in reproducing the design. Since the photolithographic process is reportedly accurate to $2\ \mu\text{m}$, the limiting factor in our ability to make chrome apertures to our design specifications is our ability to generate the artwork. The rms errors introduced at different stages in making the chrome apertures are summarized in Table 5.2. To calculate the total rms error from these independent sources, we take the square root of the sum of the squares of the individual errors; the total rms error from these four sources is $7.3\ \mu\text{m}$.

To determine the effect of this total error on the angular rms roughness, we model the deviation from the design by adding an error term $\varepsilon(\alpha_i)$ to each radius value

| Step | Source(s) | RMS Error (final aperture scale) |
|--------------------------|---|--------------------------------------|
| Computer design | Byte limit (double precision) | $10-12\ \mu\text{m}$ (calculated) |
| Ink plot | pen jitter, ink bleeding | $5\ \mu\text{m}$ (measured) |
| Intermediate emulsion | defocus, magnification error, film grain noise | $5\ \mu\text{m}$ (estimated) |
| Chrome lithography | exposing and etching process | $2\ \mu\text{m}$ (reported) |

Table 5.2. Error budget for photolithographic aperture production. The total rms error is $7.3\ \mu\text{m}$.

$s(a_i)$. The set of error terms $\varepsilon(a_i)$ is uncorrelated and has a zero angular mean and an rms deviation of $7.3 \mu\text{m}$. The new aperture function is then given by

$$s'(a_i) = s(a_i) + \varepsilon(a_i) . \quad (5.5)$$

The angular variance of this new aperture is found in the usual manner. Neglecting the small deviation of the angular mean of $s(a)$ from zero, we calculate

$$\begin{aligned} \{[s'(a)]^2\}_a &= \frac{1}{m} \sum_{i=1}^m [s(a_i) + \varepsilon(a_i)]^2 \\ &= \frac{1}{m} \sum_{i=1}^m s^2(a_i) + \frac{2}{m} \sum_{i=1}^m s(a_i) \varepsilon(a_i) + \frac{1}{m} \sum_{i=1}^m \varepsilon^2(a_i) \\ &= \{s^2(a)\}_a + 2\{s(a) \varepsilon(a)\}_a + \{\varepsilon^2(a)\}_a . \end{aligned} \quad (5.6)$$

If we assume that the error is independent of the original aperture function, we can separate the middle term:

$$\{[s'(a)]^2\}_a = \{s^2(a)\}_a + 2\{s(a)\}_a \{\varepsilon(a)\}_a + \{\varepsilon^2(a)\}_a . \quad (5.7)$$

We see that the first term in Eq. (5.7) is the variance of the original aperture function and that the last term is the variance of the error. Since $\varepsilon(a)$ has a zero angular mean, the middle term is identically zero. Thus, the variance of the new aperture is equal to the sum of the variances of the original aperture and the added error. Adding $7.3 \mu\text{m}$ angular rms error to an aperture with $75 \mu\text{m}$ angular rms roughness results in a new rms roughness of $[(75 \mu\text{m})^2 + (7.3 \mu\text{m})^2]^{1/2}$ or $75.4 \mu\text{m}$. The angular mean radius will not be affected by the added error since $\{\varepsilon(a)\}_a$ is equal to zero. Thus, referring to the ensemble values listed in Table 5.1, we see that even with the errors introduced in the photolithographic

aperture fabrication the aperture is well within the limits of the ensemble in terms of the angular mean and angular rms roughness.

5.3.3. Aperture Production by Electron-Beam Lithography

The error introduced to our aperture fabrication process by photolithography does not put our aperture in a new ensemble. However, we can expect to see some change in the Fourier transform of the aperture. In order to study these changes experimentally, we need an improved method of aperture fabrication. With a more precise production method, we will be able to model in chrome apertures the error described in the previous section. The improved aperture fabrication method we choose is electron-beam lithography. Although this technique is very similar to photolithography in concept, the application is quite different and is summarized below.

For electron-beam lithography, the desired pattern is drawn by a computer-controlled electron gun directly onto the substrate. Therefore, instead of sending artwork to the manufacturer, we send our aperture data in a format that meets the manufacturer's standards. In our case, Photo Sciences⁹ requested AutoCAD¹⁰ format. Since this software allows specification of filled polygons, conversion of our aperture design to the required format was a straightforward task. Photo Sciences used these supplied data to control the electron-beam plotter used to "write" the apertures on quartz-based photoresist. Since a negative resist was used, only the aperture interior was written.

When writing the aperture, the beam travels in only one direction relative to the substrate. Thus, rather than drawing the aperture edge and then filling this outline as was done for the photolithographic method, the beam is scanned across the substrate in

one direction and turned on when the beam coordinates lie within the aperture. The negative resist responds as described in the preceding section to the developing, coating, and etching process, and we are left with an aperture in chrome on a quartz substrate.

The accuracy of this method is superior to that of photolithography for several reasons. First, referring back to Table 5.2, we note that the two production steps that introduced the greatest error, the ink plot and the intermediate emulsion, have been eliminated. Second, the accuracy of the lithographic step is improved by using a beam with a $1\ \mu\text{m}$ spot size and $0.25\ \mu\text{m}$ positioning accuracy. The results of this overall increased accuracy is easily seen in Fig. 5.5, where the lower photos in (a) and (b) are of an aperture produced from the same design as the photolithographic aperture shown, but by electron-beam lithography. With the 10X objective, we can clearly see the shape of the designed aperture edge, with straight sides between the discrete points used to define the edge. In the photolithographic case, this crisp shape is hidden in both the tooling and the aperture by the errors introduced in the ink plot. With the 50X objective, we can see the signature of the electron beam in the scalloping along the edge. These details measure less than $1\ \mu\text{m}$ (the beam spot size); the resulting accuracy of the design reproduction is thus on the order of $1\ \mu\text{m}$.

5.3.4. Comparison of Computer Simulation and Optical Experiments

Although we have seen clearly the differences between the computer-generated design, the photolithographic aperture, and the electron-beam lithographic aperture, examination of the corresponding Fourier transforms is necessary to evaluation of the appropriateness and applicability of each method. In this section, we will compare for a single aperture the computer simulation of the Fourier transform of the aperture design, the optical Fourier transform of the photolithographically-produced chrome

aperture, and the optical Fourier transform of the aperture fabricated by electron-beam lithography. These three transforms are shown together in Fig. 5.6 for an aperture taken from the ensemble represented in Fig. 5.1, which has a $75\ \mu\text{m}$ rms roughness on a $5.0\ \text{mm}$ mean radius, a correlation angle of $\pi/8$ rad, and the triangular correlation function. The upper transform is a photograph of the optical Fourier transform of the photolithographic aperture, while the center transform photograph corresponds to the electron-beam lithographic aperture. The lower transform is a photograph of the computer simulation display, shown as before as a half transform.

The optical Fourier transforms of the two chrome apertures were recorded on Panatomic-X film². First, we compare these photographs. Looking at the spike structure shown in each, we note excellent agreement between the two optical Fourier transforms. Even the substructure on individual spikes is very similar. The differences between the two transforms are seen in the higher spatial frequencies (i.e., at larger radius values). The $7.3\ \mu\text{m}$ error introduced in the photolithographic method is detectable in these photographs. Thus in the optical Fourier transform we can see small aperture differences that are well within the limits of the ensemble. At the same time, these aperture differences do not affect significantly the transform features that we associate with the ensemble, namely, the ring fragmentation and spike structure. Therefore, despite the $7.3\ \mu\text{m}$ error in photolithographic apertures, we are confident that such apertures are appropriate for use as members of the ensembles they represent.

For completeness, we now compare our computer simulation to the two optical Fourier transforms. Again, we note excellent agreement for the transform features of interest. The spikes in all three transforms correspond not just in position but

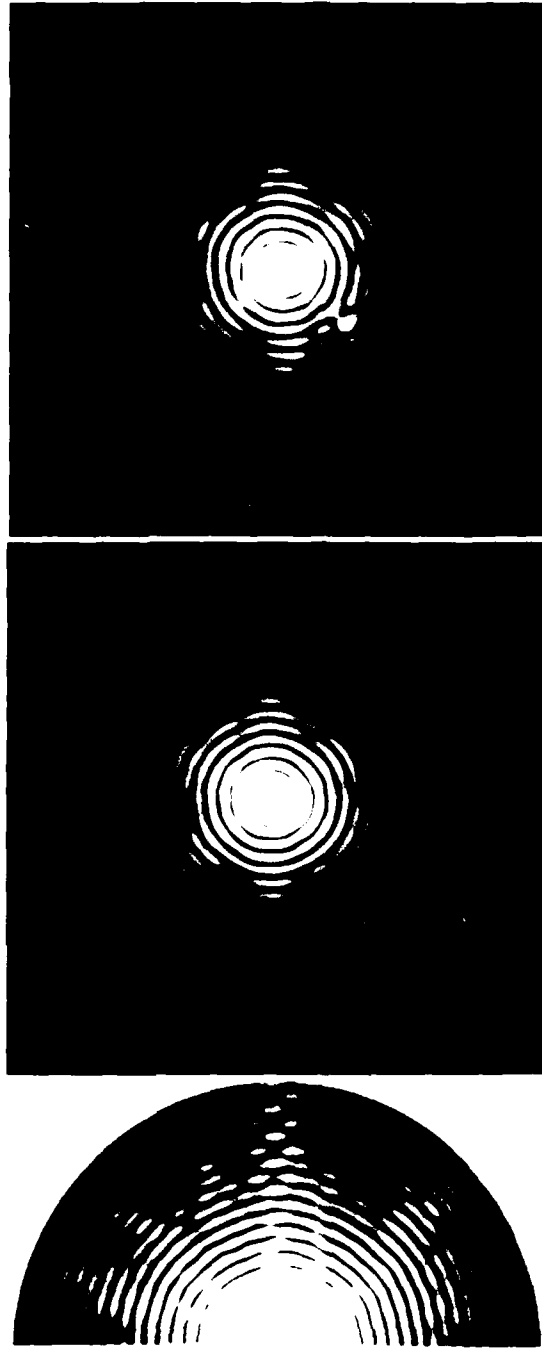


Fig 5.6 Three realizations of the transform of a single aperture design: the optical Fourier transforms of the (upper) photolithographic and (center) electron-beam lithographic apertures, and (lower) the calculated Fourier transform

in shape and substructure as well. We are confident that our computer calculation of the Fourier transforms of serrated circular apertures is correct. Consequently, the transforms of large sets of apertures, such as those shown in Fig. 5.1, can be produced quickly (and relatively inexpensively) using computer methods.

5.4. Electron-Beam Generated Masks with Controlled Deviations

5.4.1. Model of Noise in the Fabrication Process

In this last study in this chapter, we investigate more closely our ability to detect small aperture deviations in the optical Fourier transform. We design a set of apertures based on a typical serrated aperture, that of Fig. 5.6, but with noise added as follows. To each of the 512 radius values $s(\alpha_i)$ used to define the aperture edge, we add a noise term $\varepsilon(\alpha_i)$. This noise is uncorrelated and has zero angular mean. For each aperture in the set, we choose a different value for the angular rms deviation of the additive noise; these values are 0, 2, 5, 10, and 20 μm . This noise model, designed to approximate the error that noise in the aperture fabrication process might produce, is demonstrated visually in Fig. 5.7. On the left, we show a section of the original aperture; straight line segments join the discrete points used to define the aperture edge. When we add the noise term, each of the discrete points is moved a distance $\varepsilon(\alpha_i)$ along the aperture radius. On the right, then, the dashed line shows the edge of the original aperture, and the solid line traces the edge of the new, noisy aperture.

With the electron-beam technology described in Section 5.3.3, direct digital plotting is used to etch each of these noisy aperture designs in chrome on quartz. To check the reliability of the electron-beam lithography process, we include two apertures with 0 μm rms noise, *i.e.*, two copies of the original serrated aperture design. These two

apertures, as well as those to which noise was added, were placed individually in the optical Fourier transform system shown in Fig. 5.4. On Panatomic-X film², we photographed the resulting transforms; these photographs are reproduced in Fig. 5.8. For reference, the rms roughnesses that result from adding rms noise of each of these four magnitudes to an aperture with 75 μm angular rms roughness are listed in Table 5.3.

5.4.2. Fourier Transforms of Noisy Apertures

We begin by comparing the first two photographs, which show the optical Fourier transforms of the two apertures with no added noise. These two apertures, and thus the transforms, should be identical within the limits of the fabrication process. Beyond slight variations attributable to fluctuations in laser power and small differences in the framing of each photograph, this author is hard-pressed to find any disagreement

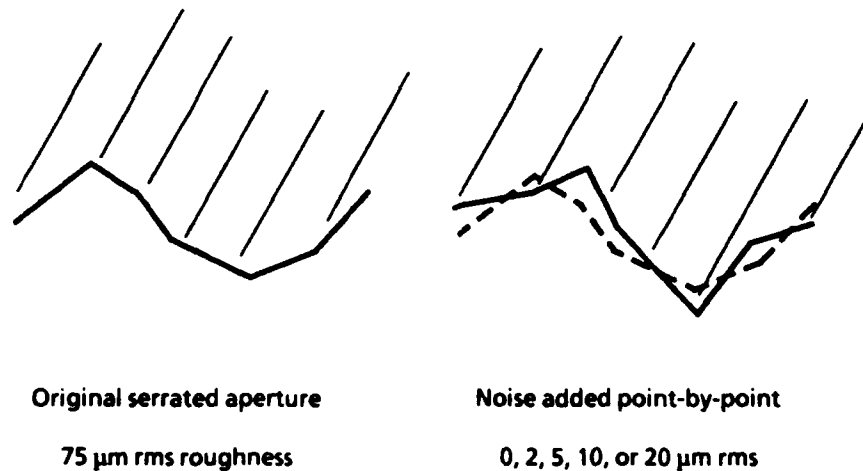


Fig. 5.7. Model used to simulate the noise introduced in fabricating serrated circular apertures for optical experiments.

between these two transforms. Thus, we continue with our examination of the transforms of this set of apertures confident that the differences we see are due to our designed noise rather than other noise sources.

From the next photograph in the series, we see that 2 μm rms noise on the aperture has a visible effect on the transforms. In particular, changes are seen in the speckle pattern at large radius values and in some of the darker regions of the transform, between the spikes. Although these differences are slight, they are visible in these photographs. As we continue through the series of transforms in Fig. 5.8, we see an increase in the number and severity of the deviations in the transforms as the added noise increases. We also find deviations closer to the center of the transform; this effect is akin to increasing the roughness on a circular aperture and seeing the effects in rings closer to the center of the transform.

In comparing these transform photographs, we can detect rms noise as small as 2 μm on the aperture, but even when the rms noise is as high as 20 μm the spike structure remains intact. There are slight changes in the spike sub-structure at higher

| Angular rms deviation of added noise (μm) | Resulting angular rms aperture roughness (μm) |
|--|--|
| 2 | 75.0 |
| 5 | 75.2 |
| 10 | 75.7 |
| 20 | 77.6 |

Table 5.3. Added rms noise and resulting rms roughness for an original aperture design with 75 μm angular rms roughness.

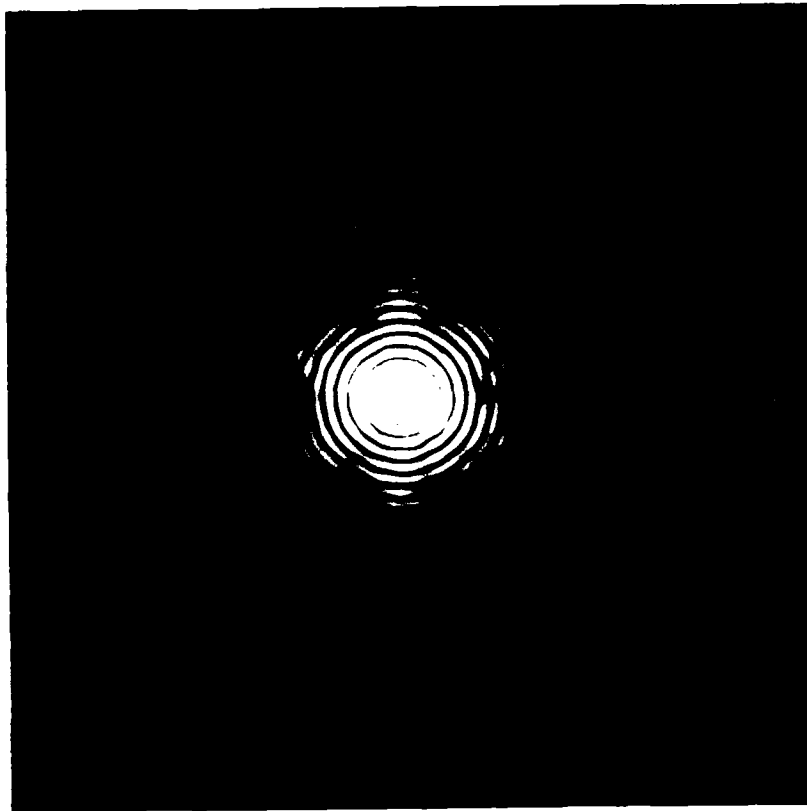


Fig 5.8 Optical Fourier transforms of serrated circular apertures with added noise. (a) 0 μm rms noise

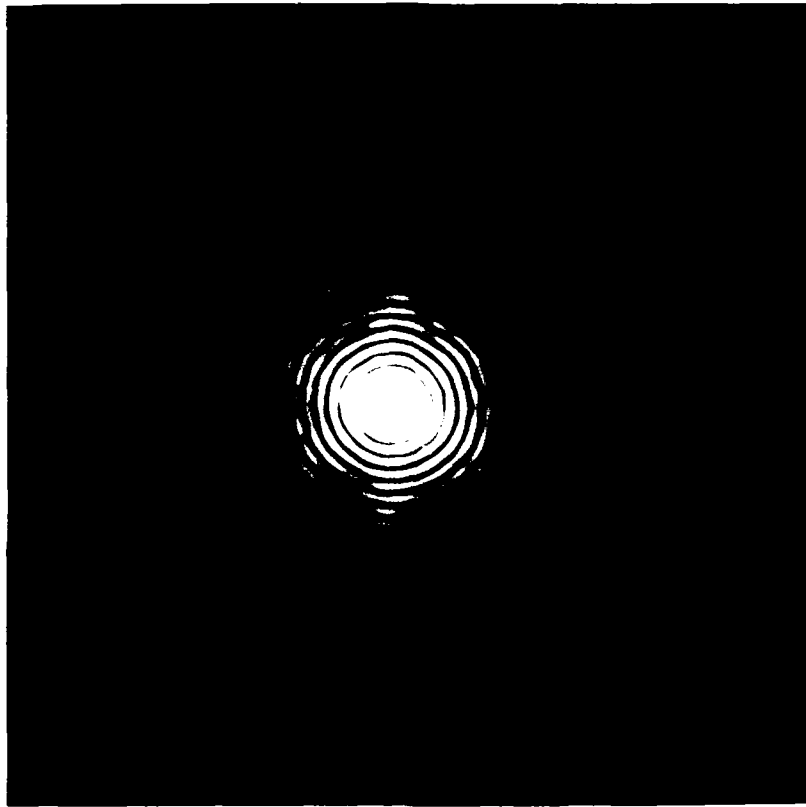


Fig 5 8 (Continued) (b) 0 μm rms noise

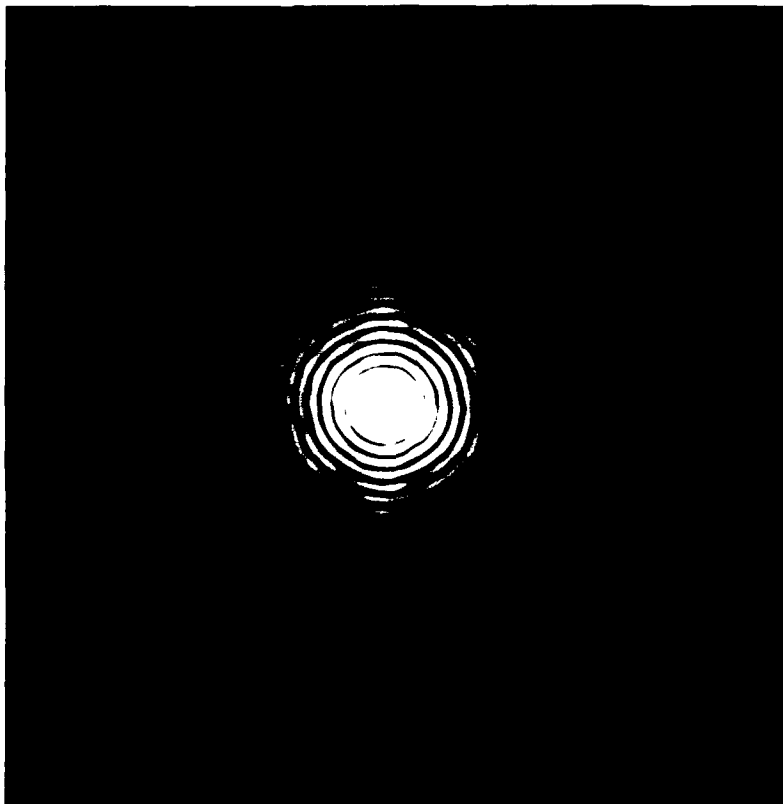


Fig. 5.8. (Continued) (c) $2\ \mu\text{m}$ rms noise

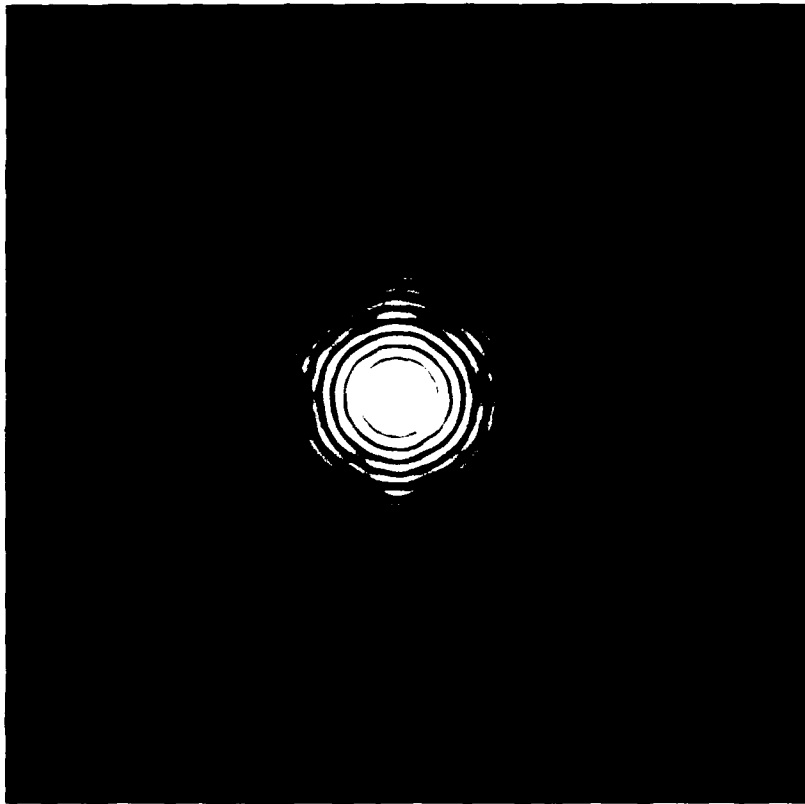


Fig. 5.8 (Continued) (d) $5\ \mu\text{m}$ rms noise

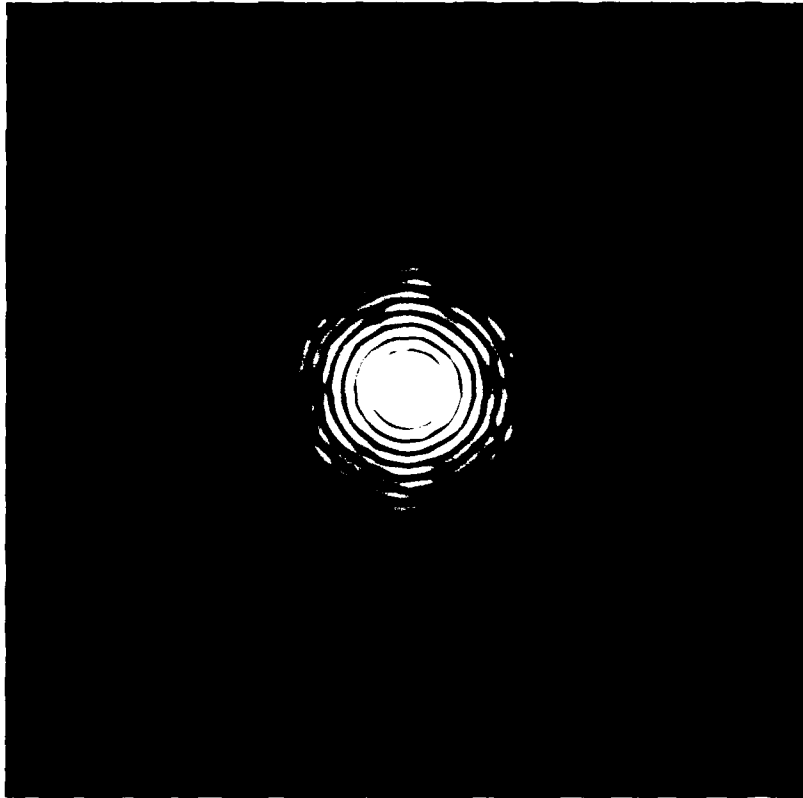


Fig. 5.8. (Continued) (e) $10\ \mu\text{m}$ rms noise.

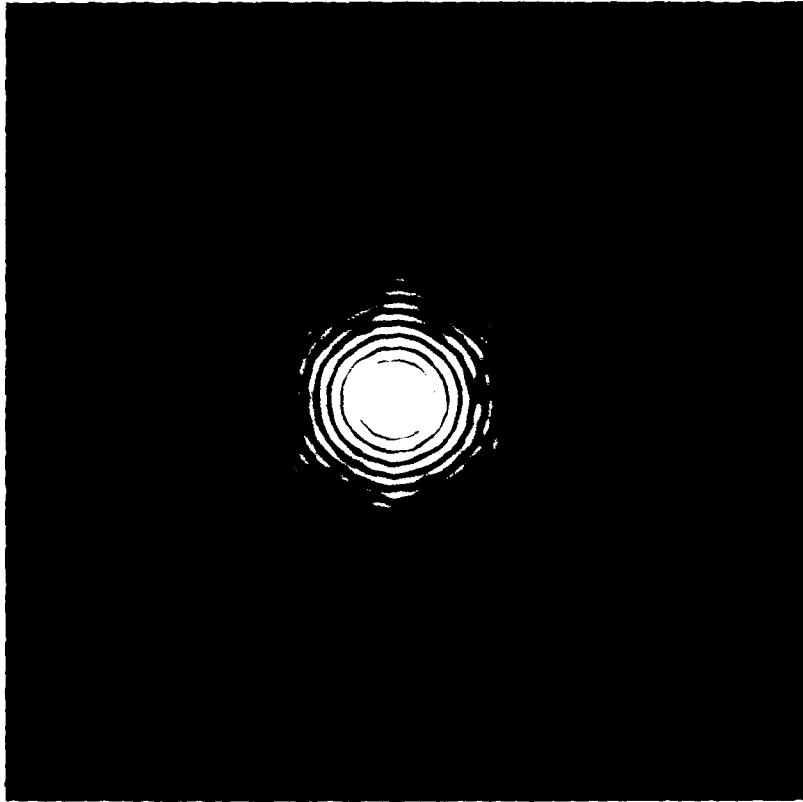


Fig 5 8 (Continued) (f) 20 μm rms noise

radius values, but if we look at the region that has been of interest to us in earlier sections, that is, near the fifteenth ring, we see no significant differences in the spike structure, even in this extreme case of 20 μm rms noise added to an aperture with 75 μm rms roughness.

5.5. Conclusions

In this chapter, we have presented four major points. First, from the examination in Section 5.2 of twelve members of an aperture ensemble and the corresponding Fourier transforms, we learned that variations within the ensemble produce noticeable differences in the spatial statistics of the individual apertures and in the Fourier transforms. The ensemble, however, is still identifiable by the grosser features of the transforms, the ring and spike structures, with some variations in these structures a natural result of variations within the ensemble of apertures. Second, we noted in Section 5.3 that some error is introduced in the fabrication of chrome apertures from our designs; the rms error was as high as 7.3 μm for the photolithographic apertures. However, the changes in the angular rms roughness of the aperture and the changes in the Fourier transform that result from this error are shown to be well within the limits of the ensemble variations. In addition, the computer simulation of the Fourier transform produces results that are comparable to those of the experiments in the regime of interest. Finally, using precise, electron-beam-lithographic apertures, we demonstrated our ability to see very small (2 μm rms) deviations in a serrated aperture by examining the optical Fourier transform. This result is encouraging for those who wish to use optical Fourier transform techniques in the analysis of precision-fabricated structures.

Chapter 5 References

1. A.M. Mood, F.A. Graybill, and D.C. Boes, *Introduction to the Theory of Statistics*, 3rd ed., McGraw-Hill, New York (1963), Ch. VI, Sect. 4.
2. Panatomic-X is a registered trademark of Eastman Kodak Company, Rochester, NY 14650. The ISO number of this black-and-white print film is 32.
3. Applied Image, Main St. Rochester, NY 14609.
4. Several sets of apertures were made by Applied Image at different times. Slight variations of the basic method described here were used for some sets.
5. M.C. King, "Principles of Optical Lithography", in *VLSI Electronics: Microstructure Science*, v. 1, ed. N.G. Einspruch (Academic Press, NY, 1981), p. 51.
6. P. Burggraaf, "Photomasks and Reticle Blanks", *Semicond. Intern.*, 38-42 (Dec. 1987).
7. Towne Labs, One U.S. Highway 206, P.O. Box 460-T, Somerville NJ 08876.
8. G.M. Morris, *Serrated Apertures: Statistical Diffraction Theory and Experiments* (Ph.D. Thesis, California Institute of Technology, 1979).
9. Photo Sciences, 2542 West 237th St., Torrance, CA 90505.
10. AutoCAD is a product of Autodesk, Inc., Sausalito, CA.

Chapter 6

Comparison of Features in the Experimental and Calculated Transforms

6.1. Introduction

Experiments in which the Fourier transform of the transmission function of a serrated aperture is obtained optically are essential to the verification of the diffraction theory presented in Chapters 2 and 4. In addition, comparing these optical Fourier transforms with computer simulations tests the limits of the computer model and of the theory. In Chapter 5, we demonstrated for one aperture the excellent agreement between the optical and calculated Fourier transforms; this preliminary result was presented in Fig. 5.6. The comparison continues in this chapter in conjunction with the investigation of the features in the transform.

The optical Fourier transform system used in these experiments is described in Section 5.3.1. We designed three sets of serrated apertures for use in studying three aperture parameters. The first set, described in Section 6.2, has varied rms roughnesses. Experiments with these apertures yield information about the dependence of ring fragmentation in the Fourier transform on the roughness of the aperture. In Section 6.3, we present apertures of varied correlation angle and the transforms of these apertures, paying particular attention to the relationship between the correlation angle of the aperture and the number of spikes in the transform. The apertures in the third set have different correlation functions. Section 6.4 contains a discussion of the appearance of the spikes in the optical Fourier transforms of these apertures and of the dependence of this appearance on the shape of the correlation function of the aperture. In each of these three cases, we compare the results of these experiments and the corresponding

computer simulation with the predictions we made in Chapter 4 about the features in the transform.

6.2. Aperture Roughness and Ring Fragmentation

The apertures in experimental set 1, which vary only in roughness, are shown in Fig. 6.1. These apertures represent four ensembles, each of which has a 5-mm mean radius, a correlation angle A of $\pi/8$ rad, and a triangular correlation function, given by

$$r_s(a'' - a') = \Lambda\left(\frac{a'' - a'}{A}\right) = \begin{cases} 1 - \frac{|a'' - a'|}{A} & , \text{ for } |a'' - a'| \leq A; \\ 0 & , \text{ otherwise .} \end{cases} \quad (6.1)$$

We used the same set of random numbers in generating each aperture design; only the roughness scaling factors differ. Table 6.1 includes the angular mean radius, the angular rms roughness, and the fractal dimension of each aperture in this set. From these designs, we fabricated photolithographic apertures for use in our optical Fourier transform

| Aperture | Angular Mean Radius (mm) | Angular RMS Roughness (μm) | Fractal Dimension |
|----------|--------------------------|---|-------------------|
| a | 4.98 | 44 | 1.01 |
| b | 4.97 | 88 | 1.02 |
| c | 4.93 | 177 | 1.06 |
| d | 4.87 | 353 | 1.24 |

Table 6.1. Statistical and fractal parameters for experimental set 1.

system. The resulting transforms, each photographed on Panatomic-X film¹, can be seen along with the apertures and computer simulations in Fig. 6.1.

When viewing these diffraction patterns, one is immediately aware of the tendency of the bright, circular Airy rings first to become uneven and then, with increased roughness, to fragment, particularly at large radius values. As discussed in earlier chapters, by fragmentation we mean that at some angular values the intensity drops essentially to zero across the annulus. The transform simulations shown in Fig. 2.6 and the intensity calculations presented in Fig. 4.9 also demonstrate this effect. In Chapter 4, we discussed the behavior of the intensity correlation function at a fixed radius as the roughness on the aperture increased, noting that the ratio of the height of the correlation peak to the background level increased under these conditions. Since the continuity of a diffraction ring depends on the behavior of the angular correlation function of the intensity at that radius, ring fragmentation is a feature related to the correlation of the transform. Therefore, it is a useful measure of the effects of aperture roughness on the correlation in the Fourier transform.

With the two-dimensional diffraction patterns shown in Fig. 6.1, There are two easy ways to see the correlation effects described above. First, we can choose a particular ring and watch what happens to it as the roughness on the aperture changes. This is what we did with the plots of intensity versus angle at a fixed radius for varied aperture roughness, shown in Fig. 4.9. The other choice is to pick a level of degradation, e.g., the first ring in a diffraction pattern to become fragmented, and find the location of that feature in each transform.

Performing this task for the optical Fourier transforms shown in Fig. 6.1, we find that the following rings are the first to break in each transform: for 44 μm rms

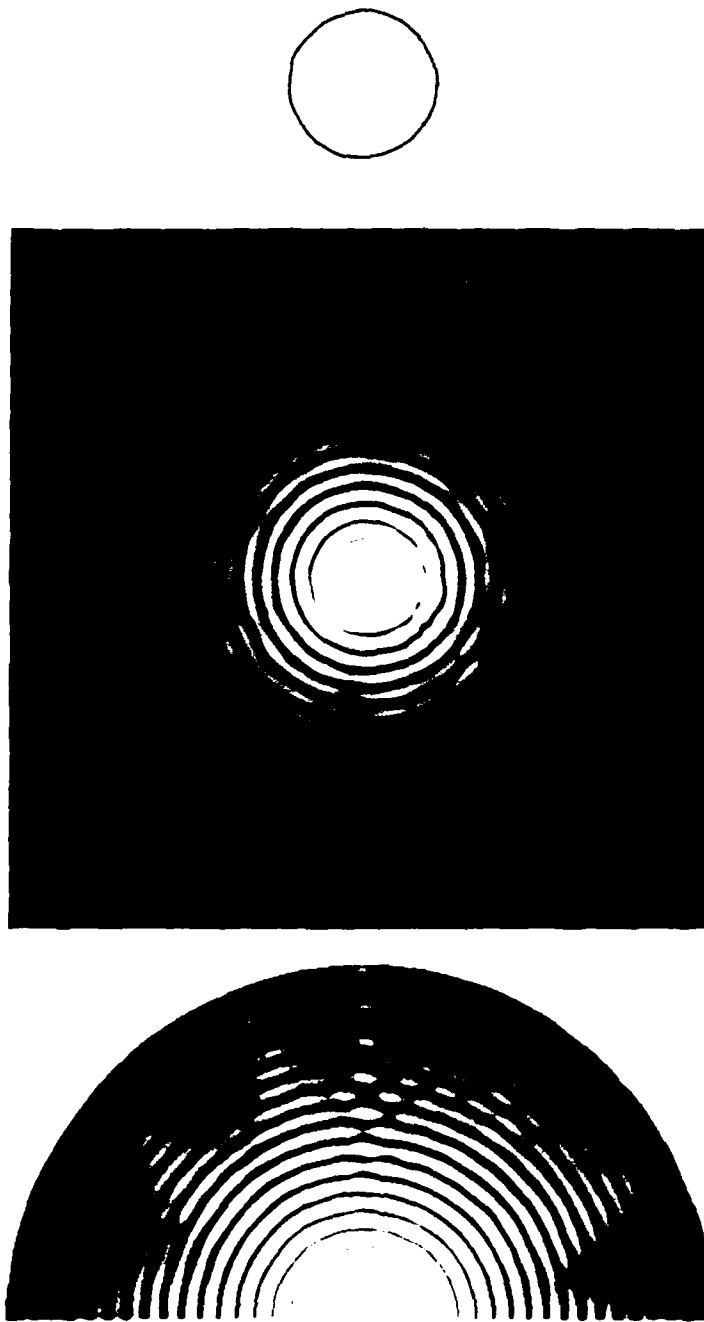


Fig. 6.1 (a) (Upper) Apertures from experimental set 1, with (center) optical and (lower) calculated transforms. For each aperture in this figure, the correlation function is triangular, defined in Eq. (6.1), with A equal to $\pi/8$ rad. Each ensemble mean radius is equal to 5.0 mm; the angular mean radius and rms roughness of each aperture is listed in Table 6.1. The rms roughness for this aperture is 44 μm .

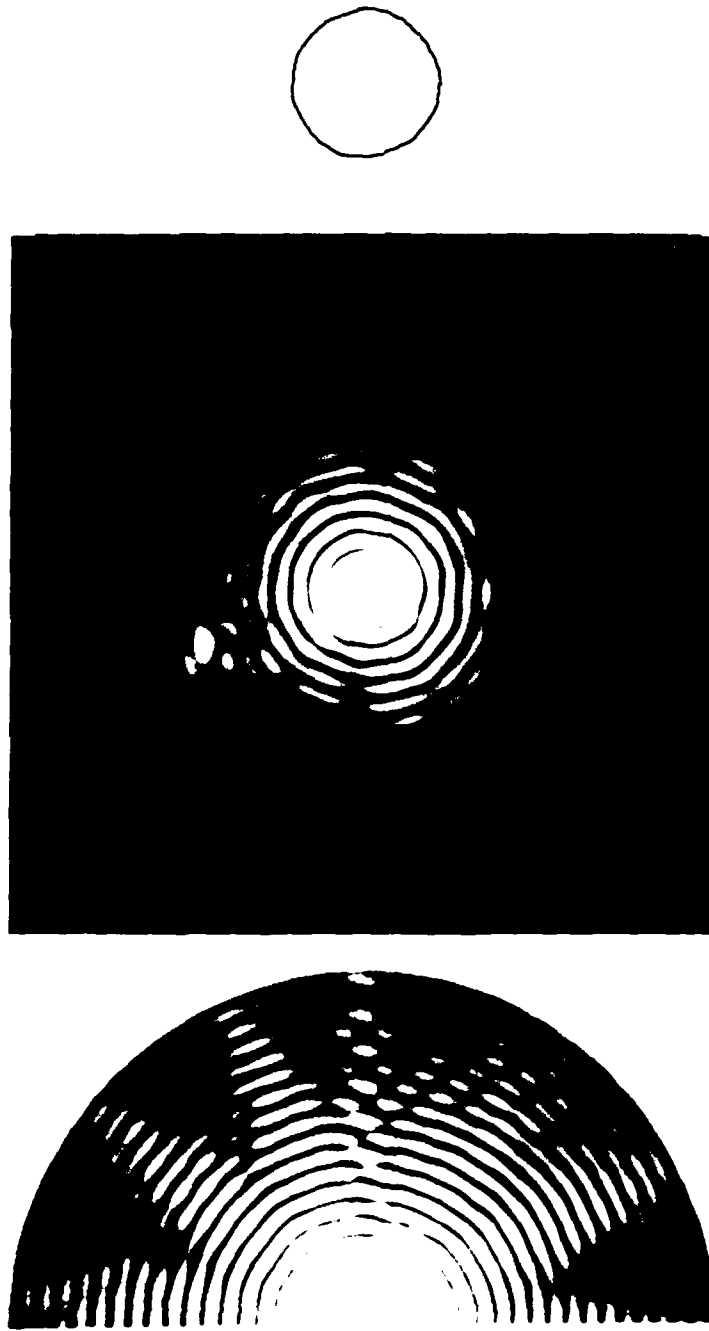


Fig. 6.1. (b) The rms roughness of the aperture is $88 \mu\text{m}$.

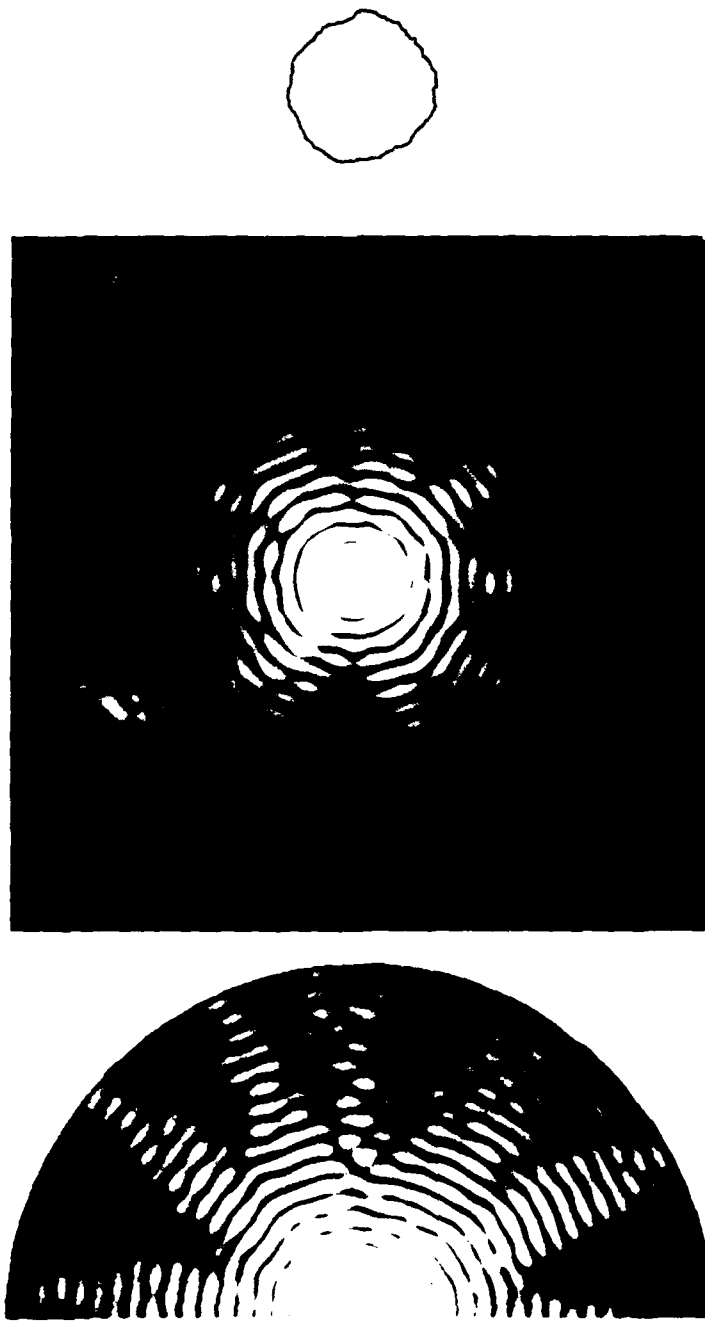


Fig. 6.1. (c) The rms roughness of the aperture is $177\ \mu\text{m}$.

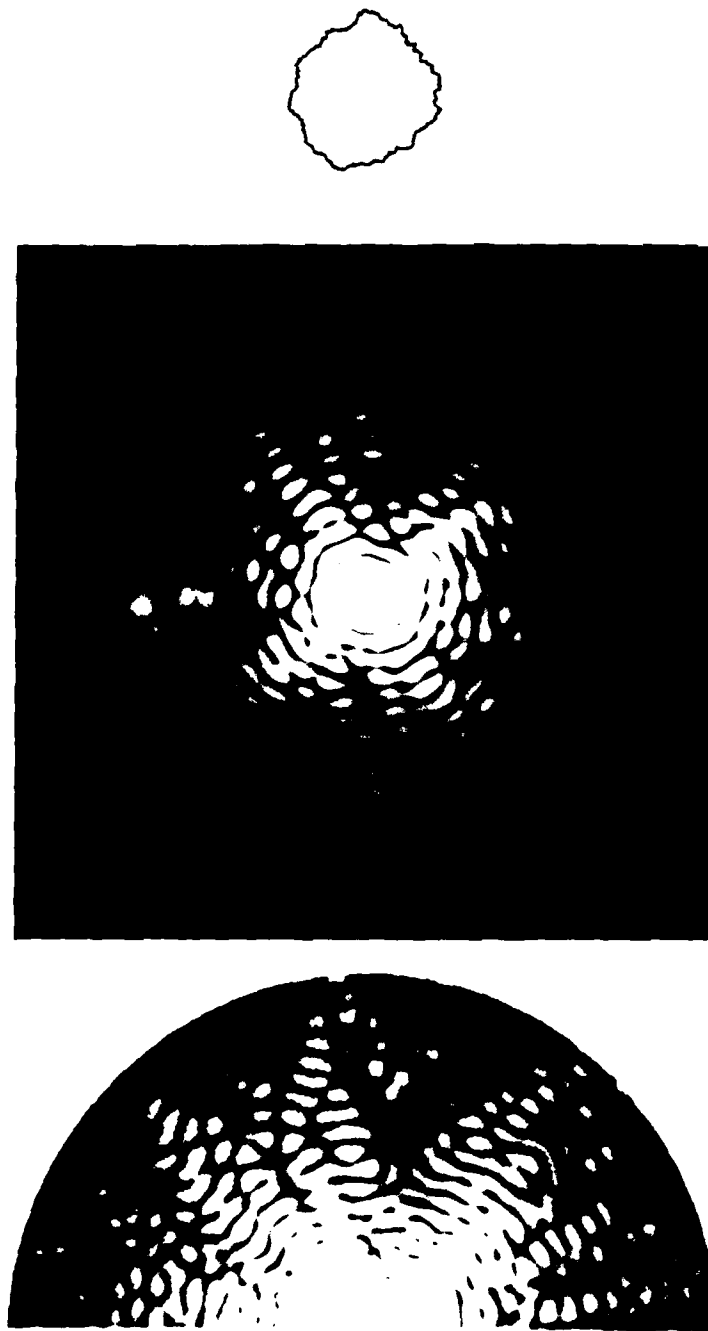


Fig. 6.1. (d) The rms roughness of the aperture is $353 \mu\text{m}$.

roughness, ring 15; for 88 μm , ring 11; for 177 μm , ring 8; and for 353 μm , ring 3. This measure is subjective and depends on the photographic exposure chosen for each diffraction pattern. However, with this technique we can quickly and easily determine the effects of aperture roughness on the Fourier transform.

The computer simulations displayed in Fig. 6.1 compare well with the photographs from the optical experiments. At the feature level, the patterns show excellent agreement. The spikes in both cases fall in the same position and have similar sub-structure. Dark regions in the two transforms also correspond well. The order of the first fragmented ring in each of the computer simulations agrees closely with the corresponding experimental result. As discussed in Chapter 4, complete agreement in the details of two corresponding transforms is neither found nor expected. In particular, in the experimental patterns we note asymmetries that are due to defects in the glass substrate which introduce phase errors to the wavefront in the aperture plane. However, the excellent comparison of the symmetric features over the wide range of roughness values shows that our theory and computer model accurately represent the optical Fourier transform at our level of interest.

6.3. Correlation Angle of the Aperture Serration and the Number of Transform Spikes

In Section 4.4.3, we found that an increase in the correlation angle of the aperture corresponds to an increase in the correlation angle of the diffracted field. The apertures in experimental set 2, designed to address this point, have all parameters fixed except the correlation angle. These apertures, shown with the corresponding optical and calculated transforms in Fig. 6.2, represent ensembles that have correlation angles of $\pi/16$, $\pi/8$, and $\pi/4$ rad. Each of the ensembles from which these apertures are taken has a triangular correlation function, given by Eq. (6.1), an rms roughness of 75 μm , and a mean

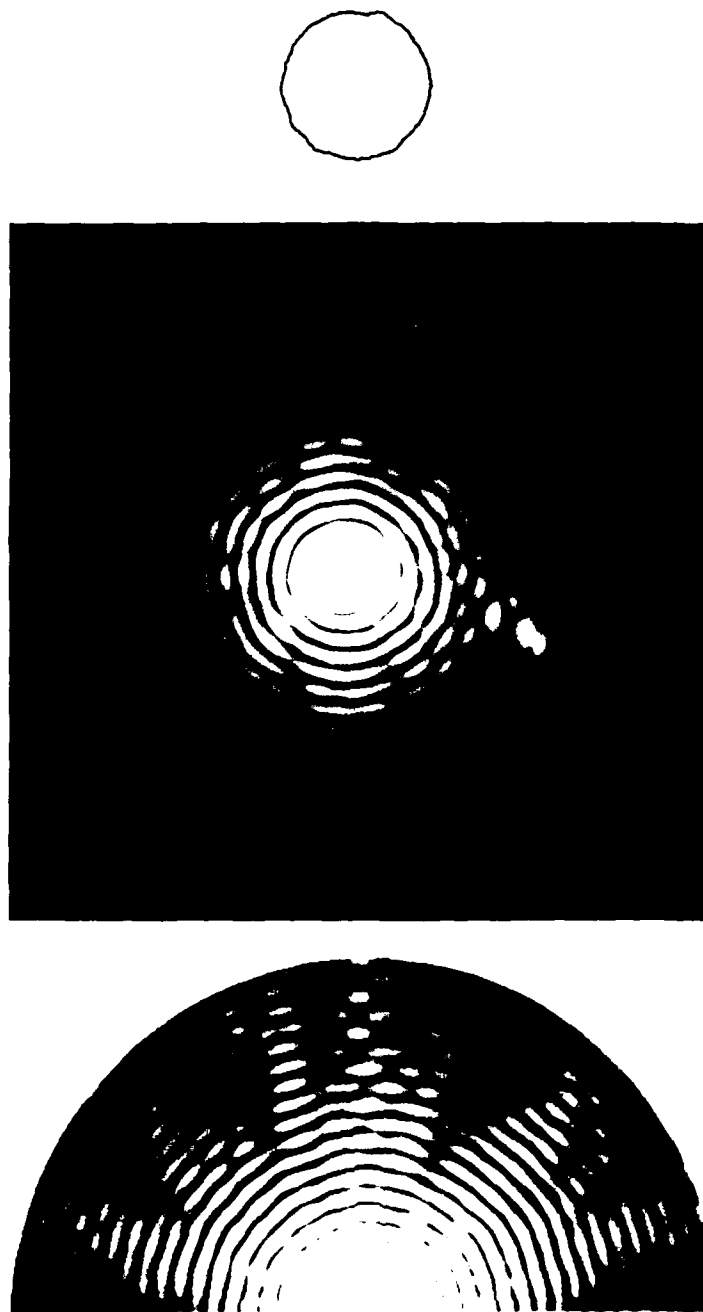


Fig. 6.2. (a) (Upper) Apertures from experimental set 2, with (center) optical and (lower) calculated transforms. The three apertures in this figure represent three ensembles; for each ensemble, the correlation function is triangular, given by Eq. (6.1); the mean radius is equal to 5.0 mm; and the rms roughness is 75 μm . Here, the correlation angle on the aperture is $\pi/16$ rad.

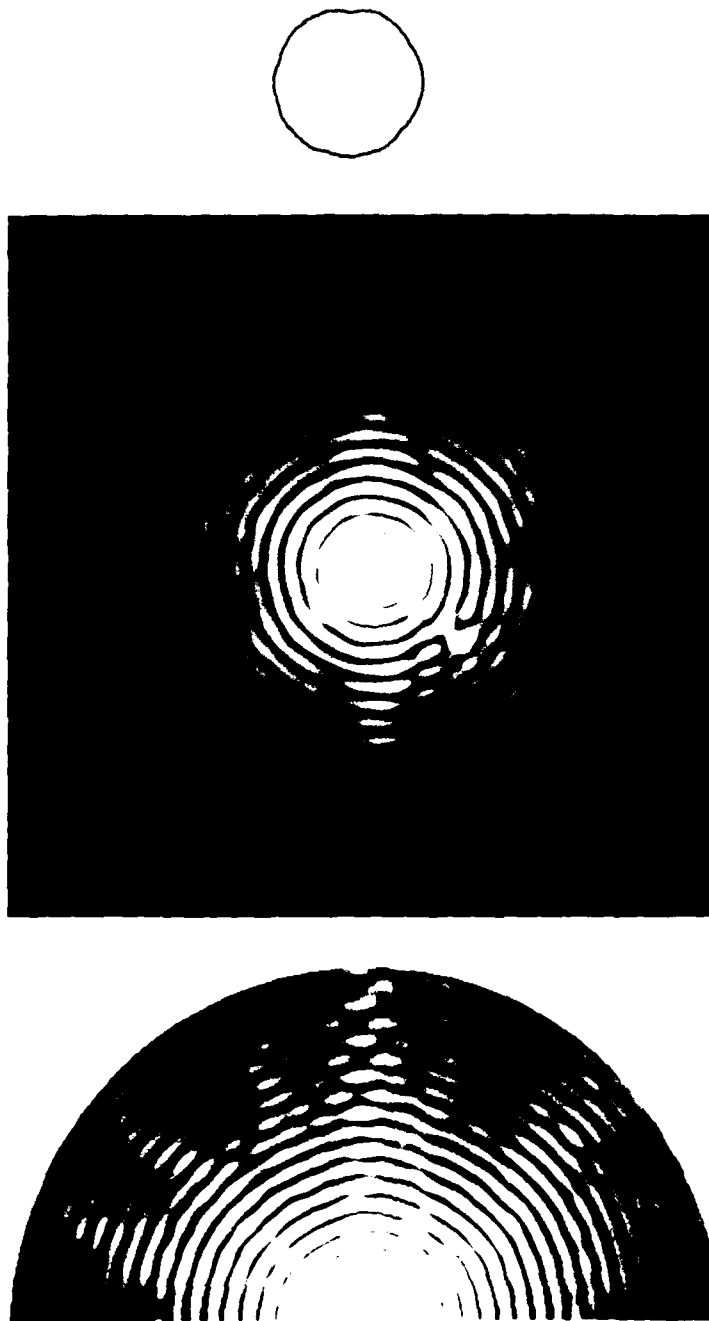


Fig. 6.2. (b) α equal to $\pi/8$ rad.

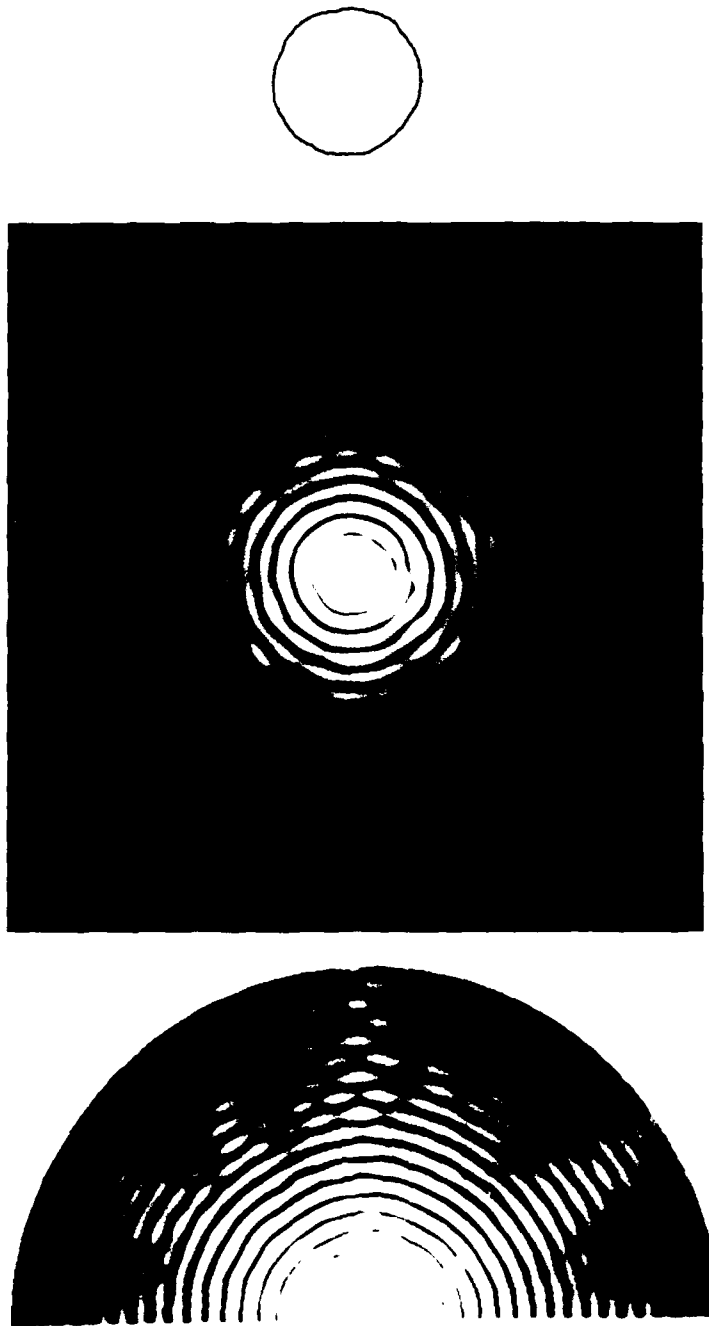


Fig. 6.2. (c) α equal to $\pi/4$ rad.

radius of 5.0 mm. In generating each of the three apertures in experimental set 2, we used the same starter set of uncorrelated random numbers.

In the corresponding series of Fourier transforms, we note a decrease in the number of spikes in the transform with the increase in the correlation angle of the aperture. We noted with Fig. 4.6 that the spikes must be counted at a fixed radius from transform to transform for consistency. In Fig. 6.2, we see some spikes that split as the radius increases. The reader who is unsure how to count such a spike, as one or as two or more, will recognize the importance of fixing the output radius before counting. We choose to count spikes at the fifteenth ring, as we did in Chapter 4, so that we might establish the level of agreement between counting spikes in a photograph and counting from a plot.

In the photographs of the optical Fourier transforms, then, we count 18 spikes in the full transform (0 to 2π) when A is equal to $\pi/16$ rad, 16 for A equal to $\pi/8$ rad, and 14 for A equal to $\pi/4$ rad. These values are close to the spike counts made in Fig. 4.1, where 18, 16, and 16 spikes were found at the fifteenth ring of the Fourier transform for these same aperture designs. The subjectivity of counting spikes in a photograph is most likely responsible for this discrepancy. To check this, we count the spikes in the calculated Fourier transforms shown in Fig. 6.2; at the fifteenth ring, the calculated values here are the same as those in the plots in Fig. 4.11. Doubling the number of spikes seen in each half transform displayed, we find 18 spikes for A equal to $\pi/16$ rad, 16 for A equal to $\pi/8$ rad, and 14 for A equal to $\pi/4$ rad, the same as the numbers found for the optical Fourier transforms. In the two-dimensional display of the calculated transform, we lose some of the objectivity of the analysis, but gain an understanding of the discrepancies between the photographs from the optical experiments and the curves of intensity versus angle shown in Chapter 4.

The calculated and optical Fourier transforms in Fig. 6.2 show excellent agreement in the remainder of the transform as well. If we look closely at the series of photographs in Fig. 6.2, we note that the spikes in each case have similar positions. The change from one pattern to the next is the broadening and overlap of some spikes as the correlation angle of the aperture increases. A similar effect takes place for the apertures. With increased correlation angle, the very jagged edge on the aperture with $\pi/16$ rad correlation angle becomes smoother through a broadening of the features on the edge, while the ensemble roughness remains constant.

6.4. Correlation Function of the Aperture Serration and Spike Appearance

With this last set of apertures, we study the relationship between the shape of the correlation function of the aperture and the appearance of the spikes in the Fourier transform. The plots shown in Fig. 4.12 demonstrate changes in the two-point intensity moment that correspond to changes in the correlation function of the serration. At a fixed radius, the sharper aperture correlation produced a sharper transform correlation. The Fourier transforms of aperture set 3 will show the effect this correlation shape has on the diffracted intensity.

The three apertures in this set, shown in Fig. 6.3, represent three ensembles with different correlation functions. Each ensemble has $75 \mu\text{m}$ roughness on a 5 mm mean radius and a correlation angle (A in the equations below) of $\pi/8$ rad. The correlation functions are triangular, given by Eq. (6.1),

$$r_s(a'' - a') = \Lambda \left(\frac{a'' - a'}{A} \right) = \begin{cases} 1 - \frac{|a'' - a'|}{A} & , \text{ for } |a'' - a'| \leq A ; \\ 0 & , \text{ otherwise ;} \end{cases} \quad [(6.1)]$$

negative exponential,

$$r_s(\alpha'' - \alpha') = n \exp [(\alpha'' - \alpha') / A] = \exp (-|\alpha'' - \alpha'| / A) ; \quad (6.2)$$

and Gaussian,

$$r_s(\alpha'' - \alpha') = G [(\alpha'' - \alpha') / A] = \exp [- ((\alpha'' - \alpha') / A)^2] . \quad (6.3)$$

Two of these, the triangular and negative exponential functions, have moderately sharp peaks, with slopes of $\pm 1/A$ in the limit as $\alpha'' - \alpha'$ approaches zero. The Gaussian function has a smooth peak, with a slope of zero when $\alpha'' - \alpha'$ is equal to zero.

There are pronounced likenesses in all three apertures, as seen in Fig. 6.3. Each aperture has the same basic non-circular shape; this arises from the use of the same starter set of random numbers, correlation functions of comparable width, and equal rms roughnesses in the design. The first two apertures, however, show jagged edges; the irregularities are similar for the two because of the equality of the slopes of the correlation functions in the limit as $\alpha'' - \alpha'$ approaches zero. The Gaussian-correlated aperture, however, has a smooth edge, corresponding to the zero slope of the correlation angle at $\alpha'' - \alpha'$ equal to zero.

The optical Fourier transforms, shown with each aperture in Fig. 6.3, fall into the same grouping. The spikes in the transforms of the first two apertures are similar to each other in appearance; beyond the fifteenth ring, they break into narrower spikes. The spikes in the transform of the aperture with the Gaussian correlation function remain single spikes as far out in the transform plane as is shown in these photographs. The number of spikes in a given transform at different radius values gives us information about the shape of the correlation function of the aperture. In the apertures shown, an

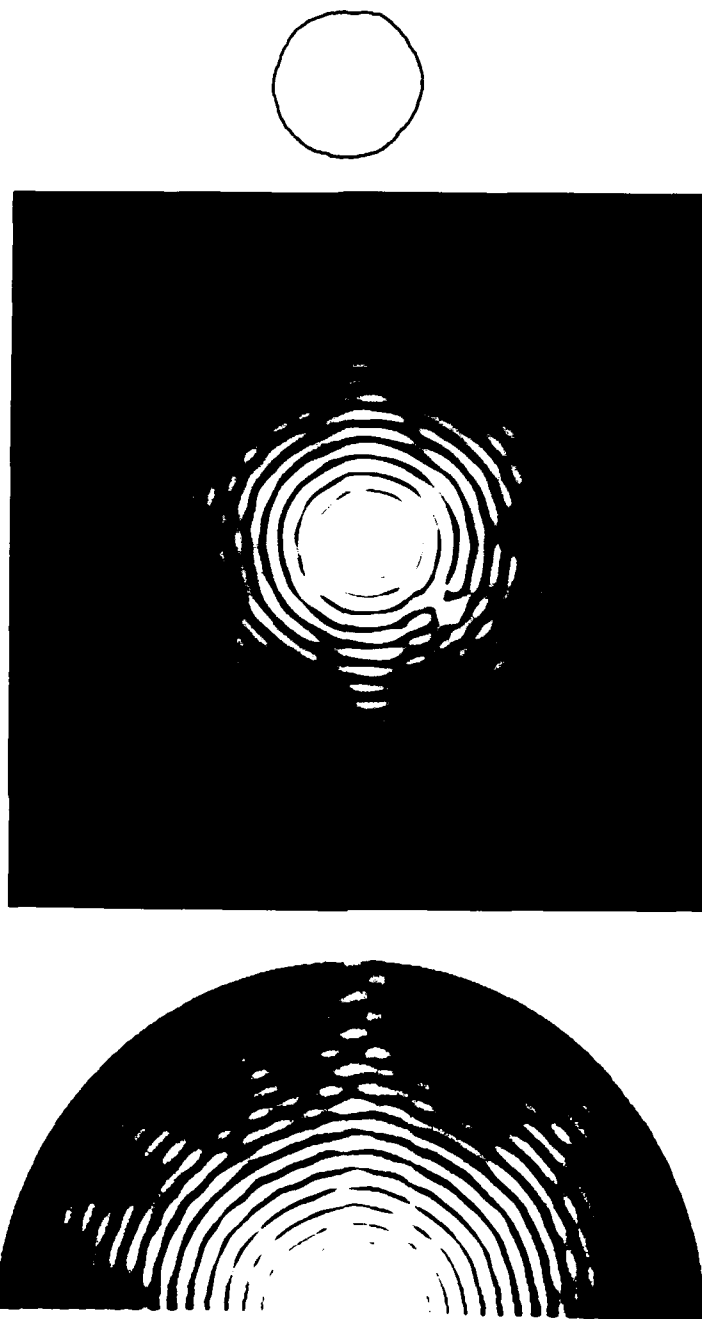


Fig. 6.3. (a) (Upper) Apertures from experimental set 3, with (center) optical and (lower) calculated transforms. Each ensemble represented has a 5.0 mm mean radius, a 75 μm roughness, and a $\pi/8$ correlation angle. Shown here is the aperture with the triangular correlation function, given by Eq. (6.1).

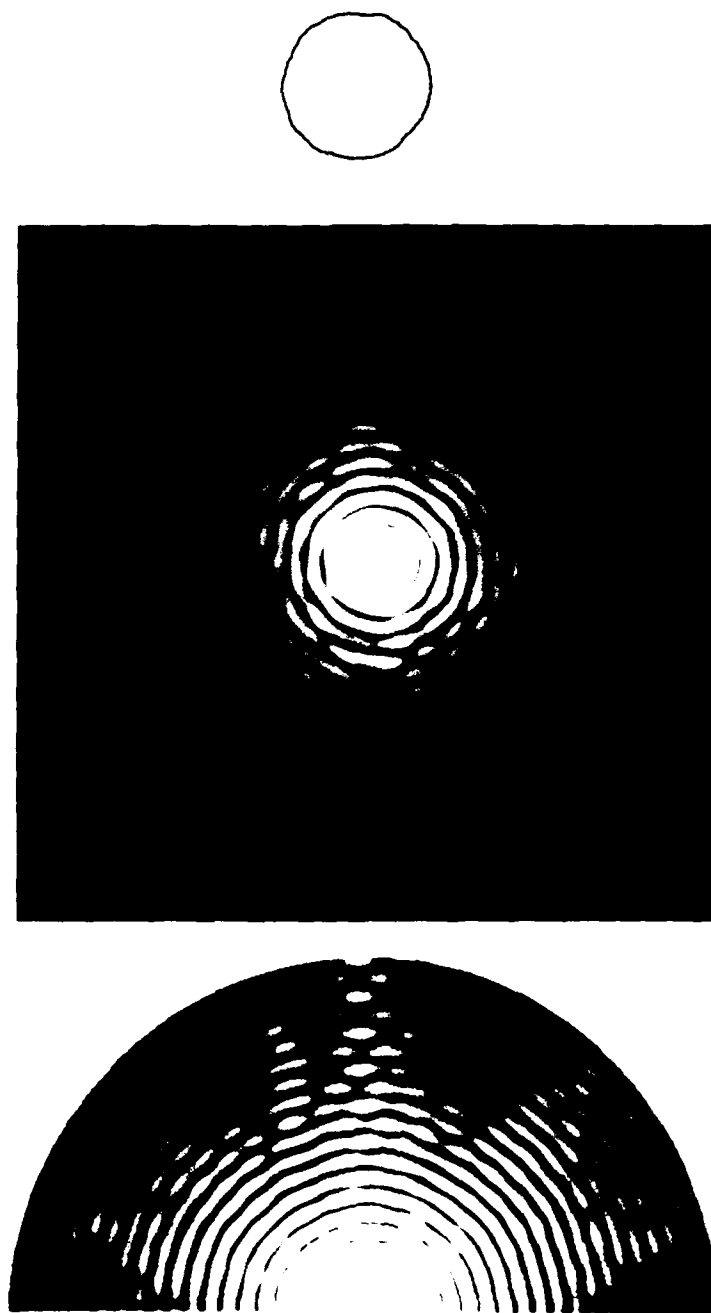


Fig. 6.3. (b) The aperture has a negative exponential correlation function, given by Eq. (6.2).

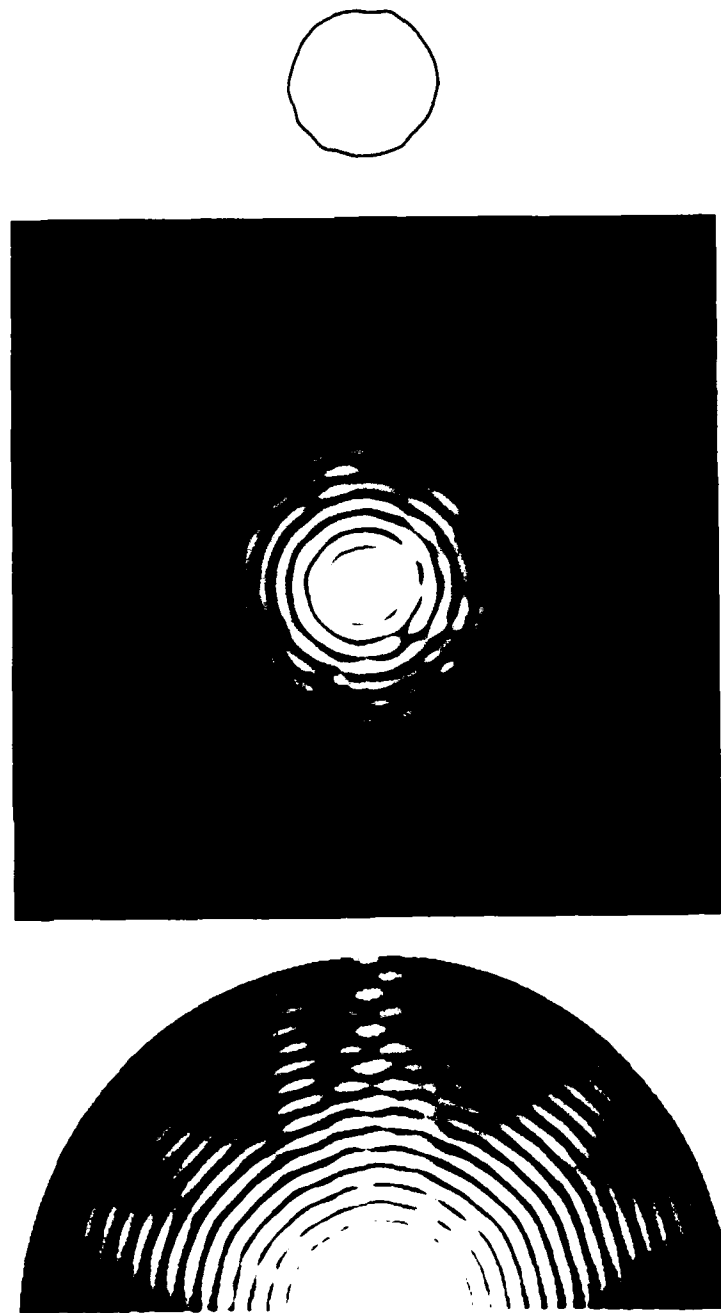


Fig. 6.3. (c) The aperture has a Gaussian correlation function, given by Eq. (6.3).

increase from ring 12 to ring 18 indicates a sharp-peaked correlation function, while a constant number of spikes corresponds to the Gaussian correlation function.

Once again, there is excellent agreement between the features in the optical and calculated transforms. Since all the transforms shown in Fig. 6.3 have the same spike positions, the comparison of the calculation and the experiment show the ability of the computer model to match the finer substructure in the spikes. In the computer simulations, the difference in the appearance of the spikes for different aperture correlations is more pronounced than in the optical Fourier transforms. We attribute this effect to the lack of significant noise in the computer model. Since the edge of the Gaussian-correlated aperture is smooth, the $7.3 \mu\text{m rms error}^2$ on the apertures produced by the photolithographic method is more noticeable in this optical Fourier transform. The limitation of this computer simulation is the inability to reproduce the effects of fabrication errors. For some applications this limitation is an advantage.

6.5. Conclusions

The results of both the optical experiments and the computer simulations presented in this chapter support our theory-based predictions, given in Chapter 4, for the features of the Fourier transform of the serrated circular aperture. The following statements summarize the main points of this chapter.

As a circular aperture is roughened, the familiar rings of the Airy diffraction pattern show unevenness and fragmentation, especially at larger radius values. As the roughness increases, the serration affects the rings with smaller radii. We predicted that the radial location of the first fragmented ring would be inversely proportional to the rms

roughness. This relationship is supported by a set of apertures of varied roughness and the related transforms, shown in Fig. 6.1.

Changes in the serration correlation angle of an aperture alter the correlation angle and spike structure of the optical transform. As the serration correlation angle decreases, the intensity correlation angle also decreases, resulting in more rapid angular variations in intensity and thus an increase in the number of spikes in the transform. We see these effects in the Fourier transforms shown in Fig. 6.2. Increases in the width of the spikes and the resulting overlap reduce the number of spikes as the correlation angle of the aperture increases.

The shape of the peak of the serration correlation function affects the shape of the angular correlation function of the intensity in the transform. As seen in Fig. 6.3, this shape influences the appearance of the transform spikes. Smooth-peaked correlation functions correspond to angularly smooth spikes in the transform. Another method used to identify this feature is counting the number of spikes at different radial positions in a given diffraction pattern. If this number increases significantly, the correlation function is likely to have a sharp peak.

These results are valid for both the optical experiments and the computer simulations. In addition, we note excellent agreement between the features seen in the two transforms, optical and calculated, over the wide range of aperture parameters investigated. We conclude that our theory and computer model are accurate in the regime of interest.

Chapter 6 Notes and References

1. **Panatomic-X is a registered trademark of Eastman Kodak Company, Rochester, NY 14650. The ISO number of this black-and-white print film is 32.**
2. **See Section 5.3.2.**

Summary

As stated in the Introduction, we have had two primary objectives in this study of serrated circular apertures. The first was to determine the relationship between the parameters of the aperture and the features of the optical Fourier transform. Our second objective was to understand the relationship between the statistical and fractal descriptions of the aperture. Understanding both the optical Fourier transform and the fractal attributes of the serrated aperture has yielded new insights into the interplay of the statistical parameters of the aperture. In this summary, we present the major conclusions of this research.

We began our discussion in Chapter 2 by defining a serrated circular aperture by means of the radius function in cylindrical coordinates, $r_c = a + s(\alpha)$, where (r_c, α) is a point on the aperture edge, a is the average aperture radius, and $s(\alpha)$ is the zero-mean function that describes the aperture serration as a function of the angular coordinate. The formulation of the Fourier transform of the serrated circular aperture in terms of $s(\alpha)$ is presented here. We used the analytic signal representation of the diffracted field and kept the wavelength dependence explicit.

The important parameters of the serration, namely, the rms roughness, correlation angle, and correlation function, are determined from $s(\alpha)$. After describing a computer technique used to generate apertures with specific statistical parameters, we showed examples of aperture sets in which each aperture parameter was varied in turn. In order to see quickly the effects of variations in the roughness, correlation angle, and correlation function of the serration on the transform, we performed a computer simulation of the optical transform intensity for several apertures. These images demonstrate the degradation of the familiar Airy ring pattern with increased aperture

roughness. The number and structure of the spikes in the transform change with variations in the width and shape of the correlation function of the serration are varied.

In Chapter 3, we presented our study of the relationship between the statistical and fractal descriptions of the aperture. Two methods, namely, Richardson curves and grid interrogation, are used to determine the fractal dimensions of serrated apertures. The fractal dimension of the aperture increases as the rms roughness increases and decreases as the correlation angle of the serration increases. In the Richardson curves in particular, there is evidence of structural differences in the apertures at different levels of scrutiny. When measured with a scale finer than the design resolution, a serrated aperture is a Euclidean object with a fractal dimension of 1. For a range of measurement scales bounded approximately by the design resolution below and by the correlation angle above, the Richardson curve describes the fractal structure of the edge roughness. At lower resolutions, the Richardson curve shows the fractal nature of the overall noncircular shape of the aperture.

When we applied these methods to apertures with varied correlation functions, the evidence of structural differences at different resolutions was supported further. The Richardson curve for the Gaussian-correlated aperture, which is noncircular but smooth-edged, reached the Euclidean limit quickly as the resolution increased, whereas the other apertures continued to demonstrate a fractal structure.

For completeness, we included in our investigation a study of the Weierstrass function, a mathematically-defined function which possesses fractal characteristics, and several variations of this function that have been used to model physical objects. The definition of the Weierstrass function includes a parameter D_w that has been promoted by some authors as the fractal dimension of the function. Our results show that

this claim is valid for the original function but not necessarily valid for scaled and bandlimited versions. Scaling and/or bandlimiting the function affects the statistical properties of the function and also the fractal dimension, as is expected from our results for serrated apertures.

The last aspect of this investigation of the statistical-fractal relationship that we discussed was the dependence of the fractal dimension on the ratio of the rms roughness σ to the correlation length d . For serrated edges, we have shown graphically that the fractal dimension increases as the ratio of the spatial rms roughness σ_h to the correlation length L increases, but that this relationship depends strongly on the correlation function of the serration. Sharp-peaked correlation functions result in a more rapid increase in the fractal dimension of the aperture as the ratio σ_h / L increases than that produced by apertures with smooth-peaked correlation functions. This evidence corresponds well with our uninformed expectations. If the fractal dimension is a measure of the smoothness of an aperture, then we expect the fractal dimension of the serration to increase when the roughness increases, when the correlation angle decreases, and when the correlation function is sharpened. Overall, the results of this study of the fractal dimension of a serrated aperture have shown that apertures with very different statistical parameters can have the same fractal dimension, and that one must therefore be cautious in defining and describing apertures fractally.

In Chapter 4, we presented our calculations for the two-point intensity moment $\langle I(\rho_1, \phi_1) I(\rho_2, \phi_2) \rangle$ of the Fourier transform, which contains essential information about the correlation properties of the diffracted field and the dependence of these properties on the parameters of the aperture. To simplify the calculations, the two-point intensity moment, which is a fourth-order moment of the scalar field, was

expanded into a sum of second-order moments through use of a Gaussian moment theorem. Due to the polar symmetry of the Fourier transform, two of the four terms in the moment expansion contain the two-point attributes of the fourth-order moment. This is in contrast to the case of circular complex Gaussian statistics, in which only one term contributes to the correlation properties. The two terms of interest are identical but for a π rotation. Thus, detailed study of only one of these second-order moments, μ_{12} , leads to an understanding of the transform properties.

In μ_{12} , which is expressed in integral form, we identified parts of the integrand which contribute significantly to the magnitude and shape of the field correlation. These terms depend on the roughness, correlation angle, and correlation function of the aperture serration; therefore, features in the Fourier transform which correspond to each of the three statistical parameters of the aperture can be extracted from the theory. The features identified were the ring fragmentation, the number of spikes, and the spike appearance. From our expression for μ_{12} , we predicted that as roughness increased there would be a decrease in the smallest radius at which the rings in the transform pattern would become fragmented due to the serration. We also predicted an increase in the correlation angle of the transform with an increase in the correlation function of the aperture, and that the shape of the transform correlation function would be smoother for smoother serration correlation functions. These changes in the width and shape of the transform correlation function would be seen in the number and appearance, respectively, of the spikes in the transform. Plots of the two-point intensity moment for several ensembles with varied aperture parameters and of the intensity for representative members of these ensembles support this feature identification.

Chapter 5 contains a discussion of the processes used in fabricating serrated circular apertures. Apertures made with photolithography and electron-beam lithography, and the corresponding optical Fourier transforms, are studied and compared; the following conclusions are drawn. The photolithographic process introduces $7.3 \mu\text{m}$ rms error, but the resulting apertures are still well within the limits of the design ensemble and the apertures are therefore suitable for our experiments. Electron-beam lithography produces much more accurate apertures, mostly because of the elimination of intermediate steps between the design and the final apertures. Computer simulation of the Fourier transform of a particular aperture compares well in the regime of interest with the two transforms obtained experimentally; the ring and spike structures that are characteristic of the transforms of an ensemble of apertures are not affected by the differences in these three methods. However, the details of the transforms are affected by rms errors as small as $2 \mu\text{m}$ on the aperture; the ability to see the effects of these errors indicates the potential of optical Fourier transform techniques in the analysis of precisely fabricated structures.

The results of optical experiments using apertures from ensembles of varied roughness, correlation angle, and correlation function are reported in Chapter 6. The computer simulations of the transforms of these apertures show excellent agreement with the optical Fourier transforms from the experiments over the wide range of serration parameters covered by these apertures. Both types of transforms support the theory-based predictions concerning the features of the transform and the parameters of the serration on the aperture. The rings in the transforms are seen to fragment at smaller radii as the roughness increases. The number of spikes increases as the correlation angle of the serration decreases, demonstrating a decrease in the correlation angle of the Fourier transform. When the correlation function of the serration has a smooth peak, the

spikes in the transform do not break into smaller spikes as the distance from the center of the transform increases, at least not in the region in which we are interested. The resulting spikes appear to be smooth compared to those corresponding to a sharp-peaked aperture correlation. In the latter case, the number of spikes increases as the output radius increases.

Bibliography

- K.J. Allardyce and N. George, "Diffraction analysis of rough reflective surfaces," *Appl. Opt.* **26**, 2364-2375 (1987).
- H.H. Arsenault, ed., *International Conference on Speckle*, Proc. SPIE **556** (1985).
- M.M. Beal and N. George, "Features in the optical transforms of serrated apertures and disks," *J. Opt. Soc. Am. A* **6** (1989).
- E. Berry, "Making a multiscale random rough surface," *Optica Acta* **32**, 147-153 (1985).
- M.V. Berry, "Diffractals," *J. Phys. A: Math. Gen.* **12**, 781-797 (1979).
- M.V. Berry and T.M. Blackwell, "Diffractal echoes," *J. Phys. A: Math. Gen.* **14**, 3101-3110 (1981).
- M.V. Berry and Z.V. Lewis, "On the Weierstrass-Mandelbrot fractal function," *Proc. Roy. Soc. Lond. A* **370**, 459-484 (1980).
- C. Bourrely, B. Torresani, and P. Chiappetta, "Scattering of an electro-magnetic wave by an irregularly shaped object," *Opt. Commun.* **58**, 365-368 (1986).
- R.N. Bracewell, *The Fourier Transform and its Applications* (McGraw-Hill, New York, 1985).
- P. Burggraaf, "Photomasks and Reticule Blanks," *Semicond. Intern.* (Dec. 1987).

F.M. Caimi and M.S. Schmalz, "Geometric properties of non-differentiable contours: concurrent spatial harmonic and fractal analyses," *SPIE Particle Sizing and Spray Analysis* **573**, 21-30 (1985).

W.H. Carter, ed., *Applications of Speckle Phenomena*, Proc. SPIE **243** (1980).

J.C. Dainty, ed., *Laser Speckle and Related Phenomena* (Springer-Verlag, New York, 1975).

R.E. English and N. George, "Diffraction from a circular aperture: on-axis field strength," *Appl. Opt.* **26**, 2360-2363 (1987).

L.H. Enloe, "Noise-like structure in the image of diffusely reflecting objects in coherent illumination," *Bell System Tech. J.* **46**, 1479-1489 (1967).

R.K. Erf, ed., *Speckle Metrology* (Academic Press, New York, 1978).

M. Françon, *Laser Speckle and Applications in Optics* (Academic Press, New York, 1979).

H. Fujii, J. Uozumi, and T. Asakura, "Computer simulation study of image speckle patterns with relation to object surface profile," *J. Opt. Soc. Am.* **66**, 1222-1236 (1976).

N. George, "Speckle," *Applications of Speckle Phenomena*, W.H. Carter, ed., Proc. SPIE **243**, 124-140 (1980).

N. George, "Speckle at various planes in an optical system," *Opt. Eng.* **25**, 754-764 (1986).

N. George and A. Jain, "Space and wavelength dependence of speckle intensity," *Appl. Phys.* **4**, 201-212 (1974).

N. George and G.M. Morris, "Diffraction by serrated apertures," *J. Opt. Soc. Am.* **70**, 6-17 (1980).

- J. Gleick, *Chaos: Making a New Science* (Viking Penguin, 1987).
- L.I. Goldfischer, "Autocorrelation function and power spectral density of laser-produced speckle patterns," *J. Opt. Soc. Am.* **55**, 247-253 (1965).
- J.W. Goodman, "Statistical properties of laser speckle patterns," *Laser Speckle and Related Phenomena*, J.C. Dainty, ed. (Springer-Verlag, New York, 1975).
- J.W. Goodman, *Statistical Optics* (Wiley-Interscience, New York, 1985).
- E. Hecht and A. Zajac, *Optics*, (Addison-Wesley, Reading, Mass., 1979).
- J.R. Hodgkinson, "Particle sizing by means of the forward scattering lobe," *Appl. Opt.* **5**, 839-844 (1966).
- D.L. Jaggard and Y. Kim, "Diffraction by band-limited fractal screens," *J. Opt. Soc. Am. A* **4**, 1055-1062 (1987).
- E. Jakeman and J.H. Jefferson, "Scintillation in the Fresnel region behind a sub-fractal diffuser," *Optica Acta* **31**, 853-865 (1984).
- D.L. Jordan, R.C. Hollins, and E. Jakeman, "Experimental measurements of non-Gaussian scattering by a fractal diffuser," *Appl. Phys. B* **31**, 179-186 (1983).
- B.H. Kaye, "Specification of the ruggedness and/or texture of a fine particle profile by its fractal dimension," *Powder Technology* **21**, 1-16 (1978).
- B.H. Kaye, J.E. Leblanc, and P. Abbot, "Fractal description of the structure of fresh and eroded aluminum shot fineparticles," *Particle Charact.* **2**, 56-61 (1985).
- Y. Kim, *Wave Propagation in Bandlimited Fractal Media* (Ph.D. Thesis, University of Pennsylvania, 1987).

- Y. Kim and D.L. Jaggard, "Band-limited fractal model of atmospheric refractivity fluctuation," *J. Opt. Soc. Am. A* **5**, 475-480 (1988).
- Y. Kim and D.L. Jaggard, "Optical beam propagation in a band-limited fractal medium," *J. Opt. Soc. Am. A* **5**, 1419-1426 (1988).
- Y. Kim, H. Grebel, and D.L. Jaggard, "Diffraction from fractally serrated circular apertures," *Technical Digest of the Annual Meeting of the Optical Society of America*, 121 (1988).
- M.C. King, "Principles of Optical Lithography," in *VLSI Electronics: Microstructure Science* **1**, ed. N.G. Einspruch (Academic Press, New York, 1981).
- Y.A. Kravstov, C.M. Rytov, and V.I. Tatarskii, "Statistical problems in diffraction theory," *Usp. Fiz. Nauk* **115**, 239-262 (1975) [*Sov. Phys.-Usp.* **18**, 118-130 (1975)].
- A. Lakhtakia, N.S. Holter, V.K. Varadan, and V.V. Varadan, "Self-similarity in diffraction by a self-similar fractal screen," *IEEE Trans. on Antennas and Propag.* **AP-35**, 236-239 (1987).
- B.M. Levine, "Non-Gaussian speckle caused by thin phase screens of large root-mean-square phase variations and long single-scale autocorrelations," *J. Opt. Soc. Am. A* **3**, 1283-1292 (1986).
- S. Lowenthal and H. Arsenault, "Image formation for coherent diffuse objects: statistical properties," *J. Opt. Soc. Am.* **60**, 1478-1483 (1970).
- B.B. Mandelbrot, "How long is the coast of Britain? Statistical self-similarity and fractional dimension," *Science* **156**, 636-638 (1967).

- B.B. Mandelbrot, *The Fractal Geometry of Nature* (W.H. Freeman, New York, 1983).
- B.B. Mandelbrot, D.E. Passoja, and A.J. Paullay, "Fractal character of fracture surfaces of metals," *Nature* **308**, 712-722 (1984).
- J.C. Marron, "Accuracy of Fourier-magnitude estimation from speckle intensity correlation," *J. Opt. Soc. Am. A* **5**, 864-870 (1988).
- D.F.R. Mildner *et al.*, "Small-angle scattering of shaly rocks with fractal pore interfaces," *Appl. Phys. Lett.* **48**, 1314-1316 (1986).
- A.M. Mood, F.A. Graybill, and D.C. Boes, *Introduction to the Theory of Statistics*, 3rd ed. (McGraw-Hill, New York, 1963).
- G.M. Morris, *Serrated Apertures: Statistical Diffraction Theory and Experiments* (Ph.D. Thesis, California Institute of Technology, 1979).
- G.A. Niklasson, "Optical properties of gas-evaporated metal particles: effects of a fractal structure," *J. Appl. Phys.* **62**, 258-265 (1987).
- A.D. Poularikas and C. Katsinis, "Similarities of fourier spectra from random edge variations," *Opt. Eng.* **26**, 1120-1123 (1987).
- I.S. Reed, "On a moment theorem for complex Gaussian processes," *IRE Trans. Inf. Theory* **IT-8**, 194-195 (1962).
- L.F. Richardson, "The problem of contiguity: an appendix to *Statistics of Deadly Quarrels*," *General Systems Yearbook* **6**, 139-187 (1961).

B. Ruffing, "Application of speckle-correlation methods to surface-roughness measurement: a theoretical study," *J. Opt. Soc. Am. A* **3**, 1297-1304 (1986).

L.G. Shirley, *Laser Speckle from Thin and Cascaded Diffusers* (Ph.D. Thesis, University of Rochester, 1988).

L.G. Shirley and N. George, "Wide-angle diffuser transmission functions and far-zone speckle," *J. Opt. Soc. Am. a* **4**, 734-745 (1987).

L.G. Shirley and N. George, "Speckle from a cascade of thin diffusers," *J. Opt. Soc. Am. A* **6**, 765-781 (1989).

Special Issue on Speckle, *J. Opt. Soc. Am.* **66**, No. 11 (1976).

Special Issues on Speckle, *Opt. Eng.* **25**, Nos. 5-6 (1986).

N. Takai and T. Asakura, "Statistical properties of laser speckles produced under illumination from a multimode optical fiber," *J. Opt. Soc. Am. A* **2**, 1282-1290 (1985).

U. Vry, "Calculation of complex correlation coefficients of two speckle fields of different wavelengths and their application to two-wavelength-measurement techniques," *J. Opt. Soc. Am. A* **5**, 114-125 (1988).

P.-Z. Wong, J. Howard, and J.-S. Lin, "Surface roughening and the fractal nature of rocks," *Phys. Rev. Lett.* **57**, 637-640 (1986).

Appendix A

Aperture Generation Process

A.1. Theoretical Analysis

The serrated apertures used in the computer simulation, the fractal analysis, and the experiments described in this dissertation were computer-designed, with controlled diameter, roughness, correlation angle, and correlation function. This process was begun by generating a set of uncorrelated, Gaussian-distributed random numbers with zero mean. (For the apertures discussed, sets of 512 random numbers were used.) The uncorrelated data were then convolved with an appropriate window function to impose the desired correlation function, and the mean radius was added to each data point. These data are used as values of the aperture radius at equiangular increments, and the continuous aperture edge is determined from these discrete data by linear interpolation. In relation to speckle studies and modeling of rough surfaces, the first use of this data generation scheme appears in the literature by Fujii, Uozumi, and Asakura¹. Later this technique was used to generate the rough edges studied by George and Morris², as described in the thesis by Morris³.

This convolution technique, to be described here in detail, is used to generate members of aperture ensembles. We define the ensemble as follows. For each member of the ensemble, a different set of uncorrelated, Gaussian-distributed, random numbers is used. All of these starter sets belong to the same ensemble of starter sets and thus have the same ensemble variance; one can think of each set as a 512-element section of a much larger data set. The apertures are then generated by convolving the same window function with each starter set. In this appendix, we show the derivation of

expressions for the variance and correlation function of the aperture ensemble. Thus, ensemble expectations are used to define the statistical parameters of the uncorrelated data and of the apertures. For clarity, we define the important ensemble expectations here and compare them to the corresponding angular averages.

Consider an ensemble of apertures described by a collection of functions $S_i(a) = a + s_i(a)$, where the subscript i denotes the i^{th} member of the ensemble. For a given aperture, we define the angular mean radius by the following spatial average:

$$\{S_i(a)\}_a = \frac{1}{2\pi} \int_{-\pi}^{+\pi} S_i(a) da, \quad (\text{A.1})$$

where the subscripted braces, $\{\}_a$, are used to indicate the spatial average over angular coordinate a . Again using spatial averages, we define the angular variance as follows:

$$\{[S_i(a) - \{S_i(a)\}_a]^2\}_a = \frac{1}{2\pi} \int_{-\pi}^{+\pi} [S_i(a) - \{S_i(a)\}_a]^2 da. \quad (\text{A.2})$$

We define also the normalized angular correlation function:

$$\begin{aligned} & \frac{\{[S_i(a) - \{S_i(a)\}_a][S_i(a + \Delta a) - \{S_i(a + \Delta a)\}_a]\}_a}{\{[S_i(a) - \{S_i(a)\}_a]^2\}_a} \\ &= \frac{\frac{1}{2\pi} \int_{-\pi}^{+\pi} [S_i(a) - \{S_i(a)\}_a][S_i(a + \Delta a) - \{S_i(a + \Delta a)\}_a] da}{\{[S_i(a) - \{S_i(a)\}_a]^2\}_a}; \quad (\text{A.3}) \end{aligned}$$

We note that these spatially-averaged quantities will vary for different members of the ensemble.

In contrast, we define corresponding quantities for the ensemble with ensemble expectations or averages. The ensemble mean radius is given by the following expectation:

$$a = \langle S_i(a) \rangle = \lim_{M \rightarrow \infty} \left[\frac{1}{M} \sum_{i=1}^M S_i(a) \right], \quad (\text{A.4})$$

where, following the usual notation in the literature, we denote by angular brackets, $\langle \rangle$, the expectation taken over an ensemble. Similarly, we use ensemble expectations to define the notation for the ensemble variance by

$$\sigma^2 = \langle [S_i(a) - \langle S_i(a) \rangle]^2 \rangle = \lim_{M \rightarrow \infty} \left[\frac{1}{M} \sum_{i=1}^M [S_i(a) - \langle S_i(a) \rangle]^2 \right] \quad (\text{A.5})$$

and for the normalized ensemble correlation by

$$\begin{aligned} r_s(a_1, a_2) &= \frac{\langle [S_i(a_1) - a][S_i(a_2) - a] \rangle}{\sigma^2} \\ &= \frac{1}{\sigma^2} \lim_{M \rightarrow \infty} \left[\frac{1}{M} \sum_{i=1}^M [S_i(a_1) - a][S_i(a_2) - a] \right]. \end{aligned} \quad (\text{A.6})$$

We have simplified the notation for these ensemble expectations by using a to denote the ensemble mean radius; σ^2 , the ensemble variance; and $r_s(\Delta a)$, the ensemble correlation function. These quantities, which are constant due to the wide-sense stationarity of the apertures, are of particular interest in our study. The assumption of wide-sense stationarity is valid because of the arbitrary orientation of the aperture. Since no preference is given to any orientation, the statistical parameters must be independent of angular position. Due to the importance of these statistical parameters and that of the convolution method of generating correlated data in studying ensembles of surfaces¹, edges^{2,3}, and apertures, we will review³ and describe the foundations of the method in

the following paragraphs, with the goal of obtaining expressions for the variance and correlation function appropriate to this generation scheme.

We begin with a function $q(a)$, from an ensemble of functions, as input to a linear system which convolves $q(a)$ with window function $w(a)$ to yield output function $s(a)$. This output function would then be described by

$$s(a) = C \int_{-\infty}^{+\infty} q(\xi) w(a - \xi) d\xi, \quad (\text{A.7})$$

where C is a scaling factor. This output function describes the aperture serration, as in Eq. (2.15). For the input, we choose a Gaussian-distributed, wide-sense-stationary random process with mean value zero, variance σ_q^2 , and normalized correlation function $r_q(a_2 - a_1)$:

$$\langle q(a) \rangle = 0, \quad (\text{A.8})$$

$$\langle q^2(a) \rangle = \sigma_q^2, \quad (\text{A.9})$$

$$\frac{\langle q(a_1)q(a_2) \rangle}{\sigma_q^2} = r_q(a_2 - a_1). \quad (\text{A.10})$$

From this foundation, we wish to determine the variance σ^2 and the normalized correlation function $r_s(a_1, a_2)$ of the ensemble of functions which contains $s(a)$. Both of these quantities can be determined from the autocorrelation function of $s(a)$, which is defined

$$R_{12}(a_1, a_2) = \langle s(a_1)s(a_2) \rangle. \quad (\text{A.11})$$

The variance σ^2 is found by setting a_1 equal to a_2 in $R_{12}(a_1, a_2)$, and $r_q(a_1, a_2)$ is $R_{12}(a_1, a_2)$ normalized by σ^2 . Thus, we proceed to evaluate and simplify $R_{12}(a_1, a_2)$.

Using Eq. (A.7) in Eq. (A.11) and switching the order of integration and averaging, we have the following expression for the autocorrelation:

$$R_{12}(a_1, a_2) = C^2 \int_{-\infty}^{+\infty} \int_{-\infty}^{+\infty} \langle q(\xi') q(\xi'') \rangle w(a_1 - \xi') w(a_2 - \xi'') d\xi' d\xi'' \quad (\text{A.12})$$

We recognize $\langle q(\xi') q(\xi'') \rangle$ as the autocorrelation of input function q and use Eq. (A.10) to write:

$$R_{12}(a_1, a_2) = C^2 \sigma_q^2 \int_{-\infty}^{+\infty} \int_{-\infty}^{+\infty} r_q(\xi'' - \xi') w(a_1 - \xi') w(a_2 - \xi'') d\xi' d\xi'' \quad (\text{A.13})$$

The ξ'' integration in Eq. (A.13),

$$B_{rw} = \int_{-\infty}^{+\infty} r_q(\xi'' - \xi') w(a_2 - \xi'') d\xi'' \quad (\text{A.14})$$

is seen, with the variable change $\eta = \xi'' - \xi'$, to be a convolution integral:

$$B_{rw} = \int_{-\infty}^{+\infty} r_q(\eta) w[(a_2 - \xi') - \eta] d\eta \quad (\text{A.15})$$

We note that B_{rw} is the convolution of the correlation function of $q(a)$ with window function $w(a)$. With Eq. (A.15), we rewrite Eq. (A.13):

$$R_{12}(a_1, a_2) = C^2 \sigma_q^2 \int_{-\infty}^{+\infty} w(a_1 - \xi') B_{rw}(a_2 - \xi') d\xi' \quad (\text{A.16})$$

Now, with the variable change $\xi = a_1 - \xi'$, we see that R_{12} can also be written in convolution form:

$$R_{12}(a_2 - a_1) = C^2 \sigma_q^2 \int_{-\infty}^{+\infty} w(\xi) B_{rw}[(a_2 - a_1) + \xi] d\xi, \quad (\text{A.17})$$

where we note that R_{12} depends on a_2 and a_1 as the difference $a_2 - a_1$. Equation (A.17) is the general form for autocorrelation $R_{12}(a_2 - a_1)$. From it, we can determine the two quantities of interest: the variance of $s(a)$,

$$\sigma^2 = R_{12}(0) = C^2 \sigma_q^2 \int_{-\infty}^{+\infty} w(\xi) B_{rw}(\xi) d\xi, \quad (\text{A.18})$$

and the normalized correlation function,

$$r_s(a_2 - a_1) = \frac{R_{12}(a_2 - a_1)}{\sigma^2} = \frac{w(a) \star B_{rw}(a)}{\int_{-\infty}^{+\infty} w(\xi) B_{rw}(\xi) d\xi}. \quad (\text{A.19})$$

We can further simplify these expressions for our special case, in which the correlation function of $q(a)$ is narrow compared to the window function. If Δa is the correlation angle of input function $q(a)$ and L is the width of window function $w(a)$, then when $\Delta a \ll L$ the convolution representing B_{rw} in Eq. (A.15) causes only a slight spreading in the shape of the window function:

$$B_{rw}(a_2 - \xi') \approx \Delta a w(a_2 - \xi'). \quad (\text{A.20})$$

Using Eq. (A.20), we rewrite Eqs. (A.18) and (A.19) for this case of interest:

$$\sigma^2 \approx C^2 \sigma_q^2 \Delta a \int_{-\infty}^{+\infty} w^2(a) da; \quad (\text{A.21})$$

$$r_s(a_2 - a_1) \approx \frac{w(a) \star w(a)}{\int_{-\infty}^{+\infty} w^2(a) da}. \quad (\text{A.22})$$

For our calculations, σ_q^2 is the variance of the original (uncorrelated) data and Δa is the sample spacing. Scaling constant C can be chosen to produce the desired variance σ^2 for the correlated data, and \star denotes a convolution. We note that the variance and the correlation function are computed using the deterministic window function $w(a)$. For simplicity in our calculations, we choose to normalize the window function so that

$$\int_{-\infty}^{+\infty} w^2(a) da = 1 . \quad (\text{A.23})$$

Then, since $\Delta a = 1$ point, we preserve the variance by choosing $C = 1$,

$$\sigma^2 \approx \sigma_q^2 , \quad (\text{A.24})$$

and the normalized correlation function $r_s(a_2 - a_1)$ is simply the autoconvolution of window function $w(a)$,

$$r_s(a_2 - a_1) \approx w(a) \star w(a) . \quad (\text{A.25})$$

The relationships given in Eqs. (A.24) and (A.25) are approximate because they are based on the assumption that Δa is much smaller than the window width, a valid approximation in the discrete data scheme when the original data are uncorrelated and the convolving window is more than a few points wide.

In Eq. (A.25), we see that by choosing the appropriate window we can impose any desired correlation function on our uncorrelated data. The window function can be determined by taking a Fourier transform of Eq. (A.25),

$$R_s(f_a) = \left[W(f_a) \right]^2 , \quad (\text{A.26})$$

and then solving for $w(a)$:

$$w(\alpha) = F^{-1} \left\{ \left[R_g(f_\alpha) \right]^{1/2} \right\}, \quad (\text{A.27})$$

where $R_g(f_\alpha)$ and $W(f_\alpha)$ are the Fourier transforms of $r_g(\alpha)$ and $w(\alpha)$, respectively, and F^{-1} denotes an inverse Fourier transform.

As an example, consider the triangular correlation function of base width $2A$. From Eqs. (2.4) and (A.27), we have

$$w(\alpha) = F^{-1} \left\{ \left[A \operatorname{sinc}^2(\delta f_\alpha) \right]^{1/2} \right\} = F^{-1} \left\{ \left[A \frac{\sin^2(\pi A f_\alpha)}{(\pi A f_\alpha)^2} \right]^{1/2} \right\}. \quad (\text{A.28})$$

The square root of $\operatorname{sinc}^2(Af_\alpha)$ is not unique; we use $\operatorname{sinc}(Af_\alpha)$ so that the inverse transform yields the simple window function:

$$w(\alpha) = A^{-1/2} \operatorname{rect} \left(\frac{\alpha}{A} \right). \quad (\text{A.29})$$

Thus, convolving the uncorrelated data $q(\alpha)$ with the rectangular $w(\alpha)$ given by Eq. (A.29), we generate a function $s(\alpha)$ with a triangular correlation, Eq. (2.4).

To implement this aperture generation scheme, we employ a computer and fast Fourier transform (FFT) algorithms; the computational details that follow are incorporated in program "stat.fft.c", which is included later in this appendix. We start by generating uniformly distributed, uncorrelated data and convert it to normally distributed, uncorrelated data by use of a transformation routine. We next define the desired correlation function. The FFT is used to Fourier-transform both the uncorrelated data and the correlation function. Taking the square root of the transform of the correlation function gives us the transform of the window function; see Eq. (A.27). This square root and the transformed data are multiplied together and then inverse-Fourier-

transformed, yielding the correlated, zero-ensemble-mean aperture function. Adding the desired ensemble mean radius value to each data point is the final step in preparing the aperture function. This function is Gaussian-distributed and has the desired ensemble mean, variance, correlation angle and correlation function.

When using a sequence of correlated random numbers to model a serrated, circular aperture, an important consideration is the correlation of the last few numbers in the sequence with the first few. The starting and ending points of the circle should not be uncorrelated. The FFT method of convolution we use assures a cyclic convolution⁴, so that the ends of the sequence are properly correlated.

The computer output format of the design program is compatible with the program used to calculate the Fourier transform of the serrated aperture and also with the software used to calculate the fractal dimension of the aperture. The aperture designs were also used in the optical experiments. In the photolithographic case, the data were plotted angularly for use as the outline of a serrated, circular aperture. This 10X enlargement was filled and used as artwork from which chrome-on-glass masks were made photolithographically by Applied Image⁵, as described in Section 5.3.2. For apertures made by electron-beam lithography, the data were formatted for input to the computer drafting program AutoCAD⁶, which was used to generate instructions for drawing the apertures. The AutoCAD files were sent to Photo Sciences⁷, where the drawing instructions were converted to instructions for the electron-beam plotter. This plotter was used to produce apertures in chrome on glass, as described in Section 5.3.3.

A.2. Computer Program

In this section, we provide a copy of the code for the program "stat.fft.c" used to generate the serrated apertures. This program is based on the method discussed above and is written in the C programming language for use on the Masscomp 6700 computer, a UNIX system.

```

***          stat.fft.c

          To generate serrated apertures of specified statistics
***/

#include <stdio.h>
#include <math.h>
extern int fft(), ibitr(), ifft(), swapdata();

main() {

int M,mp,nphi,ms,kk,ij,ij1,ij2,ij3,i,m,nrho,wflag,sflag,rflag;
float mean,rlamda,z0,delta,ravg,sigmad,sigmac;
float phimax,phimin,pstep,rhomin,rhomin,angmean,angsigma;
float rstep,small,C,arc,rk,w1,sj,lg,sum,a;
double *sr,*si,*rr,*ri,*wr,*wi;
double *dsr,*dsi,*drr,*dri,*dwr,*dwi;
double x,y,z,vrr,vri,vsr,vsr,vwr,vwi,arg,arg2,ctr,pi;
int Mpow, itest;
float gamma,var,sumsq,M2,ftest;
unsigned seed;
double *buf;
char *calloc();
FILE *fout,*fplot,*fwin,*fty,*fopen();

/**/ read input constants /**/

fscanf (stdin,
"%f%f%f%d%f%f%f%f%f%f%f%f%f%f"
"%f%f%f%f%f%f%f",
&rlamda, &z0, &m, &delta, &mp, &ravg, &sigmad,
&phimax, &phimin, &pstep, &rhomin, &rhomin,
&rstep, &small, &wflag, &sflag, &rflag);

/**/ define constants /**/

fplot = fopen ("stat.plot","w");
fty = fopen ("/dev/tty","r");

```



```

for (i=0; i<m; + i){
    x = buf[i]/lg;
    z = (double)((float)random0)/lg;
    if (z == 0.0) z = 0.0000001;
    y = log(z) * -2.0;
    z = sqrt(y);
    x = cos(2*pi*x);
    y = z * x;
    buf[i] = y * sigmac;
    *rr = buf[i];
    *ri = 0.;
    if (i + m < M) {
        *(rr + m) = buf[i];
        *(ri + m) = 0.;
    }
    rr + +;
    ri + +;
}

rr = drr;
ri = dri;

/** define correlation function */

/** triangular correlation */

if (wflag == 1) {
    for (i=0; i<M; + i) {
        if (i < M/2 - ms) *wr = 0.;
        else if (i < M/2 + ms) *wr = 1. - fabs((float)(i - M/2))/(float)ms;
        else *wr = 0.;
        *wi = 0.;
        wr + +;
        wi + +;
    }
}

/** negative exp correlation */

else if (wflag == 3) {
    for (i=0; i<M; + i) {
        arg = (float)(i - M/2)/ms;
        arg2 = -fabs(arg);
        *wr = exp(arg2);
        *wi = 0.;
        wr + +;
        wi + +;
    }
}
}

```

```

/** Gaussian correlation */

else if (wflag == 4) {
    for (i=0; i<M; ++i) {
        arg = (float)(i-M/2)/ms;
        arg2 = -arg*arg;
        *wr = exp(arg2);
        *wi = 0.;
        wr ++;
        wi ++;
    }
}

/** Eiffel correlation (0.25) */

else if (wflag == 5) {
    for (i=0; i<M; ++i) {
        if (i<M/2-ms) *wr = 0.;
        else if (i<M/2+ms) *wr = 1. - pow(fabs((float)(i-M/2))/(float)ms, 0.25);
        else *wr = 0.;
        *wi = 0.;
        wr ++;
        wi ++;
    }
}

/** Eiffel correlation (0.5) */

else if (wflag == 6) {
    for (i=0; i<M; ++i) {
        if (i<M/2-ms) *wr = 0.;
        else if (i<M/2+ms) *wr = 1. - pow(fabs((float)(i-M/2))/(float)ms, 0.5);
        else *wr = 0.;
        *wi = 0.;
        wr ++;
        wi ++;
    }
}

else {
    fprintf(stderr, "%d not a valid window function number\n",
            wflag);
}

wr = dwr;
wi = dwi;
rr = drr;
ri = dri;

```

```

for (i = 0; i < M; ++i) {
    fprintf(fwin, "%fn", *wr);
    wr++;
}
wr = dwr;

/** fft correlation function & random numbers ***/

fft(drr,dri,M,Mpow);
fft(dwr,dwi,M,Mpow);

/** take square root of transformed correlation function ***/

for (i = 0; i < M; ++i) {
    if (*wr < 0) *wr = -(*wr);
    *wr = sqrt(*wr);
    wr++;
}
wr = dwr;

/** multiply & inverse fft ***/

for (i = 0; i < M; ++i) {
    vrr = *rr++;
    vri = *ri++;
    vwr = *wr++;
    vwi = *wi++;
    *sr = vrr*vwr - vri*vwi;
    *si = vrr*vwi + vri*vwr;
    sr++;
    si++;
}

sr = dsr;
si = dsi;
rr = drr;
ri = dri;
wr = dwr;
wi = dwi;

ifft(sr,si,M,Mpow);

/** calculate angular mean and standard deviation ***/

sum = 0.;
sumsq = 0.;

```

```
for (i = 0; i < m; ++i) {
    sum = sum + *sr;
    sumsq = sumsq + *sr * *sr;
    sr ++;
}
angmean = sum/m;
var = sumsq/m - mean*mean;
angsigma = sqrt((double)var);
sr = dsr;

/** add bias and write radius values to file */

for (ij = 0; ij < m; ++ij) {
    *sr = *sr + ravg;
    fprintf(stdout, "%d %f\n", ij, *sr);
    fprintf(fplot, "%f ", *sr);
    sr ++;
}
fprintf(stderr, "mean %f sigma %f\n", mean, sigmaa);
fprintf(stdout, "%f %f\n", mean, sigmaa);
}
```

Appendix A References

1. H. Fujii, J. Uozumi, and T. Asakura, "Computer simulation study of image speckle patterns with relation to object surface profile," *J. Opt. Soc. Am.* **66**, 1222-1236 (1976).
2. N. George and G.M. Morris, "Diffraction by serrated apertures," *J. Opt. Soc. Am.* **70**, 6-17 (1980).
3. G.M. Morris, *Serrated Apertures: Statistical Diffraction Theory and Experiments* (Ph.D. Thesis, California Institute of Technology, 1979).
4. R. N. Bracewell, *The Fourier Transform and its Applications* (McGraw-Hill, New York, 1978), p. 362-363.
5. Applied Image, 1653 E. Main St., Rochester, NY 14609.
6. AutoCAD is a product of Autodesk, Inc., Sausalito, CA.
7. Photo Sciences, 2542 West 237th St., Torrance, CA 90505.

Appendix B

Generation of the Curves Shown in Fig. 3.1.

Plots of four functions, each a single realization of a different random process, are shown in Fig. 3.1. To generate each of these functions, we used the convolution method described in Appendix A. Herein, the reader will find details on the rms roughness, correlation length, and correlation function used in the design of each of these curves.

Actually, that's a lie. The convolution method was not used to generate the function shown in Fig. 3.1(a), since this function is just a straight line. However, by setting the rms roughness equal to zero in the generation process, we could have easily produced this curve. More interesting are the details involved in generating the functions from Fig. 3.1(b)-(d). For Fig. 3.1(b), we choose the triangular correlation function, given by Eq. (3.42) and shown in Fig. B.1(a). The rms roughness used in the design is 0.50 mm; the correlation length, 0.436 mm. The fractal dimension of this realization is 1.24. For the next function, shown in Fig. 3.2(c), the correlation function is sharper, as seen in Fig. B.1(b). This is the Eiffel function,

$$\text{Eif} \left(\frac{\Delta x}{X}, \beta \right) = \left\{ \begin{array}{ll} 1 - \left(\frac{|\Delta x|}{X} \right)^\beta, & \text{for } |\Delta x| \leq X, \\ 0, & \text{otherwise} \end{array} \right\}, \quad \beta = 0.5, \quad (3.43)$$

which is described more thoroughly in Section 3.4.4. For present purposes, we simply note the shape of this correlation function, in particular the sharpening of the peak. The curve in Fig. 3.1(c) also has an increased roughness, 0.75 mm, and a decreased correlation length, 0.316 mm, in the design. The resulting fractal dimension is 1.67 for this particular curve. Finally, for the function shown plotted in Fig. 3.1(d), we pull out most of the stops

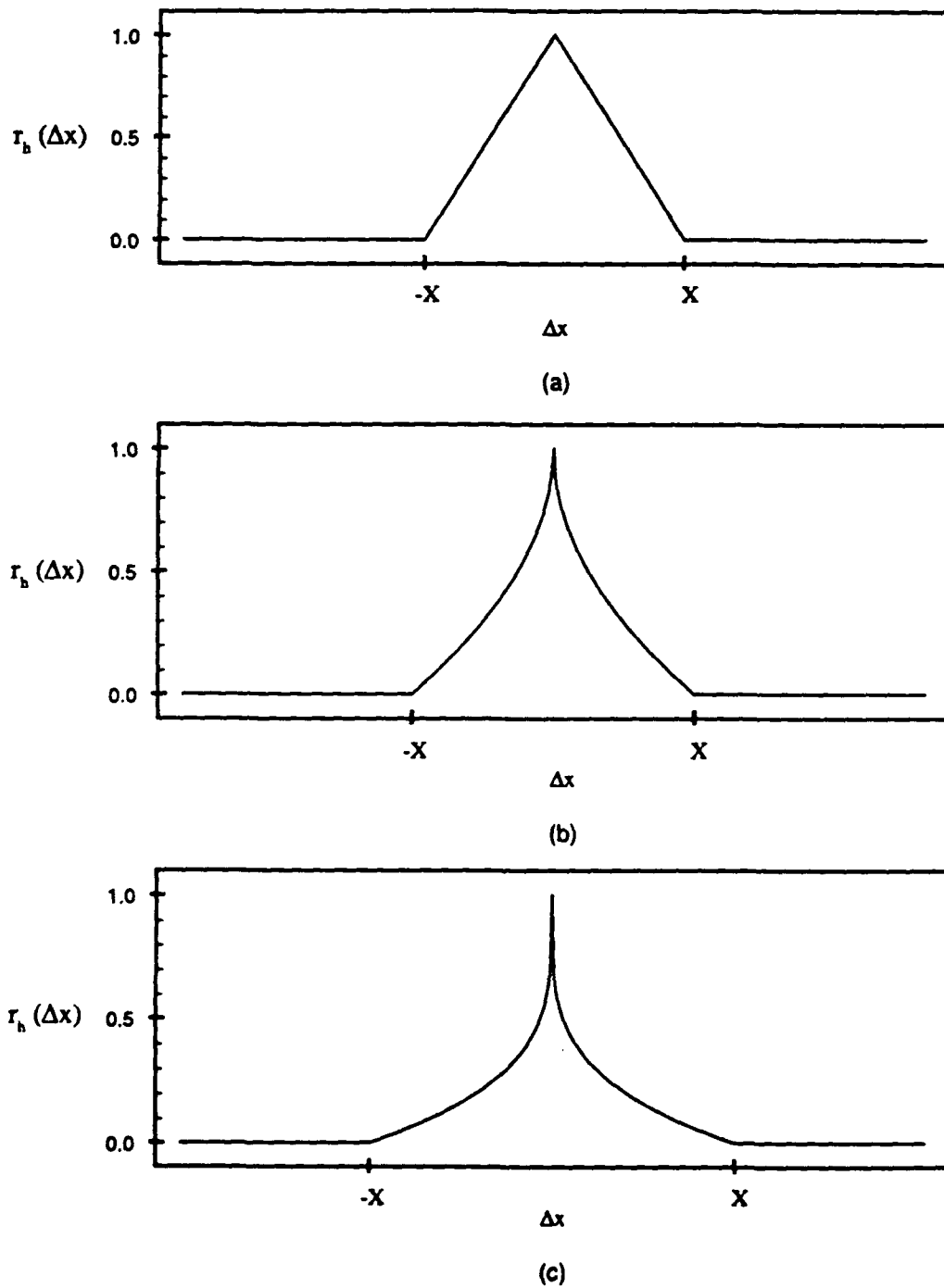


Fig. B.1. Correlation functions used in designing the curves shown in Fig. 3.1: (a) for Fig. 3.1(b), the triangular function, Eq. (B.1); (b) for Fig. 3.1(c), the Eiffel function, Eq. (B.2), $\beta=0.5$, and (c) for Fig. 3.1(d), the Eiffel function, $\beta=0.25$. Width X is chosen for each function to give the desired correlation angle.

and use the Eiffel function with β equal to 0.25, shown in Fig. B.11(c), for the correlation function and choose an rms roughness equal to 0.70 mm and a correlation length of 0.249 mm for the design. With these values for the edge parameters, we have produced a function with a fractal dimension of 1.95.

The choice of parameters for each of the cases discussed is not done blindly; we used Fig. 3.14 as a guide. In this figure, we have plotted the fractal dimension versus the ratio of the roughness of the edge to the correlation length for several correlation functions. Although the detailed description of this plot is left until the end of Chapter 3, the reader can see now that, with this plot, we are able to find a suitable set of edge parameters for use in generating an edge with a fractal dimension near a particular value.

Appendix C

Programs for Computing the Fractal Dimension

In Section 3.1.3, two procedures were outlined for determining the fractal dimension of a serrated, circular aperture. In this appendix, we include the two major computer programs used in these procedures. The first, "frac.c", calculates the perimeter estimates needed to plot the Richardson curve of the aperture. Program "grid.c" is used to count the aperture-grid intersections in the grid interrogation method. Both programs are written in the C programming language for use on a Masscomp 6700 UNIX-based computer.

```
/**/ frac.c
    To calculate data for an aperture's Richardson curve.
    In stepping, the farthest intersection is used.
/**/

#include <math.h>
#include <stdio.h>

main() {

int ia[6],i, j, k, l, M, m, *flag, f1, f2, window, Max, intflag, K;
float f[13];
double *s, *x, *y, *sl, *b, D, xp, yp, xp2, yp2, *P, dsq, dlsq, drsq;
double A, B, C, *eps, epgs, *epsq, dx, dy, arc, pi, div, divsq, xx;
double ravg, rmin, dummy, *alph, r1, r2, d1, d2, min, max, delta, sigma, arg;
double y1, y2, ang1, ang2;
char *calloc();
FILE *fty, *fopen(), *fout;

fty = fopen ("/dev/tty", "r");
fout = fopen ("frac.out", "w");

/**/ read header /**/

fscanf (stdin,

"% f\n% f\n% d\n% f\n% d\n% f\n% f\n% f\n% f\n% f\n% f\n% f\n% d\n% d\n% d\n"
&f[1], &f[2], &ia[1], &f[3], &ia[2], &f[4], &f[5],
&f[6], &f[7], &f[8], &f[9], &f[10],
```

```

    &f[11], &f[12], &ia[3], &ia[4], &ia[5]);

fprintf (fout,

"%f\n%f\n%d\n%f\n%d\n%f\n%f\n%f\n%f\n%f\n%f\n%f\n%f\n%d\n%d\n%d\n",
    f[1], f[2], ia[1], f[3], ia[2], f[4], f[5],
    f[6], f[7], f[8], f[9], f[10],
    f[11], f[12], ia[3], ia[4], ia[5]);

/** define variables; set up arrays ***/

m = ia[1];      /* # pts in aperture */
ravg = f[4];    /* average radius */
rmin = ravg;    /* minimum radius */
pi = acos(0.)*2.;
arc = 2*pi/m;
delta = f[3];  /* correl. angle */
sigma = f[5];  /* rms roughness */
window = ia[3]; /* correl. fn. i.d. */
div = 1.2;    /* division factor for subsequent step sizes */
divsq = div*div;

s = (double *) calloc (m + 1, sizeof(double)); /* aperture radii */
x = (double *) calloc (m + 1, sizeof(double)); /* cartesian coordinates */
y = (double *) calloc (m + 1, sizeof(double)); /* of aperture */
sl = (double *) calloc (m + 1, sizeof(double)); /* slope, intercept of */
b = (double *) calloc (m + 1, sizeof(double)); /* line segs. */
alph = (double *) calloc (m + 1, sizeof(double)); /* angular coordinate */
flag = (int *) calloc (m + 1, sizeof(int)); /* for infinite slope */

/** read radius data ***/

for (i = 0; i < m; + + i) {
    fscanf (stdin, "%d%lf", &s[i]);
    fprintf (fout, "%d %f\n", i, s[i]);
    if (s[i] < rmin) rmin = s[i];
}
s[m] = s[0];

/** determine # of step sizes to reach resolution limit ***/

M = (log10(2*pi*ravg/4.) - log10(arc*ravg))/log10(div);
fprintf (stderr, "M = %d\nMax value: ", M);
fscanf (fty, "%d", &Max);
fprintf (stderr, "m %d Max %d\n", M, Max);
fprintf (fout, "%d\n", Max);

P = (double *) calloc (Max + 1, sizeof(double)); /* perimeter
estimates */
eps = (double *) calloc (Max + 10, sizeof(double)); /* step sizes... */

```

```

epsq = (double *) calloc (Max + 1, sizeof(double));    /*squared */
eps[0] = pi*ravg/2.5;
epsq[0] = eps[0]*eps[0];

/** Calculate x, y, m, b arrays ***/

x[0] = s[0];
y[0] = 0.;
alph[0] = 0.;
for (i = 1; i <= m; ++i) {
    alph[i] = i*arc;
    x[i] = s[i]*cos(alph[i]);
    y[i] = s[i]*sin(alph[i]);
    if ((D = x[i] - x[i-1]) != 0) {
        sl[i-1] = (y[i] - y[i-1])/D;
        b[i-1] = (y[i-1]*x[i] - y[i]*x[i-1])/D;
        flag[i-1] = 0;
    }
    else {
        flag[i-1] = 1;
    }
}

/** Walk around aperture; find endpoints of increments and add to P ***/

for (i = 0; i <= Max; ++i) {
    fprintf(stderr, "%d ", i);
    j = 0;          /* starting point */
    P[j] = 0.;
    xp = x[0];     /* endpoint of */
    yp = y[0];     /* step */
    arg = 1. - epsq[i]/(2*rmin*rmin);
    K = acos(arg)/arc + 1;          /* K is the estimated # of
    points */
    k = K;         /* per step along the
    aperture. */
    dx = xp - x[k]; /* eps = 2*rmin*rmin*
    (1-cos(K*arc)) */
    dy = yp - y[k];
    epsg = dx*dx + dy*dy;
    while (j < m) {
        intflag = 0;

/** Search for intersections ***/

        while (intflag == 0) {
            dsq = ((xp-x[k+1])*(y[k]-y[k+1])-(yp-y[k+1])*(x[k]-x[k+1]));
            dsq = dsq*dsq/((x[k]-x[k+1])*(x[k]-x[k+1]) + (y[k]-y[k+1])*(y[k]-y[k+1]));
            if (dsq <= epsq[i]) {
                disq = (xp-x[k])*(xp-x[k]) + (yp-y[k])*(yp-y[k]);
            }
        }
    }
}

```

```

drsq = (xp-x[k+1])*(xp-x[k+1]) + (yp-y[k+1])*(yp-y[k+1]);
if (dlsq >= epsq[i] || drsq >= epsq[i]) {

```

```

    /*** Solve for roots:

```

```

        (r-xp)*(r-xp) + (sl*r + b-yp)*(sl*r + b-yp) = epsq ***/

```

```

        A = 1 + sl[k]*sl[k];
        B = 2*(sl[k]*(b[k]-yp) - xp);
        C = xp*xp + (b[k]-yp)*(b[k]-yp) - epsq[i];
        r1 = (sqrt(B*B-4*A*C) - B)/(2*A);
        r2 = (0-sqrt(B*B-4*A*C) - B)/(2*A);
        if (x[k] < x[k+1]) {
            min = x[k];
            max = x[k+1];
        }
        else {
            min = x[k+1];
            max = x[k];
        }
        if (r1 >= min && r1 <= max) f1 = 1;
        else f1 = 0;
        if (r2 >= min && r2 <= max) f2 = 1;
        else f2 = 0;

```

```

    /*** Calculate corresponding y-value ***/

```

```

    /*** Only one root in interval ***/

```

```

        if (f1 == 1 && f2 == 0) {
            xp2 = r1;
            yp2 = sl[k]*xp2 + b[k];
            intflag = 1;
        }
        else if (f1 == 0 && f2 == 1) {
            xp2 = r2;
            yp2 = sl[k]*xp2 + b[k];
            intflag = 1;
        }
    }

```

```

    /*** Both roots in interval (choose the closer) ***/

```

```

        else if (f1 == 1 && f2 == 1) {
            y1 = sl[k]*r1 + b[k];
            y2 = sl[k]*r2 + b[k];
            ang1 = atan2(y1, r1);
            if (ang1 < 0) ang1 = ang1 + 2*pi;
            ang2 = atan2(y2, r2);
            if (ang2 < 0) ang2 = ang2 + 2*pi;
            if (ang1 > ang2) {
                xp2 = r1;
                yp2 = y1;
            }
        }
    }

```

```

        else {
            xp2 = r2;
            yp2 = y2;
        }
        intflag = 1;
    }
}
}
if (intflag == 0) { /* No root found: reduce k */
    -k;
}
else break; /* step complete; next step */
}

/** Increment P[i]; reinitialize */

P[i] = P[i] + eps[i];
xp = xp2;
yp = yp2;
j = k;
k = K + k;
if (k >= m-1) {
    dx = xp - x[m];
    dy = yp - y[m];
    epsg = dx*dx + dy*dy;
    if (epsg <= epsq[i]) {
        P[i] = P[i] + sqrt(epsg);
        break;
    }
    else k = m-1;
}
}
eps[i+1] = eps[i]/div;
epsq[i+1] = epsq[i]/divsq;

/** Write data to file */

fprintf (fout, "%f %f; %f %f\n",
        eps[i], P[i], log10(eps[i]), log10(P[i]));
}
fprintf (stderr, "\n");
fprintf (stdout, "%d\n", Max + 1);
for(i = Max; i >= 0; --i) {
    fprintf(stderr, "%d ", i);
    fprintf (stdout, "%f\n", log10(P[i]));
    fprintf (stdout, "%f\n", log10(eps[i]));
}
}
}

```

```

/** grid.c

    To calculate data for the grid interrogation
    curve of a serrated aperture (after Kaye).

*/

#include <math.h>
#include <stdio.h>

main () {

int m, window, seed, i, M, Max, ix, iy, nx, ny, xl, xr, nxmax, nymax;
int ycount, xcount, upcount, j, k, ia[6], nyp1, oldval;
float f[13];
double delta, mean, sigma, Ds, ymin, ymax, xmax, xmin, *g, gmin, *sum, div;
double *s, *x, *y, *px, *py, *sl, *b, newmean, sigmaa, *val, *Y, *X, pi, arc;
double alpha, *d;
char *calloc();
FILE *fopen(), *fty, *fout;

fout = fopen("grid.out", "w");
fty = fopen("/dev/tty", "r");

fscanf (stdin,

"%f\n%f\n%d\n%f\n%d\n%f\n%f\n%f\n%f\n%f\n%f\n%f\n%d\n%d\n%d\n",
",
    &f[1], &f[2], &ia[1], &f[3], &ia[2], &f[4], &f[5],
    &f[6], &f[7], &f[8], &f[9], &f[10],
    &f[11], &f[12], &ia[3], &ia[4], &ia[5]);

/** Define variables; set up arrays */

m = ia[1];    /* # pts in aperture */
mean = f[4];    /* avg. radius */
xmin = xmax = ymin = ymax = 0.;
delta = f[3];    /* correl. angle */
sigma = f[5];    /* rms roughness */
window = ia[3];    /* correl. fn. i.d. */
pi = acos(0.)*2.;
arc = 2*pi/m;

s = (double *) calloc (m + 1, sizeof (double)); /* aperture radii */
x = (double *) calloc (m + 1, sizeof (double)); /* cartesian */
y = (double *) calloc (m + 1, sizeof (double)); /* coordinates */
d = (double *) calloc (m + 1, sizeof (double)); /* difference in x-coords. */
sl = (double *) calloc (m + 1, sizeof (double)); /* slope, intercept of */
b = (double *) calloc (m + 1, sizeof (double)); /* line segment */

/** Read aperture radii, calculate Cartesian data */

```

```

for (i = 0; i < m; ++i) {
    fscanf(stdin, "%*d%f", &s[i]);
    alpha = i*arc;
    x[i] = s[i]*cos(alpha);
    if (xmin > x[i]) xmin = x[i];
    else if (xmax < x[i]) xmax = x[i];
    y[i] = s[i]*sin(alpha);
    if (ymin > y[i]) ymin = y[i];
    else if (ymax < y[i]) ymax = y[i];
}
x[m] = x[0];
y[m] = y[0];

div = 1.2; /* division factor for subsequent grid sizes */
Ds = 2*pi*mean/m; /* estimated segment length */

/** Determine # of grid sizes to reach resolution limit ***/

if (ymax-ymin > xmax-xmin)
    M = (log10((ymax-ymin)/2.) - log10(Ds))/log10(div);
else
    M = (log10((xmax-xmin)/2.) - log10(Ds))/log10(div);
fprintf(stderr, "M = %d; Max = ", M);
fscanf(fty, "%d", &Max);
fprintf(stderr, "M = %d, Max = %d\n", M, Max);
fprintf(fout, "%d\n", Max);

g = (double *) calloc (Max + 2, sizeof(double)); /* grid size */
sum = (double *) calloc (Max + 2, sizeof(double)); /* # of intersections */

g[0] = pi*mean/2.5; /* largest (1st) grid size */
gmin = g[0]/pow(div, (double)Max + 1.); /* smallest grid size */
nxmax = (xmax-xmin)/gmin + 1;
nymax = (ymax-ymin)/gmin + 1;

val = (double *) calloc ((nxmax + 1)*(nymax + 1), sizeof(double)); /* flag for
intersection type */
px = (double *) calloc (nxmax + 1, sizeof(double)); /* Cartesian
values for */
py = (double *) calloc (nymax + 1, sizeof(double)); /* grid
points */
X = (double *) calloc (m + 1, sizeof(double)); /* Cartesian values for */
Y = (double *) calloc (m + 1, sizeof(double)); /* intersections */

/** Calculate slopes and intercepts for aperture line segments ***/

for (j = 0; j < m; ++j) {
    d[j] = x[j + 1] - x[j];
    if (d[j] != 0.) {
        sl[j] = (y[j + 1] - y[j])/d[j];
    }
}

```

```

        b[j] = y[j] - sl[j]*x[j];
    }
}

for (i = 0; i <= Max; ++i) {
    fprintf(stderr, "%d ", i);
    sum[i] = 0.;
    nx = (xmax-xmin)/g[i] + 1;
    ny = (ymax-ymin)/g[i] + 1;
    nyp1 = ny + 1;

    /** Assign Cartesian values to grid points ***/

    for (ix = 0; ix <= nx; ++ix) {
        px[ix] = xmin + ix*g[i];
    }
    for (iy = 0; iy <= ny; ++iy) {
        py[iy] = ymin + iy*g[i];
    }
    val[0] = 0;

    /** Find intersections ***/

    for (ix = 0; ix <= nx; ++ix) {
        ycount = 0;
        for (j = 0; j < m; ++j) {
            if ((x[j] <= px[ix] && x[j + 1] >= px[ix]) || (x[j] >= px[ix] && x[j + 1] <= px[ix])) {
                if (d[j] != 0.) {
                    Y[ycount] = sl[j]*px[ix] + b[j];
                    ++ycount;
                }
                else {
                    Y[ycount] = y[j];
                    ++ycount;
                }
            }
        }
        for (iy = 0; iy <= ny; ++iy) {
            val[ix*nyp1 + iy] = -2.;
            upcount = 0;
            for (k = 0; k < ycount; ++k) {
                if (py[iy] == Y[k]) {
                    val[ix*nyp1 + iy] = -1;          /* aperture point on grid */
                    break;
                }
                else if (py[iy] < Y[k]) ++upcount; /* upcount: # intersections above */
            }
            /* this grid point */
            if (val[ix*nyp1 + iy] != -1) {
                if ((float)(upcount/2) == (float)upcount/2.)
                    val[ix*nyp1 + iy] = 0;          /* even # above */
                else

```

```

        val[ix*nyp1 + iy] = 1;           /* odd # above */
    }
}

/** Add up intersections in both directions */

for (ix=0; ix<=nx; ++ix) {
    oldval = 0;
    for (iy=0; iy<=ny; ++iy) {
        if (val[ix*nyp1 + iy] == -1) sum[i] = sum[i] + 0.5;
        else if (oldval != -1 && val[ix*nyp1 + iy] != oldval) sum[i] = sum[i] + 1.;
        oldval = val[ix*nyp1 + iy];
    }
}
for (iy=0; iy<=ny; ++iy) {
    if (py[iy]<y[0]) oldval = 1;
    else if (py[iy]>y[0]) oldval = 0;
    else oldval = -1;
    for (ix=0; ix<=nx; ++ix) {
        if (val[ix*nyp1 + iy] == -1) sum[i] = sum[i] + 0.5;
        else if (oldval != -1 && val[ix*nyp1 + iy] != oldval) sum[i] = sum[i] + 1.;
        oldval = val[ix*nyp1 + iy];
    }
}

/** Output */

fprintf(stderr, "%d %f %fn", i, g[i], sum[i]);
g[i+1] = g[i]/div;
}
fprintf(stderr, "\n");
for (i = Max; i >= 0; --i) {
    fprintf(stdout, "%f, %f; %f, %fn", g[i], g[i]*sum[i], log10(g[i]),
log10(g[i]*sum[i]));
    fprintf(fout, "%f %fn", log10(g[i]), log10(g[i]*sum[i]));
}
}

```